

# Efficient modeling and mitigation of quadrupole errors in synchrotrons and their beam transfer lines

Dissertation  
zur Erlangung des Doktorgrades  
der Naturwissenschaften

vorgelegt beim Fachbereich Physik  
der Johann Wolfgang Goethe-Universität  
in Frankfurt am Main

von

Dominik Vilsmeier

aus Regensburg



Frankfurt 2023  
(D 30)

Vom Fachbereich Physik der  
Johann Wolfgang Goethe-Universität als Dissertation angenommen.

**Dekan:**

Prof. Dr. Roger Erb

**Gutachter/in:**

Prof. Dr. Holger Podlech

Dr. Mei Bai

**Datum der Disputation:**

10. Juni 2024





## Zusammenfassung

Diese Arbeit beschäftigt sich mit der Bestimmung von Fehlern der Quadrupolfeldstärken in Synchrotronen sowie der Minderung des Einflusses ebensolcher Fehler in Strahltransportlinien. Der Beschleunigerkomplex wird hierbei in seiner Gesamtheit betrachtet, indem die Notwendigkeit verdeutlicht wird, die möglichen Fehlerquellen in allen Abschnitten einer Beschleunigeranlage gleichermaßen zu betrachten, um gleichbleibend gute Konditionen für die laufenden Experimente zu gewährleisten. Während die vorgestellten Methoden exemplarisch für das SIS18 Synchrotron und die HEST Transferlinien am GSI Helmholtzzentrum für Schwerionenforschung untersucht wurden, sind diese ebenso relevant und anwendbar für die zukünftigen Beschleunigeranlagen und Transferlinien der Facility for Antiproton and Ion Research in Europe (FAIR).

Teil 1 dieser Arbeit beschäftigt sich mit dem Problem der Bestimmung von Fehlern der Quadrupolfeldstärken mittels Response-Matrix Messungen an Synchrotronen. Der Fokus der Untersuchung liegt hierbei auf dem Einfluss der Verfügbarkeit von Steerer Magneten und Strahlage Monitoren (BPMs) sowohl auf die Lösbarkeit des dazugehörigen inversen Problems als auch auf die durch die Messungenauigkeit bedingten Abweichungen der zu bestimmenden Fehler der Quadrupolfeldstärken. Hierfür wird zunächst ein mathematischer Ausdruck für die Ableitung der Response-Matrix bezüglich der Quadrupolfeldstärken, also für die Jacobi-Matrix, hergeleitet. Diese analytische Version der Jacobi-Matrix wird weiter untersucht, um schließlich die Lösbarkeit des inversen Problems bezüglich der Verfügbarkeit von Steerern und BPMs herzuleiten und mithilfe von konkreten Bedingungen zu beschreiben. Diese analytisch erzielten Ergebnisse werden darüber hinaus mithilfe von Simulationen belegt. Ein Defekt der Jacobi-Matrix impliziert, dass das dazugehörige inverse Problem keine eindeutige Lösung für den gewählten Parametersatz an Quadrupolfeldstärken zulässt. Es wird gezeigt, dass bestimmte Abfolgen von Quadrupol-Magneten, welche nicht durch Steerer oder BPMs unterbrochen sind, einen solchen Defekt der Jacobi-Matrix hervorrufen. Betrachtet man die horizontale oder vertikale Response-Matrix separat, so führt eine Abfolge von drei oder mehr Quadrupolmagneten zu einem Defekt der Jacobi-Matrix. Werden beide Response-Matrizen gemeinsam berücksichtigt, so führt eine Abfolge von sechs oder mehr Quadrupolmagneten (bzw. fünf oder mehr Quadrupolmagneten falls  $Q_h - Q_v = \text{Ganzzahl}$ , wobei  $Q_{h,v}$  der horizontale und vertikale Tune sind) zu einem Defekt der Jacobi-Matrix. Des

---

Weiteren wird der Einfluss der Verfügbarkeit von Steuerern und BPMs auf die Fehlerfortpflanzung der Messungenauigkeiten mithilfe der Jacobi-Matrix untersucht. Die Singulärwerte der Jacobi-Matrix geben zusammen mit den dazugehörigen Singulärvektoren Aufschluss über die Fehlerfortpflanzung in Bezug auf die verschiedenen Quadrupolfeldstärken des gewählten Parametersatzes. Die Verfügbarkeit von Steuerern und BPMs ist hierbei maßgeblich für die Existenz von bestimmten Parameterkombinationen, die besonders anfällig für den Einfluss der Messungenauigkeit im Rahmen der Fehlerfortpflanzung sind. Dies impliziert, dass die betroffenen Kombinationen an Parametern weniger genau im Rahmen der Lösung des inversen Problems bestimmt werden können. Eine solche Kombination an Quadrupolfeldstärken existiert für das SIS18 Synchrotron am GSI Helmholtzzentrum für Schwerionenforschung in Form der sogenannten D- und T-Quadrupole. Diese Quadrupole zeichnen sich durch einen geringen Abstand im Sinne des Phasenvorschubs der Betatronschwingungen aus und sind zudem weder durch Steerer Magnete noch durch BPMs separiert.

Darüber hinaus wird gezeigt, dass der zuvor hergeleitete analytische Ausdruck für die Jacobi-Matrix anstelle der exakten Jacobi-Matrix, welche typischerweise mittels Differenzenquotienten berechnet wird, während des Fitting-Vorgangs verwendet werden kann. Der analytische Ausdruck für die Jacobi-Matrix benötigt lediglich die Twiss-Daten der aktuellen Beschleuniger-Konfiguration während des Fitting-Vorgangs. Die Beschleuniger-Konfiguration wird in diesem Kontext über die spezifischen Werte der relevanten Parameter des inversen Problems definiert. Die Verwendung des analytischen Ausdrucks für die Jacobi-Matrix reduziert den benötigten Rechenaufwand maßgeblich, verglichen mit der Verwendung von Differenzenquotienten. Der Faktor, um den der Rechenaufwand bezüglich der involvierten Beschleuniger-Elemente reduziert wird, ist  $N_{Steerer} \times N_{Quadrupole}$ , wobei das Symbol  $N$  die Anzahl der Beschleuniger-Elemente des jeweiligen Typs bezeichnet. Der Fitting-Vorgang mittels der analytischen Jacobi-Matrix wird mithilfe von umfangreichen Simulationen sowie mithilfe von zweckbestimmten Messungen am SIS18 Synchrotron am GSI Helmholtzzentrum für Schwerionenforschung getestet. Darüber hinaus werden verschiedene Methoden zur Minderung des Einflusses der Messungenauigkeiten auf bestimmte Parameterkombinationen in gemeinsamer Verwendung mit der analytischen Jacobi-Matrix getestet. Die Ergebnisse, die mithilfe der analytischen Jacobi-Matrix erzielt wurden, stimmen gut mit den Ergebnissen überein, die mithilfe der herkömmlichen Methode unter Verwendung von Differenzenquotienten erzielt wurden. Die verwendete Fitting-Methode wurde zusammen mit der Berechnung der analytischen Jacobi-Matrix als Python Paket implementiert und verfügbar gemacht [1]. Dies erlaubt eine unkomplizierte Adaptierung der vorgestellten Methode, auch für andere Konfigurationen oder Beschleuniger.

Die Messungen am SIS18 Synchrotron wurden speziell konzipiert, um eine hohe Präzision der erzielten Ergebnisse zu gewährleisten. Eine Messungenauigkeit von  $\lesssim 1 \mu\text{m}$  wurde für die Orbit Messung erzielt und eine Messungenauigkeit von  $\lesssim 5 \mu\text{m}/\text{mrad}$  für die Bestimmung der Response-Matrix. Hierfür wurde eine Java Anwendung entwickelt, um die Messung

---

der Response-Matrix, einschließlich der Dispersion, vollständig zu automatisieren. Die Java Anwendung ist auf dem Gitlab Server der GSI verfügbar [2]. Der Setup des Experiments sowie die Java Anwendung sind modular aufgebaut und beliebig erweiterbar und bilden somit die Grundlage für Messungen der Response-Matrix mit hoher Präzision auch für weitere Beschleuniger des GSI und zukünftigen FAIR Campus.

Darüber hinaus können die Zusammenhänge des Einflusses der Verfügbarkeit und der Platzierung von Steerern und BPMs innerhalb eines Beschleunigers auf die Bestimmbarkeit von Fehlern der Quadrupolfeldstärken bei der Planung von neuen Beschleunigern berücksichtigt werden, um eine effiziente Lösung des entsprechenden inversen Problems zu gewährleisten. Die erzielten Ergebnisse können außerdem für das Fitting von großtechnischen Beschleunigern, wie z.B. dem Large Hadron Collider (LHC) am CERN, verwendet werden. Große Beschleuniger besitzen eine hohe Anzahl an Steerern und BPMs und dies kann zu einer Größe der Jacobi-Matrix führen, die in diesem Umfang nicht für das Fitting verwendet werden kann oder die benötigte Rechenzeit massiv erhöht. Dennoch kann eine Teilmenge der Elemente der Jacobi-Matrix für den Fitting-Vorgang verwendet werden. Dies reduziert die effektive Größe der verwendeten Jacobi-Matrix und reduziert darüber hinaus die benötigte Rechenzeit. Um eine optimale Auswahl der Elemente der Jacobi-Matrix zu gewährleisten, ist es notwendig, deren Einfluss auf die Lösbarkeit des inversen Problems und auf die Fehlerfortpflanzung zu erfassen. Darüber hinaus bietet der analytische Ausdruck der Jacobi-Matrix eine effiziente Alternative mit geringem Rechenaufwand verglichen mit der Verwendung von Differenzenquotienten, was besonders bei großen Beschleunigern mit einer großen Jacobi-Matrix einen Vorteil in Bezug auf die benötigte Rechenzeit liefert.

Komplementär zu Teil 1 beschäftigt sich Teil 2 dieser Arbeit mit dem Einfluss von Fehlern der Quadrupolfeldstärken in Transferlinien bezüglich der Erfüllung der durch die Experimente vorgegebenen Anforderungen an die Transferlinie. Generell ist es möglich, diese Fehler mit ähnlichen der in Teil 1 dieser Arbeit beschriebenen Verfahren zu ermitteln, dies erfordert jedoch exklusive Messzeit, die dem Experimentbetrieb somit abhanden kommt. Teil 2 dieser Arbeit beschäftigt sich daher mit einem präventiven Ansatz, welcher das Ziel hat, den Einfluss möglicher Fehler der Quadrupolfeldstärken auf die resultierende Leistung der Transferlinie durch die gezielte Auswahl geeigneter Konfigurationen der Quadrupolfeldstärken zu minimieren. Dieser Ansatz macht sich die Flexibilität der Transferlinien in Bezug auf die möglichen Quadrupolkonfigurationen, die zur Erfüllung der durch die Experimente vorgegebenen Anforderungen verwendet werden können, zu Nutze. Verschiedene Quadrupolkonfigurationen unterscheiden sich durch deren Robustheit in Bezug auf die Leistung der Transferlinie unter Einfluss möglicher Fehler der Quadrupolfeldstärken. Eine robuste Quadrupolkonfiguration impliziert eine gleichbleibend hohe Leistung der Transferlinie auch in Gegenwart von Fehlern der Quadrupolfeldstärken. Solch robuste Quadrupolkonfigurationen ermöglichen einen stabilen Betrieb zur Versorgung der Experimente und reduzieren die Zeit, die Operateure aufwenden

---

müssen, um die Transferlinien nachzujustieren. Dies wiederum ermöglicht es, den Experimenten mehr effektive Strahlzeit zur Verfügung zu stellen.

Zunächst wird das Konzept der robusten Quadrupolkonfigurationen erläutert sowie die beiden für diese Studie exemplarisch genutzten Transferlinien vorgestellt. Die eine Transferlinie repräsentiert den Abschnitt der GSI HEST Infrastruktur, der vom SIS18 Synchrotron zu dem Leuchtschirm TH2DFA, oberhalb des Pion-Production-Targets, führt. Dieser Abschnitt der Transferlinie wurde gewählt, um eine adäquate Verifizierung der theoretischen Ergebnisse mittels experimenteller Daten mithilfe des TH2DFA Leuchtschirms zu gewährleisten. Der TH2DFA Leuchtschirm bietet hervorragende Voraussetzungen für die Messungen, da die zugehörige Kamera über FESA ausgelesen wird und somit mittels JAPC kontrolliert werden kann. Darüber hinaus kann die Kamera im Trigger-Modus betrieben werden und erlaubt somit eine Synchronisierung der Datenerfassung mit der Extraktion des Strahls aus dem SIS18 Synchrotron. Des Weiteren ist die Kamera vollständig kalibriert und stellt das horizontale und vertikale Strahlprofil, welche aus den aufgenommenen Bildern berechnet werden, zur Verfügung. Die zweite Transferlinie befindet sich am Forschungszentrum Jülich und repräsentiert den Abschnitt des Strahltransports, der vom Verzweigungspunkt der verschiedenen Transferlinien zur BIGKARL Targethalle führt. Während die Polarität der Quadrupolmagnete der HEST Transferlinie festgelegt ist, ist die der Quadrupolmagnete der BIGKARL Transferlinie variabel. Manche der Quadrupolmagnete der BIGKARL Transferlinie teilen sich außerdem ein Netzgerät. Die beiden Transferlinien unterscheiden sich somit in ihren grundlegenden Eigenschaften und bieten daher die Möglichkeit, die allgemeine Anwendbarkeit der entwickelten Methoden zu verifizieren.

Zu Beginn wird die Robustheit von Quadrupolkonfigurationen unter Herleitung eines mathematischen Ausdrucks für ebendiese Eigenschaft mithilfe von Twiss-Parametern untersucht. Die analytischen Ergebnisse werden dann mit den Daten von umfangreichen Simulationen, welchen eine systematische Untersuchung des gesamten Konfigurationen-Raums der TH2DFA Transferlinie zugrunde liegt, verglichen und belegt. Die Simulationen wurden auf Basis von MADX realisiert, was eine hohe Kompatibilität mit bestehenden Beschreibungen von Transferlinien gewährleistet. Mithilfe der Simulationsdaten werden des Weiteren verschiedene charakterisierende Eigenschaften von robusten Quadrupolkonfigurationen identifiziert. Es wird gezeigt, dass der Verlauf der Beta-Funktionen im vorderen Abschnitt der Transferlinie einen entscheidenden Einfluss auf die Robustheit der Quadrupolkonfiguration hat. Indem extreme Werte der Beta-Funktionen in diesem Abschnitt vermieden werden, kann eine Steigerung der Robustheit der erzeugten Quadrupolkonfigurationen erzielt werden. Des Weiteren erlaubt die Verwendung einer zusätzlichen Optimierungsroutine, welche der von MADX verwendeten Optimierungsroutine LMDIF vorgeschaltet wird, eine weitere Steigerung der Robustheit der erzeugten Quadrupolkonfigurationen. Für die vorliegende Problemstellung hat sich besonders die Klasse der sogenannten Differential Evolution Algorithmen als vorteilhaft erwiesen. Als



---

weitere Methode zur Steigerung der Robustheit der erzeugten Quadrupolkonfigurationen wurde ein sogenanntes Surrogate Model in Bezug auf die zu erwartende Robustheit in Abhängigkeit der Twiss-Parameter und Quadrupolfeldstärken einer Quadrupolkonfiguration gefittet. Das Surrogate Model erlaubt eine höchst recheneffiziente Evaluierung der Robustheit anstelle von rechenaufwendigen Monte Carlo Simulationen. Eine weitere entscheidende Verbesserung wurde erzielt, indem das gefittete Surrogate Model auf den Einfluss der für das Fitting verwendeten Parameter hin untersucht wurde. Dies wurde mithilfe sogenannter Feature Importance Methoden realisiert. Die Anwendung dieser Methoden erlaubt es, solche Parameter zu identifizieren, die sich im Rahmen des Fittings als einflussreich auf die resultierende Robustheit von Quadrupolkonfigurationen gezeigt haben. Da sich die verwendeten Parameter aus den Twiss-Parametern und Quadrupolfeldstärken der Quadrupolkonfigurationen zusammensetzen, können diese Ergebnisse wiederum verwendet werden, um die Effizienz der zugrunde liegenden Optimierungsroutine LMDIF mithilfe entsprechender zusätzlicher Beschränkungen deutlich zu steigern. Die so erzielten Ergebnisse werden schließlich verwendet, um die Gesamteffizienz des Rechenprozesses, der der Identifizierung von robusten Quadrupolkonfigurationen dient, maßgeblich zu verbessern. Dieser Rechenprozess wird als *Robuste Optimierung* bezeichnet.

Die Ergebnisse und Methoden, welche im Rahmen der Untersuchung der TH2DFA Transferlinie erzielt wurden, werden schließlich auf die Robuste Optimierung der zweiten Transferlinie, der BIGKARL Transferlinie, angewandt. Es wird gezeigt, dass dieselben Methoden für eine effiziente Berechnung von robusten Quadrupolkonfigurationen verwendet werden können. Abschließend werden die Simulationsergebnisse mithilfe von zweckbestimmten Messungen an beiden Transferlinien, am GSI Helmholtzzentrum für Schwerionenforschung und am Forschungszentrum Jülich, verifiziert. Die experimentellen Daten bestätigen die unterschiedlichen Eigenschaften der Quadrupolkonfigurationen der Transferlinien bezüglich der Variabilität der Strahlfleckgröße auf den Target-Profil-Monitoren, die im Vorhinein mithilfe von Simulationen ermittelt wurden. Darüber hinaus verdeutlichen die experimentellen Ergebnisse die Realisierbarkeit des Auffindens und der Anwendung von robusten Quadrupolkonfigurationen. Für beide Messungen wurden Software Pakete in Java bzw. Python implementiert, die eine vollständige Automatisierung der beiden Messungen ermöglichen. Die Anwendungen sind auf dem GSI Gitlab Server bzw. dem FZJ Gitlab Server verfügbar [3, 4]. Die erzielten Ergebnisse bilden somit die Grundlage für die Robuste Optimierung und deren experimentelle Überprüfung für eine Vielzahl an Transferlinien der GSI HEST Infrastruktur sowie darüber hinaus für Transferlinien an anderen Beschleunigerinstituten. Die erzielten Ergebnisse sind ebenfalls relevant für die zukünftigen Transferlinien der FAIR Beschleunigeranlagen.



If I have seen further, it is by standing  
on the shoulders of giants.

---

*Isaac Newton*



## Acknowledgements

I would like to take the opportunity to thank all those people who have supported me during my doctoral work and beyond and who have thus contributed to the success of this thesis.

First of all, I would like to thank Prof. Dr. Holger Podlech for the supervision of my doctoral work, for the support with various administrative matters and for reviewing this thesis.

I would like to express my sincere gratitude to Dr. Mei Bai for providing the inspiration for this thesis, for her constant support and guidance throughout my doctoral work, for answering my many questions and for teaching me numerous aspects of the field of accelerator physics and beyond. Also, Dr. Mei Bai has provided lots of helpful feedback and ideas for improving this thesis and I am very thankful for all her efforts.

I am deeply grateful to Dr. Mariusz Sapinski for his constant support, trust and encouragement throughout the past decade. He was always ready to help as well as to provide inspiration and guidance whenever I needed it. I gratefully look back on years full of fruitful collaboration.

This endeavor would not have been possible without Dr. Rahul Singh. I deeply appreciate his constant support and encouragement during the past years. Our many discussions on various topics always helped me to arrive at a better understanding of the problems at hand and his guidance has helped me in solving some of the major problems during my work.

During the writing of this thesis, Apl. Prof. Dr. Giuliano Franchetti has provided feedback and suggested various improvements and I would like to thank him for his encouragement and guidance.

Many thanks to Jutta Fitzek and Dr. Harald Bräuning for their help in creating the software for automatizing the measurements at GSI. Special thanks to Tino Giacomini for his general support with the SIS18 IPMs as well as for his nightly support to get the IPM software ready just in time for my measurement. I would like to acknowledge Dr. Youssef El Hayek for answering many questions about the MADX SIS18 lattice description. I would like to thank Kevin Lang for answering my questions about the SIS18 BPM system and for his help during the analysis of the data. I would like to acknowledge Dr. Stephan Reimann and Dr. Jens Stadlmann for their support during the allocation and preparation of my measurements at SIS18. Lastly, I'd like to mention the support of the operating crew of SIS18 who have made the measurements possible.

I would like to extend my sincere thanks to Dr. Bernd Lorentz for his support during the ORM measurement at SIS18 as well as for his support during the preparation of the measurement at Forschungszentrum Jülich.

---

I am also grateful to Dr. Dieter Prasuhn from Forschungszentrum Jülich (FZJ) for his comprehensive support during the preparation and execution of my measurements at FZJ. Similarly, I would like to thank Michael Simon for his great support and assistance in creating the software to automate the measurement at FZJ. All in all, the measurement campaign at FZJ has been a fruitful experience and so I would like to thank the other members of the FZJ team who have made this measurement possible.

Without the past, there is no future, and so I would like to thank my high school physics teacher A. Seitz for organizing the impressive school trip to CERN which sparked the initial interest for my career in the field of accelerator physics.

I am deeply indebted to my parents for their lifelong support and for enabling me to pursue my education and academic studies which eventually led to the creation of this thesis.

Finally, words cannot express my gratitude to my wife Melanie for her constant encouragement and for her loving care for our family.







# Table of Contents

|                                                                                      |              |
|--------------------------------------------------------------------------------------|--------------|
| <b>Title Page</b>                                                                    | <b>i</b>     |
| <b>Zusammenfassung</b>                                                               | <b>v</b>     |
| <b>List of Figures</b>                                                               | <b>xxi</b>   |
| <b>List of Tables</b>                                                                | <b>xxv</b>   |
| <b>Abbreviations</b>                                                                 | <b>xxvii</b> |
| <b>1 Introduction</b>                                                                | <b>1</b>     |
| <b>2 Linear optics in synchrotrons and beam transfer lines</b>                       | <b>7</b>     |
| 2.1 Conventions . . . . .                                                            | 7            |
| 2.1.1 Terminology . . . . .                                                          | 7            |
| 2.1.2 Coordinate systems . . . . .                                                   | 8            |
| 2.2 Equations of motion . . . . .                                                    | 9            |
| 2.2.1 Hamiltonian formalism . . . . .                                                | 9            |
| 2.2.2 Electromagnetic field configurations . . . . .                                 | 13           |
| 2.2.3 Transfer maps . . . . .                                                        | 14           |
| 2.3 Synchrotron optics . . . . .                                                     | 22           |
| 2.3.1 Transverse optics . . . . .                                                    | 22           |
| 2.3.2 Dispersion function . . . . .                                                  | 32           |
| 2.4 Deviations from the ideal lattice . . . . .                                      | 33           |
| 2.4.1 Steering contributions . . . . .                                               | 33           |
| 2.4.2 Quadrupole errors . . . . .                                                    | 35           |
| 2.4.3 Effect of multipole errors . . . . .                                           | 37           |
| 2.5 Closed orbit based measurements of linear optics . . . . .                       | 38           |
| 2.5.1 Orbit response matrix (ORM) . . . . .                                          | 39           |
| 2.5.2 Jacobian matrix . . . . .                                                      | 40           |
| 2.5.3 Optimization algorithms . . . . .                                              | 40           |
| 2.5.4 Gain errors . . . . .                                                          | 42           |
| 2.5.5 Dispersion . . . . .                                                           | 44           |
| 2.6 Beam extraction from synchrotrons and transport in beam transfer lines . . . . . | 44           |
| 2.6.1 Resonant slow extraction of beams in synchrotrons . . . . .                    | 45           |
| 2.6.2 Quadrupole scan for emittance measurement in beam transfer lines . . . . .     | 47           |

|          |                                                                                                          |           |
|----------|----------------------------------------------------------------------------------------------------------|-----------|
| <b>3</b> | <b>Estimating quadrupole errors in the presence of degeneracy for the SIS18 synchrotron</b>              | <b>49</b> |
| 3.1      | The SIS18 synchrotron . . . . .                                                                          | 50        |
| 3.1.1    | Beam position monitors . . . . .                                                                         | 50        |
| 3.1.2    | Orbit response matrix . . . . .                                                                          | 50        |
| 3.2      | Degeneracy for estimated quadrupole strengths . . . . .                                                  | 54        |
| 3.2.1    | Analytical derivative of orbit response . . . . .                                                        | 55        |
| 3.2.2    | Pure degeneracy . . . . .                                                                                | 55        |
| 3.2.3    | Quasi-degeneracy . . . . .                                                                               | 58        |
| 3.2.4    | Exemplification using the SIS18 lattice . . . . .                                                        | 62        |
| 3.2.5    | Counteracting quasi-degeneracy . . . . .                                                                 | 63        |
| 3.3      | Fitting the orbit response matrix . . . . .                                                              | 64        |
| 3.3.1    | Improving the accuracy of the analytical Jacobian . . . . .                                              | 66        |
| 3.4      | Experiment at the SIS18 synchrotron . . . . .                                                            | 67        |
| 3.4.1    | Preparation . . . . .                                                                                    | 67        |
| 3.4.2    | Summary of measurement . . . . .                                                                         | 71        |
| 3.4.3    | Orbit measurement . . . . .                                                                              | 72        |
| 3.4.4    | ORM measurement . . . . .                                                                                | 75        |
| 3.4.5    | Dispersion measurement . . . . .                                                                         | 78        |
| 3.4.6    | Tune measurement . . . . .                                                                               | 78        |
| 3.4.7    | Fitting of quadrupole errors . . . . .                                                                   | 79        |
| 3.4.8    | Fitting of gain errors . . . . .                                                                         | 84        |
| 3.4.9    | Fitting with dispersion . . . . .                                                                        | 84        |
| <b>4</b> | <b>Mitigating the effect of quadrupole errors on beam transfer lines with robust optimization</b>        | <b>89</b> |
| 4.1      | Configurations of quadrupole strengths for beam transfer lines . . . . .                                 | 92        |
| 4.2      | Robustness with respect to quadrupole errors . . . . .                                                   | 94        |
| 4.2.1    | Definition of robustness . . . . .                                                                       | 94        |
| 4.2.2    | Improving robustness of quadrupole configurations obtained via matching of beta functions . . . . .      | 96        |
| 4.2.3    | Evaluating robustness of quadrupole configurations . . . . .                                             | 97        |
| 4.2.4    | Approximating robustness from Twiss data . . . . .                                                       | 102       |
| 4.3      | Robust optimization . . . . .                                                                            | 106       |
| 4.3.1    | Improved matching criteria by limiting the beta functions in the upstream part of the beamline . . . . . | 108       |
| 4.3.2    | Application of an additional global optimizer . . . . .                                                  | 109       |
| 4.3.3    | Surrogate model for evaluating robustness and for deriving important Twiss parameters . . . . .          | 112       |
| 4.3.4    | Comparison of methods . . . . .                                                                          | 116       |
| 4.3.5    | Error analysis . . . . .                                                                                 | 118       |
| 4.4      | Experiment at GSI Helmholtzzentrum für Schwerionenforschung . . . . .                                    | 120       |
| 4.4.1    | Preparation . . . . .                                                                                    | 120       |
| 4.4.2    | Results . . . . .                                                                                        | 123       |

|          |                                                                                |            |
|----------|--------------------------------------------------------------------------------|------------|
| 4.5      | Application to BIGKARL beamline at Forschungszentrum Jülich . . . . .          | 126        |
| 4.5.1    | Simulations . . . . .                                                          | 129        |
| 4.5.2    | Experimental setup and results . . . . .                                       | 130        |
| <b>5</b> | <b>Conclusions &amp; Outlook</b>                                               | <b>135</b> |
|          | <b>References</b>                                                              | <b>139</b> |
|          | <b>Appendix A Appendix</b>                                                     | <b>147</b> |
| A.1      | Transfer matrix between two lattice positions . . . . .                        | 147        |
| A.2      | One-turn transfer matrix in exponential form . . . . .                         | 147        |
| A.3      | Slicing of thick BPMs and steerers for linear closed orbits . . . . .          | 148        |
| A.3.1    | Slicing of steerer . . . . .                                                   | 148        |
| A.3.2    | Slicing of BPM . . . . .                                                       | 150        |
| A.4      | Derivative of orbit response with respect to quadrupole strength . . . . .     | 150        |
| A.5      | Derivative of orbit response with respect to quadrupole strength for beamlines | 153        |
| A.6      | Proof: S,Q3,B Jacobian is rank deficient . . . . .                             | 154        |
| A.7      | Proof: Sh,Sv,Q6,Bh,Bv Jacobian is rank deficient . . . . .                     | 160        |



# List of Figures

|      |                                                                                                                                                                                                          |    |
|------|----------------------------------------------------------------------------------------------------------------------------------------------------------------------------------------------------------|----|
| 2.1  | Coordinate systems. . . . .                                                                                                                                                                              | 9  |
| 2.2  | Illustration of geometrical focusing. . . . .                                                                                                                                                            | 16 |
| 2.3  | Schematic of the cross section of a dipole magnet with curved pole faces that produce a radial field gradient. . . . .                                                                                   | 23 |
| 2.4  | Necktie plot for the field indices $n_1$ and $n_2$ for the example of 100 superperiods. . . . .                                                                                                          | 27 |
| 2.5  | Illustration of the phase-space ellipse for transverse particle motion. . . . .                                                                                                                          | 28 |
| 2.6  | Phase-space evolution for a matched vs. mismatched particle distribution. . . . .                                                                                                                        | 32 |
| 2.7  | Example of distorted closed orbit from a single error source. . . . .                                                                                                                                    | 34 |
| 2.8  | Resonance lines up to third order for a lattice with 1 superperiod. . . . .                                                                                                                              | 38 |
| 2.9  | Phase-space trajectories near a third-order resonance under the influence of sextupole contributions. . . . .                                                                                            | 46 |
| 3.1  | Schematic of SIS18 lattice together with optics functions. . . . .                                                                                                                                       | 51 |
| 3.2  | Simulated ORM for nominal extraction optics of SIS18. . . . .                                                                                                                                            | 53 |
| 3.3  | Example for the orbit response change of a single BPM/steerer pair when varying a single quadrupole. . . . .                                                                                             | 55 |
| 3.4  | $K_1L$ residuals for artificially introducing pure degeneracy to the SIS18 lattice. . . . .                                                                                                              | 57 |
| 3.5  | $J^T J$ matrix for horizontal and vertical dimension of the SIS18 lattice together with their eigenvalue spectra. . . . .                                                                                | 60 |
| 3.6  | Eigenvectors that correspond to the smallest eigenvalue of the $J^T J$ matrices in horizontal and vertical dimension of the SIS18 lattice. . . . .                                                       | 60 |
| 3.7  | $(J^T J + \alpha I)^{-1}$ for the horizontal, vertical and combined dimensions of the SIS18 lattice. . . . .                                                                                             | 61 |
| 3.8  | Globally symmetric eigenmodes of the $J^T J$ matrix in vertical dimension of the SIS18 lattice. . . . .                                                                                                  | 62 |
| 3.9  | Covariance of $K_1L$ residuals for the SIS18 lattice under the influence of $7\mu\text{m}/\text{mrad}$ orbit response uncertainty. . . . .                                                               | 63 |
| 3.10 | Eigenvalues of $J^T J$ for different BPM placements in the SIS18 lattice. . . . .                                                                                                                        | 64 |
| 3.11 | Comparison of simulation results for various levels of model errors as well as various levels of orbit response uncertainty. The analytical and numerical Jacobian methods are compared as well. . . . . | 66 |
| 3.12 | Improvement of the analytical Jacobian by using multiple thin slices for each quadrupole. . . . .                                                                                                        | 68 |

## LIST OF FIGURES

---

|      |                                                                                                                                                                                                                                      |     |
|------|--------------------------------------------------------------------------------------------------------------------------------------------------------------------------------------------------------------------------------------|-----|
| 3.13 | Steerer trim pattern that is used for trimming the steerer's kick value via the LSA API during the measurement. . . . .                                                                                                              | 70  |
| 3.14 | Maximal variation of the SIS18 horizontal and vertical ORM under a shift of, respectively, the horizontal and vertical BPMs. . . . .                                                                                                 | 72  |
| 3.15 | Position data from the horizontal BPM in section 1 during measurement of the horizontal steerer in section 5. . . . .                                                                                                                | 73  |
| 3.16 | Position data from the horizontal and vertical BPM in section 1 during measurement of the the vertical steerer GS01KM2DV together with FFT spectra. . . . .                                                                          | 73  |
| 3.17 | Position data from the horizontal BPMs in sections 1 and 2. . . . .                                                                                                                                                                  | 74  |
| 3.18 | Position data from the horizontal and vertical BPM in section 6 during flattop together with corresponding orbit estimates. The influence of 2 s and 4 s margin at beginning of flattop on the orbit estimates are compared. . . . . | 75  |
| 3.19 | Measured ORM for nominal extraction optics. . . . .                                                                                                                                                                                  | 77  |
| 3.20 | Comparison of measured dispersion and model dispersion. . . . .                                                                                                                                                                      | 78  |
| 3.21 | Measurement of tunes for the two different optics. . . . .                                                                                                                                                                           | 79  |
| 3.22 | Estimated quadrupole errors when all quadrupoles of the SIS18 lattice are included in the fit. . . . .                                                                                                                               | 80  |
| 3.23 | Estimated quadrupole errors when the F- and D-quadrupoles from the SIS18 lattice are fitted. . . . .                                                                                                                                 | 81  |
| 3.24 | Comparison of mean squared error of the diagonal and coupling blocks of the simulated ORM with respect to the measured ORM for the SIS18 lattice. . . . .                                                                            | 81  |
| 3.25 | Comparison of inverse modeling results for the F-quadrupoles when using different methods for counteracting quasi-degeneracy. The analytical and numerical Jacobian methods are compared as well. . . . .                            | 83  |
| 3.26 | Difference between predicted and measured tunes for the various optics and inverse modeling methods. . . . .                                                                                                                         | 85  |
| 3.27 | Estimated BPM and steerer gain errors. . . . .                                                                                                                                                                                       | 86  |
| 3.28 | The inverse sensitivity $1/S$ for the horizontal and vertical SIS18 BPMs. . . . .                                                                                                                                                    | 86  |
| 3.29 | Measured and estimated dispersion after fitting the ORM with and without the dispersion. . . . .                                                                                                                                     | 87  |
| 3.30 | Estimated quadrupole errors when the F- and D-quadrupoles from the SIS18 lattice are fitted and the dispersion is included in the fit. . . . .                                                                                       | 87  |
| 4.1  | Schematic of the HEST network of beamlines. . . . .                                                                                                                                                                                  | 90  |
| 4.2  | Photo of the pion production target in the lab. . . . .                                                                                                                                                                              | 92  |
| 4.3  | Beta function along the TH2DFA beamline for an example beamline configuration. . . . .                                                                                                                                               | 94  |
| 4.4  | Beta functions at the target screen for different quadrupole variations. . . . .                                                                                                                                                     | 95  |
| 4.5  | Flow chart showing the procedure for computing robust beamline configurations together with example beta functions. . . . .                                                                                                          | 98  |
| 4.6  | Histogram plot of the robustness scores for the 10 000 configurations of the baseline dataset. . . . .                                                                                                                               | 100 |
| 4.7  | Comparison of different methods for computing robustness estimates. . . . .                                                                                                                                                          | 107 |

4.8 Comparison of beta functions for a configuration obtained with the baseline procedure and a configuration obtained when additionally limiting excursions of the beta function at the first five quadrupoles of the beamline. . . . . 109

4.9 Robustness scores for the low-beta dataset. . . . . 110

4.10 Distance traveled within the problem domain during LMDIF matching. . . . . 111

4.11 Robustness scores for the optimizer-based, low-beta dataset. . . . . 111

4.12 Predictions for robustness scores from a Random Forest regression model. . . . . 113

4.13 Permutation feature importance for a random forest surrogate model. . . . . 114

4.14 Robustness of the configurations of the TH2DFA beamline in dependency on different Twiss parameters along the beamline. . . . . 115

4.15 Robustness scores for the low-beta, feature-importance-based dataset. . . . . 115

4.16 Robustness scores for the optimizer-based, low-beta, feature-importance-based dataset. . . . . 117

4.17 Robustness scores under additional random Twiss parameter variations and longitudinal position errors for the quadrupoles of the TH2DFA beamline. . . . . 120

4.18 Variations of the beta function at the target screen under influence of various model errors for a configuration with high robustness. . . . . 121

4.19 Robustness scores under the influence of additional random Twiss parameter variations and longitudinal position errors of the quadrupoles of the TH2DFA beamline. . . . . 121

4.20 Beta functions for the four TH2DFA beamline configurations which have been tested during the measurement. . . . . 122

4.21 Diagram for the various steps in the Java App for automated quadrupole control to measure beamline robustness. . . . . 123

4.22 Example for beam scraping in the vertical dimension during TH2DFA measurement. . . . . 124

4.23 Quadrupole scan measurement for different configurations of the TH2DFA beamline. . . . . 124

4.24 Measured beam profiles obtained with the IPMs at SIS18 during flattop. . . . . 125

4.25 Variations of beam position at the target screen TH2DFA under the influence of artificial quadrupole errors. . . . . 126

4.26 Measured beam size variations for the configurations of the TH2DFA beamline. 127

4.27 Schematic of COSY and the beamlines leading to the experimental areas including BIGKARL. . . . . 128

4.28 Beta functions for an example configuration of the BIGKARL beamline. . . . . 129

4.29 Flow diagram for the Python application for automatizing the BIGKARL measurement. . . . . 131

4.30 Beta functions of the configurations used for the measurement at BIGKARL. . 132

4.31 Measured beam size variations for the three different beamline configurations tested on the BIGKARL beamline. . . . . 133





# List of Tables

|     |                                                                                                                                                                                    |     |
|-----|------------------------------------------------------------------------------------------------------------------------------------------------------------------------------------|-----|
| 2.1 | Overview of different methods for slicing beamline elements. . . . .                                                                                                               | 21  |
| 2.2 | Definitions for beam emittance. . . . .                                                                                                                                            | 30  |
| 3.1 | Rank deficiency of the Jacobian for various BPM/steerer placements around groups of consecutive quadrupoles. . . . .                                                               | 58  |
| 3.2 | Resulting tunes from the various fitting methods compared to measured tunes for the SIS18 lattice. . . . .                                                                         | 85  |
| 4.1 | Minimum number of Monte Carlo samples to test whether the robustness $\rho$ of a given configuration is no less than the threshold $\tau$ for different values of $\tau$ . . . . . | 102 |
| 4.2 | LMDIF success rates and fraction of high robustness configurations for different optimization methods and different stages during the optimization. . . . .                        | 118 |
| A.1 | Expressions for the coefficient vectors for the different phase advance relationship types A,B,C. . . . .                                                                          | 155 |
| A.2 | Simplified expressions for the coefficient vectors for the different phase advance relationship types A,B,C. . . . .                                                               | 156 |
| A.3 | Further simplified expressions for the coefficient vectors for the different phase advance relationship types A,B,C. . . . .                                                       | 156 |



# Abbreviations

- AGS** Alternating Gradient Synchrotron at Brookhaven National Laboratory. 22
- API** Application Programming Interface. xxii, 68, 70, 122, 123
- BLM** Beam Loss Monitor. 123
- BPM** Beam Position Monitor. v–vii, xxi, xxii, xxv, 2, 4, 39, 40, 42–44, 49–51, 54–59, 61–65, 68, 70–76, 78, 84, 86
- CERN** European Organization for Nuclear Research. vii
- COFB** Closed Orbit Feedback. 65
- COSY** Cooler Synchrotron. xxiii, 92, 126, 128, 130–133
- CSV** Comma-Separated Values. 69, 70
- DiPAS** Differentiable Particle Accelerator Simulations. 51
- EPICS** Experimental Physics and Industrial Control System. 130
- ESR** Experimental Storage Ring. 2, 44, 90
- FAIR** Facility for Antiproton and Ion Research in Europe. vii, ix, 3, 4, 44, 50, 136, 137
- FESA** Front-End Software Architecture. viii, 122
- FFT** Fast Fourier Transform. xxii, 72, 73
- FRS** Fragment Separator. 2
- FZJ** Forschungszentrum Jülich. viii, ix, 5, 92, 93, 126, 137
- GSI** Gesellschaft für Schwerionenforschung. vi–ix, 2, 4, 5, 22, 50, 70, 89, 92, 97, 123, 135–137
- GUI** Graphical User Interface. 67, 130
- HADES** High Acceptance Di-Electron Spectrometer. 44, 47, 90–92
- HEST** High Energy Beam Transport. viii, ix, xxii, 47, 89–93, 97, 126, 137
- IPM** Ionization Profile Monitor. xxiii, 122, 125
- JAPC** Java API for Parameter Control. viii, 122
- LHC** Large Hadron Collider at CERN. vii, 136
- LMDIF** Matching routine in MADX using the Levenberg-Marquardt algorithm. viii, ix, xxiii, xxv, 93, 96–99, 106, 108–112, 114–118, 121, 129, 136, 137
- LSA** LHC Software Architecture. xxii, 68–71, 122, 123
- MADX** Methodical Accelerator Design. viii, 67, 68, 90, 91, 93, 96, 98, 106, 118, 125, 127, 129, 136, 137
- MWPC** Multi-Wire Proportional Chamber. 130
- ORM** Orbit Response Matrix. xxi, xxii, 2, 4, 39, 40, 43, 49, 50, 53–56, 59, 61–63, 65–67, 71, 72, 76–78, 81–83, 86, 136
- PS** Proton Synchrotron at CERN. 22, 27
- PV** Process Variable in EPICS. 130
- RF** Radio Frequency. 9, 39, 43, 44, 46, 47, 131
- SHIP** Separator for Heavy Ion reaction Products. 2
- SIS100** Schwerionensynchrotron with 100 Tm rigidity at FAIR. 3, 44, 50
- SIS18** Schwerionensynchrotron with 18 Tm rigidity at GSI. vi, viii, xxi–xxiii, xxv, 2–4, 22, 44, 47, 50, 51, 53, 54, 56, 58, 60, 61, 63, 67, 68, 71, 79, 84, 86, 90, 122, 125, 135, 136
- SVD** Singular Value Decomposition. 43, 64, 79, 80, 82, 83, 85
- Tcl** Tool Command Language (programming language). 130
- Tk** Cross-platform widget toolkit. 130



# 1

## Introduction

The need for stable beam focusing for particle accelerators to reach high energies has been already recognized by Wideröe in 1928 [5]. A dedicated magnet design to accomplish such focusing for a betatron accelerator has been proposed by Steenbeck in 1935 [6] and a detailed mathematical analysis has been established by Kerst and Serber in 1941 [7]. Likewise, the first synchrotrons used bending magnets with curved or slanted pole faces in order to generate the radial field gradient that provides the necessary focusing [8, 9, 10, 11]. With the discovery of the strong focusing principle in the 1950s [12, 13, 14], dedicated quadrupole magnets were introduced for beam focusing and they constitute a major building block of any modern circular accelerator. The influence of magnet imperfections and associated field errors has been studied since the strong focusing principle has been first introduced. The effect of magnetic field errors on the behavior of the beam inside the accelerator was well known and it imposed tight bounds for the construction tolerances compared to the already existing constant gradient accelerators [15, 16, 17, 18].

Early methods for correcting the influence of magnet errors on the optics of an accelerator relied on the formulas which had been derived in the context of the strong focusing theory. These methods aim to fit the measured beta functions and phase advances in order to derive the field gradient errors under a linear approximation. This type of correction is still used in recent studies [19, 20]. Since its first introduction, the strong focusing principle has been adopted by many other accelerator facilities and, today, synchrotrons are operated at many different accelerator institutes worldwide. However, with the ever increasing demand in the performance of machines such as storage rings at synchrotron light sources, already smaller quadrupole errors became a hindrance for the successful operation of the machines. Thus, it became necessary to systematically correct these errors. One of the first approaches which aimed to fit the observed data from beam position monitors with the data generated by a linear optics simulation program was presented in 1987 [21]. It required the manual interaction of a user to select possible error sources in the lattice which the program then varied in order to find an optimal solution.

An automatic method for fitting of linear optics was introduced in 1993 [22]. This method used the recordings of beam position monitors in terms of the beam orbit movement induced

by variations of steerer dipole magnets, in form of the Orbit Response Matrix (ORM). The numerical accelerator model, including the modeled quadrupole errors, was then fitted to match the measured data. Since then, the technique has been further improved and is typically referred to as extracting linear optics from closed orbit measurements [23]. It has been successfully employed at various synchrotron light sources [24, 25, 26, 27, 28, 29, 30]. Following the success of the method for synchrotron light sources, it has been applied at other facilities operating hadron synchrotrons [31, 32, 33, 34, 35, 36]. However, the results were often affected by degeneracy present in the system or could not be verified in terms of the optics of the accelerator. While synchrotron light sources typically have many BPMs installed, the available BPMs at hadron synchrotrons are rather limited and are typically not dual plane. Also, the number of steerer magnets can be small compared to synchrotron light sources. These devices, however, provide the necessary information in form of the measured orbit response which is used to accurately model and correct the quadrupole errors in the lattice. Lack of BPMs or steerers enhances the degree to which measurement uncertainty is propagated and might cause specific lattice parameters to be especially susceptible to the influence of measurement uncertainty. In some situations it might even cause the inverse problem of estimating quadrupole errors to be ill-posed in such a way that the estimated errors are not uniquely determined by the measured ORM data. So far, there has been not much effort to study the influence of the availability and placement of steerer magnets and beam position monitors in the lattice on the feasibility of extracting linear optics and model errors from closed orbit measurements as well as on the quality of obtained results. A profound understanding of this relationship is, however, required in order to obtain reliable results from the inverse modeling process and for designing corresponding measurements in order to reach the desired uncertainty in the estimated model parameters.

At GSI Helmholtz Centre for Heavy Ion Research in Darmstadt (Germany), the SIS18 synchrotron is a flexible synchrotron for the acceleration of a wide variety of ion species up to a magnetic rigidity of 18 T m. It has been used to successfully accelerate ions of various kinds from Hydrogen to Uranium. Starting in 1988, the first beam has been injected into SIS18. After operation has started in 1990, SIS18 has served many fixed target experiments as well as the Fragment Separator (FRS) and Experimental Storage Ring (ESR). This has led to the discovery of various new elements, ranging from atomic number 107 (Bohrium) to 112 (Copernicium), at the Separator for Heavy Ion reaction Products (SHIP). In addition to the discovery of new elements, SIS18 has enabled various other discoveries at GSI, for example, the bound-state beta decay in 1992 or the two-proton decay in 2002. Beyond these scientific discoveries, GSI has led pioneering work in the field of heavy-ion radiotherapy by conducting a successful pilot study using carbon ions for treatment.

Despite the successful operation of SIS18 over many decades, a tune discrepancy compared to the accelerator model has long been observed and a basic correction of the accelerator model relying on the experience of machine experts has been realized [37]. The first attempt for inverse modeling of linear optics of SIS18 via closed orbit measurements has been conducted from 2006 until 2008 [38]. This work reports the ORM measurements at injection energy from three distinct measurement campaigns together with the corresponding estimates of model parameters. The issues that were encountered during that study include low resolution

---

of beam orbit measurement ( $\sigma_h \approx 0.5 \text{ mm}$ ,  $\sigma_v \approx 0.14 \text{ mm}$ ) and only six of the now twelve horizontal steerer magnets were available <sup>1</sup>. Due to these complications, the obtained results had large error bars and not all quadrupoles of SIS18 could be included in the fitting. Also, the dispersion could not be measured. This indicates the necessity to redo inverse modeling under the improved conditions available today. A thorough understanding and control of the linear optics of SIS18 is especially important for the high intensity booster operation as part of the Facility for Antiproton and Ion Research in Europe (FAIR) [39] where SIS18 acts as an injector for the SIS100 synchrotron [40]. Also for SIS100 the high intensity operation will pose stringent requirements on the optics correction and the thorough understanding and control of linear optics forms the basis for any further improvements [41, 42, 43]. Studies of nonlinear effects such as dynamic aperture require precise knowledge of the lattice parameters in order to yield accurate results. As an approximation, it might be assumed that the beta beating is fully corrected in the lattice [43]. However, the quadrupole units in hadron accelerators, including those of SIS18 and SIS100, are typically divided into groups and each group is powered in series. Because each quadrupole in a group shares the same power supply, individual quadrupole errors cannot be fully corrected. As a consequence, the beta beating cannot not be fully corrected either but only brought to some minimal yet nonzero state. The residual beta beating must be taken into account during simulation studies and, thus, the precise knowledge of the linear optics and the corresponding lattice element parameters is important.

For a storage ring based synchrotron light source the ring itself is the final destination for the beam and, thus, the quality of the ring optics determines the quality of the beam and of the produced synchrotron light. At synchrotron based fixed target facilities, on the other hand, the beam must be further transported from the synchrotron to the experimental areas where it will be used. This means that not only the synchrotron optics determines the quality of the beam at the experimental target but also the optics along the beam transfer line or, in short, beamline. Similarly, errors in the quadrupole magnets can result in a degradation of the beam quality at the experimental target. This effect can be significant already for small quadrupole errors, due to the typically strong beam focus at the experimental target. While it is possible to perform an inverse modeling-based correction for beamlines [44], conducting this costs valuable experimental time. Also, when multiple experiments are to be served by the beamlines, the magnetic hysteresis plays a role and can lead to a degradation of the beamline optics. In the long run, also the stability of power converters or other environmental effects can lead to a change of the nominal quadrupole strengths and, thus, cause a degradation of the optics. It is therefore desirable to minimize the impact of quadrupole errors on the beamline optics. The behavior of the optics with respect to quadrupole errors is a property of the beamline's specific quadrupole configuration and, usually, beamlines are underconstrained in terms of the feasible quadrupole settings such that many different quadrupole configurations exist which meet the requirements of the beamline. Ideally, the beamline operates a configuration which is particularly robust against the expected quadrupole errors over the course of the experiment such that the quality of the beam does not degrade below the experimental requirements. Albeit the effects of field errors find basic treatment in some publications [45], so far, there has not been much effort towards a detailed and general study of the robustness of beamline

---

<sup>1</sup>The remaining six steerer magnets have been installed in the beginning of 2008.

configurations with respect to quadrupole errors. A profound understanding of beamline configuration robustness and reliable methods for identifying those configurations will benefit the operation of beamlines in terms of their reliability as well as reduce the time operators must spend on fine-tuning the beamlines' optics and, hence, allow to increase the beam-on-target time at the experiments.

In the following, the structure of the thesis is described.

In chapter 2, the relevant concepts and results from beam physics in synchrotrons are introduced which are then used throughout the main part of the thesis.

In chapter 3, the study of inverse modeling of linear optics in the presence of degeneracy is presented. First, the inverse problem is explained with regard to degeneracy of its solutions. An analytical expression for the Jacobian matrix of the inverse problem is derived. This expression for the Jacobian is used to derive the theoretical limitations of the inverse problem in terms of the placement of steerer magnets and beam position monitors. Further, the influence of different BPM/steerer placement patterns on the resulting uncertainty of the parameter estimates is investigated. Depending on the placement pattern, some of the parameters might have substantially increased uncertainties compared to others, which manifests as a quasi-degeneracy. In addition, it is shown that during the fitting procedure the analytical version of the Jacobian can be used in place of the exact Jacobian which is obtained numerically via finite-difference approximation. Usage of the analytical Jacobian allows for greatly reduced computation times during the inverse modeling process. The scaling of the computation in terms of the number of relevant lattice elements is improved by a factor  $N_{steerers} \times N_{quadrupoles}$  by using the analytical Jacobian approach. The inverse modeling process by using the analytical Jacobian approach is tested with large-scale simulations and also with dedicated measurements conducted at the heavy-ion synchrotron SIS18 at GSI. The fitting procedure is tested in conjunction with various methods for mitigating quasi-degeneracy. The results obtained with the analytical Jacobian agree well with those obtained with the numerical Jacobian. A complete Python software package, including the implementation of the analytical Jacobian approach, has been created and made publicly available [1]. A dedicated setup for the ORM measurement at SIS18 is presented. This includes the development of a Java application for fully automatizing the measurement [2]. The measurement has achieved high precision with an orbit uncertainty of  $\lesssim 1 \mu\text{m}$  and an ORM uncertainty of  $\lesssim 5 \mu\text{m}/\text{mrad}$ . The developed setup is extensible and, thus, provides the foundation for high precision ORM measurements and inverse modeling also for other accelerators of the GSI and future FAIR campus.

In chapter 4, a complementary approach for application to beamlines is presented which aims to mitigate the influence of quadrupole errors in order to minimize the need for beamline re-tuning or for estimating quadrupole errors in general. This approach can be used to identify robust beamline quadrupole configurations, i.e., those configurations whose performance is particularly robust against possible quadrupole errors. First, the concept of beamline robustness is introduced and the beamlines which are used exemplary for this study are introduced. An analytical derivation is presented which can be used to assess the robustness property of a beamline configuration in terms of its Twiss data. The findings are supported by the data obtained from systematic exploration of the beamline configuration space via large-scale simulations. Various important properties of robust configurations are derived



---

from the simulated data. It is shown that the previously derived analytical expression for beamline robustness largely correlates with the simulated robustness scores. Based on these findings, the initially purely Monte Carlo based procedure for identifying robust configurations is greatly improved in terms of compute efficiency. These findings are then applied to the robust optimization of a second beamline where it is shown that the same approach can be used to efficiently identify robust beamline configurations. This emphasizes the general applicability of the methods. Eventually, the simulation results are supported by dedicated experimental data which has been collected at GSI and at Forschungszentrum Jülich. The measurements compare different quadrupole configurations in terms of their robustness. For both measurements, dedicated software has been developed which allows to fully automatize the measurements [3, 4].

Finally, chapter 5 presents the conclusions and outlook with respect to applicability to other accelerators and beamlines.



# 2

## Linear optics in synchrotrons and beam transfer lines

This chapter introduces the concepts and results from the field of accelerator physics which are relevant for the main part of the thesis. First, the conventions which will be used throughout the remainder of the manuscript are presented. Then, the derivation of relevant aspects from beam dynamics under the Hamiltonian formalism is introduced which ultimately leads to the transfer matrices of various beamline elements. Those transfer matrices can be used to describe the linear effects on the beam motion which will be used during the assessment of quadrupole errors. Following this, the derivation of synchrotron optics is introduced. With the help of the previously derived transfer matrices, the relevant formulas for linear optics errors are derived. Lastly, different methods for particle beam extraction are introduced, followed by an introduction of the quadrupole scan method, since these are relevant for the remaining chapters of the thesis.

### 2.1 Conventions

#### 2.1.1 Terminology

The term *design orbit* is used to describe the foreseen trajectory of an ideal reference particle with an energy that matches the magnet settings. However, due to the existence of various possible dipole-like error sources, the actual trajectory of the beam will necessarily deviate from the design orbit. Most notably are alignment errors of quadrupole magnets with respect to the design orbit. If a quadrupole magnet is placed such that the design orbit does not lie in the magnetic center of the quadrupole, the corresponding offset of particles will produce a dipole-like contribution to the motion. This causes the trajectory of the reference particle to deviate from the design orbit. Courant & Snyder identify this deviating trajectory as follows [14]:

"We further assume that there is a closed curve in [the bending plane] such that a particle of a certain magnetic rigidity  $P_0/q$  can move on this curve. We call this curve the *equilibrium orbit*."

The bending plane is the plane to which the dipole fields of all bending magnets are perpendicular. This does not account for roll errors of bending magnets about the longitudinal axis, but a similar closed curve can exist without the existence of such a bending plane (this is derived later in [14]). The term *closed orbit* is used synonymously for the equilibrium orbit.

The *magnetic rigidity* of a beam particle is defined as the ratio of its momentum to its electrical charge,  $P_0/q$ , and this quantity is similarly denoted as  $(B\rho)$ . This emphasizes the fact that an accelerator with bending dipole field  $B$  and radius of curvature  $\rho$  can host a beam with rigidity equal to  $(B\rho)$ .

### 2.1.2 Coordinate systems

A strong focusing circular accelerator consists of alternating straight and bending sections. The reference orbit is the closed trajectory of a particle with reference momentum  $P_0$ . To describe the straight sections of the accelerator a Cartesian coordinate system labeled by  $(x, y, z)$  will be used where the  $z$ -axis points in the direction of the reference orbit. For the bending sections a curvilinear coordinate system labeled by  $(x, y, s)$  will be used where the  $s$ -axis is tangent to the (curved) reference orbit which lies in the  $(x, s)$ -plane. The  $x$ -axis points radially outwards with respect to the reference orbit. The coordinate systems are illustrated in Figure 2.1.

The  $x$  and  $y$  coordinates describe the transverse deviations from the reference orbit. The longitudinal coordinate,  $z$  or  $s$ , describes the negative time-difference of a particle with respect to the reference particle, multiplied by the speed of light  $c$ :

$$\{z, s\} = -c\Delta t \quad (2.1)$$

The transformation from a Cartesian to the curvilinear coordinate system with bending radius  $\rho$  is given by:

$$\begin{aligned} x &= (\rho + \tilde{x}) \cos\left(\frac{s}{\rho}\right) - \rho \\ y &= \tilde{y} \\ z &= (\rho + \tilde{x}) \sin\left(\frac{s}{\rho}\right) \end{aligned} \quad (2.2)$$

where  $\tilde{x}$  and  $\tilde{y}$  denote the transverse coordinates in the curvilinear coordinate system.

In the curvilinear coordinate system, the gradient of a scalar field  $\phi$  is given by [46, 47]:

$$\begin{aligned} (\nabla\phi)_x &= \frac{\partial\phi}{\partial x} \\ (\nabla\phi)_y &= \frac{\partial\phi}{\partial y} \\ (\nabla\phi)_s &= \frac{1}{1 + hx} \frac{\partial\phi}{\partial s} \end{aligned} \quad (2.3)$$

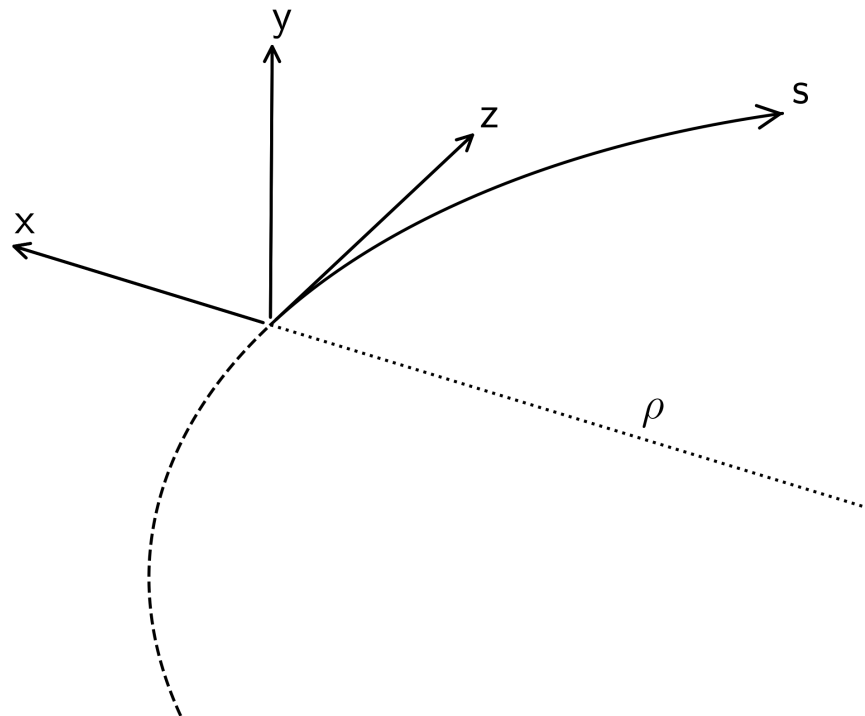


**Figure 2.1:** Coordinate systems. The system  $(x, y, z)$  is used to describe straight sections of the accelerator while the system  $(x, y, s)$  is used to describe the curved sections.  $\rho$  is the bending radius corresponding to the magnetic rigidity of the beam and the field strength of the bending magnets.

In the curvilinear coordinate system, the curl of a vector field  $\mathbf{A}$  is given by [46, 47]:

$$\begin{aligned}
 (\nabla \times \mathbf{A})_x &= \frac{\partial A_s}{\partial y} - \frac{1}{1+hx} \frac{\partial A_y}{\partial s} \\
 (\nabla \times \mathbf{A})_y &= \frac{1}{1+hx} \frac{\partial A_x}{\partial s} - \frac{h}{1+hx} A_s - \frac{\partial A_s}{\partial x} \\
 (\nabla \times \mathbf{A})_s &= \frac{\partial A_y}{\partial x} - \frac{\partial A_x}{\partial y}
 \end{aligned} \tag{2.4}$$

## 2.2 Equations of motion

Since the particles in an accelerator undergo the interaction with various electromagnetic fields generated by magnets and RF-cavities, it is of importance to understand the dynamics of the particles subject to the corresponding fields. This section of the introduction mostly follows [48] and [49, 50] (a similar approach is described in the Appendix B of [14]).

### 2.2.1 Hamiltonian formalism

The Hamiltonian formalism [51] provides a convenient framework for deriving beam dynamics. In this framework, the equations of motion are derived from the so called *Hamiltonian*  $H(\mathbf{x}, \mathbf{p}, t)$

which is a function in the particle coordinates  $\mathbf{x}$ , the canonical momentum  $\mathbf{p}$  and the time  $t$ :

$$\begin{aligned}\frac{dx_i}{dt} &= \frac{\partial H}{\partial p_i} \\ \frac{dp_i}{dt} &= -\frac{\partial H}{\partial x_i}\end{aligned}\tag{2.5}$$

The Hamiltonian  $H$  and the conjugate momentum  $\mathbf{p}$  can be derived from the *Lagrangian*  $L(\mathbf{q}, \dot{\mathbf{q}}, t)$  given in particle coordinates  $\mathbf{q} \equiv \mathbf{x}$  and velocity  $\dot{\mathbf{q}} \equiv d\mathbf{q}/dt$ :

$$\begin{aligned}p_i &= \frac{\partial L}{\partial \dot{q}_i} \\ H &= \sum_i \dot{q}_i p_i - L\end{aligned}\tag{2.6}$$

The Lagrangian is based on the principle of least action, that is, a physical system is expected to behave such that the following condition is satisfied:

$$\delta S \equiv \delta \left( \int_{t_1}^{t_2} L(\mathbf{q}(t), \dot{\mathbf{q}}(t), t) dt \right) = 0\tag{2.7}$$

where  $\delta$  indicates a variation of the path from  $\mathbf{q}(t_1)$  to  $\mathbf{q}(t_2)$ .

In many cases, the Lagrangian  $L$  is given by the kinetic energy  $T$  subtracted by the potential energy  $V$  of the system:

$$L = T - V\tag{2.8}$$

Similarly, in many cases, the Hamiltonian is the total energy of the system, that is,  $H = T + V$ . Part of establishing a physics theory consists of writing down the Lagrangian or, equivalently, the Hamiltonian of the system. The correctness of the theory then depends on the correctness of the Lagrangian or Hamiltonian since anything else is derived from it.

It is noted that, in general, the equations of motion can also be derived within the Lagrangian formalism by the Euler-Lagrange equations which also satisfy the principle of least action from equation 2.7:

$$\frac{\partial L}{\partial q_i} - \frac{d}{dt} \left( \frac{\partial L}{\partial \dot{q}_i} \right) = 0\tag{2.9}$$

The Lagrangian (eq. 2.9) and Hamilton (eq. 2.5) formalism are equivalent with regard to the derived physics, but their mathematical formulation is different and for a specific problem one formalism may be advantageous over the other.

### 2.2.1.1 Non-relativistic case

For a classical system involving electromagnetic forces, the Lagrangian can be written in terms of the electric scalar potential  $\phi(\mathbf{x})$ , the magnetic vector potential  $\mathbf{A}(\mathbf{x})$  and the particle's mass  $m$  and charge  $q$ :

$$L = \frac{1}{2}m\dot{\mathbf{x}}^2 - q\phi + q\mathbf{A}\dot{\mathbf{x}}\tag{2.10}$$

Inserting into Hamilton's equations (2.5) and (2.6) gives the following equations of motion:

$$\frac{d}{dt} (m\dot{\mathbf{x}}) = q(\mathbf{E} + \dot{\mathbf{x}} \times \mathbf{B})\tag{2.11}$$

where the vector fields  $\mathbf{E}$  and  $\mathbf{B}$  represent the following quantities:

$$\begin{aligned}\mathbf{E} &= -\nabla\phi - \frac{\partial\mathbf{A}}{\partial t} \\ \mathbf{B} &= \nabla \times \mathbf{A}\end{aligned}\tag{2.12}$$

and  $\times$  denotes the cross product between two 3-vectors.

Of course,  $\mathbf{E}$  and  $\mathbf{B}$  are, respectively, the electric and magnetic field of the system and equation 2.11 describes the motion subject to the Lorentz force. Thus, it is equivalent to the result that would have been obtained by considering Newton's equations. Nevertheless, the Hamiltonian approach is more flexible and can be generalized to the relativistic case, too.

### 2.2.1.2 Relativistic case

In special relativity, in the absence of electromagnetic fields, the total energy of a particle is given by:

$$E = \sqrt{(\mathbf{p}c)^2 + (mc^2)^2}\tag{2.13}$$

where  $\mathbf{p}$  is the mechanical momentum of the particle <sup>1</sup>,  $m$  is its rest mass and  $c$  is the speed of light in vacuum.

In the presence of electromagnetic fields, the momentum in equation 2.13 must be replaced by the conjugate momentum which includes the vector potential, that is,  $\mathbf{p} \rightarrow \mathbf{p} - q\mathbf{A}$ ; also, the potential energy  $q\phi$  due to the electric potential must be added. Again, the Hamiltonian is considered to represent the total energy of the particle and, thus, is given by:

$$H = \sqrt{(\mathbf{p} - q\mathbf{A})^2 c^2 + (mc^2)^2} + q\phi\tag{2.14}$$

### 2.2.1.3 Transformation to accelerator coordinates

The Hamiltonian from equation 2.14 is given in terms of the time  $t$  as the independent variable. In the framework of accelerator physics, a more convenient choice for the independent variable is, however, the path length along the reference orbit. This is because after constructing an accelerator lattice, it is known where along the beamline the various electromagnetic elements are located. A change in the independent variable of the Hamiltonian from time to path length implies that the longitudinal conjugate coordinates  $(z, p_z)$  are replaced with  $(-t, E)$  where  $E$  is the total energy of the particle. Because later in the derivation of beam dynamics it will be necessary to make approximations to the Hamiltonian in form of a Taylor series expansion, it is advantageous to work with a set of variables whose values generally remain small ( $\ll 1$ ) during the course around the accelerator lattice. The transverse coordinates  $x$  and  $y$  are already small as they describe the deviation from the reference orbit. Their conjugate momenta can be normalized by the reference momentum  $P_0$ . Similarly, the longitudinal coordinates can be transformed to indicate the deviation from the reference particle in terms of time and energy. To accomplish this, another canonical transformation can be applied which replaces

<sup>1</sup>Depending on the considered physics of the system, the mechanical momentum might not be identical to the conjugate momentum from equation 2.6.

## 2. Linear optics in synchrotrons and beam transfer lines

---

the transverse momenta and the longitudinal conjugate coordinates:

$$\begin{aligned}
 p_{x,y} &\rightarrow p_{x,y} &= \frac{p_{x,y}}{P_0} \\
 -t &\rightarrow \{\tilde{z}, \tilde{s}\} &= \frac{\{z, s\}}{\beta_0} - ct \\
 E &\rightarrow \delta &= \frac{E}{P_0 c} - \frac{1}{\beta_0}
 \end{aligned} \tag{2.15}$$

where  $\beta_0$  is the magnitude of the velocity of a particle with reference momentum  $P_0$  divided by the speed of light. The symbols on the left-hand side of  $\rightarrow$  denote the old coordinates (before the canonical transformation) and the symbols on the right-hand side of  $\rightarrow$  indicate the new coordinates in dependency on the old coordinates (on the right-hand side of  $=$ ). Due to the normalization with the reference momentum  $P_0$ , the values of the new conjugate momenta remain small. In the remainder of this section, accelerator coordinates are used exclusively and, thus, the transformed longitudinal coordinates  $\{\tilde{z}, \tilde{s}\}$  are written as  $\{z, s\}$  to simplify the notation.<sup>2</sup>

The canonical transformations also yields a transformed version of the Hamiltonian. For a straight section the Hamiltonian is given by:

$$H = \frac{\delta}{\beta_0} - \sqrt{\left(\frac{1}{\beta_0} + \delta - \frac{q\phi}{P_0 c}\right)^2 - (p_x - a_x)^2 - (p_y - a_y)^2 - \frac{1}{\beta_0^2 \gamma_0^2}} - a_z \tag{2.16}$$

where  $\mathbf{a} \equiv q\mathbf{A}/P_0$  is the magnetic vector potential normalized by the magnetic rigidity of the reference particle.

For a bending section of the accelerator, the Hamiltonian from equation 2.14 must be transformed into the curvilinear coordinate system  $(x, y, s)$  via a canonical transformation, similar to the transformation from equation 2.15 for the straight sections  $(x, y, z)$ . In curvilinear coordinates, the Hamiltonian for a bending section is given by:

$$H = -(1+hx)\sqrt{\left(\frac{1}{\beta_0} + \delta - \frac{q\phi}{P_0 c}\right)^2 - (p_x - a_x)^2 - (p_y - a_y)^2 - \frac{1}{\beta_0^2 \gamma_0^2}} - (1+hx)a_s + \frac{\delta}{\beta_0} \tag{2.17}$$

where  $h = \rho^{-1}$  is the curvature and  $\rho$  is the bending radius of the dipole magnets.

Equations 2.16 and 2.17 allow to derive the equations of motion for various electromagnetic field configurations by inserting the appropriate values for the electric potential  $\phi$  and the magnetic potential  $\mathbf{a}$ .

---

<sup>2</sup>It is noted that  $(\{z, s\}, \delta)$  is not the only possible choice for the conjugate coordinates and in the field of accelerator physics other definitions are sometimes used, too. For example, the TRANSPORT simulation program [52] uses  $(\Delta z, \Delta P/P_0)$  as the longitudinal conjugate pair, where  $\Delta z$  and  $\Delta P$  are, respectively, the path length deviation and momentum deviation from the reference particle with momentum  $P_0$ . In the limit  $\beta_0 \rightarrow 1$  the two definitions are equivalent.



### 2.2.2 Electromagnetic field configurations

The electric field  $\mathbf{E}$  and magnetic field  $\mathbf{B}$  are defined in terms of the electric scalar potential  $\phi$  and the magnetic vector potential  $\mathbf{A}$ :

$$\begin{aligned}\mathbf{E} &= -\nabla\phi - \frac{\partial\mathbf{A}}{\partial t} \\ \mathbf{B} &= \nabla \times \mathbf{A}\end{aligned}\tag{2.18}$$

Only those field configurations are physically relevant which satisfy Maxwell's equations [46]:

$$\begin{aligned}\nabla\mathbf{E} &= \frac{\rho_c}{\epsilon_0} \\ \nabla\mathbf{B} &= 0 \\ \nabla \times \mathbf{E} &= -\frac{\partial\mathbf{B}}{\partial t} \\ \nabla \times \mathbf{B} &= \mu_0\mathbf{J} + \mu_0\epsilon_0\frac{\partial\mathbf{E}}{\partial t}\end{aligned}\tag{2.19}$$

where  $\rho_c$  denotes the charge density,  $\mathbf{J}$  denotes the electric current density and  $\epsilon_0$  and  $\mu_0$  are, respectively, the vacuum permittivity and vacuum permeability.

#### 2.2.2.1 Magnetic multipole expansion

The magnetic field inside a long straight multipole, which is aligned with the  $z$ -axis, can be specified with the help of the following magnetic multipole field expansion [49]:

$$B_y + iB_x = \sum_{n=0}^{\infty} (b_n + ia_n) \left( \frac{x + iy}{r_0} \right)^n\tag{2.20}$$

where  $a_n, b_n$  are coefficients that must be chosen according to the actual field configuration and  $r_0$  is an arbitrary reference radius. This definition using  $r_0$  has the convenience that all coefficients  $a_n, b_n$  have the same physical unit as the magnetic field  $B_x, B_y$ . The coefficients  $b_n$  denote the *normal* components of the multipole while the coefficients  $a_n$  denote the *skew* components.

A possible choice for the magnetic vector potential  $\mathbf{A}$  which generates the magnetic field from equation 2.20 is given by:

$$\mathbf{A}(x, y, z) = \begin{pmatrix} 0 \\ 0 \\ -\text{Re} \left\{ \sum_{n=0}^{\infty} (b_n + ia_n) \frac{r_0}{n+1} \left( \frac{x+iy}{r_0} \right)^{n+1} \right\} \end{pmatrix}\tag{2.21}$$

Since in a dipole field the trajectory of particles will be bent, the set of curvilinear coordinates must be used to describe the corresponding vector potential. In the  $(x, y, s)$  system of curvilinear coordinates the magnetic vector potential of a dipole bending magnet is given by [49]:

$$\mathbf{A}_{\text{dipole}}(x, y, s) = \begin{pmatrix} 0 \\ 0 \\ -B_0 \left( x - \frac{1}{2} \frac{hx^2}{1+hx} \right) \end{pmatrix}\tag{2.22}$$

### 2.2.3 Transfer maps

The transfer maps of the various accelerator elements can be obtained by inserting the corresponding field configurations from equations 2.21 and 2.22 into the Hamiltonians from equations 2.16 and 2.17. While for a field-free region, i.e.,  $\phi \equiv 0$  and  $\mathbf{a} \equiv 0$ , it is possible to obtain an exact solution for the equations of motion, for nonzero field regions it is necessary to make an approximation in form of a Taylor expansion. The resulting transformation of particle coordinates  $\vec{x} \equiv (x, p_x, y, p_y, z, \delta)$  through an accelerator element can then be expressed as a series expansion in  $\vec{x}$  since all elements of  $\vec{x}$  have been properly normalized such that  $\vec{x}_i \ll 1$  (see equation 2.15):

$$\vec{x}_i \leftarrow d_i + \sum_{j=1}^6 R_{ij} \vec{x}_j + \sum_{j,k=1}^6 T_{ijk} \vec{x}_j \vec{x}_k + O(\vec{x}^3) \quad (2.23)$$

where  $d_i$  denotes the zeroth-order contribution to the  $i$ -th component of  $\vec{x}$ ,  $R_{ij}$  denotes the first-order contribution and  $T_{ijk}$  denotes the second order contribution.  $R_{ij}$  is also called the *transfer matrix*, as it describes the linear properties of the transformation.

In [53] the general transport coefficients  $R_{ij}$  and  $T_{ijk}$  for a combined-function dipole (bending magnet), including quadrupole and sextupole fields, are derived. It allows to obtain the transport coefficients for specific magnetic elements by setting those magnetic fields values to zero which are not present for a specific magnet. In the following, the derivation of linear transport coefficients, i.e., the transfer matrices, is presented by using a second order expansion of the Hamiltonian. For a drift space, the exact solution is presented as well.

#### 2.2.3.1 Transfer map of a drift space

A drift space is characterized as a field-free region, i.e.,  $\phi \equiv 0$  and  $\mathbf{a} \equiv 0$ . From equation 2.16 the equations of motion can be obtained via equation 2.5 and their solution for a drift space of length  $L$  is given by:

$$\begin{aligned} \frac{\Delta x}{L} &= \frac{p_x}{\sqrt{\left(\frac{1}{\beta_0} + \delta\right)^2 - p_x^2 - p_y^2 - \frac{1}{\beta_0^2 \gamma_0^2}}} \\ \frac{\Delta y}{L} &= \frac{p_y}{\sqrt{\left(\frac{1}{\beta_0} + \delta\right)^2 - p_x^2 - p_y^2 - \frac{1}{\beta_0^2 \gamma_0^2}}} \\ \frac{\Delta z}{L} &= \frac{1}{\beta_0} - \frac{\frac{1}{\beta_0} + \delta}{\sqrt{\left(\frac{1}{\beta_0} + \delta\right)^2 - p_x^2 - p_y^2 - \frac{1}{\beta_0^2 \gamma_0^2}}} \\ \Delta p_x &= \Delta p_y = \Delta p_z = 0 \end{aligned} \quad (2.24)$$

This is the exact transfer map for a drift space of length  $L$  and this exact representation is used by particle tracking codes, for example. However, for other purposes, specifically linear optics calculations, the expressions in equation 2.24 can be simplified with the help of a Taylor expansion while retaining only the linear terms. This results in the following linear transfer

map:

$$\begin{aligned}
 \Delta x &\approx p_x L \\
 \Delta y &\approx p_y L \\
 \Delta z &\approx \frac{L}{\beta_0^2 \gamma_0^2} \\
 \Delta p_x &= \Delta p_y = \Delta p_z = 0
 \end{aligned} \tag{2.25}$$

A similar result is obtained when the Hamiltonian from equation 2.16 is expanded to second order in the coordinates and then the equations of motion are derived via equation 2.5:

$$H_{\text{drift}} = \frac{p_x^2}{2} + \frac{p_y^2}{2} + \frac{1}{\beta_0^2 \gamma_0^2} \frac{\delta^2}{2} \tag{2.26}$$

The corresponding transfer matrix of a drift space of length  $L$  is:

$$R_{\text{drift}} = \begin{pmatrix} 1 & L & 0 & 0 & 0 & 0 \\ 0 & 1 & 0 & 0 & 0 & 0 \\ 0 & 0 & 1 & L & 0 & 0 \\ 0 & 0 & 0 & 1 & 0 & 0 \\ 0 & 0 & 0 & 0 & 1 & \frac{L}{\beta_0^2 \gamma_0^2} \\ 0 & 0 & 0 & 0 & 0 & 1 \end{pmatrix} \tag{2.27}$$

### 2.2.3.2 Transfer map of a bending magnet

The Hamiltonian for a bending section from equation 2.17 can be used together with the field configuration from equation 2.22 to derive the equations of motion for a dipole bending magnet. To obtain a solution for the equations of motion, the Hamiltonian can be expanded up to second order in the dynamical variables:

$$H_{\text{dipole}} = \frac{p_x^2}{2} + \frac{p_y^2}{2} + (k_0 - h)x + hk_0 \frac{x^2}{2} - \frac{h}{\beta_0} x \delta - \frac{1}{\beta_0^2 \gamma_0^2} \frac{\delta^2}{2} \tag{2.28}$$

where  $k_0 = b_0/(B\rho)$  is the dipole magnetic field normalized by the magnetic rigidity of the reference particle.

The corresponding transfer matrix is given by:

$$R_{\text{dipole}} = \begin{pmatrix} \cos(k_0 L) & \frac{\sin(k_0 L)}{k_0} & 0 & 0 & 0 & \frac{1 - \cos(k_0 L)}{k_0 \beta_0} \\ -k_0 \sin(k_0 L) & \cos(k_0 L) & 0 & 0 & 0 & \frac{\sin(k_0 L)}{\beta_0} \\ 0 & 0 & 1 & L & 0 & 0 \\ 0 & 0 & 0 & 1 & 0 & 0 \\ -\frac{\sin(k_0 L)}{\beta_0} & -\frac{1 - \cos(k_0 L)}{k_0 \beta_0} & 0 & 0 & 1 & \frac{L}{\beta_0^2 \gamma_0^2} - \frac{k_0 L - \sin(k_0 L)}{k_0 \beta_0^2} \\ 0 & 0 & 0 & 0 & 0 & 1 \end{pmatrix} \tag{2.29}$$

The  $R_{\{1,2,5\}6}$  elements of the transfer matrix describe the dispersion generated by the bending magnet. That is, a particle with momentum greater than the reference momentum will receive less bending from the magnet which results in an additional horizontal and longitudinal offset. The transfer matrix also implies a focusing in the horizontal dimension. This is

sometimes called geometrical focusing because it is of geometrical nature; the trajectories of two particles with different horizontal offset will oscillate about each other, as illustrated in Figure 2.2.

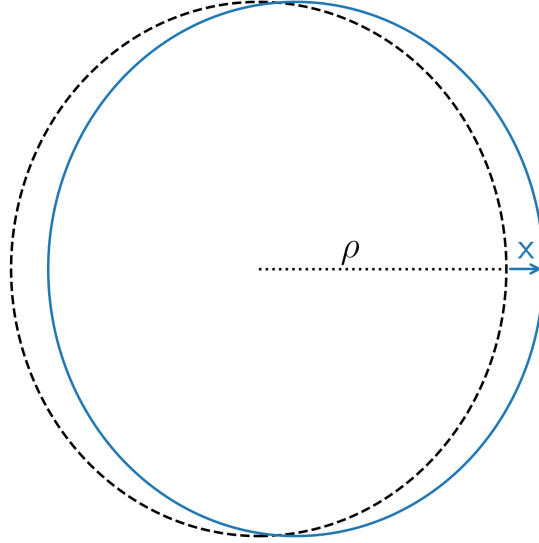


**Figure 2.2:** Illustration of geometrical focusing. The dashed line indicates the trajectory of the reference particle and the solid line indicates the trajectory of a particle with horizontal deviation  $x$  from the reference trajectory.

It is noted that in case the field of the dipole  $k_0$  is not matched to the design orbit with curvature  $h$ , then the particles will pick up a zeroth-order contribution which is represented by the  $(k_0 - h)$  term in the Hamiltonian (eq. 2.28).

### 2.2.3.3 Transfer map of a quadrupole magnet

**Normal quadrupole** The second order Hamiltonian of a normal quadrupole magnet ( $b_1 \neq 0$  in equation 2.21) of length  $L$  is given by:

$$H_{\text{quadrupole}}^{\text{normal}} = \frac{p_x^2}{2} + \frac{p_y^2}{2} + k_1 \frac{x^2}{2} - k_1 \frac{y^2}{2} + \frac{1}{\beta_0^2 \gamma_0^2} \frac{\delta^2}{2} \quad (2.30)$$

where  $k_1 = (b_1/r_0)/(B\rho)$  is the normalized quadrupole gradient.

The corresponding transfer matrix for a normal quadrupole with  $k_1 > 0$  is:

$$R_{\text{quadrupole}}^{\text{normal}} = \begin{pmatrix} \cos(\omega L) & \omega^{-1} \sin(\omega L) & 0 & 0 & 0 & 0 \\ -\omega \sin(\omega L) & \cos(\omega L) & 0 & 0 & 0 & 0 \\ 0 & 0 & \cosh(\omega L) & \omega^{-1} \sinh(\omega L) & 0 & 0 \\ 0 & 0 & \omega \sinh(\omega L) & \cosh(\omega L) & 0 & 0 \\ 0 & 0 & 0 & 0 & 1 & \frac{L}{\beta_0^2 \gamma_0^2} \\ 0 & 0 & 0 & 0 & 0 & 1 \end{pmatrix} \quad (2.31)$$

where  $\omega = \sqrt{k_1}$ . The  $\{\cos, \sin\}$  terms correspond to a focusing motion in  $x$ -dimension whereas the  $\{\cosh, \sinh\}$  terms correspond to defocusing motion in  $y$ -dimension. Thus, a quadrupole with  $k_1 > 0$  is said to be horizontally focusing. For a horizontally defocusing quadrupole with

$k_1 < 0$  the diagonal blocks corresponding to the two transverse dimensions are interchanged and  $k_1$  is replaced by  $-k_1$  (which causes the quadrupole to be vertically focusing).

**Skew quadrupole** The second order Hamiltonian of a skew quadrupole magnet ( $a_1 \neq 0$  in equation 2.21) of length  $L$  is given by:

$$H_{\text{quadrupole}}^{\text{skew}} = \frac{p_x^2}{2} + \frac{p_y^2}{2} + k_{1,s}xy + \frac{1}{\beta_0^2\gamma_0^2} \frac{\delta^2}{2} \quad (2.32)$$

where  $k_{1,s} = -(a_1/r_0)/(B\rho)$  is the normalized skew quadrupole gradient. The term  $k_{1,s}xy$  implies a coupling between the horizontal and vertical motion.

The corresponding transfer matrix for a skew quadrupole with  $k_{1,s} > 0$  is:

$$R_{\text{quadrupole}}^{\text{skew}} = \frac{1}{2} \begin{pmatrix} c_x + c_y & \omega^{-1}(s_x + s_y) & c_x - c_y & \omega^{-1}(s_x - s_y) & 0 & 0 \\ -\omega(s_x - s_y) & c_x + c_y & -\omega(s_x + s_y) & c_x - c_y & 0 & 0 \\ c_x - c_y & \omega^{-1}(s_x - s_y) & c_x + c_y & \omega^{-1}(s_x + s_y) & 0 & 0 \\ -\omega(s_x + s_y) & c_x - c_y & -\omega(s_x - s_y) & c_x + c_y & 0 & 0 \\ 0 & 0 & 0 & 0 & 2 & \frac{2L}{\beta_0^2\gamma_0^2} \\ 0 & 0 & 0 & 0 & 0 & 2 \end{pmatrix} \quad (2.33)$$

where  $c_x = \cos(\omega L)$ ,  $c_y = \cosh(\omega L)$ ,  $s_x = \sin(\omega L)$ ,  $s_y = \sinh(\omega L)$  and  $\omega = \sqrt{k_{1,s}}$ . The coupling is represented by the off-diagonal blocks in the transfer matrix. For  $k_{1,s} < 0$ ,  $\omega$  is replaced by  $\sqrt{-k_{1,s}}$  and the trigonometric terms are interchanged:  $c_x \leftrightarrow c_y$  and  $s_x \leftrightarrow s_y$ .

#### 2.2.3.4 Transfer map of a combined function dipole

A combined function dipole includes both dipole and quadrupole fields. The second order Hamiltonian of a combined function dipole is given by [53]:

$$H_2 = \frac{1 - n(s)}{\rho(s)^2} \frac{x^2}{2} + \frac{n(s)}{\rho(s)^2} \frac{y^2}{2} + \frac{p_x^2}{2} + \frac{p_y^2}{2} + \frac{1}{\beta^2\gamma^2} \frac{\delta^2}{2} - \frac{1}{\beta\rho(s)} x\delta \quad (2.34)$$

where the radius of curvature of the reference orbit,  $\rho(s)$ , is given by

$$\rho(s) = \frac{(B\rho)}{B_y(s)} \quad (2.35)$$

and the normalized radial field gradient  $n(s)$  is given by

$$n(s) = -\frac{\rho(s)^2}{(B\rho)} \frac{\partial B_y(s)}{\partial x} \quad (2.36)$$

Details are given in Appendix B of [14].

The corresponding equations of motion are:

$$\begin{aligned} \frac{d^2x}{ds^2} + \frac{1 - n(s)}{\rho(s)^2} x &= \frac{\delta}{\beta\rho(s)} \\ \frac{d^2y}{ds^2} + \frac{n(s)}{\rho(s)^2} y &= 0 \end{aligned} \quad (2.37)$$

## 2. Linear optics in synchrotrons and beam transfer lines

The corresponding transfer matrix is given by [53]:

$$R_{\text{combined function dipole}} = \begin{pmatrix} \cos(\omega_x L) & \omega_x^{-1} \sin(\omega_x L) & 0 & 0 & 0 & \frac{k_0}{\beta_0} \frac{1 - \cos(\omega_x L)}{\omega_x^2} \\ -\omega_x \sin(\omega_x L) & \cos(\omega_x L) & 0 & 0 & 0 & \frac{k_0}{\beta_0} \frac{\sin(\omega_x L)}{\omega_x} \\ 0 & 0 & \cos(\omega_y L) & \omega_y^{-1} \sin(\omega_y L) & 0 & 0 \\ 0 & 0 & -\omega_y \sin(\omega_y L) & \cos(\omega_y L) & 0 & 0 \\ -\frac{k_0}{\beta_0} \frac{\sin(\omega_x L)}{\omega_x} & -\frac{k_0}{\beta_0} \frac{1 - \cos(\omega_x L)}{\omega_x^2} & 0 & 0 & 1 & \frac{L}{\beta_0^2 \gamma_0^2} - \frac{k_0^2}{\beta_0^2} \frac{L - \omega_x^{-1} \sin(\omega_x L)}{\omega_x^2} \\ 0 & 0 & 0 & 0 & 0 & 1 \end{pmatrix} \quad (2.38)$$

where  $\omega_x = \sqrt{k_0^2 + k_1}$  and  $\omega_y = \sqrt{-k_1}$  and  $k_0, k_1$  are the normalized dipole and quadrupole fields defined in, respectively, sections 2.2.3.2 and 2.2.3.3.

### 2.2.3.5 Transfer map of a sextupole magnet

Since the magnetic vector potential for a sextupole magnet ( $b_2 \neq 0$  in equation 2.21) does not contain any terms that depend on the positions  $x$  and  $y$  up to second order, the second order Hamiltonian is the same as the second order Hamiltonian for a drift space. Thus, the linear contribution of a sextupole to the beam dynamics is the same as for a drift space:

$$R_{\text{sextupole}} = R_{\text{drift}} \quad (2.39)$$

The second order contributions of a thin sextupole with strength ( $K_2 L$ ) are [53]:

$$\begin{aligned} T_{211} &= -\frac{1}{2}(K_2 L) \\ T_{233} &= \frac{1}{2}(K_2 L) \\ T_{413} = T_{431} &= \frac{1}{2}(K_2 L) \end{aligned} \quad (2.40)$$

### 2.2.3.6 Transfer map of dipole fringe fields

Due to the finite length of magnetic elements, the fields extend beyond the physical dimension of the magnets. These fringing fields also influence the particles and the effect is most notable for dipole magnets with a pole face rotation  $\psi$  relative to the beam path ( $\psi = 0$  means that the pole face is perpendicular to the beam path). In the approximation of a short fringe field region, the transfer matrix is given by [50]:

$$R_{\text{dipole fringe field}} = \begin{pmatrix} 1 & 0 & 0 & 0 & 0 & 0 \\ \frac{B_0}{(B\rho)} \tan \psi & 1 & 0 & 0 & 0 & 0 \\ 0 & 0 & 1 & 0 & 0 & 0 \\ 0 & 0 & -\frac{B_0}{(B\rho)} \tan \psi & 1 & 0 & 0 \\ 0 & 0 & 0 & 0 & 1 & 0 \\ 0 & 0 & 0 & 0 & 0 & 1 \end{pmatrix} \quad (2.41)$$

### 2.2.3.7 Contraction of transfer maps

The contraction of two transfer maps is the process of combining their coefficients in such a way that the resulting expression has the form of a single transfer map, describing the transformation through both elements. In the following,  $x$  is used instead of  $\vec{x}$  to denote the six-dimensional phase-space coordinates  $(x, p_x, y, p_y, z, \delta)$ .

**Linear optics** Under the approximation of linear optics, each transfer map includes only coefficients up to first order:

$$x_i^{(1)} = d_i^{(1)} + R_{ij}^{(1)} x_j^{(0)} \quad (2.42)$$

where  $R$  represents the transfer matrix and  $d$  represents the zeroth-order term. Superscript is used to denote the stage of tracking;  $(0)$  corresponds to the initial coordinates (before the first element) and  $(1)$  corresponds to the first element, that is,  $x^{(1)}$  are the coordinates downstream of the first element. Similarly,  $(n)$  corresponds to the  $n$ -th element and  $x^{(n)}$  are the coordinates downstream of that element.

The transformation through the second element takes a similar form as the one above:

$$x_i^{(2)} = d_i^{(2)} + R_{ij}^{(2)} x_j^{(1)} \quad (2.43)$$

Substituting equation 2.42 for the first transformation into equation 2.43 for the second transformation, one obtains:

$$x_i^{(2)} = d_i^{(2)} + R_{ij}^{(2)} \left( d_j^{(1)} + R_{jk}^{(1)} x_k^{(0)} \right) \quad (2.44)$$

Grouping by power in  $x$  yields the following expression:

$$x_i^{(2)} = \left( d_i^{(2)} + R_{ij}^{(2)} d_j^{(1)} \right) + R_{ij}^{(2)} R_{jk}^{(1)} x_k^{(0)} \quad (2.45)$$

Equation 2.45 can be rewritten as a first order transfer map with coefficients  $d^{(c)}$  and  $R^{(c)}$ :

$$x_i^{(2)} = d_i^{(c)} + R_{ij}^{(c)} x_j^{(0)} \quad (2.46)$$

where

$$\begin{aligned} d_i^{(c)} &= d_i^{(2)} + R_{ij}^{(2)} d_j^{(1)} \\ R_{ij}^{(c)} &= R_{ik}^{(2)} R_{kj}^{(1)} \end{aligned} \quad (2.47)$$

Since the resulting first order transfer map completely describes the transformation through both elements this process can be repeated for an arbitrary number of elements without losing exactness of the transformations. This method can be used to obtain the one-turn transfer map for linear optics.

**Second order contributions** Including the second order contribution  $T$ , the transfer map is given as:

$$x_i^{(n)} = d_i^{(n)} + R_{ij}^{(n)} x_j^{(n-1)} + T_{ijk}^{(n)} x_j^{(n-1)} x_k^{(n-1)} \quad (2.48)$$

When two such transfer maps are chained in order to obtain the coordinates  $x_i^{(2)}$  as a function of the initial coordinates  $x_i^{(0)}$ , it becomes obvious that higher order contributions in  $x$  are introduced by the term

$$T_{ijk}^{(2)} x_j^{(1)} x_k^{(1)} \quad (2.49)$$

Here  $x^{(1)}$  is itself a second order function of the initial coordinates  $x^{(0)}$  and, hence, the resulting expression contains third and fourth order contributions in  $x$ . In order to cast it to a second order transfer map, which is required to obtain a single transfer map describing both elements, the higher order terms need to be discarded. As a result, the two-element second order transfer map will be an approximation of the actual transformation that would be obtained by tracking both elements separately. The resulting two-element second order transfer map is then given by:

$$x_i^{(2)} = d_i^{(c)} + R_{ij}^{(c)} x_j^{(0)} + T_{ijk}^{(c)} x_j^{(0)} x_k^{(0)} \quad (2.50)$$

where

$$\begin{aligned} d_i^{(c)} &= d_i^{(2)} + R_{ij}^{(2)} d_j^{(1)} + T_{ijk}^{(2)} d_j^{(1)} d_k^{(1)} \\ R_{ij}^{(c)} &= R_{ik}^{(2)} R_{kj}^{(1)} + 2T_{ikl}^{(2)} R_{kj}^{(1)} d_l^{(1)} \\ T_{ijk}^{(c)} &= T_{ilm}^{(2)} R_{lj}^{(1)} R_{mk}^{(1)} + 2T_{ilm}^{(2)} T_{ljk}^{(1)} d_m^{(1)} + R_{il}^{(2)} T_{ljk}^{(1)} \end{aligned} \quad (2.51)$$

Because the second order contributions to  $R^{(c)}$  may lead to a transfer matrix which is non-symplectic, it should be symplectified in a separate postprocessing step in order to be physically correct. Otherwise, it would infringe the conservation of phase-space density according to Liouville's theorem.

**Symplectification of transfer matrices** As described above, the transfer matrix representing the linear coefficients of a concatenated second (or higher) order transfer map may be non-symplectic. However, there exists an algorithm which restores this property [54]. The method is based on symmetrizing a related matrix  $W$  which can then be used to construct a symplectic version  $R'$  of the original matrix  $R$ :

$$V = S \frac{1-R}{1+R} \quad \rightarrow \quad W = \frac{1}{2} (V + V^T) \quad \rightarrow \quad R' = \frac{1+SW}{1-SW} \quad (2.52)$$

The matrix  $W$  is symmetric by definition and in [54] it is shown that the resulting matrix  $R'$  is symplectic.

### 2.2.3.8 Computation of closed orbit

Various applications require to find the closed orbit for a given lattice configuration. The closed orbit is defined as the fixed point of the (non-contracted) one-turn transfer map. That is, the task is to find a value for  $x^{(0)}$  such that when it is tracked through the entire lattice, one element after another, the resulting value coincides with the initial  $x^{(0)}$ , i.e., the orbit closes on itself. For linear optics, the one turn transfer map can be represented exactly as a contraction of individual transfer maps and is given by equations 2.46. This equation can be solved for  $x^{(0)}$  and the result is given by:

$$x_i^{(0)} = \left(1 - R^{(c)}\right)_{ij}^{-1} d_j^{(c)} \quad (2.53)$$



When second order contributions are included, then the closed orbit can be found in an iterative procedure where the linear contribution from the contracted one-turn map  $R^{(c)}$  is used as the Jacobian for the orbit with respect to itself. During each step, the current guess for  $x^{(0)}$  is updated via:

$$x_i^{(0)} \leftarrow x_i^{(0)} + \left(1 - R^{(c)}\right)_{ij}^{-1} \left(x^{(n)} - x^{(0)}\right)_j \quad (2.54)$$

where  $x^{(n)}$  represents the orbit that emerges from  $x^{(0)}$  being tracked through the entire lattice consisting of  $n$  elements. This procedure is repeated until the agreement between  $x^{(0)}$  and  $x^{(n)}$  is sufficiently close <sup>3</sup>.

### 2.2.3.9 Slicing of beamline elements

For particle tracking, it is desirable that the description of the lattice in terms of the transfer maps of its elements is symplectic. For thick elements with non-linear effects such as quadrupoles this is, however, not the case. In order to make the lattice description symplectic, these devices can be represented as a sequence of thin multipoles separated by a number of drift spaces such that the total length  $L$  of the element is preserved:

$$\delta \mid \Delta \mid \Delta \mid \dots \mid \Delta \mid \delta \quad (2.55)$$

In the above depiction,  $\delta$  and  $\Delta$  represent drift spaces of, respectively, length  $L\delta$  and  $L\Delta$  and  $\mid$  represents the thin multipole slices. In order to agree with the total length of the element,  $2\delta + (n-1)\Delta = L$  must hold where  $n$  is the number of slices. A slicing pattern is specified by the choice for the values  $\delta$  and  $\Delta$ . Table 2.1 shows an overview of various slicing methods in terms of their choices for  $\delta$  and  $\Delta$ . Among all slicing patterns, the Teapot method gives the most accurate representation of the  $R_{21}$  matrix element of a thick quadrupole; it is accurate up to second order in the integrated strength  $K_1L$  of the quadrupole [55].

**Table 2.1:** Overview of different methods for slicing beamline elements according to equation 2.55.  $n$  represents the number of slices.

|        | $\delta$           | $\Delta$          |
|--------|--------------------|-------------------|
| Edge   | 0                  | $\frac{1}{n-1}$   |
| Simple | $\frac{1}{2n}$     | $\frac{1}{n}$     |
| Teapot | $\frac{1}{2(n+1)}$ | $\frac{n}{n^2-1}$ |

### 2.2.3.10 Summary of beamline elements

Dipole bending magnets are used to force the beam on its circular trajectory around the accelerator. The necessary focusing in the transverse dimensions is provided either by a radial field gradient in the dipole magnets or by using dedicated quadrupole magnets. Skew quadrupole magnets can be used to correct the transverse coupling in the lattice. Sextupole

<sup>3</sup>Where "sufficient" has to be specified by the user.

magnets can be used to correct higher order effects such as the chromaticity or to excite a third-order resonance for resonant slow extraction. RF-cavities provide the longitudinal focusing for the bunches and, of course, they are used to accelerate the particles to higher energies. Fringe fields of magnetic elements are an undesired, however, unavoidable property of these devices. However, clever magnet design aims to minimize the influence of the fringe fields on the beam.

### 2.3 Synchrotron optics

The advantage of describing a synchrotron via its optics properties is that the properties of the machine can be described without the notion of an actual beam. For example, at SIS18 at GSI, a wide variety of ion species can be accelerated to various energies. Also, the distribution of particles inside the beam may vary. But the optics description of the machine is agnostic of that and, thus, allows for a general description of the accelerator properties and this description is compatible with any type of particle beam. The derivations in this section mostly follow [14, 48] but using the notation introduced in section 2.1.2 with the difference that  $s$  is used exclusively to denote the path length along the reference orbit.

From a mathematical viewpoint, the differential equations 2.37 are examples of Hill's equation, i.e., second-order linear ordinary differential equations with periodic coefficients. The only difference between the horizontal and vertical dimension is the additional energy dependent term on the right-hand side of the horizontal equation. This additional term indicates the energy-dependence of the horizontal motion and it makes the corresponding differential equation nonhomogeneous. The general solution to a nonhomogeneous linear differential equation is given by the sum of a particular solution to that differential equation and the general solution to the complementary homogeneous differential equation. Section 2.3.1 discusses the properties of the homogeneous equation while the nonhomogeneous equation is discussed in section 2.3.2.

#### 2.3.1 Transverse optics

When neglecting the energy-dependent term <sup>4</sup>, both equations of motion can be written in the form

$$\frac{d^2\zeta}{ds^2} = -K(s)\zeta \quad (2.56)$$

where  $\zeta \equiv \{x, y\}$  and  $K(s)$  is the corresponding coefficient from equation 2.37. Since the reference orbit is a closed trajectory around the accelerator lattice,  $K(s)$  satisfies the periodicity relation  $K(s + C) = K(s)$  where  $C$  is the path length of the reference orbit.

From equations (2.35), (2.36) and (2.56) it becomes apparent that in order to obtain focusing motion in both transverse dimensions,  $x$  and  $y$ , the bending field  $B_y(s)$  must have a gradient in the radial direction  $x$ . In early synchrotrons which had no dedicated quadrupole magnets, this was achieved by using curved pole faces for the dipole magnets, as illustrated in Figure 2.3. Different magnet shapes, so called E- and C-shape magnets, have been proposed for the AGS and PS machines [12, 11].

---

<sup>4</sup>This implies the assumption that the momentum of particles coincides with the reference momentum.

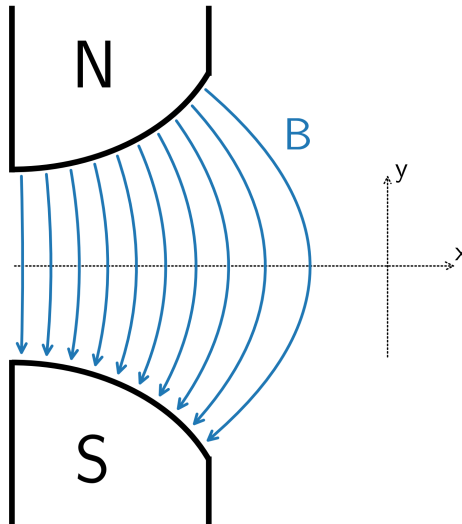


**Figure 2.3:** Schematic of the cross section of a dipole magnet with curved pole faces that produce a radial field gradient. The density of field lines decreases when moving towards positive  $x$  values and this field gradient provides vertical focusing. The curvature of the pole faces is exaggerated for the purpose of illustration.

A general solution for the differential equation 2.56 can be written in the following form [56]:

$$\begin{pmatrix} \zeta(s) \\ \zeta'(s) \end{pmatrix} = \begin{pmatrix} a(s|s_0) & b(s|s_0) \\ c(s|s_0) & d(s|s_0) \end{pmatrix} \begin{pmatrix} \zeta(s_0) \\ \zeta'(s_0) \end{pmatrix} \equiv M(s|s_0) \begin{pmatrix} \zeta(s_0) \\ \zeta'(s_0) \end{pmatrix} \quad (2.57)$$

where  $\zeta(s_0), \zeta'(s_0)$  are the initial values of the functions  $\zeta(s), \zeta'(s)$  evaluated at  $s_0$ . The matrix  $M(s|s_0)$  only depends on the coefficient function  $K(s)$  between  $s_0$  and  $s$  and its determinant is equal to unity [56]:

$$\det M = 1 \quad (2.58)$$

It is noted that for constant values of  $K$  between  $s_0$  and  $s$ , the matrix  $M$  represents the transfer matrices obtained for the various beamline elements in section 2.2.3. The matrix for one revolution around the reference orbit, starting at position  $s$ , is given by  $M(s + C|s)$  and the matrix for  $k$  revolutions is given by:

$$M(s + kC|s) = M(s + C|s)^k \quad (2.59)$$

In the following the symbol  $M$  is used as shorthand notation for  $M(s + C|s)$ .

### 2.3.1.1 Stability of the motion

The motion according to equation 2.57 is stable if and only if all elements of the matrix  $M^k$  remain bounded for  $k \rightarrow \infty$ . A square matrix raised to a power can be represented via its eigendecomposition

$$M = Q\Lambda Q^{-1} \quad (2.60)$$

where  $Q$  is the matrix that is obtained by stacking all eigenvectors of  $M$  as columns and  $\Lambda$  is the diagonal matrix whose elements are the corresponding eigenvalues. The eigendecomposition

## 2. Linear optics in synchrotrons and beam transfer lines

---

of  $M$  is guaranteed to exist since  $\det(M) = 1$ . Therefore, the expression  $M^k$  can be written as

$$M^k = Q\Lambda^k Q^{-1} \quad (2.61)$$

Thus, the matrix elements of  $M^k$  remain bounded if and only if  $\Lambda^k$  remains bounded. The eigenvalues of  $M$ ,  $\lambda_{1,2}$ , are determined by the equation

$$\det(M - \lambda_{1,2}I) = 0 \quad (2.62)$$

where  $I$  is the identity matrix. The eigenvalues are then given by

$$\lambda_{1,2} = \cos(\mu) \pm i \sin(\mu) \quad (2.63)$$

where  $i$  is the imaginary unit and  $\cos(\mu)$  is defined as

$$\cos(\mu) \equiv \frac{1}{2}(a + d) = \frac{1}{2} \operatorname{tr}(M) \quad (2.64)$$

In the context of accelerator physics, the quantity  $\mu$  is referred to as *phase advance*. In addition, the quantities  $\alpha, \beta, \gamma$ , the so-called Twiss parameters, are defined as

$$\begin{aligned} \alpha &\equiv \frac{a - d}{2 \sin(\mu)} \\ \beta &\equiv \frac{b}{\sin(\mu)} \\ \gamma &\equiv -\frac{c}{\sin(\mu)} \end{aligned} \quad (2.65)$$

These definitions allow rewriting the matrix  $M$  in the following way:

$$M = \begin{pmatrix} 1 & 0 \\ 0 & 1 \end{pmatrix} \cos(\mu) + \begin{pmatrix} \alpha & \beta \\ -\gamma & -\alpha \end{pmatrix} \sin(\mu) \equiv I \cos(\mu) + J \sin(\mu) \quad (2.66)$$

Because  $\det(M) = 1$  it follows that

$$\beta\gamma - \alpha^2 = 1 \quad (2.67)$$

and

$$J^2 = -I \quad (2.68)$$

This allows further rewriting  $M$  in the following form (see appendix A.2):

$$M = \exp(J\mu) \quad (2.69)$$

From the trigonometric identities  $\sin(x + y) = \sin(x) \cos(y) + \cos(x) \sin(y)$  and  $\cos(x + y) = \cos(x) \cos(y) - \sin(x) \sin(y)$  it follows that

$$M^k = I \cos(k\mu) + J \sin(k\mu) \quad (2.70)$$

as well as

$$M^{-1} = I \cos(\mu) - J \sin(\mu) \quad (2.71)$$

From equation 2.70 follows that the elements of  $M^k$  remain bounded if and only if  $\mu$  is a real number and, thus, by equation 2.64, if and only if

$$|\operatorname{tr}(M)| < 2 \quad (2.72)$$

Equation 2.72 is a necessary and sufficient condition for the one-turn transfer matrix  $M$  to produce stable motion around the accelerator lattice. It is noted that in case there exist similar periods of the accelerator lattice which are shorter than the entire circumference, so called superperiods, then the same condition applies to the matrix  $M(s+L|s)$  where  $L$  is the length of a superperiod. This is because the derivation of equation 2.72 is based on the periodicity of the coefficient  $K(s)$  from the equations of motion 2.37.

One can define another set of coordinates that emerge from the following transformation:

$$\begin{pmatrix} \tilde{\zeta}(s) \\ \tilde{\zeta}'(s) \end{pmatrix} = \frac{1}{\sqrt{\beta(s)}} \begin{pmatrix} 1 & 0 \\ \alpha(s) & \beta(s) \end{pmatrix} \begin{pmatrix} \zeta(s) \\ \zeta'(s) \end{pmatrix} = \begin{pmatrix} \sqrt{\beta(s)}^{-1} \zeta(s) \\ \sqrt{\beta(s)}^{-1} \alpha(s) \zeta(s) + \sqrt{\beta(s)} \zeta'(s) \end{pmatrix} \quad (2.73)$$

For the coordinates  $(\tilde{\zeta}(s), \tilde{\zeta}'(s))$ , the one-turn transfer matrix from equation 2.66 is given by

$$\tilde{M} = \begin{pmatrix} \cos \mu & \sin \mu \\ -\sin \mu & \cos \mu \end{pmatrix} \quad (2.74)$$

which represents a rotation in the normalized phase-space  $(\tilde{\zeta}(s), \tilde{\zeta}'(s))$  [57].

### 2.3.1.2 Solutions for constant magnetic field gradient

Equation 2.57 introduced the matrix  $M$  as the solution to the equations of motion 2.37. For sections with constant  $K(s) \equiv K$ , the solution to the equations of motion is given as:

$$M(s|s_0) = \begin{cases} \begin{pmatrix} \cos(\sqrt{K}(s-s_0)) & \sqrt{K}^{-1} \sin(\sqrt{K}(s-s_0)) \\ -\sqrt{K} \sin(\sqrt{K}(s-s_0)) & \cos(\sqrt{K}(s-s_0)) \end{pmatrix}, & K > 0 \\ \begin{pmatrix} \cosh(\sqrt{-K}(s-s_0)) & \sqrt{-K}^{-1} \sinh(\sqrt{-K}(s-s_0)) \\ -\sqrt{-K} \sinh(\sqrt{-K}(s-s_0)) & \cosh(\sqrt{-K}(s-s_0)) \end{pmatrix}, & K < 0 \end{cases} \quad (2.75)$$

which is the transfer matrix of a combined function dipole magnet with  $K = k_0^2 + k_1$  (i.e., a magnet with dipole and quadrupole field components). If either  $k_0 \equiv 0$  or  $k_1 \equiv 0$  then equation 2.75 represents the transfer matrix for, respectively, a quadrupole or dipole magnet (compare with equations 2.31 and 2.29).

### 2.3.1.3 Weak focusing

In a constant gradient synchrotron the field coefficients  $K(s)$  are constant along the entire accelerator lattice and, thus, the condition for stable motion is that  $\sqrt{K}$  is a real number in both dimensions,  $x$  and  $y$ . In conjunction with equation 2.37 this leads to the following

conditions:

$$\begin{aligned} (y) \quad & 0 < n \\ (x) \quad & n < 1 \end{aligned} \tag{2.76}$$

Because of the upper limit on the field gradient,  $n < 1$ , this is referred to as *weak focusing*. Equation 2.37 implies that when  $n$  increases, the restoring force from the magnetic field decreases in the horizontal dimension. The net focusing that is achieved for  $n < 1$  is due to the curved path and, thus, of geometrical nature (see section 2.2.3.2 and Figure 2.2).

### 2.3.1.4 Strong focusing

The breakthrough of the alternating gradient synchrotron theory was to use sections with alternating positive and negative values of  $n(s)$  which allows for much larger magnitudes  $|n(s)| \gg 1$ ; thus, this is referred to as *strong focusing*. The advantage of strong focusing is that it allows for greatly reduced magnet apertures compared to weak focusing and, thus, decreases the effort and cost to construct such accelerators. In its simplest form, the accelerator lattice consists of  $N$  identical superperiods and each superperiod is a segment with  $n = n_1$  followed by a segment with  $n = -n_2$  for  $n_{1,2} > 0$ . The transfer matrix for a superperiod is obtained by multiplying the transfer matrix for the  $n_1$  segment with the transfer matrix for the  $n_2$  segment obtained from equation 2.75. The stability of the motion is determined by the trace of the resulting matrix which is given by

$$\begin{aligned} \cos(\mu_x) &= \cos(\phi_x) \cosh(\psi_x) - \frac{2 - n_1 + n_2}{2\sqrt{(n_2 + 1)(n_1 - 1)}} \sin(\phi_x) \sinh(\psi_x) \\ \cos(\mu_y) &= \cos(\phi_y) \cosh(\psi_y) - \frac{n_1 - n_2}{2\sqrt{n_1 n_2}} \sin(\phi_y) \sinh(\psi_y) \end{aligned} \tag{2.77}$$

where

$$\begin{aligned} \frac{\phi_x}{\pi} &= \frac{\sqrt{n_2 + 1}}{N} \\ \frac{\psi_x}{\pi} &= \frac{\sqrt{n_1 - 1}}{N} \\ \frac{\phi_y}{\pi} &= \frac{\sqrt{n_1}}{N} \\ \frac{\psi_y}{\pi} &= \frac{\sqrt{n_2}}{N} \end{aligned} \tag{2.78}$$

Figure 2.4 shows the well-known "necktie" plot which indicates the region of  $n_1, n_2$  values for which the motion is stable according to equation 2.77 (see for example [14, 17]).

### 2.3.1.5 Phase-space motion

The general solution to the equations of motion 2.37 can also be written as [48, 58]:

$$\zeta(s) = A\sqrt{\beta(s)} \cos(\mu(s) + \varphi) \tag{2.79}$$

where  $A$  and  $\varphi$  are constants which are determined by the initial values  $(\zeta(s_0), \zeta'(s_0))$  and  $\mu(s)$  is defined as

$$\mu(s) = \int_0^L \frac{1}{\beta(s)} ds \tag{2.80}$$

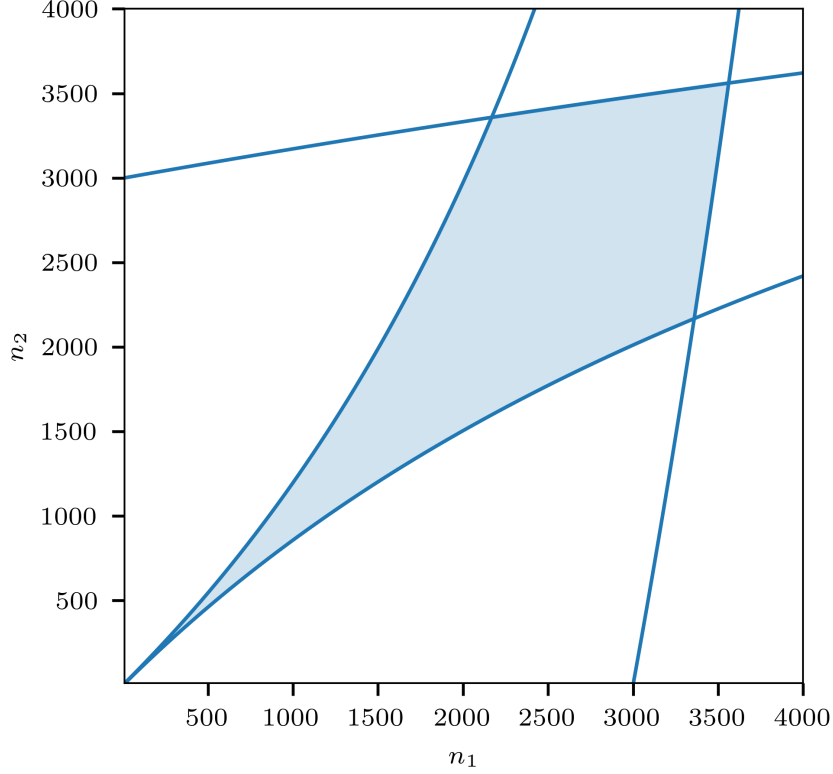


**Figure 2.4:** Necktie plot for the field indices  $n_1$  and  $n_2$  for the example of  $N = 100$  superperiods (used for PS). The solid lines indicate the values for which  $\cos(\mu_{x,y}) = \pm 1$ . The shaded area is the region of values for which the motion is stable according to equation 2.77.

and represents the phase advance of the transverse motion through one superperiod of the lattice. The definition of the phase advance via equation 2.80 is similar to the definition via equation 2.64 except that equation 2.64 allows for multiples of  $2\pi$  to be added while equation 2.80 is unambiguous. It is noted that equation 2.67 guarantees that  $\beta(s)$  does not vanish<sup>5</sup> and, thus, equation 2.80 is well defined. Further, the following relations hold between the quantities  $\alpha, \beta, \gamma$ :

$$\begin{aligned}\alpha(s) &= -\frac{1}{2} \frac{d\beta(s)}{ds} \\ \gamma(s) &= \frac{1 + \alpha(s)^2}{\beta(s)}\end{aligned}\tag{2.81}$$

In order to satisfy the differential equation 2.56,  $\beta(s)$  has to satisfy the following relationship [48]:

$$2\beta(s)\beta''(s) - \beta'(s)^2 + 4\beta(s)^2K(s) - 4 = 0\tag{2.82}$$

This equation determines the values of  $\beta(s)$  in dependence on  $K(s)$  around the accelerator lattice.

From the definition 2.79 and the relations 2.81, by using the trigonometric identity  $\cos(x)^2 + \sin(x)^2 = 1$ , it follows that the quantity

$$\gamma(s)\zeta(s)^2 + 2\alpha(s)\zeta(s)\zeta'(s) + \beta(s)\zeta'(s)^2 = A^2\tag{2.83}$$

<sup>5</sup>Provided that the motion is stable.

## 2. Linear optics in synchrotrons and beam transfer lines

is independent of  $s$  and, thus, is an invariant of the motion. Equation 2.83 can be rewritten as

$$\begin{pmatrix} \zeta(s) & \zeta'(s) \end{pmatrix} \begin{pmatrix} \gamma(s) & \alpha(s) \\ \alpha(s) & \beta(s) \end{pmatrix} \begin{pmatrix} \zeta(s) \\ \zeta'(s) \end{pmatrix} - A^2 = 0 \quad (2.84)$$

and because according to equation 2.67

$$\det \begin{pmatrix} \gamma(s) & \alpha(s) \\ \alpha(s) & \beta(s) \end{pmatrix} \equiv 1 \quad (2.85)$$

it follows that equation 2.83 represents the implicit equation of a tilted ellipse in the  $(\zeta(s), \zeta'(s))$  phase-space [59]. The motion of a particle in the  $(\zeta(s), \zeta'(s))$  phase-space from one (super-)period to the next is therefore constrained to the circumference of that ellipse. In equation 2.83 the term  $A^2$  is independent of  $s$  and, thus, each point along the accelerator lattice is characterized by an ellipse of different shape and orientation but with constant area  $\pi A^2$ . Figure 2.5 shows an example for a phase-space ellipse together with the maximum extent in  $\zeta(s)$  and  $\zeta'(s)$ . It is noted that in the transformed phase-space  $(\sqrt{\beta(s)}^{-1}\zeta(s), \sqrt{\beta(s)}^{-1}\alpha(s)\zeta(s) + \sqrt{\beta(s)}\zeta'(s))$  from equation 2.73, the ellipse becomes a circle with radius  $A$ .

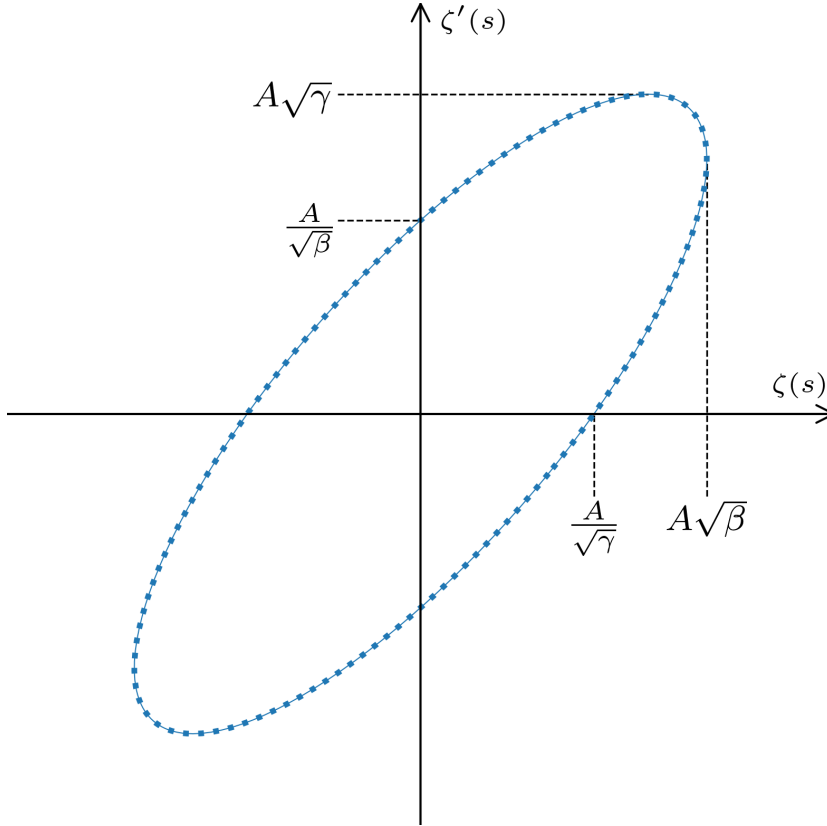


**Figure 2.5:** Illustration of the phase-space ellipse which is defined by equation 2.83.



**Transformation of Twiss parameters** According to equation 2.57, the phase-space coordinates  $(\zeta, \zeta')$  from one position  $s_0$  to another position  $s$  transform as

$$\begin{pmatrix} \zeta(s) \\ \zeta'(s) \end{pmatrix} = M(s|s_0) \begin{pmatrix} \zeta(s_0) \\ \zeta'(s_0) \end{pmatrix} \quad (2.86)$$

Thus, with the help of equation 2.58 the invariant of the motion given by equation 2.83 at position  $s_0$  can be expressed in terms of the coordinates  $(\zeta(s), \zeta'(s))$  at position  $s$ :

$$\begin{aligned} A^2 = & \left( M_{21}^2 \beta_0 - 2M_{21}M_{22}\alpha_0 + M_{22}^2 \gamma_0 \right) \zeta(s)^2 \\ & + 2 \left( -M_{11}M_{21}\beta_0 + (M_{11}M_{22} + M_{12}M_{21})\alpha_0 - M_{12}M_{22}\gamma_0 \right) \zeta(s)\zeta'(s) \\ & + \left( M_{11}^2 \beta_0 - 2M_{11}M_{12}\alpha_0 + M_{12}^2 \gamma_0 \right) \zeta'(s)^2 \end{aligned} \quad (2.87)$$

where  $\{\beta, \alpha, \gamma\}_0 \equiv \{\beta, \alpha, \gamma\}(s_0)$ . Comparing equation 2.87 with equation 2.83 it can be seen that both equations are of the same quadratic form and the coefficients in equation 2.87 determine the coefficients  $\beta(s), \alpha(s), \gamma(s)$  in equation 2.83. The new coefficients  $\beta(s), \alpha(s), \gamma(s)$  emerge as a linear combination of the old coefficients  $\beta(s_0), \alpha(s_0), \gamma(s_0)$  and, thus, determine how these parameters transform from one lattice position to another:

$$\begin{pmatrix} \beta(s) \\ \alpha(s) \\ \gamma(s) \end{pmatrix} = \begin{pmatrix} M_{11}^2 & -2M_{11}M_{12} & M_{12}^2 \\ -M_{11}M_{21} & M_{11}M_{22} + M_{12}M_{21} & -M_{12}M_{22} \\ M_{21}^2 & -2M_{21}M_{22} & M_{22}^2 \end{pmatrix} \begin{pmatrix} \beta(s_0) \\ \alpha(s_0) \\ \gamma(s_0) \end{pmatrix} \quad (2.88)$$

**Tune** The *tune*  $Q$ <sup>6</sup> describes the (fractional) number of betatron oscillations for one revolution around the entire accelerator lattice. It is defined as

$$Q = \frac{1}{2\pi} \int_{s_0}^{s_0+C} \frac{1}{\beta(s)} ds \quad (2.89)$$

where  $C$  is the circumference of the lattice and  $s_0$  is an arbitrary position<sup>7</sup>. The integral represents the phase advance for one revolution around the lattice.

**Admittance** The *admittance* of an accelerator is defined in terms of the half-aperture  $a(s)$  of its beamline<sup>8</sup>:

$$\arg \min_s \frac{\pi a(s)^2}{\beta(s)} \quad (2.90)$$

**Emittance** The *emittance* of a particle beam, on the other hand, is defined as the total phase-space area that is occupied by the particles. For practical purposes it may also refer to the area of the bounding ellipse that encloses a certain fraction of particles. For a stationary Gaussian phase-space distribution in the  $(\zeta(s), \alpha(s)\zeta(s) + \beta(s)\zeta'(s))$  phase-space (compare

<sup>6</sup>The symbol  $Q$  is conventionally used in European literature. In American literature, the tune is typically denoted by  $\nu$ .

<sup>7</sup>The resulting value of the integral is independent of  $s_0$ . Thus, if a well defined expression for the tune is desired, one may set  $s_0 = 0$ .

<sup>8</sup>The aperture may vary along the beamline, hence the dependence on  $s$ .

## 2. Linear optics in synchrotrons and beam transfer lines

---

with equation 2.73; scaled by  $\sqrt{\beta(s)}$ , an expression for the emittance  $\epsilon$  is given by [48]

$$\epsilon = -\frac{2\pi\sigma(s)^2}{\beta(s)} \log(1 - F) \quad (2.91)$$

where  $\sigma(s)$  is the standard deviation of the Gaussian distribution and is similar in both dimensions  $\zeta(s)$  and  $\alpha(s)\zeta(s) + \beta(s)\zeta'(s)$ , and  $F$  is the fraction of particles to be included in the ellipse. Table 2.2 shows various definitions of the emittance  $\epsilon$  in dependence on  $F$  which are commonly used by the accelerator community.

**Table 2.2:** Definitions for beam emittance which are commonly used by the accelerator community [48].

| $\beta\epsilon$ | $F$  |
|-----------------|------|
| $\sigma^2$      | 0.15 |
| $\pi\sigma^2$   | 0.39 |
| $4\pi\sigma^2$  | 0.87 |
| $6\pi\sigma^2$  | 0.95 |

Because the amplitude of transverse oscillations decreases when the total momentum of a particle increases, the emittance will shrink as well. This is referred to as *adiabatic damping*<sup>9</sup>. It is therefore convenient to define a *normalized emittance* which is independent of the particle energy:

$$\epsilon_N \equiv \epsilon\gamma\beta \quad (2.92)$$

where  $\beta = v/c$  is the total velocity of the particle divided by the speed of light and  $\gamma = \sqrt{1 - \beta^2}^{-1}$  is the corresponding relativistic factor.

**Transformation of beam distributions** The implicit equation for an ellipse in any number of dimensions can be written as

$$u^T \Sigma^{-1} u = 1 \quad (2.93)$$

where  $u$  is the  $n$ -dimensional coordinate vector and  $\Sigma$  is the  $n \times n$  matrix which describes the ellipse properties. For two dimensions this coincides with equation 2.84 with

$$\Sigma = A^2 \begin{pmatrix} \beta & -\alpha \\ -\alpha & \gamma \end{pmatrix} \quad (2.94)$$

For a Gaussian particle distribution inside the beam, the matrix  $\Sigma$  coincides with the covariance matrix of the particle distribution:

$$\begin{pmatrix} \langle \zeta_i^2 \rangle & \langle \zeta_i \zeta_i' \rangle \\ \langle \zeta_i' \zeta_i \rangle & \langle \zeta_i'^2 \rangle \end{pmatrix} = A^2 \begin{pmatrix} \beta & -\alpha \\ -\alpha & \gamma \end{pmatrix} \quad (2.95)$$

---

<sup>9</sup>Here, *adiabatic* implies that the change in particle momentum is slow compared to the frequency of the transverse motion.

where  $\zeta_i$  and  $\zeta'_i$  refer to the phase-space coordinates of the  $i$ -th particle according to equation 2.79 and  $\langle \cdot \rangle$  denotes the average over the distribution of particles. To use the covariance matrix

$$\Sigma_{ij} \equiv \langle u_i u_j \rangle \quad (2.96)$$

as the beam matrix is a general solution that is applicable for any number of dimensions and also for any underlying particle distribution (not necessarily Gaussian). Given that  $M \equiv M(s_1|s_0)$  is the transfer matrix for the phase-space coordinates from one lattice position to another, the ellipse equation 2.93 transforms as

$$\begin{aligned} u_1^T \Sigma_1^{-1} u_1 &= u_0^T \Sigma_0^{-1} u_0 \\ &= \left( M^{-1} u_1 \right)^T \Sigma_0^{-1} \left( M^{-1} u_1 \right) \\ &= u_1^T \left( M \Sigma_0 M^T \right)^{-1} u_1 \end{aligned} \quad (2.97)$$

Thus, the beam matrix  $\Sigma$  transforms as

$$\Sigma_1 = M \Sigma_0 M^T \quad (2.98)$$

This relationship allows to deduce the value of the emittance from dedicated profile measurements during a so-called quadrupole scan (see section 2.6.2).

**Phase-space matching** When particles are transferred from one section to another in the accelerator, it is important that their phase-space distribution emerging from the upstream section matches the optics of the downstream section. Given that the particle distribution in the upstream section follows the Twiss parameters  $(\beta_u, \alpha_u, \gamma_u)$ , this requires that the values of the parameters match with those of the downstream section:  $(\beta_u, \alpha_u, \gamma_u) = (\beta_d, \alpha_d, \gamma_d)$ . Only in that case, the emittance of the beam is preserved and particles continue to perform similar betatron oscillations as in the upstream section. If there is a mismatch, the phase-space distribution will be diluted and, as a consequence, the effectively occupied phase-space area will grow, leading to an increase in emittance. This behavior is visualized in Figure 2.6. The mismatched distribution evolves such that it effectively occupies a larger phase-space ellipse; this implies an increase of the emittance of the beam. The degree of mismatch (or, equivalently, the degree of overlap) of the initial particle distribution with the space-space ellipse defined by the optics determines the increase of the effectively occupied phase-space area. Actually, since the optics of an accelerator are defined without the notion of a beam (excluding the need to specify an emittance), the degree of mismatch is determined by the mismatch of the orientation of the eigenvectors of the covariance matrix of the particle distribution given by the upstream optics and the eigenvectors of the covariance matrix of the downstream optics given by

$$\begin{pmatrix} \beta_{u,d} & -\alpha_{u,d} \\ -\alpha_{u,d} & \gamma_{u,d} \end{pmatrix} \quad (2.99)$$

In Figure 2.6 the eigenvectors are rotated by  $\pi/2$  with respect to each other, resulting in a maximal mismatch.

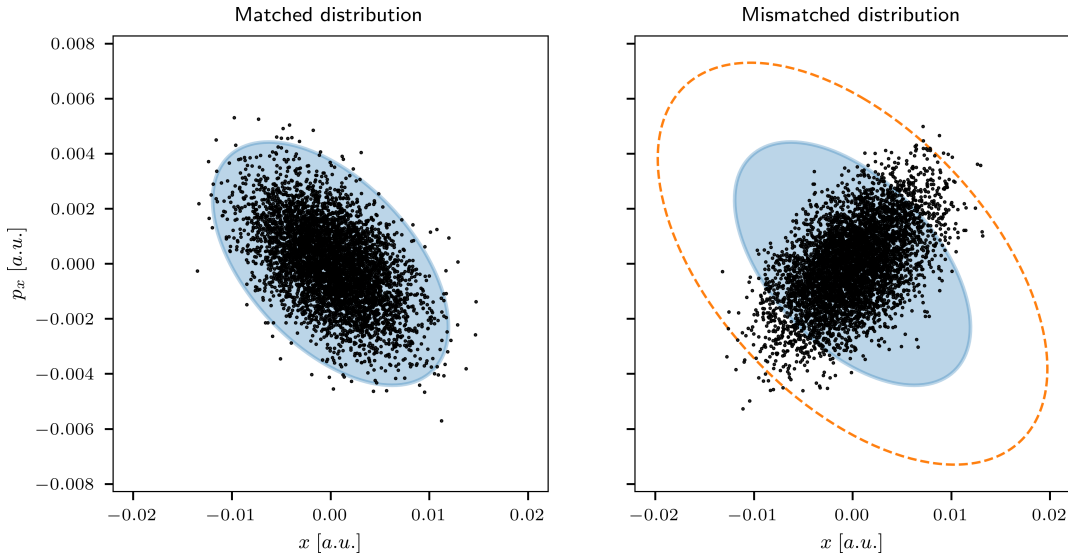


**Figure 2.6:** Phase-space evolution for a matched (left) vs. mismatched (right) particle distribution. The black dots represent the initial particle distribution. The blue area indicates the phase-space area as defined by the Twiss parameters and by using an emittance similar to the one corresponding to phase-space area occupied by the initial particle distribution. For the matched case, the particle distribution evolves such that it remains within the defined blue area. For the mismatched case, the particle distribution evolves such that it occupies a larger phase-space area indicated by the orange dashed ellipse.

### 2.3.2 Dispersion function

Equation 2.37 for the horizontal motion constitutes a nonhomogeneous linear differential equation. The general solution to a nonhomogeneous linear differential equation is given by the sum of the general solution to the complementary homogeneous differential equation (see section 2.3.1) and a particular solution to the nonhomogeneous equation. In the context of accelerator physics, this particular solution is referred to as *momentum dispersion*<sup>10</sup> or, short, *dispersion* and is given by [47]

$$D = \int_{s_0}^s \frac{1}{\rho(\tilde{s})} G(s, \tilde{s}) d\tilde{s} \quad (2.100)$$

where  $G(s, \tilde{s})$  is an appropriate Green's function. The above definition treats  $\delta$  in equation 2.37 as a constant and, thus, requires that the frequency of betatron oscillations is much higher than that of longitudinal oscillations, i.e., that  $\delta(s)$  changes slowly compared to  $\zeta(s)$ . The function  $G(s, \tilde{s})$  can be constructed in terms of the general solution  $M(s|s_0)$  defined by equation 2.57 [47]:

$$G(s, \tilde{s}) = M_{12}(s)M_{11}(\tilde{s}) - M_{11}(s)M_{12}(\tilde{s}) \quad (2.101)$$

Because of the linear nature of the equation of motion 2.37, the contribution of the dispersion, multiplied by the momentum deviation, adds linearly to the transverse motion. Thus, the dispersion evolves similarly to the transverse coordinates around the accelerator lattice, as

<sup>10</sup>The term *momentum* indicates that the contribution to the transverse motion is proportional to the momentum deviation since  $\frac{\Delta p}{p} = \frac{\delta}{\beta}$  where  $\delta$  is given by equation 2.15.

described by equation 2.57:

$$\begin{pmatrix} D(s) \\ D'(s) \\ 1 \end{pmatrix} = \begin{pmatrix} M & M_{13} \\ 0 & M_{23} \\ 0 & 0 & 1 \end{pmatrix} \begin{pmatrix} D(s_0) \\ D'(s_0) \\ 1 \end{pmatrix} \quad (2.102)$$

where  $M \equiv M(s|s_0)$  and  $M_{13}, M_{23}$  represent the particular solution and are given by the  $\beta R_{16}$  and  $\beta R_{26}$  matrix elements of the various transfer matrices presented in section 2.2.3.

## 2.4 Deviations from the ideal lattice

In the previous sections all derivations were made for a perfect lattice, that is, without the influence of possible magnet errors. However, in a real machine there are numerous magnet imperfections, introduced during, for example, construction or by the magnet power supplies. These magnet imperfections influence the motion of the beam particles and result in properties of the real machine that are different from those of the ideal model.

### 2.4.1 Steering contributions

A steering contribution adds in zeroth order to the phase-space coordinates  $(\zeta, \zeta')$ . It may come directly from steerer magnets or from transverse alignment errors of quadrupole magnets. These contributions result in a deviation of the closed orbit trajectory. Suppose there is a single contribution  $\Delta\zeta' = \theta$  in the entire lattice located at position  $s_0$ . In the following,  $M \equiv M(s_0|s_0)$  represents the one-turn transfer matrix at position  $s_0$ . Then the transformation of phase-space coordinates for a single turn is given by:

$$\begin{pmatrix} \zeta \\ \zeta' \end{pmatrix}_{turn\ n+1} = M \begin{pmatrix} \zeta \\ \zeta' \end{pmatrix}_{turn\ n} + \begin{pmatrix} 0 \\ \theta \end{pmatrix} \quad (2.103)$$

For  $(\zeta, \zeta')$  to represent the closed orbit, the values at turn  $n + 1$  must equal the values at turn  $n$ . Thus, the closed orbit can be computed by solving a system of linear equations:

$$\begin{pmatrix} \zeta(s_0) \\ \zeta'(s_0) \end{pmatrix} = (I - M)^{-1} \begin{pmatrix} 0 \\ \theta \end{pmatrix} \quad (2.104)$$

This can be solved with the help of equation 2.69 and noting that the phase advance for a single turn is given by  $\mu = 2\pi Q$ :

$$\begin{aligned} (I - M)^{-1} &= (I - \exp(J2\pi Q))^{-1} \\ &= [\exp(J\pi Q) (\exp(-J\pi Q) - \exp(J\pi Q))]^{-1} \\ &= -[2J \sin(\pi Q)]^{-1} [\exp(J\pi Q)]^{-1} \end{aligned} \quad (2.105)$$

## 2. Linear optics in synchrotrons and beam transfer lines

---

In the above equation, the identity of the matrix exponential and the sin function follows similarly to appendix A.2. Equation 2.68 implies that  $J^{-1} = -J$  and, thus, it follows that

$$\begin{aligned} (I - M)^{-1} &= \frac{1}{2 \sin(\pi Q)} J \exp(-J\pi Q) \\ &= \frac{J \cos(\pi Q) + I \sin(\pi Q)}{2 \sin(\pi Q)} \end{aligned} \quad (2.106)$$

Thus, the solution to equation 2.104 is given by:

$$\begin{pmatrix} \zeta(s_0) \\ \zeta'(s_0) \end{pmatrix} = \frac{\theta}{2 \sin(\pi Q)} \begin{pmatrix} \beta(s_0) \cos(\pi Q) \\ \sin(\pi Q) - \alpha(s_0) \cos(\pi Q) \end{pmatrix} \quad (2.107)$$

Together with the expression for the general transfer matrix between two lattice positions given by equation A.1, the closed orbit at any other position  $s > s_0$  is given by:

$$\zeta(s) = \theta \frac{\sqrt{\beta(s)\beta(s_0)}}{2 \sin(\pi Q)} \cos(\mu(s) - \mu(s_0) - \pi Q) \quad (2.108)$$

Because of the linear nature of equation 2.104, the contributions  $\theta_i$  from different lattice positions  $s_i$  to the closed orbit at a given position  $s$  simply add up:

$$\zeta(s) = \sum_i \theta_i \frac{\sqrt{\beta(s)\beta(s_i)}}{2 \sin(\pi Q)} \cos(|\mu(s) - \mu(s_i)| - \pi Q) \quad (2.109)$$

Figure 2.7 shows an example of a distorted closed orbit that emerges from a single dipole-like error in the lattice; i.e., Figure 2.7 shows the contribution of a single term from equation 2.109.

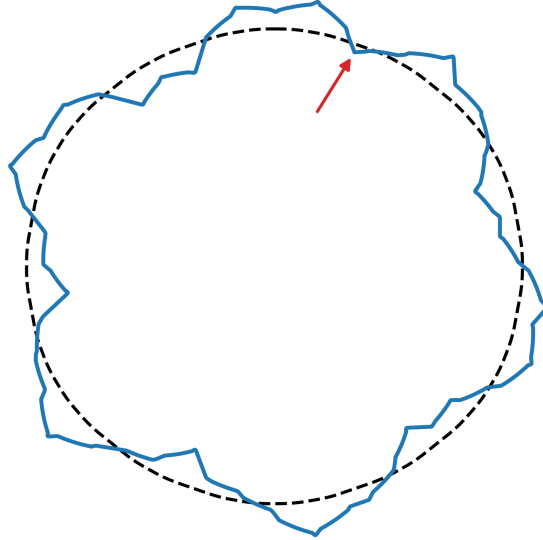


**Figure 2.7:** Example of distorted closed orbit (solid line) from a single dipole-like error in the lattice (i.e., a single term from equation 2.109). The location of the error source is marked by a red arrow. The dashed line indicates the design orbit.

### 2.4.2 Quadrupole errors

Quadrupole errors lead to a distortion of the linear lattice functions, for example the beta function and the phase advance (and, thus, the tune). Under the assumption of a localized quadrupole error, that is, the error is confined to a single position  $s_0$  along the lattice, analytical expressions for the tune and beta function distortion can be derived. The transfer matrix of a thin quadrupole<sup>11</sup> can be obtained from the thick quadrupole transfer matrix, given by equation 2.31, by taking the limit  $L \rightarrow 0$  while keeping the integrated quadrupole strength ( $K_1L$ ) constant. This gives the following transfer matrix:

$$R_{\text{quadrupole}}^{\text{thin}} = \begin{pmatrix} 1 & 0 & 0 & 0 & 0 & 0 \\ -(K_1L) & 1 & 0 & 0 & 0 & 0 \\ 0 & 0 & 1 & 0 & 0 & 0 \\ 0 & 0 & (K_1L) & 1 & 0 & 0 \\ 0 & 0 & 0 & 0 & 1 & 0 \\ 0 & 0 & 0 & 0 & 0 & 1 \end{pmatrix} \quad (2.110)$$

Thus, both transverse dimensions can be represented by the same  $2 \times 2$  transfer matrix:

$$\begin{pmatrix} 1 & 0 \\ -(K_1L) & 1 \end{pmatrix} \quad (2.111)$$

where  $(K_1L) > 0$  represents a focusing quadrupole in that dimension and  $(K_1L) < 0$  represents a defocusing quadrupole.

#### 2.4.2.1 Tune deviation

In the following, the subscript  $_1$  refers to the position  $s_1$  of a thin quadrupole error. The quantity  $\tilde{\mu} \equiv 2\pi\tilde{Q}$  is the phase advance for a single revolution around the lattice under the influence of the quadrupole error. Similarly,  $\mu \equiv 2\pi Q$  denotes the one-turn phase advance for the unperturbed lattice. The one-turn transfer matrix for the perturbed lattice at position  $s_1$  is given by:

$$\tilde{M}(s_1) = M(s_1) \begin{pmatrix} 1 & 0 \\ -(K_1L) & 1 \end{pmatrix} \quad (2.112)$$

where  $M(s_1)$  is the transfer matrix of the unperturbed lattice. The matrix  $\tilde{M}(s_1)$  can be expressed in terms of the unperturbed Twiss parameters according to equation 2.66:

$$\tilde{M}(s_1) = \begin{pmatrix} \cos(\mu) + \alpha_1 \sin(\mu) - \beta_1 \sin(\mu)(K_1L) & \beta_1 \sin(\mu) \\ -\gamma_1 \sin(\mu) - (\cos(\mu) + \alpha_1 \sin(\mu))(K_1L) & \cos(\mu) - \alpha_1 \sin(\mu) \end{pmatrix} \quad (2.113)$$

The tune is given by the trace of the one-turn transfer matrix and, thus, the tune shift is given by:

$$\cos(\tilde{\mu}) - \cos(\mu) = \frac{1}{2} \text{tr} \tilde{M}(s_1) - \frac{1}{2} \text{tr} M(s_1) = -\frac{1}{2} \beta_1 \sin(\mu)(K_1L) \quad (2.114)$$

<sup>11</sup>Here, "thin" means that the effect of the quadrupole on the optics is confined to a single position along the lattice.

Writing  $\tilde{\mu} = \mu + \Delta\mu$  with  $\Delta\mu \ll 1$  and using the first order expansions  $\cos(\Delta\mu) \approx 1$  and  $\sin(\Delta\mu) \approx \Delta\mu$  allows to simplify the l.h.s. of the equation:

$$\begin{aligned}\cos(\tilde{\mu}) &= \cos(\mu + \Delta\mu) \\ &= \cos(\mu) \cos(\Delta\mu) - \sin(\mu) \sin(\Delta\mu) \\ &\approx \cos(\mu) - \sin(\mu) \Delta\mu\end{aligned}\tag{2.115}$$

Thus, the tune deviation is given by

$$\Delta Q \equiv \tilde{Q} - Q \approx \frac{1}{4\pi} \beta_1 (K_1 L)\tag{2.116}$$

### 2.4.2.2 Deviation of beta function

Since the beta function describes the local optics properties of the lattice, the corresponding expression must take into account that the beta function can be evaluated at an arbitrary position  $s_2$  which is different from the position  $s_1$  of the quadrupole error. In the following, the subscripts  $_1$  and  $_2$  refer to, respectively, the positions  $s_1$  and  $s_2$  along the lattice. The quantities  $\tilde{\mu}, \tilde{\beta}$  refer to the perturbed lattice while the quantities  $\mu, \beta$  refer to the unperturbed lattice. The one-turn transfer matrix of the perturbed lattice at position  $s_2$ ,  $\tilde{M}(s_2)$ , can be obtained by multiplying the transfer matrices of the unperturbed lattice from position  $s_2$  to position  $s_1$ , the thin transfer matrix of the quadrupole error at  $s_1$ , and the transfer matrix from position  $s_1$  to position  $s_2 + C$  (where  $C$  is the circumference of the lattice):

$$\tilde{M}(s_2) \equiv \tilde{M}(s_2 + C|s_2) = M(s_2 + C|s_1) \begin{pmatrix} 1 & 0 \\ -(K_1 L) & 1 \end{pmatrix} M(s_1|s_2)\tag{2.117}$$

The beta function of the perturbed lattice is given by the  $\tilde{M}_{12}$  matrix element:

$$\tilde{\beta}_2 = \frac{\tilde{M}_{12}}{\sin(\tilde{\mu})}\tag{2.118}$$

Thus, the change in the  $M_{12}$  matrix element can be expressed as

$$\begin{aligned}\Delta M_{12} \equiv \tilde{M}_{12} - M_{12} &\approx \Delta\beta_2 \sin(\mu) + \tilde{\beta}_2 \cos(\mu) \Delta\mu \\ &= \Delta\beta_2 [\sin(\mu) + \cos(\mu) \Delta\mu] + \beta_2 \cos(\mu) \Delta\mu \\ &\approx \Delta\beta_2 \sin(\mu) + \beta_2 \cos(\mu) \Delta\mu\end{aligned}\tag{2.119}$$

where  $\Delta\mu \equiv \tilde{\mu} - \mu \ll 1$  has been used for the approximations. Thus, the change in the beta function  $\Delta\beta_2$  can be expressed as

$$\begin{aligned}\Delta\beta_2 \sin(2\pi Q) &= \Delta M_{12} - \beta_2 \cos(2\pi Q) (2\pi \Delta Q) \\ &= -\frac{1}{2} (K_1 L) \beta_1 \beta_2 \cos(2\pi Q + 2\mu_2 - 2\mu_1)\end{aligned}\tag{2.120}$$

where the second equality is obtained with the help of equation 2.116 and the trigonometric identities  $\sin(x + y) = \sin(x) \cos(y) + \cos(x) \sin(y)$ ,  $\sin(2x) = 2 \sin(x) \cos(x)$ , and  $\cos(2x) = 1 - 2 \sin(x)^2$ .



The case where  $s_2 > s_1$  can be treated similarly by using the corresponding perturbed one-turn transfer matrix:

$$\tilde{M}(s_2 + C|s_2) = M(s_2 + C|s_1 + C) \begin{pmatrix} 1 & 0 \\ -(K_1L) & 1 \end{pmatrix} M(s_1 + C|s_2) \quad (2.121)$$

The resulting expression for the change in the beta function is

$$\Delta\beta_2 \sin(2\pi Q) = -\frac{1}{2}(K_1L)\beta_1\beta_2 \cos(2\pi Q + 2\mu_1 - 2\mu_2) \quad (2.122)$$

Equations (2.120) and (2.122) can be combined in the following single expression:

$$\Delta\beta_2 = \frac{-1}{2\sin(2\pi Q)}(K_1L)\beta_1\beta_2 \cos(2\pi Q - 2|\mu_1 - \mu_2|) \quad (2.123)$$

### 2.4.3 Effect of multipole errors

In fact, equation 2.37 for the horizontal dimension represents a special case for a perturbation, specifically a first order perturbation since the nonhomogeneous term does not depend on neither  $x$  nor  $y$ . A more general form for a perturbation can be written as [47]:

$$\frac{d^2\zeta(s)}{ds^2} + K(s)\zeta(s) = p_{rsn}(s)x^r y^s \quad (2.124)$$

where  $\zeta \equiv \{x, y\}$ ,  $K(s)$  describes the nominal magnet coefficients and  $p_{rsn}$  is a perturbation of order  $n$  with  $r + s + 1 = n$ . Using Floquet theory, the following condition for resonances can be derived [47]:

$$iQ_x + jQ_y = kN \quad (2.125)$$

where  $N$  denotes the number of superperiods in the lattice,  $i, j, k \in \mathbb{Z}$  and  $|i| + |j|$  is the order of the resonance. Each resonance implies an unbounded growth of oscillation amplitude for particles whose tunes satisfy the corresponding resonance condition. However, the rate of growth is different for each resonance and typically decreases with increasing order of the resonance. Thus, while low order resonances might cause particles to hit the beam pipe and be lost very quickly, particles experiencing higher order resonances might have their oscillation amplitude increased by only a small amount and, therefore, survive until they are extracted. Figure 2.8 shows the emerging resonance lines up to third order with respect to the horizontal and vertical tunes. The tunes of a lattice should be chosen such that they stay away from the resonance lines up to a reasonable order. The chosen tunes are referred to as *working point*. When choosing the tunes, it must also be taken into account that the beam space-charge effect leads to an effective defocusing error (since particles repel each other) and, thus, causes a negative tune shift according to equation 2.116. Because this shift depends on the position of the particle within the beam, it is different for different particles. For that reason, it causes a spreading of the working point and is referred to as *incoherent space-charge tune shift*.

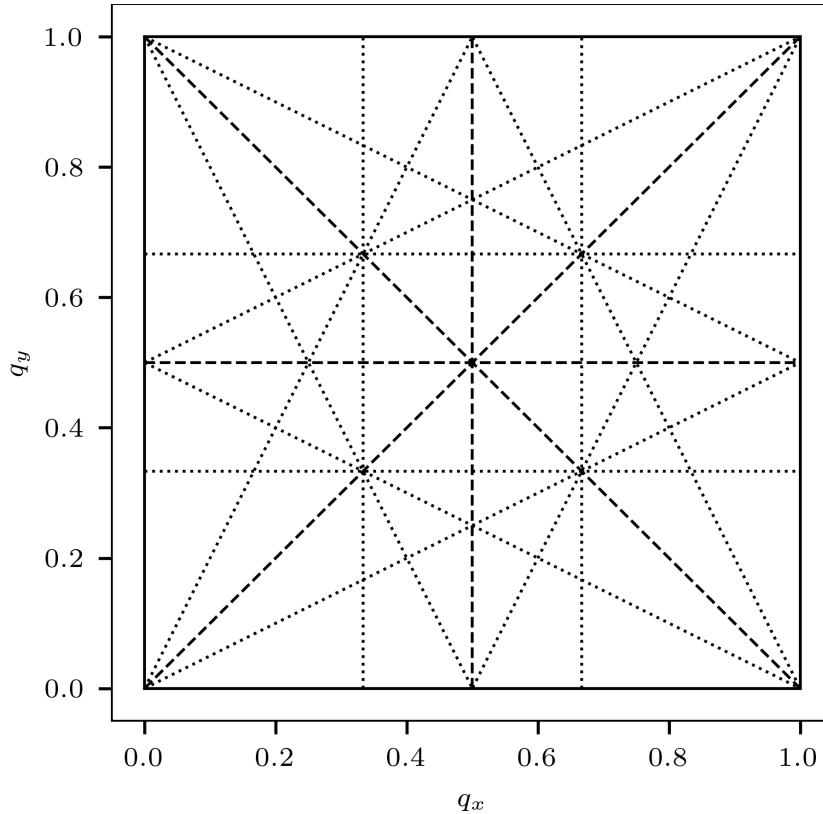


**Figure 2.8:** Resonance lines up to third order for  $N = 1$  superperiods. The axes show the fractional part of, respectively, the horizontal and vertical tune. The resonances of first, second and third order are represented with, respectively, solid, dashed and dotted lines.

## 2.5 Closed orbit based measurements of linear optics

As discussed in section 2.4, errors of the magnetic lattice elements in the real machine lead to a distortion of the optics of the accelerator compared to the design values or predictions of the ideal model. Inability to identify or counteract the discrepancies between the lattice elements in the real machine and their description in the corresponding model, also known as model errors, may result in failure to further improve the machine performance. The physics properties of lattice elements such as quadrupole gradients are rather difficult to be precisely measured directly in the machine and, for that reason, techniques for deriving those properties from measuring their effect on the beam behavior have been employed in order to improve the quality of the accelerator model with respect to the real machine. Deriving those properties constitutes an inverse problem since the observed beam behavior is used to estimate the values of the underlying lattice parameters which gave rise to this behavior and may have arbitrarily complex dependencies [60]. Solving such an inverse problem is generally referred to as *inverse modeling*. The process of inverse modeling involves various aspects:

- A set of *observables* which can be measured and which depend on the to-be-determined parameters. These observables need to provide sufficient information such that they uniquely determine the underlying parameters.

- A *simulation model* that accurately describes the real system in terms of the considered fit parameters. Any deviation from the real system beyond the fit parameters represents a model bias and, thus, will lead to biased results in the parameter estimates.
- A definition of the *cost function*, i.e., a way to produce a numerical quantity that measures the discrepancy between a given model configuration and the measured data in terms of the observables. The goal of inverse modeling is to minimize this cost function. A typical choice is to use the mean squared error, i.e., the sum of squared differences (residuals) normalized by their measurement error.
- A routine to minimize the cost function, also referred to as *optimizer*.

In this context, extracting linear optics and model errors from closed orbit measurements is a typical method for solving the inverse problem in terms of the quadrupole contributions in the lattice. This method requires a measured Orbit Response Matrix (ORM) as observable and then varies all relevant lattice parameters in a multi-dimensional optimization problem in order to match the simulated with the measured ORM. Based on the outcome of the optimization procedure, model parameters are adjusted and the adjusted model is expected to accurately represent the actual machine. Similarly, the devices in the real machine can be adjusted to better reproduce the design values.

### 2.5.1 Orbit response matrix (ORM)

The orbit change  $x_b$  at BPM  $b$  when changing the steerers indexed with  $s$  by a kick  $\delta_s$ , is given by equation 2.109:

$$x_b = \sum_s \delta_s \frac{\sqrt{\beta_b \beta_s}}{2 \sin(\pi Q)} \cos(\pi Q - |\mu_b - \mu_s|) \quad (2.126)$$

where  $\beta_{b,s}$  and  $\mu_{b,s}$  denote, respectively, the beta functions and the phase advances at BPM and steerer position, and  $Q$  is the betatron tune. If a synchrotron operates close to transition energy, another energy-dependent term must be added [57]:

$$x_b = \sum_s \delta_s \left[ \frac{\sqrt{\beta_b \beta_s}}{2 \sin(\pi Q)} \cos(\pi Q - |\mu_b - \mu_s|) - \frac{D_b D_s}{\left(\frac{1}{\gamma^2} - \frac{1}{\gamma_t^2}\right) C} \right] \quad (2.127)$$

where  $D_{b,s}$  denotes the dispersion at, respectively, BPM and steerer position and  $C$  is the circumference of the synchrotron;  $\gamma$  and  $\gamma_t$  represent, respectively, the beam energy ( $E$ ) and transition energy of the lattice ( $\gamma = \frac{E}{E_0}$  where  $E_0$  is the rest energy of the beam). This additional term describes the coupling to the longitudinal motion, that is, a distortion of the particle trajectory will cause an increased path length which results in a change of the phase with respect to the RF-system; this dependency couples back into the transverse dimension in form of the momentum dispersion. Due to the dependency on  $\gamma$  and  $\gamma_t$ , the energy-dependent term is only relevant when the beam energy is close to transition energy.

Hence, the orbit change is a linear function in the applied kick and it encodes the optics via the lattice functions  $\beta$  and  $\mu$ . The orbit response  $r_{bs}$  at BPM  $b$  reacting to a single steerer  $s$  is defined as:

$$r_{bs} = \frac{x_b}{\delta_s} \quad (2.128)$$

The Orbit Response Matrix arranges the orbit responses for all BPM/steerer pairs in a matrix form:  $r_{bs}$ , where  $b$  is the row index and refers to BPMs and  $s$  is the column index and refers to steerers:

$$r = \begin{pmatrix} \frac{x_1}{\delta_1} & \frac{x_1}{\delta_2} & \cdots & \frac{x_1}{\delta_{n_s}} \\ \frac{x_2}{\delta_1} & \frac{x_2}{\delta_2} & \cdots & \frac{x_2}{\delta_{n_s}} \\ \vdots & \vdots & \ddots & \vdots \\ \frac{x_{n_b}}{\delta_1} & \frac{x_{n_b}}{\delta_2} & \cdots & \frac{x_{n_b}}{\delta_{n_s}} \end{pmatrix} \quad (2.129)$$

where  $n_b$  and  $n_s$  are, respectively, the number of BPMs and steerers. Equation 2.127 applies to uncoupled optics, but the ORM can be defined for coupled optics, too:

$$r = \left( \begin{array}{c|c} r^{hh} & r^{hv} \\ \hline r^{vh} & r^{vv} \end{array} \right) \quad (2.130)$$

where the superscript refers to horizontal (h) and vertical (v) BPMs and steerers. That is, the ORM is composed of the two main diagonal blocks  $r^{hh}$  and  $r^{vv}$  and the two coupling blocks  $r^{hv}$  and  $r^{vh}$ .

For the purpose of simulations that involve BPMs and steerers of nonzero length, the closed orbit can be computed by representing steerers with a single thin slice placed in the center of each steerer<sup>12</sup> and the resulting orbit can be recorded in the center of the BPM (see appendix A.3).

### 2.5.2 Jacobian matrix

The derivatives of the ORM elements with respect to the relevant lattice parameters, including the quadrupole gradients, contain lots of information about the corresponding minimization problem. The matrix that is obtained by concatenating the derivatives for each lattice parameter as column-vectors is generally referred to as *Jacobian* matrix  $J$ . This Jacobian matrix is used by the optimizer, e.g., Levenberg-Marquardt, in order to improve the current best guess of lattice parameters during an iterative process.

$$J = \begin{pmatrix} \frac{dr_{11}}{d\theta_1} & \frac{dr_{11}}{d\theta_2} & \cdots & \frac{dr_{11}}{d\theta_{n_p}} \\ \frac{dr_{12}}{d\theta_1} & \frac{dr_{12}}{d\theta_2} & \cdots & \frac{dr_{12}}{d\theta_{n_p}} \\ \vdots & \vdots & \ddots & \vdots \\ \frac{dr_{n_b n_s}}{d\theta_1} & \frac{dr_{n_b n_s}}{d\theta_2} & \cdots & \frac{dr_{n_b n_s}}{d\theta_{n_p}} \end{pmatrix} \quad (2.131)$$

where  $\theta_i$  are the lattice parameters and  $n_p, n_b, n_s$  are, respectively, the number of parameters, BPMs and steerers.

### 2.5.3 Optimization algorithms

In general, an optimization algorithm seeks to minimize a nonlinear function  $f(\mathbf{x})$  in terms of a set of parameters  $\mathbf{x}$  (bold face denotes a vector). In the scope of linear optics from closed

---

<sup>12</sup>Given that the optics functions do not change noticeably on the spatial extent of the steerers. If the steerers are realized as trim coils on, for example, bending magnets, this might not be the case, though. In that case, multiple slices can be used for each steerer and the effect of the slices can be averaged.

orbits, the quantity  $\mathbf{x}$  represents the relevant parameters of the lattice and the function  $f(\mathbf{x})$  represents the sum of squared residuals inversely weighted by their measurement uncertainty:

$$\begin{aligned} f(\mathbf{x}) &= \frac{1}{2} \sum_i \frac{(m_i(\mathbf{x}) - o_i)^2}{\sigma_i^2} \\ &\equiv \frac{1}{2} \mathbf{r}(\mathbf{x})^T \mathbf{r}(\mathbf{x}) \end{aligned} \quad (2.132)$$

where  $o_i$  and  $\sigma_i$  are, respectively, the  $i$ -th observation and measurement uncertainty and  $m_i(\mathbf{x})$  is the corresponding simulated quantity obtained from the model with parameters  $\mathbf{x}$ . The quantity  $\mathbf{r}(\mathbf{x}) \equiv (\mathbf{m}(\mathbf{x}) - \mathbf{o}) / \boldsymbol{\sigma}$  is referred to as *residuals*.

Among the various algorithms that exist, there is a class of *descent algorithms* which compute a sequence of guesses  $\{\mathbf{x}_n\}$  with the goal of  $f(\mathbf{x}_{n+1}) \leq f(\mathbf{x}_n)$  in order to yield convergence. In general, an update is computed from a direction vector  $\mathbf{d}$  and a step size matrix  $\Lambda$ :

$$\mathbf{x}_{n+1} = \mathbf{x}_n - \Lambda(\mathbf{x}_n) \mathbf{d}(\mathbf{x}_n) \quad (2.133)$$

If  $(\nabla f(\mathbf{x}))^T \mathbf{d} > 0$ , then  $-\mathbf{d}$  represents a direction of descent, i.e., there exists a number  $\epsilon > 0$  for which  $f(\mathbf{x}_n - \epsilon \mathbf{d}) < f(\mathbf{x}_n)$ . Many algorithms use

$$\mathbf{d} = \nabla f(\mathbf{x})|_{\mathbf{x}=\mathbf{x}_n} \quad (2.134)$$

including those algorithms which are introduced in the remainder of this section<sup>13</sup>. Those algorithms differ in their choice of  $\Lambda$  instead.

### 2.5.3.1 Gradient descent

The idea behind *gradient descent* is to repeatedly take steps in the opposite direction of the gradient of the objective function [62] with an appropriate uniform step size. Thus,  $\Lambda = \text{diag}(\lambda(\mathbf{x}_n))$  in equation 2.133:

$$\mathbf{x}_{n+1} = \mathbf{x}_n - \lambda(\mathbf{x}_n) \nabla f(\mathbf{x})|_{\mathbf{x}=\mathbf{x}_n} \quad (2.135)$$

and  $\lambda(\mathbf{x}_n) > 0$  is the step size which may be determined anew during each iteration, e.g., via a dedicated line search method [61]. For a convex, continuous function  $f(\mathbf{x})$ , the gradient descent method with appropriate line search is guaranteed to converge to the global minimum.

### 2.5.3.2 Gauss-Newton algorithm

The *Gauss-Newton algorithm* uses the Jacobian matrix

$$J \equiv J(\mathbf{x})|_{\mathbf{x}=\mathbf{x}_n} = \nabla \cdot \mathbf{r}(\mathbf{x})^T|_{\mathbf{x}=\mathbf{x}_n} \quad (2.136)$$

in order to compute an update for the parameter estimates. Specifically,  $\Lambda = (J^T J)^{-1}$  in equation 2.133 [63]:

$$\mathbf{x}_{n+1} = \mathbf{x}_n - \left(J^T J\right)^{-1} J^T \mathbf{r}(\mathbf{x})|_{\mathbf{x}=\mathbf{x}_n} \quad (2.137)$$

<sup>13</sup>Different search directions are possible, though, and in some cases might improve the convergence [61].

It is noted that  $J^T \mathbf{r}(\mathbf{x}) = \nabla f(\mathbf{x})$  for the definition of  $f(\mathbf{x})$  according to equation 2.132.

This is closely related to *Newton's method* which uses  $\Lambda = H(\mathbf{x})$  the Hessian matrix of the system, i.e., the second order derivatives:

$$\begin{aligned} H_{ij} &= \sum_k \left( \frac{\partial r_k}{\partial x_i} \frac{\partial r_k}{\partial x_j} + \frac{\partial^2 r_k}{\partial x_i \partial x_j} r_k \right) \\ &= \left( J^T J \right)_{ij} + \sum_k \frac{\partial^2 r_k}{\partial x_i \partial x_j} r_k \end{aligned} \quad (2.138)$$

Thus, the Gauss-Newton algorithm uses an approximation of the Hessian matrix by neglecting the second order derivatives in equation 2.138. This is justified if the non-linearity of  $\mathbf{r}(\mathbf{x})$  is manageable on the considered scales.

The Gauss-Newton algorithm is not guaranteed to converge, but it can be combined with an additional step size parameter  $\lambda$  similar to equation 2.135 in order to restore that property:

$$\mathbf{x}_{n+1} = \mathbf{x}_n - \lambda(\mathbf{x}_n) \left( J^T J \right)^{-1} J^T \mathbf{r}(\mathbf{x})|_{\mathbf{x}=\mathbf{x}_n} \quad (2.139)$$

An advantage of the Gauss-Newton algorithm over Newton's method is that it requires computation of only the Jacobian but not the Hessian matrix which would be expensive to compute. The Gauss-Newton algorithm converges fast if the residuals are small, i.e., if the current guess is close to a local minimum.

### 2.5.3.3 Levenberg-Marquardt algorithm

The Levenberg-Marquardt algorithm is named after the authors of two independent publications [64, 65]. It combines aspects from both, gradient descent and the Gauss-Newton algorithm. Specifically, it uses

$$\mathbf{x}_{n+1} = \mathbf{x}_n - \left( J^T J + \text{diag}(\lambda(\mathbf{x}_n)) \right)^{-1} J^T \mathbf{r}(\mathbf{x})|_{\mathbf{x}=\mathbf{x}_n} \quad (2.140)$$

The parameter  $\lambda(\mathbf{x}_n)$  is adjusted at every iteration and can therefore shift the update towards gradient descent ( $\lambda \gg \|J^T J\|$ ) or Gauss-Newton ( $\lambda \ll \|J^T J\|$ ). In doing so, the algorithm can provide an efficient reduction in  $f(\mathbf{x})$  during every iteration also for varying behavior of  $f(\mathbf{x})$  along the sequence  $\{\mathbf{x}_n\}$ .

### 2.5.4 Gain errors

Typically, BPMs and steerers will have gain errors  $e_b$  and  $e_s$  which influence, respectively, the registered beam orbit position  $x_b$  or the effective kick strength  $\theta_s$ :

$$\begin{aligned} x_b &\rightarrow (1 + e_b)x_b \equiv g_b x_b \\ \theta_s &\rightarrow (1 + e_s)\theta_s \equiv g_s \theta_s \end{aligned} \quad (2.141)$$

Under the influence of gain errors, the Orbit Response Matrix  $R$  is given by:

$$R \rightarrow \begin{pmatrix} g_{b,1} & 0 & 0 \\ 0 & \ddots & 0 \\ 0 & 0 & g_{b,n_b} \end{pmatrix} R \begin{pmatrix} g_{s,1} & 0 & 0 \\ 0 & \ddots & 0 \\ 0 & 0 & g_{s,n_s} \end{pmatrix} \quad (2.142)$$

Hence, each ORM element  $R_{ij}$  is modified by

$$R_{ij} \rightarrow g_{b,i} R_{ij} g_{s,j} \quad (2.143)$$

The relationship from equation 2.143 is invariant under the scaling

$$\begin{aligned} g_{b,i} &\rightarrow g_{b,i} \lambda & \forall i \\ g_{s,j} &\rightarrow g_{s,j} \lambda^{-1} & \forall j \end{aligned} \quad (2.144)$$

and, thus, the gain errors are only determined up to the arbitrary multiplicative factor  $\lambda \neq 0$ . The specific value for  $\lambda$  that is reached during the optimization procedure depends on the given starting point of the lattice parameters. If the gains of BPMs and steerers are not known, they must be included in the fitting process as so-called *nuisance parameters* (i.e., parameters which are not of primary interest but, nevertheless, must be added in order to represent the observed data). During fitting, the Jacobian including BPM and steerer gain errors has thus a rank deficiency of degree 1 or degree 2 for, respectively, coupled and uncoupled optics. This is because for uncoupled optics, the horizontal and vertical block of the response matrix, as indicated in equation 2.130, are independent of each other. For coupled optics, however, a scaling of gain errors not only scales the horizontal or vertical blocks but also the coupling blocks and, therefore, only the entire response matrix possesses such a scale invariance. Therefore, the chosen optimizer must be able to deal with the rank deficiency that is present in the Jacobian (e.g., via SVD cutoff [66] or Tikhonov regularization [67]).

The ambiguity in terms of the horizontal gain errors can be eliminated by including the dispersion as an additional column to the ORM, if the measurement of dispersion does not introduce an additional calibration error from the perspective of the RF-system:

$$R \rightarrow \left( R \left| \begin{array}{c} D_1 \\ \vdots \\ D_{n_b} \end{array} \right. \right) \quad (2.145)$$

Instead of adding the dispersion as a correctly calibrated column to the ORM (i.e., no calibration error for the RF-system), one can define that any other row or column of the ORM is correctly calibrated and exclude the corresponding gain parameter from the fitting. This will similarly eliminate the ambiguity of gain errors. However, it requires accurate knowledge about the gain for at least one of the BPMs or steerers in order to yield correct results.

Nevertheless, even in the presence of the ambiguity  $\lambda$ , the ratios of strengths of BPMs or steerers, i.e.,  $\frac{g_{b,i_1}}{g_{b,i_2}}$  or  $\frac{g_{s,j_1}}{g_{s,j_2}}$ , are uniquely determined since these ratios eliminate the ambiguous factor  $\lambda$ . This information can be used to determine if individual BPMs or steerers have gains which significantly deviate from those of other devices.

### 2.5.5 Dispersion

The dispersion describes the dependency of the position of a particle on its momentum error (see section 2.3.2). Thus, the dispersion can be measured by inducing an artificial coherent momentum error on the beam and by observing the resulting position shift at the Beam Position Monitors. One option for inducing a momentum error is to change the RF-frequency  $f_{RF}$  by an amount  $\Delta f_{RF} \ll f_{RF}$  [68]:

$$\frac{\Delta p}{p} = -\frac{1}{\alpha_c - \frac{1}{\gamma^2}} \frac{\Delta f_{RF}}{f_{RF}} \quad (2.146)$$

where  $\alpha_c$  is the momentum compaction factor and  $\gamma$  is the relativistic factor of the beam. For this method to work, the energy aperture of the accelerator must be large enough to allow for the induced momentum error in order to prevent beam losses.

## 2.6 Beam extraction from synchrotrons and transport in beam transfer lines

Once the beams are accelerated to the desired energy, if the synchrotron itself is not the destination, they need to be extracted from the synchrotron in order for them to be transported to their destination. In the case of the SIS18 synchrotron, the possible destinations are the various fixed-target experimental areas such as the High Acceptance Di-Electron Spectrometer (HADES) or one of the two downstream storage rings, Experimental Storage Ring (ESR) or CRYRING. In the context of the FAIR accelerator complex, SIS18 will act as a booster for the downstream SIS100 synchrotron. Each of these scenarios may impose different requirements on the properties of the extracted beam particles, for example on the resulting beam current. Different methods for extracting beams from a synchrotron exist and they can be used to address the varying requirements of the downstream parts of an accelerator facility. The different extraction methods can be categorized as fast extraction and slow extraction methods. As the names suggest, for fast extraction the entire beam in the synchrotron is extracted in a short period of time, ideally within a single revolution in the synchrotron and, thus, producing a high beam current. This requires the usage of a fast kicker magnet with magnetic field rise time significantly shorter than the duration of a single revolution in the synchrotron. Slow extraction, on the other hand, extracts only a small portion of the beam particles during each revolution in the synchrotron and the duration until the entire beam is extracted may last from milliseconds to even hours, depending on the used slow extraction setting. Slow extraction is typically required by fixed target experiments in order to avoid saturation of the experimental detectors. For slow extraction, an important requirement is to provide a constant particle rate that is being extracted from the synchrotron. Also, for slow extraction the resulting beam properties in terms of momentum spread and beam emittance vary between the different methods.



### 2.6.1 Resonant slow extraction of beams in synchrotrons

In the following, different methods for third-order resonant slow extraction are introduced. A third-order resonance is used to increase the betatron oscillation amplitudes of particles in the plane of extraction (typically horizontal; see section 2.4.3) such that they move into the strong field of a septum which causes the particles to exit the synchrotron and move into a beam transfer line. The tune of the synchrotron is moved close to the resonance  $3Q_h = \text{integer}$  prior to extraction. The resonance is then excited via sextupole magnets.

For a particle with tune equal to  $Q_h = m \pm \frac{1}{3} + \delta Q$  with  $m = \text{integer}$  and  $\delta Q \ll 1$ , the one-turn transfer matrix for normalized coordinates  $(\tilde{\zeta}, \tilde{\zeta}')$  from equation 2.74 is given by:

$$\begin{pmatrix} \cos(2\pi(m \pm \frac{1}{3} + \delta Q)) & \sin(2\pi(m \pm \frac{1}{3} + \delta Q)) \\ -\sin(2\pi(m \pm \frac{1}{3} + \delta Q)) & \cos(2\pi(m \pm \frac{1}{3} + \delta Q)) \end{pmatrix} \quad (2.147)$$

Because of equation 2.70, the transfer matrix for  $n$  turns is obtained by replacing  $2\pi \rightarrow 2\pi n$  in the above one-turn transfer matrix.

The second order contributions of a thin sextupole from equation 2.40 are given in normalized coordinates:

$$\begin{aligned} \Delta \tilde{x}' &= \frac{1}{2} \beta_x^{\frac{3}{2}} (K_2 L) \left( \tilde{x}^2 - \frac{\beta_y}{\beta_x} \tilde{y}^2 \right) \\ \Delta \tilde{y}' &= -\frac{1}{2} \beta_x^{\frac{3}{2}} (K_2 L) \frac{\beta_y}{\beta_x} 2\tilde{x}\tilde{y} \end{aligned} \quad (2.148)$$

Because of the resonance in the extraction plane, the amplitude in  $\tilde{x}$  increases to much larger values than the amplitude in  $\tilde{y}$ . For that reason, the contribution  $\tilde{y}^2$  in equation 2.148 can be neglected and the transformation of  $\tilde{x}'$  is given by:

$$\Delta \tilde{x}' = S \tilde{x}^2 \quad (2.149)$$

where  $S = \frac{1}{2} \beta_x^{\frac{3}{2}} (K_2 L)$ .

Since after three turns, the contribution of the  $\frac{1}{3}$  term of the tune to the betatron motion vanishes, the effect of the sextupole is described as a perturbation after the first, second and third turn [69]:

$$\begin{pmatrix} \tilde{x}_3 \\ \tilde{x}'_3 \end{pmatrix} = \sum_{i=1}^3 \left[ \underbrace{\tilde{M}^i \begin{pmatrix} \tilde{x}_0 \\ \tilde{x}'_0 \end{pmatrix}}_{\begin{pmatrix} \tilde{x}_i \\ \tilde{x}'_i \end{pmatrix}} \rightarrow \underbrace{\begin{pmatrix} \tilde{x}_i \\ \tilde{x}'_i + S \tilde{x}_i^2 \end{pmatrix}}_{\begin{pmatrix} \tilde{x}_{i+\text{sextupole}} \\ \tilde{x}'_{i+\text{sextupole}} \end{pmatrix}} \rightarrow \tilde{M}^{3-i} \begin{pmatrix} \tilde{x}_{i+\text{sextupole}} \\ \tilde{x}'_{i+\text{sextupole}} \end{pmatrix} \right] \quad (2.150)$$

where  $\tilde{M}$  is the one-turn transfer matrix from equation 2.147 and  $\tilde{M}^i$  is calculated by taking into account  $\delta Q \ll 1$ . Up to linear terms in  $\delta Q$ , the transfer map for three turns under the influence of the thin sextupole is given by:

$$\begin{pmatrix} \tilde{x}_3 \\ \tilde{x}'_3 \end{pmatrix} - \begin{pmatrix} \tilde{x}_0 \\ \tilde{x}'_0 \end{pmatrix} = \begin{pmatrix} \epsilon \tilde{x}'_0 + \frac{3}{2} S \tilde{x}_0 \tilde{x}'_0 \\ -\epsilon \tilde{x}_0 + \frac{3}{4} S (\tilde{x}_0^2 - \tilde{x}'_0^2) \end{pmatrix} \quad (2.151)$$

where  $\epsilon \equiv 6\pi\delta Q$ . The Hamiltonian that corresponds to the equations of motion 2.151 is the so-called *Kobayashi Hamiltonian* [70]<sup>14</sup>:

$$H = \frac{\epsilon}{2} (\tilde{x}^2 + \tilde{x}'^2) + \frac{S}{4} (3\tilde{x}\tilde{x}'^2 - \tilde{x}^3) \quad (2.152)$$

Figure 2.9 shows various stable trajectories corresponding to the Kobayashi Hamiltonian<sup>15</sup>. For  $H = \frac{8}{27} \frac{\epsilon^3}{S^2}$ , equation 2.152 can be factorized into three straight lines, which represent the separatrix of the motion. Particles outside the separatrix will undergo unbounded motion and are therefore unstable. The separatrix is approximated by the outermost trajectory in Figure 2.9.

$$\left(\frac{S}{4}\tilde{x} + \frac{\epsilon}{6}\right) \left(\sqrt{3}\tilde{x}' + \tilde{x} - \frac{4}{3}\frac{\epsilon}{S}\right) \left(\sqrt{3}\tilde{x}' - \tilde{x} + \frac{4}{3}\frac{\epsilon}{S}\right) = 0 \quad (2.153)$$

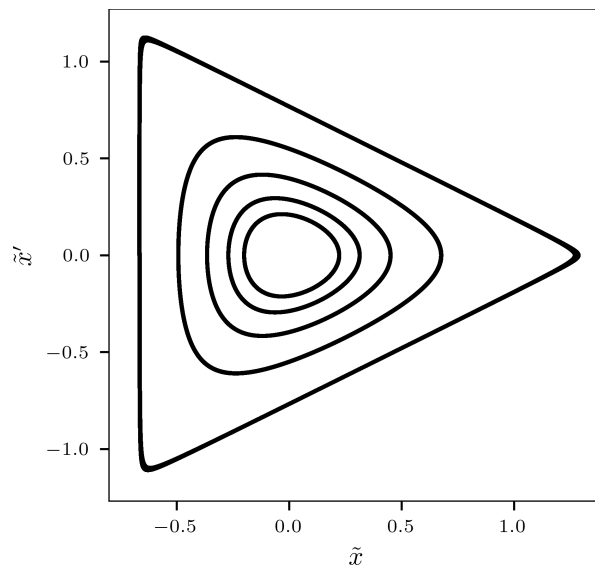


**Figure 2.9:** Phase-space trajectories near a third-order resonance under the influence of sextupole contributions. The outermost trajectory with a triangular shape approximates the separatrix. Particles outside the separatrix will undergo unbounded motion and, thus, be unstable (not shown).  $\epsilon/S = 1$  for this plot.

In order to extract particles from the synchrotron, they need to be moved from the stable to the unstable region in the  $(\tilde{x}, \tilde{x}')$  phase-space in a controlled way. There exist different ways to accomplish this.

### 2.6.1.1 Stochastic extraction

The longitudinal distribution of particles is blown up by applying stochastic noise via the RF-system [71]. This leads to an increase of the momentum error of particles and together with a nonzero chromaticity it causes the particles to move into the resonance. A large horizontal emittance implies that the amplitude and momentum error of extracted particles varies during the spill. The optics of the machine remain constant during the extraction.

<sup>14</sup>The independent variable of this Hamiltonian represents the number of turns and one unit corresponds to three turns.

<sup>15</sup>This is the phase-space distribution at the location of the sextupole. The phase-space distribution at any other location is obtained by rotating the original distribution by  $\Delta\mu$  in  $(\tilde{x}, \tilde{x}')$  phase-space where  $\Delta\mu$  is the phase advance difference between the other location and the location of the sextupole.

### 2.6.1.2 RF-knockout extraction

The beam is transversely excited via the RF-system at the revolution frequency [72]. This leads to an increase of the betatron amplitude of particles which subsequently causes the particles to become unstable. This method works at zero chromaticity which causes the amplitude and momentum spread of extracted particles to be constant during the spill. The optics of the machine remain constant during the extraction.

### 2.6.1.3 Quadrupole-driven extraction

For quadrupole-driven extraction, contrary to the above methods, the phase-space distribution of the beam remains unaltered. Instead, a quadrupole is used to slowly change the optics and, thus, the tune of the lattice in such a way that it moves the resonance across the beam distribution [72]. Depending on the horizontal emittance and the momentum spread of the beam, the size and average momentum of the extracted particles may vary during the spill. The optics of the machine change, albeit slightly, during the extraction.

## 2.6.2 Quadrupole scan for emittance measurement in beam transfer lines

Once the beam is extracted from the synchrotron, it must be transported through the downstream beam transfer line leading to the desired destination. In order to prevent the beam particles from hitting the aperture of the beamline, quadrupole magnets are used to focus the beam in the transverse dimensions. If necessary, bending magnets are used to guide the beam on a curved trajectory. For example, the HEST beamline leading to the HADES experiment uses two bending magnets to transport the beam to the experimental area which is slightly elevated with respect to the SIS18 synchrotron. Similarly to inside the synchrotron, the beam properties along the transfer line are determined by the optics that emerges from the setting of quadrupole strengths. The beamline optics can be similarly described by the Twiss parameters  $(\beta, \alpha, \gamma)$ . The Twiss parameters at the beginning of the beamline, where it connects to the synchrotron, are then transformed by the various beamline elements according to equation 2.88.

Besides the optics of the beamline, the emittance of the beam determines the resulting size of the beam inside the transfer line. A so-called *quadrupole scan* can be used to measure the emittance of the beam in a beamline with the help of a quadrupole magnet and a beam profile monitor downstream of the quadrupole [47, 68]. The principle is based on the following relationships. In one dimension, the beam distribution can be described by the beam matrix from equation 2.94:

$$\Sigma = \begin{pmatrix} \langle \zeta^2 \rangle & \langle \zeta \zeta' \rangle \\ \langle \zeta \zeta' \rangle & \langle \zeta'^2 \rangle \end{pmatrix} = \begin{pmatrix} \epsilon\beta & -\epsilon\alpha \\ -\epsilon\alpha & \epsilon\gamma \end{pmatrix} \quad (2.154)$$

and it transforms according to equation 2.98

$$\Sigma^m = M \Sigma^q M^T \quad (2.155)$$

from position  $s_q$  (quadrupole) to position  $s_m$  (monitor) where  $s_m > s_q$ . If the focal length  $1/(K_1 L)$  of the quadrupole is significantly larger than its length, the quadrupole can be

## 2. Linear optics in synchrotrons and beam transfer lines

---

approximated with a thin lens transfer matrix (see equation 2.110) and the compound transfer matrix  $M$  from the quadrupole to the profile monitor is given by:

$$M = \begin{pmatrix} 1 & d \\ 0 & 1 \end{pmatrix} \begin{pmatrix} 1 & 0 \\ -(K_1 L) & 1 \end{pmatrix} = \begin{pmatrix} 1 - (K_1 L)d & d \\ -(K_1 L) & 1 \end{pmatrix} \quad (2.156)$$

where  $d \equiv s_m - s_q$ . The beam matrix element  $\Sigma_{11}^m$  at the monitor is therefore given by the following equation:

$$\Sigma_{11}^m = \underbrace{(d^2 \Sigma_{11}^q)}_{\equiv A} (K_1 L)^2 - \underbrace{(2d \Sigma_{11}^q + 2d^2 \Sigma_{12}^q)}_{\equiv B} (K_1 L) + \underbrace{(\Sigma_{11}^q + 2d \Sigma_{12}^q + d^2 \Sigma_{22}^q)}_{\equiv C} \quad (2.157)$$

This represents a second order equation in  $(K_1 L)$  and, thus, the beam profile data  $\Sigma_{11}^m = \langle \zeta^2 \rangle$  obtained by varying the strength of the quadrupole  $(K_1 L)$  can be fitted to a parabola in order to obtain the coefficients from equation 2.157. The definition of the three coefficients  $A, B, C$  represents a linear system of equations in terms of the beam matrix elements  $\Sigma_{11}^q, \Sigma_{12}^q, \Sigma_{22}^q$  which can be solved in order to obtain the beam matrix elements from the coefficients of the fit:

$$\begin{aligned} \Sigma_{11}^q &= \frac{A}{d^2} \\ \Sigma_{12}^q &= \frac{B - 2d \Sigma_{11}^q}{2d^2} \\ \Sigma_{22}^q &= \frac{C - \Sigma_{11}^q - 2d \Sigma_{12}^q}{d^2} \end{aligned} \quad (2.158)$$

Since  $\beta\gamma - \alpha^2 = 1$  according to equation 2.67, the emittance is then given by <sup>16</sup>:

$$\epsilon = \sqrt{\det(\Sigma^q)} = \sqrt{\Sigma_{11}^q \Sigma_{22}^q - \Sigma_{12}^q \Sigma_{12}^q} \quad (2.159)$$

---

<sup>16</sup>This relationship holds only for a dispersion-free region. However, the measured data obtained from a dispersive region can be reduced to the betatronic part by using  $\langle \zeta^2 \rangle - \left(\frac{\Delta p}{p} D\right)^2$  for the fit, if the momentum spread  $\frac{\Delta p}{p}$  and dispersion  $D$  are known.

# 3

## Estimating quadrupole errors in the presence of degeneracy for the SIS18 synchrotron

Extracting linear optics and model errors from closed orbit measurements is a typical method for estimating the quadrupole errors in a lattice (see section 2.5). The goal of this inverse modeling process is to adjust the accelerator model in such a way that it accurately reproduces the measured data such as the orbit response matrix. However, even when such convergence in terms of the observed data is achieved, the lattice element parameters in the adjusted model may not necessarily converge to the corresponding actual physics properties in the real machine due to various contributing factors such as the errors of beam position monitors (BPMs) which cast an uncertainty on the measured ORM. This uncertainty then propagates through the inverse modeling process and influences the precision of derived parameters. Depending on the lattice and the optics, the effect of BPM errors can be more or less problematic for the accuracy of inverse modeling results. In some cases, the influence of BPM errors can even hinder the successful reconstruction of quadrupole errors. Also, some of the modeled lattice parameters might be affected by the measurement uncertainty much more than others, leading to significantly increased uncertainties for those parameters and, thus, decreasing the efficiency of those estimates. This is referred to as *quasi-degeneracy*. An improvement of the efficiency of quadrupole error estimates was introduced in [73] by adding specific constraints for the fit parameters. A related approach for improving the efficiency was introduced in [74] by limiting the magnitude of parameter updates during each step of the minimization. The underlying property of the lattice that is responsible for the propagation of measurement uncertainty during the inverse modeling process strongly depends on the availability and location of BPMs and steerers in the lattice as these devices produce and determine the measured data. In the following chapter, the limitations and properties of the inverse modeling process with regard to the placement of BPMs and steerers are investigated in detail.

*Parts of this chapter have previously been published in Phys. Rev. Accel. Beams. Specifically sections 3.2, 3.3 (excluding 3.3.1) and 3.4.7. Details are given in [75].*

## 3.1 The SIS18 synchrotron

SIS18 is a rapid cycling synchrotron at GSI Helmholtz Centre for Heavy Ion Research, Darmstadt which can accelerate ions of various energies and species, ranging from Hydrogen to Uranium. Operation has started in 1990 and it has been part of many important discoveries throughout the decades. In the future, SIS18 will serve as the injector for the SIS100 synchrotron which is part of the FAIR project [40]. This booster operation at very high intensities puts stringent requirements on the optics and, thus, a thorough understanding of the linear optics builds the foundation for any further improvements [39]. The lattice of SIS18 consists of 12 sections. An overview is presented in Figure 3.1. Each section contains three quadrupoles, labeled F (focusing), D (defocusing) and T (triplet), and the placement and strength of these quadrupoles is identical in each of the sections. This triplet structure is utilized to increase the transverse acceptance during beam injection. The strength of T-quadrupoles is gradually decreased by one order of magnitude during the ramp, resulting in a small strength during extraction optics. The 36 quadrupoles are connected with five distinct power supplies, separating the quadrupoles into the following families:

- 6 F-quads from odd numbered sections,
- 6 F-quads from even numbered sections,
- 6 D-quads from odd numbered sections,
- 6 D-quads from even numbered sections,
- 12 T-quads from all sections.

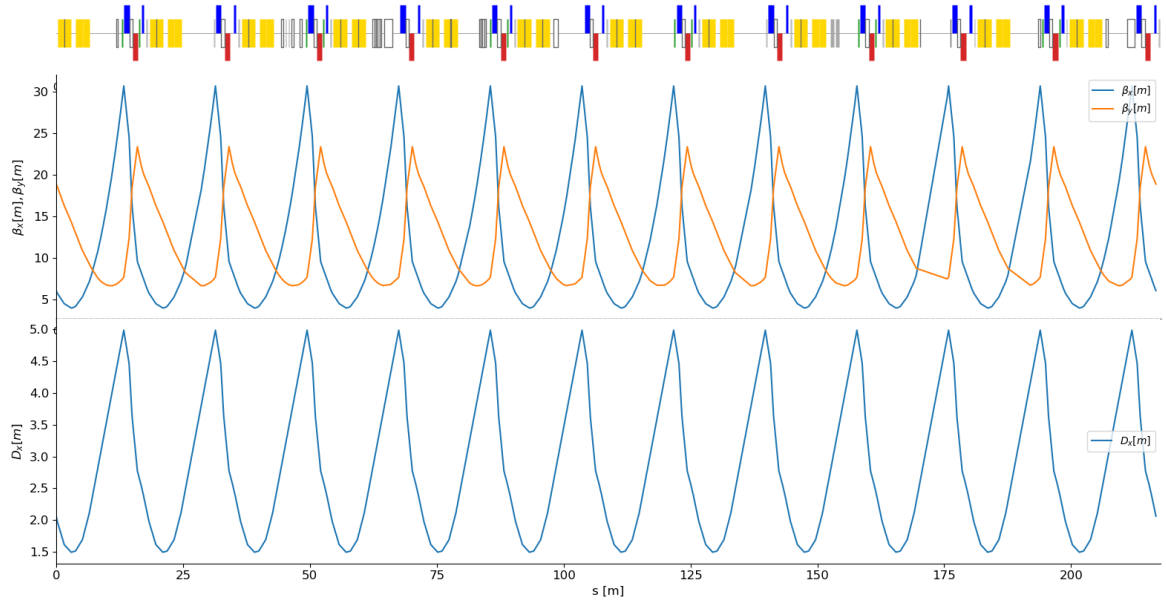
Each section contains two bending magnets next to each other. The horizontal steerers are placed on the first bending magnet, except in sections 4 and 6 where they are placed on the second bending magnet. The vertical steerers are placed between the F- and the D-quadrupole identically in each of the sections. The vertical and horizontal BPMs are placed downstream of the T-quadrupole, identically in each of the sections.

### 3.1.1 Beam position monitors

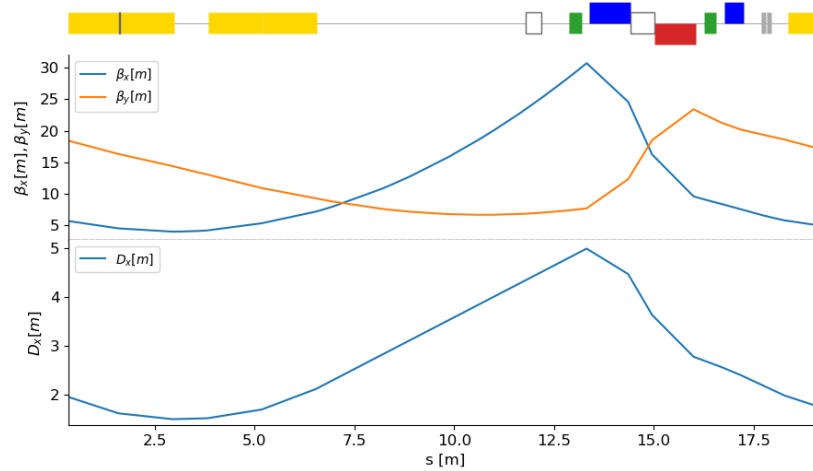
Each individual electrode of the shoebox-type capacitive pick-up structure is terminated with  $50\ \Omega$  amplifiers which is followed by direct digitization at 125 million samples per second. The orbit is calculated by least squares fitting the opposite electrode signals on a user defined time window. A detailed discussion on the orbit measurement scheme along with measurement uncertainty estimates can be found in [77].

### 3.1.2 Orbit response matrix

The nominal ORM of SIS18, shown in Figure 3.2, has a circulant structure in the vertical block due to the symmetric placement of quadrupoles, vertical steerers and BPMs within



(a) Full lattice including all 12 sections.



(b) View of the first section. [75]

**Figure 3.1:** Schematic of SIS18 lattice together with optics functions. In terms of the quadrupoles, BPMs and steerers the twelve sections are identical except that in sections 4 and 6 the horizontal steerer is located on the second bending magnet rather than the first. Blue (raised): focusing quadrupoles, red (lowered): defocusing quadrupoles, yellow (centered): bending magnets; the horizontal steerer is shown as a black line on top of the first bending magnet (in sections 4 and 6 it is located on the second bending magnet); the vertical steerer is shown as a white box with gray boundary between the focusing and defocusing quadrupole; the vertical and horizontal BPMs (in that order) are shown as gray solid boxes downstream of the third quadrupole (since they are right next to each other, they might appear as a single gray box). The first white box, downstream of the second bending magnet, is a bumper magnet. The plot has been created with the DiPAS program [76].

### **3. Estimating quadrupole errors in the presence of degeneracy for the SIS18 synchrotron**

each section. Here, circulant means that each column of the matrix is shifted by one element compared to the previous column. Thus, the entire information of a circulant matrix is encoded in a single column and in the fact that the matrix is circulant, of course [78]. In the horizontal block, the circulant structure is broken in the two lattice sections 4 and 6 because in those sections the horizontal steerer is placed on the second bending magnet rather than the first. This is reflected in Figure 3.2 by the fact that columns 4 and 6 of the response matrix contain values that don't fit with those of surrounding columns.



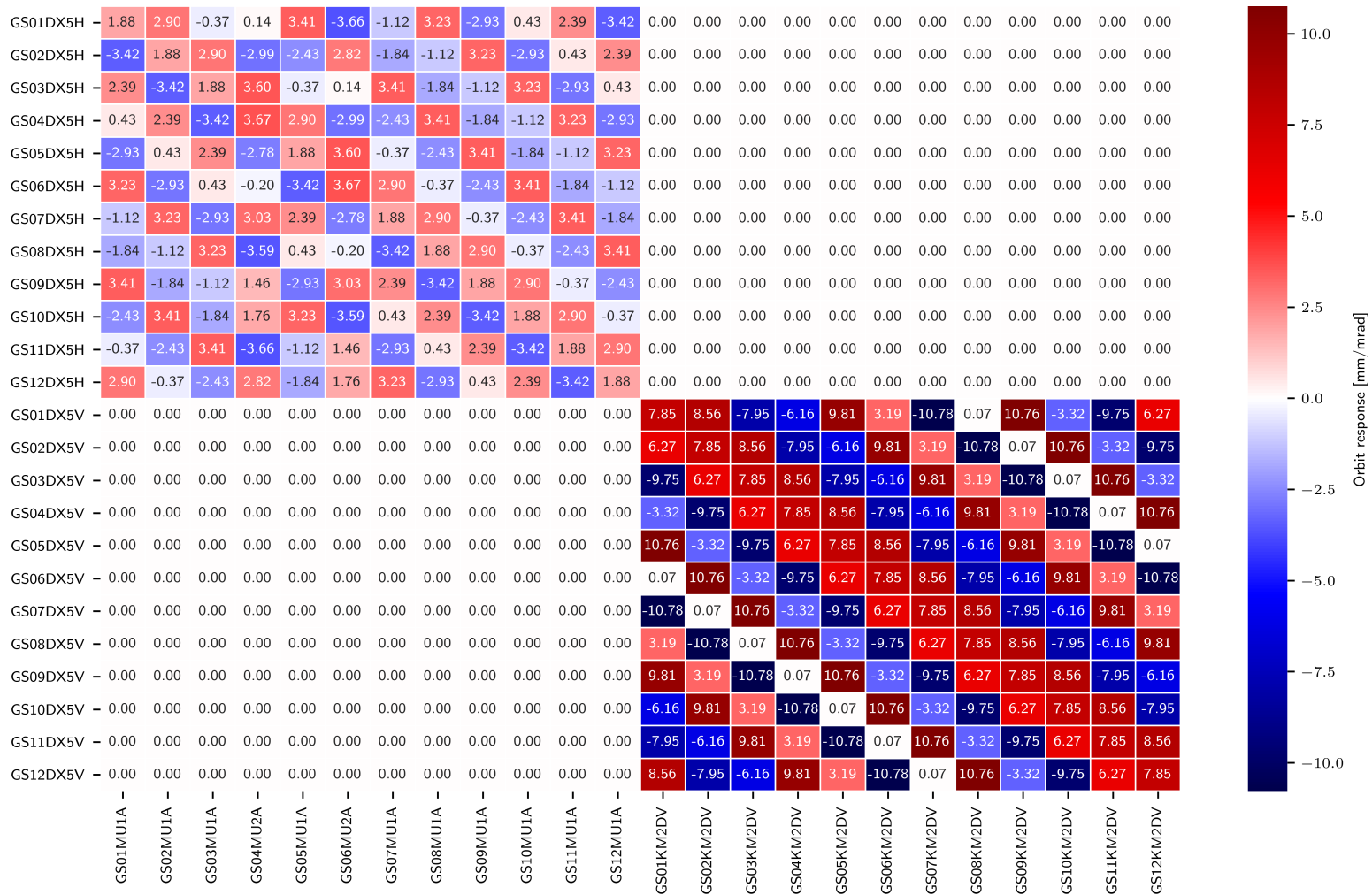


**Figure 3.2:** Simulated ORM for nominal extraction optics of SIS18. The coupling blocks of the ORM are zero because no coupling is present in the model lattice. The horizontal and vertical blocks show a circulant structure except for columns 4 and 6 of the horizontal block because the location of horizontal steerers is different in these sections. The circulant structure is reflected by the fact that each column can be obtained from the previous column shifted by one element downward (or, similarly, shifting the previous row by one element to the right).

### 3.2 Degeneracy for estimated quadrupole strengths

Any procedure with the goal of predicting a set of model parameters  $P$  which minimize the discrepancy between simulated and observed data is referred to as an *estimator*<sup>1</sup>. The efficiency of an estimator can be quantified by the spread of its predictions around the true parameter values. Thus, the mean squared error (mse) criterion serves as a measure for estimator efficiency:

$$\text{mse}[P] = \text{E}[(P - \theta)^2] = \text{Var}[P] + (\text{E}[P] - \theta)^2 \quad (3.1)$$

Here,  $P$  denotes the predicted parameter values by the estimator,  $\theta$  are the true parameter values and  $\text{E}[\cdot]$  and  $\text{Var}[\cdot]$  denote, respectively, the expectation value and the variance of its argument. The second term in equation 3.1 corresponds to the bias of the estimator. Thus, regarding the efficiency of an estimator, there is a trade-off between its variance and bias and an increase of the estimator's bias might result in an overall more efficient estimator (reducing the mean squared error of its predictions).

The first mention of quasi-degeneracy for linear optics from closed orbits was made in [73]. The proposed solution was to switch from an unbiased to a biased estimator in order to improve the overall efficiency of the estimates. This was done by augmenting the cost function with terms that correspond to the various specific quasi-degeneracy patterns of the lattice parameters. A related approach [74] limited the change of lattice parameters during each iteration of the optimization by using a dedicated set of weights in the cost function.

Regarding the terminology, a distinction between (pure) degeneracy and quasi-degeneracy is made in the following. A purely degenerate case is one for which there exist multiple distinct solutions that yield the same values for the chosen set of observables in the absence of measurement uncertainty. This is the case if, for example, there are too few BPMs available compared to the number of quadrupoles. A quasi-degenerate case, on the other hand, is one where there exist multiple solutions that are plausible in view of the measurement uncertainty, i.e., which can be plausibly explained by the measured data, and some (combinations of) parameters are noticeably more susceptible to the effect of measurement uncertainty than others. The presence of measurement uncertainty doesn't change the nature of the optimization problem though, as there is still a unique global minimum, depending on the specific data used for fitting. Rather, the quasi-degeneracy is a property of the modeled system. Depending on the lattice and optics, some directions in parameter space cause less increase in the cost function than others and, thus, are more susceptible to measurement uncertainty. This is sketched in Figure 3.3 where the orbit response of a single BPM/steerer pair is shown in dependence on the three different types of quadrupoles of the SIS18 lattice, F-, D- and T-quadrupoles. Clearly, the change in orbit response is more flat for the T-quadrupole than for the other two. This example shows only a single ORM element, so for the actual optimization problem the situation is more complex but the principle is the same: flat directions in the parameter space are more susceptible to measurement uncertainty. These directions are determined by the underlying model, i.e., the lattice and optics.

<sup>1</sup>An optimization algorithm (see section 2.5.3) with a defined set of hyperparameters and a designated starting point for the parameter estimates represents an estimator.

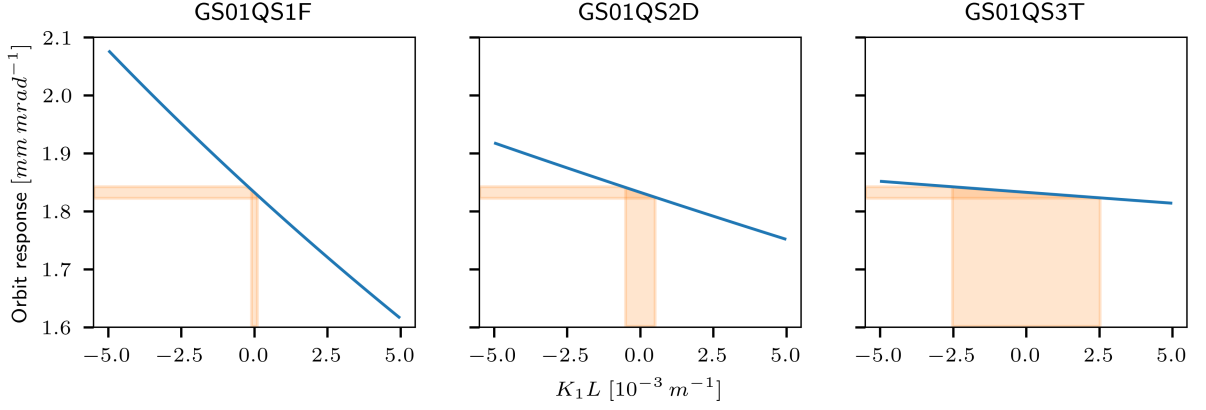


**Figure 3.3:** Example for the orbit response change of a single BPM/steerer pair when varying a single quadrupole. The horizontal orange area indicates an orbit response uncertainty of  $10 \mu\text{m}/\text{mrad}$  and is the same for all quadrupoles. The vertical orange area indicates the corresponding plausible region of the quadrupoles'  $K_1L$  strengths. Clearly, the plausible  $K_1L$  region is different for the various quadrupoles and it depends on the steepness of the orbit response change with  $K_1L$  for each quadrupole. [75]

### 3.2.1 Analytical derivative of orbit response

In order to explain the degeneracy properties for a given lattice, one can consider the orbit response formula  $r_{bs}$  for a single dipolar kick and calculate the derivative  $r'_{kbs}$  with respect to a change in the  $k$ -th quadrupole's strength. In the following it is assumed that operation is not close to transition energy and, thus, the energy-dependent term in equation 2.126 can be neglected.

$$r_{bs} = \frac{\sqrt{\beta_s \beta_b}}{2 \sin(\pi Q)} \cos(\pi Q - |\mu_s - \mu_b|) \quad (3.2)$$

where the subscripts  $b, s$  indicate, respectively, the BPM and steerer index. Taking the derivative with respect to the integrated strength  $(K_1L)_k$  of the  $k$ -th quadrupole, one obtains:

$$r'_{kbs} \equiv \frac{dr_{bs}}{d(K_1L)_k} = -r_{bs} \frac{\beta_k}{2} \left\{ \frac{1}{2 \tan(\pi Q)} + \frac{\tan(\pi Q - |\mu_b - \mu_s|)}{2} + \frac{\cos(2\pi Q - 2|\mu_b - \mu_k|) + \cos(2\pi Q - 2|\mu_s - \mu_k|)}{2 \sin(2\pi Q)} - \frac{\tan(\pi Q - |\mu_b - \mu_s|)}{\sin(2\pi Q)} \int_{\min(\mu_b, \mu_s)}^{\max(\mu_b, \mu_s)} \cos(2\pi Q - 2|\mu_k - u|) du \right\} \quad (3.3)$$

where  $\beta_k, \mu_k$  are, respectively, the beta function and phase advance at the  $k$ -th quadrupole. The full derivation is given in appendix A.4. In [79, 80] a similar result is independently derived based on the resonance driving terms  $f_{2000}, f_{0020}$ .

### 3.2.2 Pure degeneracy

A pure degeneracy exists if there is a set of quadrupoles which can assume different strengths and this is not reflected in the selected observables. Using the ORM as observable, this is the case if there are specific lattice segments of quadrupoles without BPMs nor steerers in between.

#### 3.2.2.1 Local degeneracy

By considering equation 3.3 together with the solution for the integral term given by equation A.32, one can expand the various cosine terms which contain  $\mu_k$  contributions by using the trigonometric identity  $\cos(x \pm y) = \cos(x)\cos(y) \mp \sin(x)\sin(y)$ . For the Jacobian elements corresponding to cases  $\mu_b, \mu_s < \mu_k$  (labeled (A)) or  $\mu_k < \mu_b, \mu_s$  (labeled (C)), both the cosine terms and the integral term expand into  $\sin(2\mu_k)$  and  $\cos(2\mu_k)$  terms. For the third case  $\mu_{b,s} < \mu_k < \mu_{s,b}$  (labeled (B)), the cosine terms still expand into  $\sin(2\mu_k), \cos(2\mu_k)$  while the integral term expands into  $\sin(\mu_k)^2, \cos(\mu_k)^2, \sin(\mu_k)\cos(\mu_k)$  terms. By using the trigonometric identities  $\sin(2\mu_k) = 2\sin(\mu_k)\cos(\mu_k)$  and  $\cos(2\mu_k) = \cos(\mu_k)^2 - \sin(\mu_k)^2$ , as well as the trigonometric identity  $1 = \cos(\mu_k)^2 + \sin(\mu_k)^2$  for the terms that are independent of  $\mu_k$ , one can rewrite the whole equation 3.3 in terms of  $\sin(\mu_k)^2, \cos(\mu_k)^2, \sin(\mu_k)\cos(\mu_k)$  where the coefficients for these terms only depend on  $\mu_b, \mu_s$  and  $Q$ . The spelled out version of this expanded form of the Jacobian is not presented here because it is lengthy and it varies across the three distinct cases (A, B, C). However, an overview of the grouped coefficients is given in the appendix (Table A.1). The following more general observations can be used to describe the properties of the Jacobian. Given that the Jacobian for each BPM/steerer/quadrupole triple can be written as the sum of three expressions involving  $\mu_k$  (namely,  $\sin(\mu_k)^2, \cos(\mu_k)^2, \sin(\mu_k)\cos(\mu_k)$ ) together with their coefficients which depend solely on  $\mu_b, \mu_s, Q$ , each column of the Jacobian can be written as a linear combination of  $\mathbf{v}_1 \sin(\mu_k)^2 + \mathbf{v}_2 \cos(\mu_k)^2 + \mathbf{v}_3 \sin(\mu_k)\cos(\mu_k)$  where the column vectors  $\mathbf{v}_{1,2,3}$  contain the row-wise constant coefficients depending only on  $\mu_b, \mu_s, Q$ . The expressions for these coefficients are the same for each group of quadrupoles that is not interleaved by BPMs nor steerers. Thus, the column span of the Jacobian is given by the three column vectors  $\mathbf{v}_{1,2,3}$  for each group of quadrupoles and thus, for a lattice with  $N$  sections and 3 or more non-interleaved quadrupoles per section, the rank of the Jacobian is at most  $3N$ . It should be emphasized that this holds only if all the involved quadrupoles in each section are consecutive, i.e., not interleaved by BPMs nor steerers, since otherwise their coefficients would change according to the cases (A, B, C). This implies that 4 or more consecutive quadrupoles per section will cause a pure degeneracy since their contributions to the Jacobian can still be described by only three column vectors. This result holds for one dimension (horizontal or vertical) but for uncoupled optics it is easily extended to both dimensions by considering that there are  $\sin(\mu_k)^2, \cos(\mu_k)^2, \sin(\mu_k)\cos(\mu_k)$  terms for both dimensions separately, i.e., six independent coefficient vectors  $\mathbf{v}_{1,2,3,4,5,6}$ . Thus, the dimension of the column span of the Jacobian involving both dimensions is bounded by  $6N$  and, therefore, 7 or more consecutive quadrupoles will cause a pure degeneracy.

This is in agreement with the result derived in [81] which is that for uncoupled transverse optics, a set of 7 or more consecutive quadrupoles in both dimensions (or, 4 or more quadrupoles in one dimension) can produce locally confined optics variations in between their segment. Since the orbit response is a specific combination of the lattice optics, and it depends only on the optics at the BPM and steerer locations as well as the tune, if there exist such segments of quadrupoles not interleaved with BPMs nor steerers, the optics within such segments cannot be resolved by observing the ORM. This can be seen from Figure 3.4 which shows simulated inverse modeling results for the SIS18 lattice for all 36 quadrupoles, without any simulated

measurement uncertainty, while leaving out the BPMs and steerers from an increasing number of consecutive sections. As can be seen, for the cases where none of the sections or only the first section is skipped, the quadrupole strengths can be reliably recovered down to the numerical precision of the estimator. When three or four consecutive sections are skipped, the estimates clearly become ambiguous which is reflected by the large increase in their standard deviation. This is because each section contains three distinct quadrupoles and hence, when skipping three or more sections, the corresponding segment contains more than 7 quadrupoles required to exhibit a degeneracy. For the case where two sections are skipped, i.e., six quadrupoles, there is a slight increase in standard deviation, similar to the amount that's visible for the neighboring sections in the skip-3 and skip-4 cases. This is because when the degenerate segment is extended with its neighboring sections, the variations induced by those quadrupoles at the boundaries of the segment are on the level of the numerical precision of the estimator and, hence, won't be distinguished. Nevertheless, it should be noted that the order of magnitude is much smaller. The saw-tooth pattern that can be observed between D- and T-quadrupoles will be explained as quasi-degeneracy below.

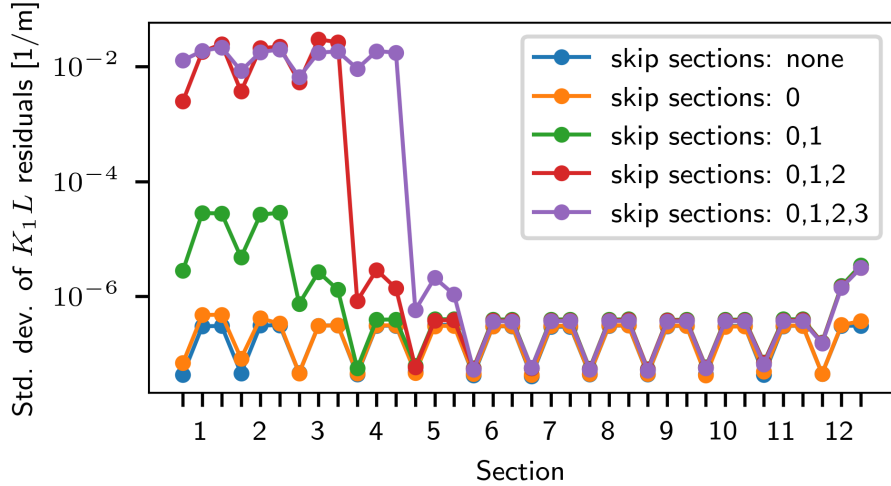


**Figure 3.4:**  $K_1L$  residuals when running Levenberg-Marquardt optimization for the nominal optics, starting from 1% random quadrupole errors, and gradually leaving out BPMs and steerers from consecutive sections in order to cause a pure degeneracy of the inverse problem. Each tick marker on the horizontal axis indicates a quadrupole (F-, D-, T-quadrupole per section). [75]

### 3.2.2.2 Global degeneracy

Besides the intra-section degeneracy discussed above, which is caused by isolated groups of consecutive quadrupoles, there can be another, global degeneracy whose existence also depends on the BPM/steerer placement. In the following, the notation  $\mathbf{S}, \mathbf{Qn+}, \mathbf{B}$  is used which means that one dimension (horizontal or vertical) is considered and the placement of lattice elements within a section is the following: steerer, followed by  $n$  quadrupoles ( $\mathbf{n+}$  means  $n$  or more), followed by a BPM. In terms of the results this is similar to  $\mathbf{B}, \mathbf{Qn+}, \mathbf{S}$ . This pattern describes the placement for one section and is repeated on a section-to-section basis. It should be emphasized that this only describes in what order BPM, steerer and quadrupoles are placed but it doesn't restrict the specific locations in terms of phase advance within each section. In fact, these specific locations may be different from section to section. For both dimensions,

### 3. Estimating quadrupole errors in the presence of degeneracy for the SIS18 synchrotron

horizontal and vertical, the notation  $\text{Sh}, \text{Sv}, \text{Qn}+, \text{Bh}, \text{Bv}$  is used, where  $\text{h}$  refers to horizontal and  $\text{v}$  refers to vertical. In terms of the results this is similar to any other pattern that swaps any steerer with any BPM. This is because the Jacobian only depends on  $|\mu_b - \mu_s|$  and it separates horizontal from vertical contributions.

It is shown that the following placements exhibit a global degeneracy:  $\text{S}, \text{Q3}+, \text{B}$  and  $\text{Sh}, \text{Sv}, \text{Q5}+, \text{Bh}, \text{Bv}$ . It is worth noting that  $\text{Sh}, \text{Sv}, \text{Q5}, \text{Bh}, \text{Bv}$  causes a rank deficiency of degree 1 in the Jacobian while  $\text{Sh}, \text{Sv}, \text{Q6}, \text{Bh}, \text{Bv}$  causes a degree 2 rank deficiency. For the presented case, the  $\text{Sh}, \text{Sv}, \text{Q5}, \text{Bh}, \text{Bv}$  rank deficiency is due to the difference in tunes being an integer number since  $Q_h = 4.29, Q_v = 3.29$  for SIS18. If the tune difference does not equal an integer, this rank deficiency will disappear. The  $\text{Sh}, \text{Sv}, \text{Q6}, \text{Bh}, \text{Bv}$  rank deficiency, however, remains regardless of the tunes according to the above arguments. For  $\text{Sh}, \text{Sv}, \text{Q7}+, \text{Bh}, \text{Bv}$  intra-section degeneracy will appear and the rank of the Jacobian is the same as for  $\text{Sh}, \text{Sv}, \text{Q6}, \text{Bh}, \text{Bv}$ . The argument for this is similar to the one for  $\text{S}, \text{Q4}+, \text{B}$  above, since exactly three column vectors are needed for each dimension in order to generate the Jacobian columns for a group of consecutive quadrupoles in that dimension. In the appendix, a proof for the rank deficiency for the  $\text{S}, \text{Q3}+, \text{B}$  (appendix A.6) and  $\text{Sh}, \text{Sv}, \text{Q6}+, \text{Bh}, \text{Bv}$  (appendix A.7) placements is presented. The rank deficiency for the  $\text{Sh}, \text{Sv}, \text{Q5}, \text{Bh}, \text{Bv}$  pattern for an integer tune difference is found from simulation results. Table 3.1 gives an overview of the various Jacobians' ranks obtained via simulations, in agreement with the analytical derivations.

**Table 3.1:** This table presents an overview of the Jacobian properties in terms of rank deficiency for the various BPM/steerer placements around groups of consecutive quadrupoles.  $N$  denotes the number of sections in the lattice ( $N \geq 3$  is assumed). It should be emphasized that the only deciding factor is the placement pattern, i.e., how many quadrupoles form a consecutive group, not where exactly these quadrupoles or the BPMs/steerers are located in each of the sections. The specific locations may vary from section to section and as long as the overall placement pattern is satisfied, the rank will be the same. For verification with simulations, the Jacobians were obtained from simulations using the `mpmath` [82] library to avoid numerical issues (`dps` set to 100). The rank is then computed as the number of singular values that are larger than or equal to  $\epsilon N^2 s_{\max}$  where  $s_{\max}$  is the largest singular value and  $\epsilon = 2^{-52}$  is the machine epsilon for double precision floating point numbers.

|                                                          |        | Jacobian  |                                                                                                           |  |
|----------------------------------------------------------|--------|-----------|-----------------------------------------------------------------------------------------------------------|--|
|                                                          | # rows | # columns | rank                                                                                                      |  |
| $\text{S}, \text{Q2}, \text{B}$                          | $N^2$  | $2N$      | $2N$                                                                                                      |  |
| $\text{S}, \text{Q3}, \text{B}$                          | $N^2$  | $3N$      | $3N - 1$                                                                                                  |  |
| $\text{S}, \text{Q4}+, \text{B}$                         | $N^2$  | $4^+N$    | $3N - 1$                                                                                                  |  |
| $\text{Sh}, \text{Sv}, \text{Q4}, \text{Bh}, \text{Bv}$  | $2N^2$ | $4N$      | $4N$                                                                                                      |  |
| $\text{Sh}, \text{Sv}, \text{Q5}, \text{Bh}, \text{Bv}$  | $2N^2$ | $5N$      | $\begin{cases} 5N - 1 & , \text{ if } Q_x - Q_y = \text{integer} \\ 5N & , \text{ otherwise} \end{cases}$ |  |
| $\text{Sh}, \text{Sv}, \text{Q6}, \text{Bh}, \text{Bv}$  | $2N^2$ | $6N$      | $6N - 2$                                                                                                  |  |
| $\text{Sh}, \text{Sv}, \text{Q7}+, \text{Bh}, \text{Bv}$ | $2N^2$ | $7^+N$    | $6N - 2$                                                                                                  |  |

Appendix A.5 includes a similar derivation for beamlines, i.e., non-circular lattices.

#### 3.2.3 Quasi-degeneracy

Even though groups of, for example, two consecutive quadrupoles do not exhibit a pure degeneracy, they can exhibit a quasi-degeneracy which means that their estimated strengths

are much more susceptible to measurement uncertainty than the ones of other quadrupoles. This type of quasi-degeneracy is explained in the following section.

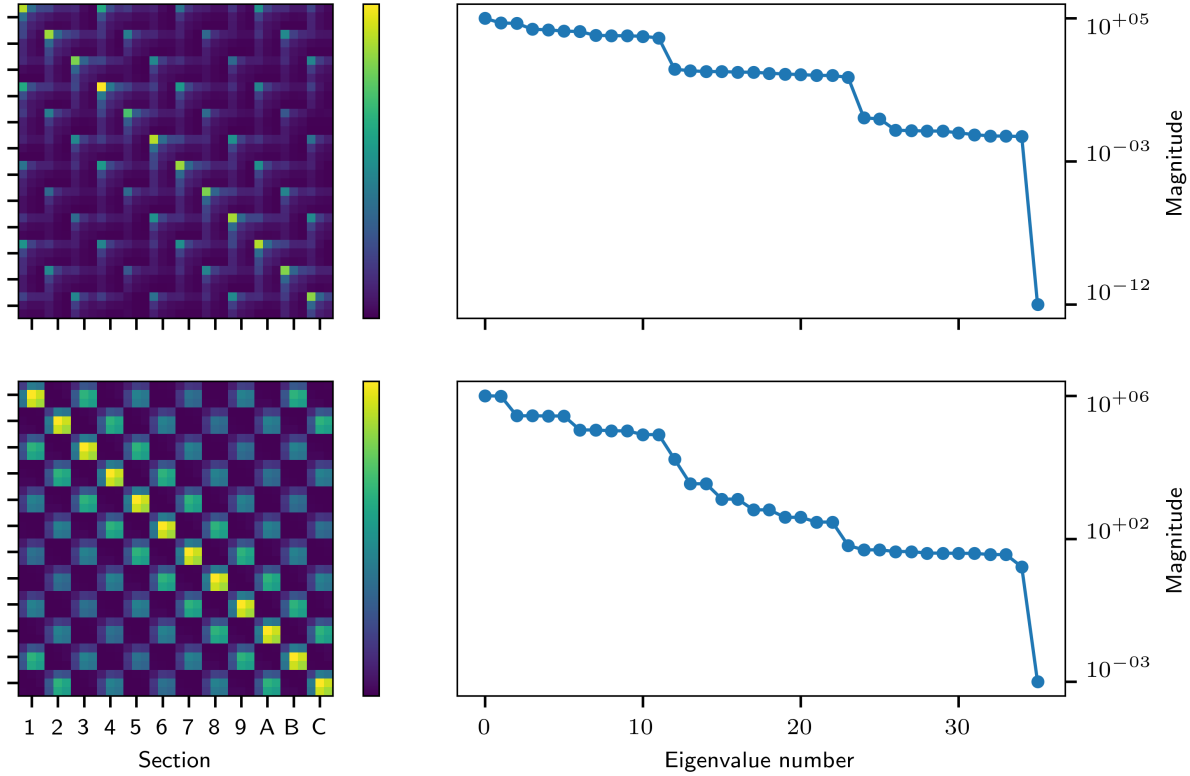
The covariance of parameter estimates under linear least squares is given by  $\sigma^2(J^T J)^{-1}$  where  $\sigma^2$  is the variance of observables and  $J$  is the Jacobian (if the various BPMs have different measurement uncertainties, it is  $(J^T \Sigma J)^{-1}$  with  $\Sigma$  being the covariance matrix of observables). This is closely related to the matrix  $J^T J$ . The eigenvectors of a matrix and its inverse are similar and the eigenvalues are reciprocal, so studying the matrix  $J^T J$  reveals important information about the error propagation. Also, in Gauss-Newton minimization,  $J^T J$  is used as an approximation of the Hessian  $H$  and, thus, a lower bound for the estimated parameter variance is given by  $\sigma^2 H^{-1}$ . This is, of course, in agreement since at the minimum of the cost function, the gradient is assumed to vanish, so the flatness of the cost function depends on how quickly that zero gradient changes in the neighborhood of the estimate which is indicated by the Hessian matrix.

Figure 3.5 shows the  $J^T J$  matrices emerging from horizontal and vertical ORMs, together with their eigenvalue spectra. There are a few things to be noted. First of all, for the vertical  $J^T J$  plot it can be seen that it indicates higher variance for the D-T-quadrupole pairs than for the F-D- or F-T-pairs. This is because of the scaling of the Jacobian with the beta function which, in vertical, is larger at D- and T-quadrupoles than at F-quadrupoles (see Figure 3.1). Secondly, it can be observed that in both dimensions there is one eigenvalue that is much smaller than others. Small eigenvalues of  $J^T J$  correspond to large eigenvalues of  $(J^T J)^{-1}$ , i.e., of the covariance estimate for model parameters. However, for the horizontal  $J^T J$  matrix, the smallest eigenvalue in this plot is only nonzero due to limited numerical precision, since in horizontal dimension the lattice features a **S,Q3,B** steerer/BPM placement which causes a pure degeneracy (see section 3.2.2.2). A zero eigenvalue for  $J^T J$  implies a pure degeneracy since the system  $J^T J \Delta p = J^T r$  ( $\Delta p$  parameter update,  $r$  residuals) is under-determined. That is, the null space of  $J^T J$  is nonzero and, hence, there exists a parameter update  $\Delta p$  that will leave the r.h.s. of the equation unchanged at zero. In general, a small eigenvalue for  $J^T J$  implies a direction of quasi-degeneracy which is given by the corresponding eigenvector. It means that the parameter update emerging from  $J^T J \Delta p = J^T r$  will be susceptible to measurement uncertainty in the direction of the corresponding eigenvector. This is what is observed for the vertical Jacobian where the vertical lattice features a **B,Q2,S** BPM/steerer placement.

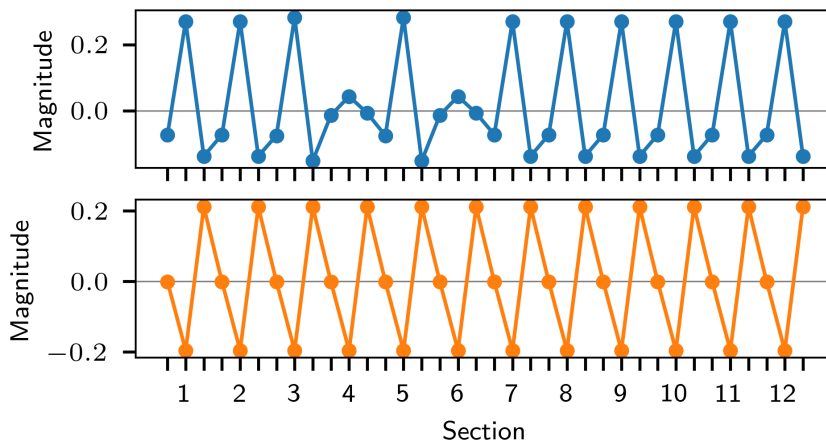
Figure 3.6 shows the two eigenvectors, in horizontal and vertical dimension, that correspond to the smallest eigenvalue of the corresponding  $J^T J$  matrix. Since the eigenvectors of a matrix and its inverse are similar, these indicate the direction of (quasi-)degeneracy in both dimensions separately. It can be observed that this is a global degeneracy in both cases, since all quadrupoles participate; hence, there is only one eigenvalue that is significantly smaller than all others. This is due to the symmetry of the lattice with respect to the BPM/steerer placement pattern. In horizontal, for the two sections 4 and 6 where the ORM's circulant structure is broken, it can be observed that a corresponding change in the quadrupole's degeneracy pattern reflects this. In vertical, it can be observed that the quasi-degeneracy is driven by the (non-interleaved) D-T-quadrupole pairs.

Figure 3.7 shows the scaling of the covariance estimate for model parameters, i.e.,  $(J^T J)^{-1}$ ; for horizontal, since it is rank deficient,  $(J^T J + \alpha I)^{-1}$  is plotted (with  $\alpha = 1 \times 10^{-8}$ , i.e.,

### 3. Estimating quadrupole errors in the presence of degeneracy for the SIS18 synchrotron



**Figure 3.5:** Top row: Horizontal dimension, bottom row: vertical dimension. Left column: The  $36 \times 36$  matrix  $J^T J$ . The axes numbering indicates the 12 sections of SIS18 in hexadecimal notation and there are 3 rows/columns per section, corresponding to the F-, D- and T-quadrupoles (in that order) of each section. Right column: The eigenvalues of corresponding  $J^T J$  matrices. The color bars and eigenvalue magnitude indicate the magnitude of  $J^T J$  in units of  $\text{m}^4/\text{rad}^2$ . The values of the color bar correspond to those of the eigenvalue plots shown on the vertical axes. For the horizontal dimension, the smallest eigenvalue  $\lambda_{35}$  is nonzero only due to limited floating point precision. When inspecting the 12 smallest horizontal eigenvalues, it can be observed that the  $\lambda_{24}, \lambda_{25}$  eigenvalues have a slightly greater magnitude than the remaining 9 eigenvalues (neglecting  $\lambda_{35}$ ). These two eigenvalues correspond to the sections 4 and 6 where the horizontal steerer is shifted by a few meters compared to the other sections. [75]



**Figure 3.6:** Eigenvectors that correspond to the smallest eigenvalue of the  $J^T J$  matrices in horizontal (top) and vertical (bottom) dimension. Each tick marker on the horizontal axis indicates a quadrupole (F-, D-, T-quadrupole per section). [75]



Tikhonov regularized, which is also used by, for example, the Levenberg-Marquardt optimizer, though it uses a flexible regularization parameter  $\alpha$ ). Clearly, the global nature of the degeneracy is reflected in the eigenvectors Figure 3.6. From Figure 3.5 it can be observed that pairwise cancellation is mostly confined to nearby sections and decreases when moving further away in terms of the phase advance. However, the final covariance of quadrupole estimates is dominated by a strong global component which is symmetric for the vertical ORM.

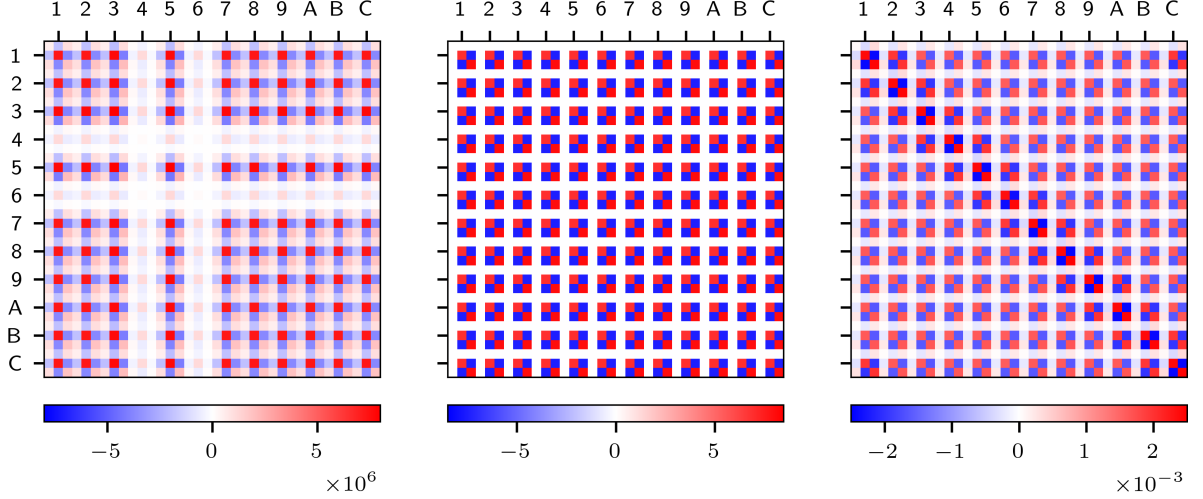


**Figure 3.7:**  $(J^T J + \alpha I)^{-1}$  for the horizontal ( $\alpha = 1 \times 10^{-8}$ ; left), vertical ( $\alpha = 0$ ; middle) and combined ( $\alpha = 0$ ; right) dimensions. The axes numbering indicates the 12 sections of SIS18 in hexadecimal notation and there are 3 rows/columns per section, corresponding to the F-, D- and T-quadrupoles (in that order) of each section. The unit of the color bars, indicating the magnitude of the matrices, is  $\text{rad}^2/\text{m}^4$ . The quasi-degeneracy pattern looks very symmetric in vertical because the BPM/steerer placement is fully symmetric from section to section. This, however, is not a requirement as shown by the horizontal data. The degeneracy pattern reflects the differently placed steerers in section 4 and 6. In fact, no symmetry whatsoever in terms of the exact phase advances of BPMs or steerers is required for a degeneracy pattern to occur; only the placement pattern in terms of upstream or downstream of quadrupoles is deciding. For the combined dimensions it can be observed that the resulting pattern is not fully symmetric but features local correlations slightly more than ones with other sections. This is because the magnitude of the smallest eigenvalue for the combined dimensions is closer to the magnitude of other eigenvalues and thus does not dominate the pattern alone. [75]

For the vertical ORM, the corresponding  $J^T J$  matrix is a block circulant matrix by the argument of section-to-section symmetry of the vertical lattice. The eigenvectors of a block circulant matrix  $B = \text{bcirc}(\mathbf{b}_0, \mathbf{b}_1, \dots, \mathbf{b}_{n-1}) \in \mathcal{BC}_{n,k}$  (where  $n$  is the number of blocks and  $k$  the size of a  $k \times k$  block;  $n = 12$ ,  $k = 3$  for the vertical ORM) are derived in [83]. They are given by:

$$\begin{bmatrix} \mathbf{v} \\ \rho_m \mathbf{v} \\ \rho_m^2 \mathbf{v} \\ \vdots \\ \rho_m^{n-1} \mathbf{v} \end{bmatrix} \quad (3.4)$$

where  $\mathbf{v}$  is a nonzero column vector of length  $k$ , which is given below, and  $\rho_m$  is one of the  $n$  complex roots of unity:  $\rho_m = \exp(2\pi i \frac{m}{n})$ . For each  $\rho_m$  there are  $k$  distinct vectors  $\mathbf{v}$  given by

### 3. Estimating quadrupole errors in the presence of degeneracy for the SIS18 synchrotron

the eigenvector equation [83]:

$$(\mathbf{b}_0 + \rho\mathbf{b}_1 + \rho^2\mathbf{b}_2 + \dots + \rho^{n-1}\mathbf{b}_{n-1})\mathbf{v} = \lambda\mathbf{v} \quad (3.5)$$

where  $\lambda$  is the corresponding eigenvalue.

Since the first of the  $n$  roots of unity is  $\rho_0 = 1$ , from equation 3.4 it becomes apparent that every block circulant matrix  $B \in \mathcal{BC}_{n,k}$  has exactly  $k$  distinct globally symmetric eigenmodes which repeat on a block-to-block basis. This is the case for the vertical  $J^T J$  matrix.

Because  $J^T J$  is real and symmetric, its eigenvalues are guaranteed to be real, too. Furthermore, since  $J^T J$  is a Gram matrix, it is positive semidefinite and its eigenvalues are guaranteed to be greater than or equal to zero. This is observed for the vertical  $J^T J$  matrix and it happens that one of the globally symmetric eigenmodes is associated with the smallest eigenvalue  $\lambda_{35}$ . Figure 3.8 shows the three globally symmetric eigenmodes corresponding to the  $\rho_0 = 1$  eigenvalues.

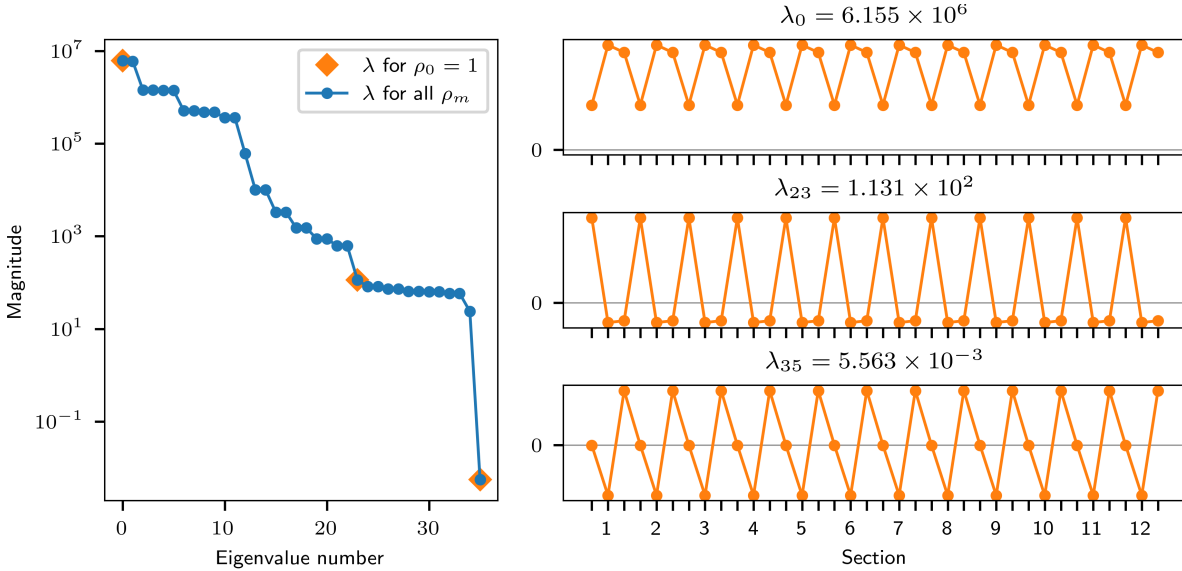


**Figure 3.8:** Globally symmetric eigenmodes of  $J^T J$  in vertical dimension which arise due to the fact that the vertical lattice is symmetric from section to section. Each tick marker on the horizontal axis of the eigenvector plots indicates a quadrupole (F-, D-, T-quadrupole per section). [75]

Because for the horizontal lattice, the circulant structure of the ORM and thus of  $J^T J$  is broken in the two sections 4 and 6, it can't have a globally symmetric eigenmode, i.e., a mode that repeats on a section-to-section basis. However, as becomes apparent from the eigenvector Figure 3.6, the global mode still affects all sections at once and reflects the breaking of symmetry in the sections 4 and 6.

#### 3.2.4 Exemplification using the SIS18 lattice

In the absence of BPM errors, inverse modeling with an optimizer such as Levenberg-Marquardt will always converge to the ground truth solution (within the boundaries of numerical precision), given that there is no additional model bias present and the initial guess is not too far from the ground truth (so that the optimizer won't cross any instabilities, for example).

Figure 3.9 shows the covariance of the various solutions obtained with Levenberg-Marquardt optimizer when no quadrupole errors are applied to the lattice and only BPM errors are present in the ORM simulation. That is, each of the inverse modeling instances is given a distinct noisy ORM emerging from the same orbit response uncertainty of  $7 \mu\text{m}/\text{mrad}$ . The initial guess is the ground truth solution, i.e., no quadrupole errors, but from the perspective of the optimizer this is not the minimum of the cost function due to the noise in the ORM; hence, it will converge to a different solution, the  $K_1L$  residuals. The structure of these solutions is determined by the underlying simulation model including the lattice optics. It can be seen that the quasi-degeneracy is mainly driven by the D-T-quadrupole pairs where much larger excursions in  $K_1L$  residuals happen. This is in agreement with Figure 3.7 which shows the predicted uncertainty from the Jacobian. For  $7 \mu\text{m}/\text{mrad}$  orbit response uncertainty, the expected covariance of D- and T-quadrupole strengths is approximately  $(7 \times 10^{-3})^2 \cdot 0.002 \text{ 1/m}^2 \approx 1 \times 10^{-7}/\text{m}^2$ . This is the amount that can be observed from the simulations with Levenberg-Marquardt optimizer in Figure 3.9. Also, the observed covariance pattern matches the one from Figure 3.7.

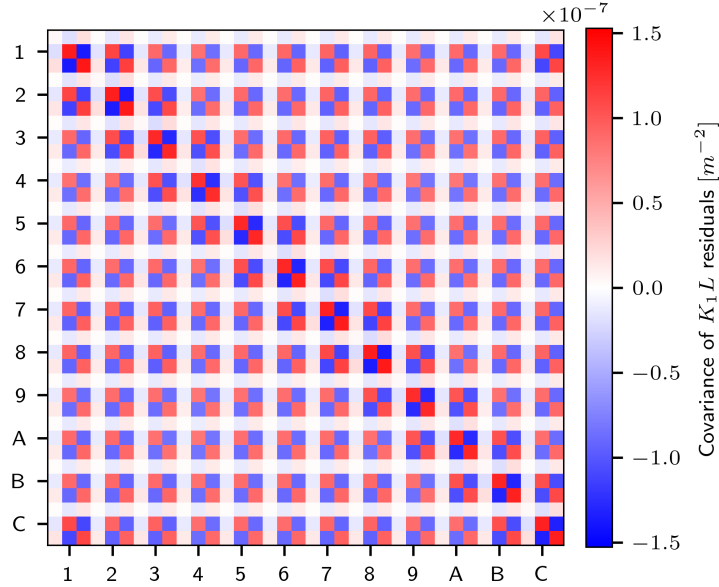


**Figure 3.9:** Covariance of  $K_1L$  residuals obtained with Levenberg-Marquardt optimizer for  $7 \mu\text{m}/\text{mrad}$  orbit response uncertainty when including both horizontal and vertical ORM. The axes numbering indicates the 12 sections of SIS18 in hexadecimal notation and there are 3 rows/columns per section, corresponding to the F-, D- and T-quadrupoles (in that order) of each section. No quadrupole errors were applied to the lattice and optimization started at the nominal quadrupole strengths. Thus, the  $K_1L$  residuals emerge purely as a result of the simulated ORM uncertainty. All 36 quadrupoles have been included in the optimization. [75]

### 3.2.5 Counteracting quasi-degeneracy

At different stages, different options for counteracting quasi-degeneracy are feasible. During the design phase of the accelerator, the placement of steerers and BPMs can be investigated in order to find a placement that reduces the amount of quasi-degeneracy compared to other placement candidates. For the SIS18 lattice, this would be achieved by positioning the BPMs between the D- and T-quadrupoles. At the stage of data analysis, the choice of optimizer allows for different strategies to counteract the quasi-degeneracy. Examples include introducing

a cutoff during Singular Value Decomposition (SVD) or adding additional constraints to the cost function.

#### 3.2.5.1 Placement of BPMs and steerer magnets

At a stage where this is still possible, the careful planning of BPM and steerer locations can help to avoid or mitigate quasi-degeneracy. The following three scenarios are compared to the results for the nominal lattice: moving either the horizontal or vertical BPM or both BPMs between the D- and T-quadrupole. Figure 3.10 shows the  $J^T J$  eigenvalue spectra for these three cases as well as for the nominal case. It can be observed that the different placements of BPMs have different effects on the amount of quasi-degeneracy. Specifically, the versions where the vertical BPMs are shifted between the D- and T-quadrupole yield significantly smaller uncertainty in the estimated parameters while the version with only horizontal BPMs shifted has a negligible effect. Thus, it is of importance to explore the different options for BPM placement in order to allow for more precise inverse modeling results for future accelerators.

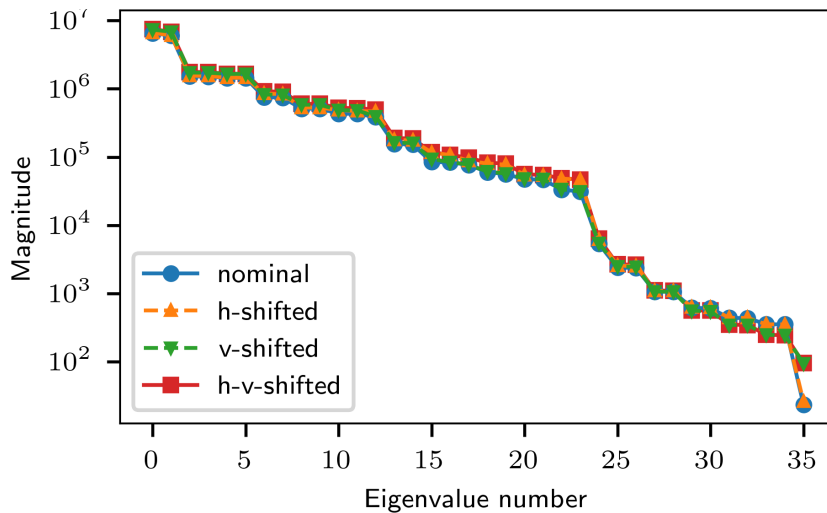


**Figure 3.10:** Eigenvalues of  $J^T J$  for different BPM placements. *nominal* refers to the original lattice, *h-shifted* refers to the lattice where the horizontal BPM has been shifted from its original position (downstream of the T-quadrupole) to in between the D- and T-quadrupole. *v-shifted* means the same for the vertical BPM and *h-v-shifted* refers to both BPMs being shifted between the D- and T-quadrupole. The different placement strategies vary in their smallest eigenvalue which is the one that drives the propagation of uncertainty. [75]

### 3.3 Fitting the orbit response matrix

The Levenberg-Marquardt optimizer uses the Jacobian at every iteration. Typically, this Jacobian is computed numerically via finite-difference approximation, with an appropriate step size  $\Delta$  for each parameter. In the following, the analytically derived Jacobian (see equation 3.3) is used for the optimization procedure<sup>2</sup>. This analytical Jacobian is obtained from the Twiss data of the lattice. While there is a mismatch between the numerical (real) and the

<sup>2</sup>It is noted that the analytical formula equation 3.3 has been derived under the assumption of uncoupled optics. In the presence of coupling, the analytical Jacobian needs to be re-derived with the coupling terms included. Once obtained, the analytical Jacobian approach can then be applied for inverse modeling of coupled optics.

analytical Jacobian, if this mismatch is manageable then the fitting will still converge. This has similarities to how Closed Orbit Feedback (COFB) correction with model mismatch works [84]. In the context of COFB, the system is assumed to be linear and there exists a true response matrix  $R$  and a model response matrix  $R_\Theta$ . In an iterative scheme, the COFB converges if all eigenvalues  $\lambda_i$  of  $1 - RR_\Theta^+$  fulfill  $-1 < \lambda_i \leq 1$  (where the superscript  $+$  denotes the pseudo-inverse). If  $R$  and  $R_\Theta$  are square matrices, the relationship has to be a strict inequality to achieve convergence, i.e.,  $-1 < \lambda_i < 1$ . Otherwise, if  $R$  and  $R_\Theta$  are  $m \times n$  matrices with  $m > n$ , then  $1 - RR_\Theta^+$  must have largest eigenvalue 1 with multiplicity  $m - n$  and all other eigenvalues must fulfill  $-1 < \lambda_i < 1$ . In the context of linear optics from closed orbits, the matrices  $R$  and  $R_\Theta$  denote, respectively, the true and analytical Jacobian. Also, the system is not entirely linear, so the lattice model reacts differently to a parameter update than the linear transformation given by  $R$ . However, if the magnitude of updates is constrained, a locally linear version can be assumed at every iteration. This implies a varying true matrix  $R \equiv R(x)$  where  $x$  is the current guess of model parameters. For an iterative scheme to converge, the eigenvalues of the sequence of matrix multiplications

$$\left(1 - RR_\Theta^+\right)_{k-1} \dots \left(1 - RR_\Theta^+\right)_0 \quad (3.6)$$

must tend to zero as  $k \rightarrow \infty$  (where  $k$  denotes the iteration count; except the  $m - n$  excess eigenvalues for rectangular  $R, R_\Theta$  remain at 1). This is provided if the eigenvalues of the individual matrices  $(1 - RR_\Theta^+)_i$ , for guess  $x_i$  during the  $i$ -th iteration, fulfill  $-1 < \lambda_i \leq 1$ , i.e., if the model mismatch is manageable for each relevant optics setting during the fitting. If the model errors are small, it might even suffice to use a single Jacobian  $R_\Theta$  for the entire fitting procedure; that is, the same Jacobian can be reused during each iteration.

The analytical Jacobian is computed via equation 3.3 from Twiss data which is obtained from the accelerator model evaluated at the current parameter guess. Due to sign convention for quadrupoles, for the vertical dimension the Jacobian needs to be multiplied by  $-1$ .

Using the analytical Jacobian from Twiss data is more efficient than computing the numerical Jacobian since Twiss data is computed only once for the entire Jacobian while the numerical approach computes one ORM per quadrupole, that is, one closed orbit per steerer per quadrupole. Thus, the speed-up factor in terms of the scaling with the number of relevant lattice elements is  $N_{steerers} \cdot N_{quadrupoles}$ . For the BPM and steerer gain parts of the ORM, the analytical equation for the orbit response equation 2.126 is similarly used with Twiss data in order to generate the corresponding columns of the analytical Jacobian.

Various tests with simulation data have been performed. The tests include random quadrupole and gain errors as well as different levels of simulated orbit response uncertainty. The Levenberg-Marquardt algorithm has been used for the fitting. The results are shown in Figure 3.11. It can be observed that the results obtained with the analytical Jacobian match closely with those obtained with the numerical Jacobian. For the simulation case which limits quadrupole errors by 3% and gain errors by 10%, the feedback-like approach using only the analytical Jacobian obtained for the nominal optics converges in 67% of the instances and it reaches unstable lattice configurations for the remaining instances. This is due to the discrepancy of the real Jacobian with respect to the employed Jacobian obtained from nominal optics being too large to allow convergence according to equation 3.6. The convergence rate is,

### 3. Estimating quadrupole errors in the presence of degeneracy for the SIS18 synchrotron

however, independent of the simulated ORM uncertainty. For simulated quadrupole errors below 2%, the feedback-like approach converges in more than 98% of instances. Thus, this approach can be used to correct a lattice that exhibits only small quadrupole drifts over time. For cases with larger deviations, it is sufficient to recompute the Jacobian during each iteration of the fitting procedure. When the analytical Jacobian is recomputed this way, it converges and yields good results also for larger simulated model errors as shown in Figure 3.11.

The software used for fitting, including the analytical Jacobian approach, has been implemented as a Python package and made publicly available [1].

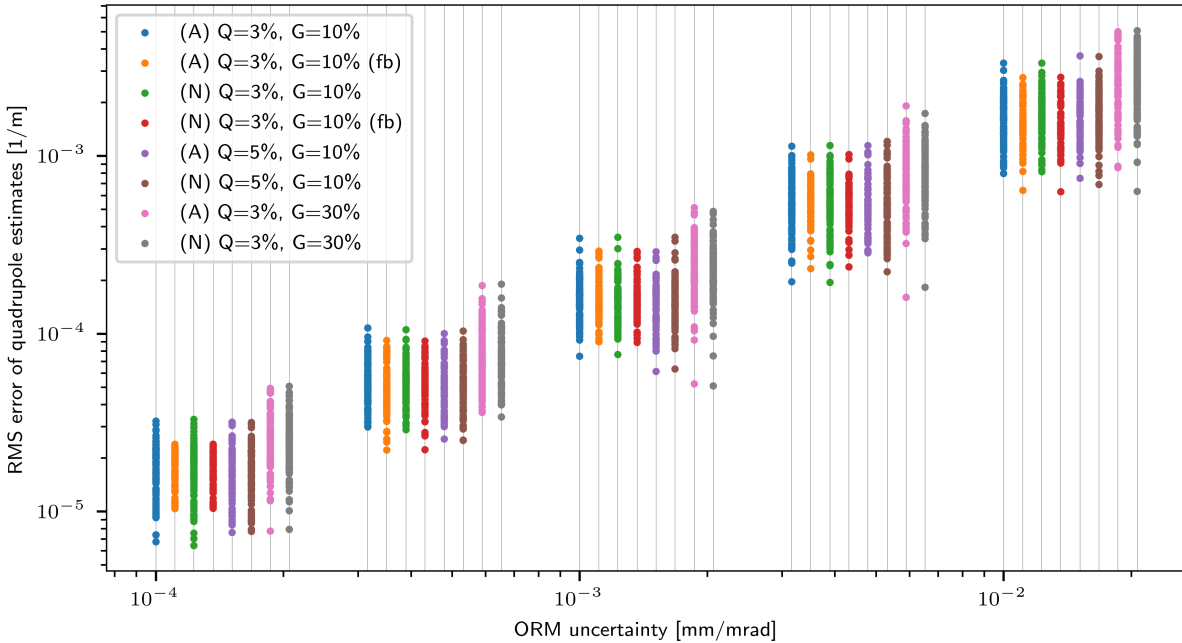


**Figure 3.11:** Comparison of simulation results for various cases. (A) and (N) denote, respectively, the usage of analytical or numerical Jacobian. Q and G denote, respectively, the percentage level of random quadrupole and gain errors, uniformly sampled within these bounds. All simulations used Levenberg-Marquardt optimizer except the ones with suffix (fb) which used a purely feedback-like approach using only the analytical or numerical Jacobian obtained for the error-free model optics setting. The feedback-like approach converged for 67% of the simulated Q=3%, G=10% instances for both, the analytical and numerical Jacobian method. For larger quadrupole or gain errors the rate of convergence decreases further and, hence, these results are not reported. However, simulating quadrupole errors below 2% (not shown) results in more than 98% convergence rate for the feedback-like approach. The convergence rate does not depend on the simulated ORM uncertainty. All other approaches converge reliably also for the larger error levels shown in the plot. The simulations have been performed for five different ORM uncertainties which are plotted on the horizontal axis: 0.1  $\mu\text{m}/\text{mrad}$ , 0.32  $\mu\text{m}/\text{mrad}$ , 1.0  $\mu\text{m}/\text{mrad}$ , 3.2  $\mu\text{m}/\text{mrad}$  and 10.0  $\mu\text{m}/\text{mrad}$ . For each uncertainty level, the eight different cases are shifted horizontally for better visibility (their order from left to right matches the order in the legend from top to bottom); however, each case used the same ORM uncertainty for simulations (the leftmost one). Each uncertainty level contains 100 random simulations per case. [75]

#### 3.3.1 Improving the accuracy of the analytical Jacobian

Whether the analytical Jacobian according to section 3.3 can be used for the fitting procedure depends on the agreement of the analytical Jacobian and the true (numerical) Jacobian. Equation 3.6 represents a necessary condition for the fitting to converge. However, for some lattices, the thin lens approximation used during the derivation of the analytical Jacobian

from equation 3.3 might not be accurate enough in order allow for fitting with the analytical Jacobian. Nevertheless, the accuracy of the analytical Jacobian can be improved by using multiple thin slices for each quadrupole. This is achieved by computing the Twiss parameters and phase advance directly upstream of each quadrupole  $(\beta_1, \alpha_1, \mu_1)$  and then computing the values at each thin slice  $(\beta_2, \alpha_2, \mu_2)$  by tracking them through the sequence of sub-elements of the sliced quadrupole. The new values can be obtained with the help of equation A.1 and the auxiliary quantities  $(u, v)$ :

$$\begin{pmatrix} u \\ v \end{pmatrix} = M \begin{pmatrix} \beta_1 \\ -\alpha_1 \end{pmatrix} \quad (3.7)$$

Then  $\beta_2, \alpha_2, \mu_2$  are given by:

$$\begin{aligned} \beta_2 &= \frac{1}{\beta_1} (u^2 + M_{12}^2) \\ \alpha_2 &= -\frac{1}{\beta_1} (uv + M_{12}M_{22}) \\ \mu_2 &= \mu_1 + \arctan \frac{M_{12}}{u} \end{aligned} \quad (3.8)$$

The locations of thin quadrupole slices are computed according to the Teapot slicing method (see section 2.2.3.9). The beta function  $\beta_k$  and phase advance  $\mu_k$  at each quadrupole slice are inserted in equation 3.3 in order to compute the contribution for that slice. Then the contributions of all slices are averaged in order to obtain the Jacobian column for the corresponding quadrupole<sup>3</sup>. Figure 3.12 shows the agreement of the analytical Jacobian with respect to the numerical Jacobian for the SIS18 lattice for a varying number of thin quadrupole slices. It can be observed that the agreement of the analytical Jacobian is improved already by using a small number of slices compared to the analytical Jacobian that is obtained by using the `twiss`, `centre` command from MADX or by using a single slice.

## 3.4 Experiment at the SIS18 synchrotron

### 3.4.1 Preparation

The following experimental data is collected to benchmark the theoretical findings and the simulation results. ORM, dispersion and tune measurements are conducted for two different optics at SIS18: nominal extraction optics and a modified version thereof by adjusting the  $K_1L$  value of the GS01QS1F quadrupole family (this quadrupole family includes the focusing quadrupoles from the odd numbered sections).

#### 3.4.1.1 Accelerator setting

At SIS18, the control system uses a program called ParamModi to expose the various accelerator parameters to the user in form of a Graphical User Interface (GUI). Inside this program, one can create so-called patterns and each pattern corresponds to a specific accelerator setting. These patterns can be saved for later reuse since the program also allows loading of previously saved patterns. The pattern also defines the extraction process to be used, i.e., whether fast

<sup>3</sup>The averaging is explained intuitively since the thin quadrupole slices enter the computation as a sequence of matrix multiplications and the derivative of a sequence of multiplications is additive in the derivatives of the multiplicands.

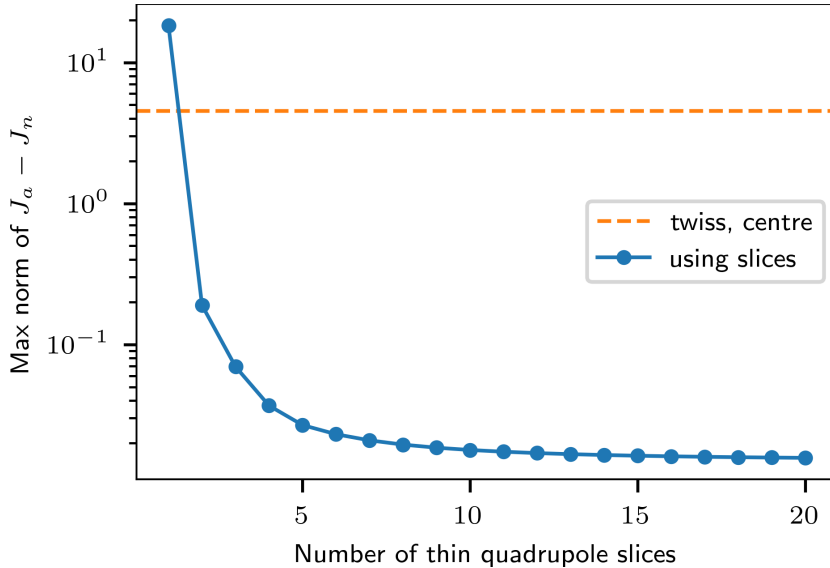


**Figure 3.12:** Improvement of the analytical Jacobian by using multiple thin slices for each quadrupole for the SIS18 lattice.  $J_a$  represents the analytical Jacobian obtained by using the indicated number of quadrupole slices and  $J_n$  represents the numerical Jacobian. The dashed line labeled `twiss, centre` represents the analytical Jacobian that is obtained from MADX by using the `centre` option for the `twiss` command. The max norm is computed as  $\max_{ij}|(J_a - J_n)_{ij}|$ .

or slow extraction should be used as well as the extraction parameters. Behind the GUI, the control of the accelerator is realized via LHC Software Architecture (LSA) which takes care of loading the parameter settings into the machine. SIS18 can replay multiple patterns in turn by dedicating one cycle to each pattern. This allows to provide beam to multiple target locations in an alternating fashion. A cycle comprises the full sequence of actions that are taken to inject, accelerate and extract the beam.

The measurement is performed with  $^{16}\text{O}^{8+}$  ions at an energy of 500 MeV per nucleon. The intensity is  $1 \times 10^9$  to  $5 \times 10^9$  particles. The harmonic number is 5 with 5 bunches in the machine. A fast extraction pattern is prepared in ParamModi with the additional beam process `RF_MANIPULATION`. Despite its name, this beam process is left empty and will only serve as the time window for the measurement of the orbit response to a single steerer. The length of that beam process determines the number of data points that can be measured for each steerer and also the resolution of the orbit at the BPMs. The goal is to acquire 5 independent measurements of orbit responses per steerer for estimation of measurement uncertainty. Each measurement takes place on a distinct cycle. When changing from one steerer to the next, the trim of the previous steerer must be reverted and an additional, unused cycle might slip in after the trim for the steerer has been reverted. Therefore, 5 to 6 cycles per steerer will be used. In order to measure all 24 steerers (12 horizontal and 12 vertical), this requires a total of  $(5 + 1) \cdot 24 = 144$  cycles. During each cycle a specific steerer will be set by applying a dedicated trim via the LSA API. This trim covers the following kick values:  $-1$  mrad,  $-0.5$  mrad,  $0$  mrad,  $0.5$  mrad and  $1$  mrad. This allows to determine the orbit response from a 5-point fit. The length of the `RF_MANIPULATION` beam process is chosen to be 11.037 s. This covers the following aspects, which are also based on experience from previous tests:



- 2 s are reserved for the beginning of the beam process since the horizontal orbit still moves during that time <sup>4</sup>.
- 256 ms are reserved for the steerer to ramp to each of the five magnetic field strengths during the trim pattern. Since for extraction the steerer kick must be back to its nominal value, an additional ramp back to 0 mrad is required at the end of the trim pattern. Thus, this requires a total of  $(5 + 1) \cdot 256 \text{ ms} = 1.536 \text{ s}$ .
- 500 ms are reserved for allowing the steerer to settle its magnetic field strength after ramping to a new value during the trim pattern. Previous experience has shown that the orbit still moves in that time window. This settling time is not necessary at the end of the beam process and, thus,  $5 \cdot 500 \text{ ms} = 2.5 \text{ s}$  are required.
- 1 s are reserved for the orbit measurement of each steerer kick value during the trim pattern (i.e., after the settling time of 500 ms). This allows for orbit resolution on the order of  $1 \mu\text{m}$ .
- 1 ms is added at the end of the beam process to allow the trim pattern to settle back to 0 mrad.

In ParamModi, the value of the `Dauer RF_MANIPULATION` parameter is therefore set to 11.037 s. During the measurement it has been realized that the horizontal orbit was moving longer than expected at the beginning of flattop and, therefore, the `Dauer RF_MANIPULATION` parameter has been increased to 13.037 s allowing for a total of 4 s margin at the beginning of the beam process. The different time windows are also visualized in Figure 3.13.

#### 3.4.1.2 Trims of LSA parameters

**Steerers** The steerer trims are prepared as a CSV file with two columns, `time_in_beam_process` and `trim_value`. The resolution of `time_in_beam_process` is 1 ms. This is the time step with which LSA will interpolate two consecutive trim values if the difference between their timestamps is greater than 1 ms. The ramp from one steerer kick value to the next must not be too steep because otherwise ParamModi will reject the trim, based on the maximal allowable ramp setting for that magnet. Thus, 256 ms are used for the ramp which is a safe value. The ramp has been realized by using the half-period of a cosine function in order to ensure the smoothness of the ramp (this is required by the horizontal steerers). Figure 3.13 shows the trim pattern which is used for the steerers.

The LSA parameters for applying the trims where `<NAME-OF-STEERER>/HKICK_COE` for the horizontal steerers and `<NAME-OF-STEERER>/VKICK_COE` for the vertical steerers. The trim is performed on `Correction` (not `Target`). The corresponding measured orbit response allows to determine the dispersion.

**RF-system** In order to measure the dispersion, the LSA parameter `SIS18BEAM/DPFREV` is trimmed in a similar fashion as the steerer kick values described in section 3.4.1.2. This parameter corresponds to the desired momentum error  $\frac{\Delta p}{p}$  and the control system computes and applies the required frequency shift. The trim values are  $\frac{\Delta p}{p} = -0.002, -0.001, 0.0, 0.001$  and  $0.002$ .

<sup>4</sup>This is because likely the bending magnets take time to attain their final magnetic field strength on flattop.

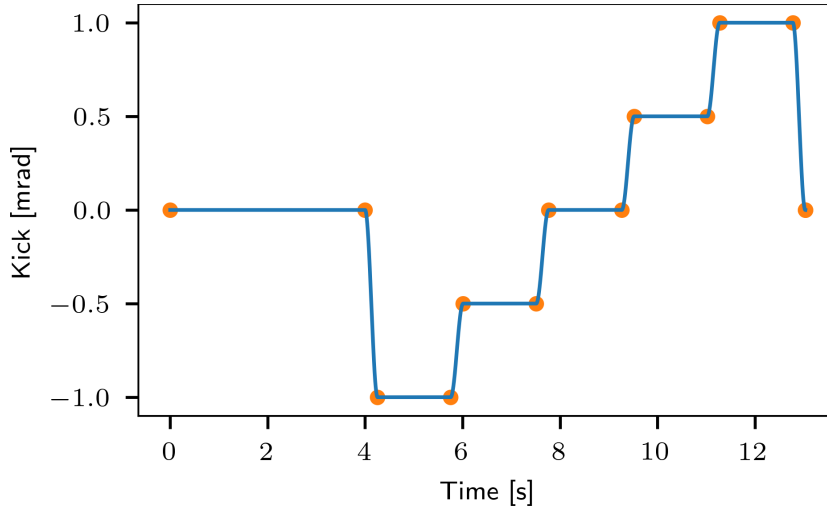


**Figure 3.13:** Steerer trim pattern that is used for trimming the steerer’s kick value via the LSA API during the measurement.

#### 3.4.1.3 Java application for automatizing the measurement

To automate the measurement, a dedicated Java App has been created which applies and reverts the various trims via the LSA Java API. The app loads the previously generated CSV file and creates a `cern.accsoft.commons.value.DiscreteFunction` from it. This function is then submitted as a `cern.lsa.domain.settings.TrimRequest`, applied to the `GsiBeamProcessPurpose.RING_RF_MANIPULATION` beam process. The app cycles through each of the 24 steerers and waits for an appropriate time that covers the 5 desired cycles per steerer before reverting the trim and applying it to the next steerer. The timestamps for each trim are saved in a log file. The Java App is available as a repository on the GSI Gitlab instance [2].

#### 3.4.1.4 Orbit measurement via TOPOS

The TOPOS app is used to collect BPM data. The start and stop triggers are set to, respectively, 45 `Flattop`<sup>5</sup> and 52 `Flattop End` with both `offset` set to zero. The gain is initially set to 40 dB and will be adjusted during the measurement by inspecting the signal intensity. The signal intensity must remain below 45 dB at all times to prevent saturation of the BPM signal. The raw BPM data (signal on the plates) is checked in TOPOS in order to verify that no saturation is present. The BPMs are set to asynchronous mode for the orbit measurement. This mode computes a single orbit value from the data points of 1024 consecutive bunch passages. This mode also greatly reduces the storage requirements for the BPM data. The data is saved in a dedicated binary format which provides information about timestamps, orbit values and signal intensity.

#### 3.4.1.5 Tune measurement via TOPOX

For the tune measurement, BPMs are set to bunch-by-bunch mode (double threshold detection). The TOPOX app is used for the measurement. This app allows to perform a frequency scan

<sup>5</sup>There is a 20  $\mu$ s offset between the trigger signal and the `RF_MANIPULATION` beam process; the signal arrives first.

around the nominal tunes by exciting the beam. The Q parameter is set to the fractional part of the nominal tune in ParamModi, the dQ parameter is set to 0.1 and the trigger is set to external (controlled by Genesys).

#### 3.4.1.6 Modification of optics

The nominal extraction optics are modified by applying a trim to the GS01QS1F quadrupole family which includes all focusing quadrupoles from odd section numbers. The corresponding LSA parameter is GS01QS1F/KL. The trim value is chosen to be  $\Delta K_1 L = -1.2 \times 10^{-3} \text{ m}^{-1}$ . The model tunes for this updated setting are  $Q_x = 4.272$  and  $Q_y = 3.296$ . Since it is known that the horizontal tune of the real machine is  $\approx 4.31$ , it is expected that this  $\Delta K_1 L$  update will cause the machine tunes to be in the vicinity of the nominal model tunes  $Q_x = 4.29, Q_y = 3.29$ . According to the simulation results from Figure 3.11, for an orbit uncertainty of order  $3 \mu\text{m}$  a change in the quadrupole strength of  $|\Delta K_1 L| > 1 \times 10^{-3} \text{ m}^{-1}$  should be resolvable. Also, it should be noted that the residuals in Figure 3.11 are obtained without mitigation of quasi-degeneracy and, thus, are mainly driven by the D-T-quadrupole pairs. With proper mitigation of quasi-degeneracy the residuals are expected to be much smaller. Hence,  $\Delta K_1 L = -1.2 \times 10^{-3} \text{ m}^{-1}$  is expected to be a safe value for the fitting of linear optics and, also, it corresponds to a tune change that is of similar magnitude than observed in the real machine.

#### 3.4.1.7 Influence of position errors of BPMs

The position of the various lattice elements of SIS18 are known with accuracy  $\lesssim 1 \text{ mm}$  due to regular survey measurements. However, the two BPMs are mounted inside a so called "Diagnosekammer" (diagnostic chamber) and while the position of that chamber is known, the position of BPMs inside that chamber is known only within a 5 mm accuracy. Therefore, it must be checked to what extent this inaccuracy might affect the results <sup>6</sup>. Figure 3.14 shows the expected variation in the orbit response and it is well below the expected measurement uncertainty. Therefore, the influence of potential BPM shifts can be neglected.

### 3.4.2 Summary of measurement

The ORM measurements were performed with 5 settings per steerer,  $-1.0 \text{ mrad}$ ,  $-0.5 \text{ mrad}$ ,  $0.0 \text{ mrad}$ ,  $0.5 \text{ mrad}$  and  $1.0 \text{ mrad}$ , during a long flattop of 11.037 s. Position data from one of the horizontal BPMs is shown in Figure 3.15. The first 2 s are skipped because the horizontal orbit still drifted during that time window; this is likely because of the bending magnets taking long time to attain their nominal strength. However, during the measurement it has been observed that the horizontal orbit was still drifting at the end of the 2 s window and, therefore, the margin has been increased to 4 s resulting in a total flattop length of 13.037 s. The long flattop duration allowed for long data integration windows of up to 1 s for each steerer setting in order to reduce the measurement uncertainty. From that 1 s window, the first 950 ms are used for data analysis. Also, sufficient time, 256 ms, was allocated for transitioning between two steerer settings plus an additional 500 ms to allow the steerers to attain the new values.

<sup>6</sup>If the inaccuracy was too large, it could also be included as a separate fit parameter

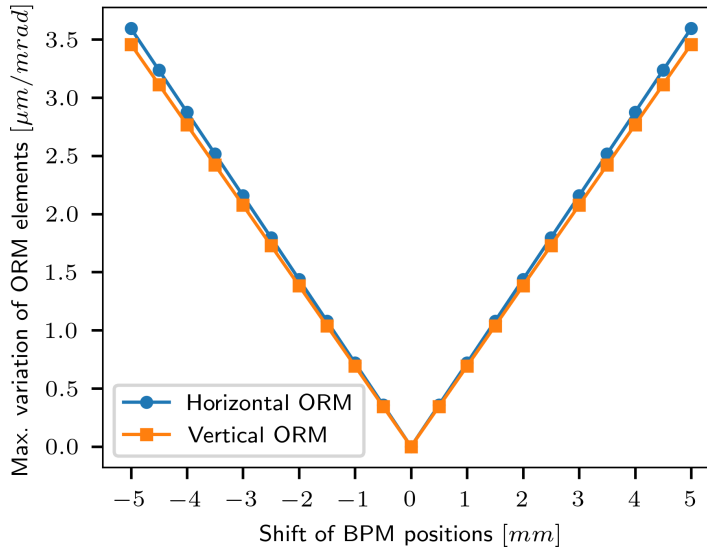


**Figure 3.14:** Maximal variation of the orbit response for the horizontal and vertical ORM block due to a shift of the position of, respectively, the horizontal and vertical BPMs.

The ORM, dispersion and tunes have been measured for two optics, the nominal extraction optics and a modified version thereof with the GS01QS1F quadrupole family adjusted by  $\Delta K_1 L = -1.2 \times 10^{-3} \text{ m}^{-1}$ . Due to the limited experimental time available (1 shift, i.e., 8 hours), the beta beating could not be measured, unfortunately. Nevertheless, the tune measurements serve as a verification for the derived quadrupole errors. For the measurement of modified optics, the horizontal BPM in section 8 malfunctioned and, thus, had to be removed from the subsequent analysis.

#### 3.4.3 Orbit measurement

Figure 3.15 shows example position data obtained from the horizontal BPM in section 1 in response to the horizontal steerer in section 5. The steerer kick values are overlaid for comparison. Figure 3.16 shows example position data in response to the vertical steerer in section 1 together with the frequency spectrum obtained via Fast Fourier Transform (FFT). Various noise lines are visible, for example the 50 Hz line due to the operating frequency of the electrical grid.

##### 3.4.3.1 Orbit drift at beginning of flattop

The orbit drift at beginning of flattop was most pronounced for the horizontal BPMs and it varied from BPM to BPM. Also, for the vertical BPMs an orbit drift could be observed, albeit of much smaller magnitude. Figure 3.17 shows the drift for different BPMs when no steerer was trimmed. In the vertical data, the drifts are up to  $20 \mu\text{m}$  and for an orbit response of similar magnitude this will introduce a small yet noticeable bias ( $\approx 10 \mu\text{m}/\text{mrad}$ ).

##### 3.4.3.2 Orbit stability during flattop

From Figure 3.17 it becomes already apparent that the orbit stability during the foreseen measurement window, which starts 2 s (nominal optics) and 4 s (modified optics) respectively after the beginning of the beam process, is influenced by orbit drifts but also by the fluctuation

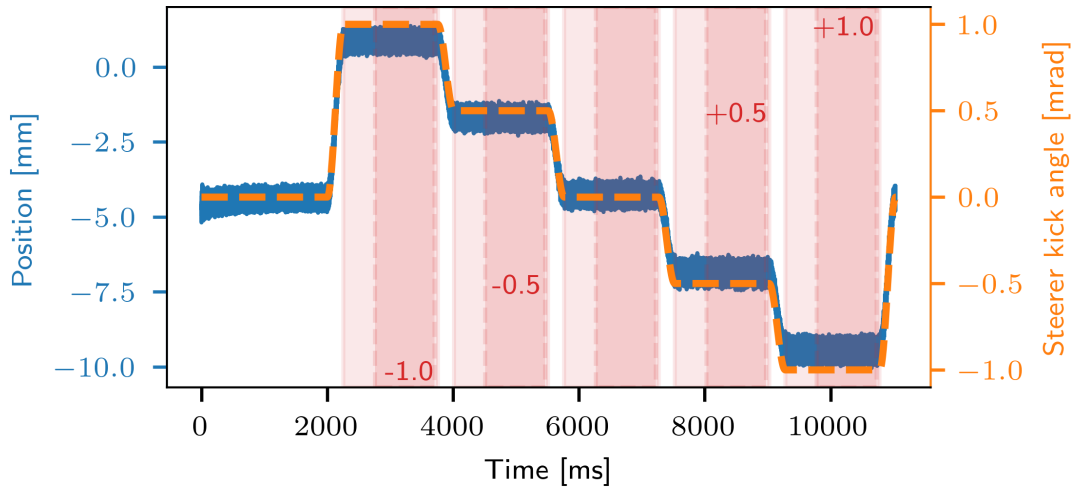


**Figure 3.15:** Position data from the horizontal BPM in section 1 during measurement of the horizontal steerer in section 5. The steerer setting is overlaid as the dashed curve (the curve is inverted for better visibility). The two vertical axes are not aligned, i.e., there is no meaning in the vertical position of the steerer relative to the position data. The red shaded areas indicate the time windows available for orbit computation. The light shaded area (500 ms) has been excluded because the orbit was still slightly drifting during those time windows. The solid shaded area (950 ms) is used for orbit computation. The white area between two shaded areas is the allocated transition time for the steerer magnets which is 256 ms. An additional 2s are skipped at the beginning of flattop because the horizontal orbit was still drifting during that time window. This margin was later during the measurement increased to 4 s. [75]

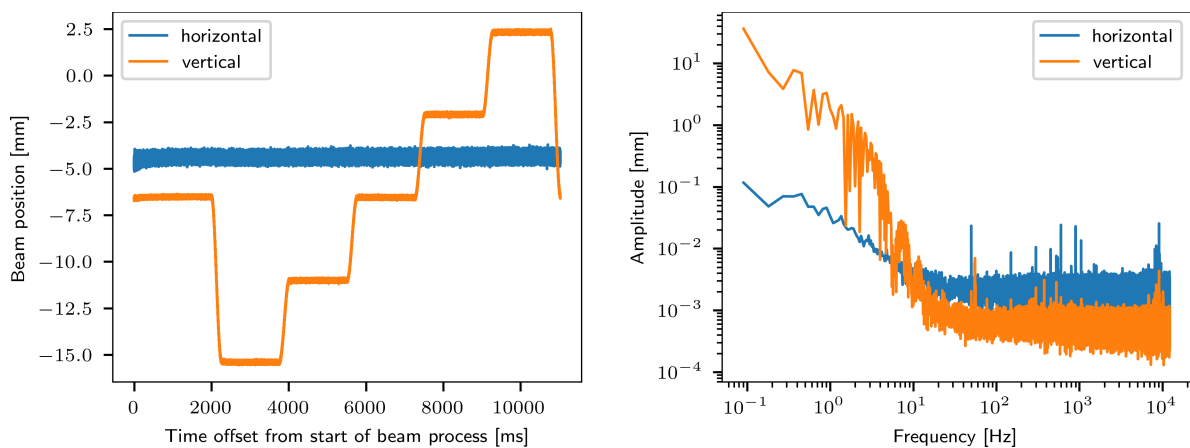
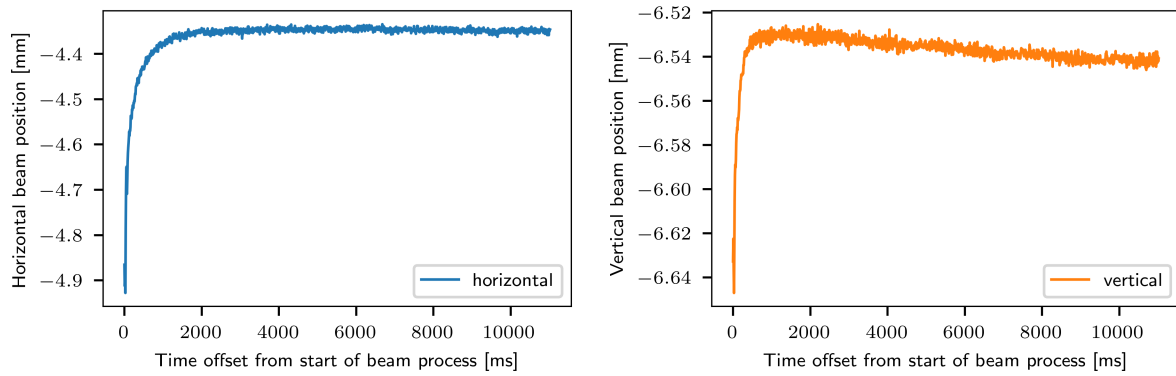
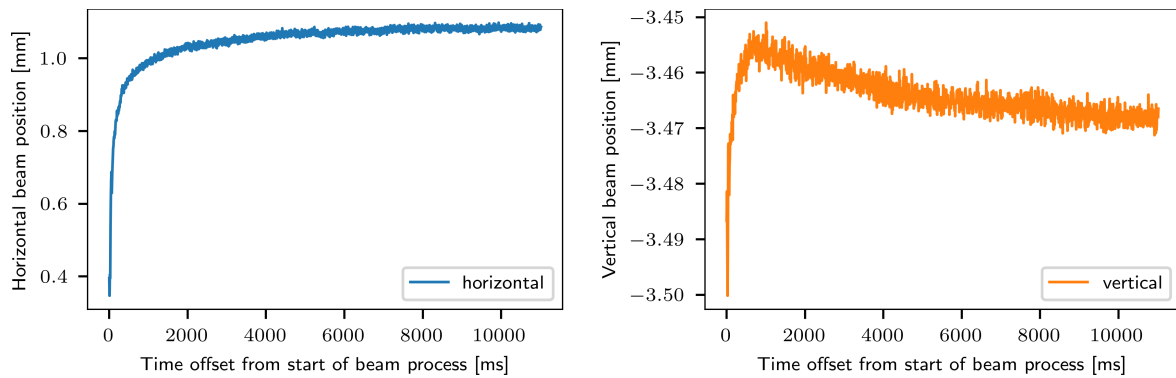


**Figure 3.16:** Left: Position data from the horizontal and vertical BPM in section 1 during measurement of the the vertical steerer GS01KM2DV also in section 1. Right: The corresponding frequency spectrum obtained via FFT. For example, the line at 50 Hz due to the power supply being connected to the electrical grid is clearly visible.

### 3. Estimating quadrupole errors in the presence of degeneracy for the SIS18 synchrotron



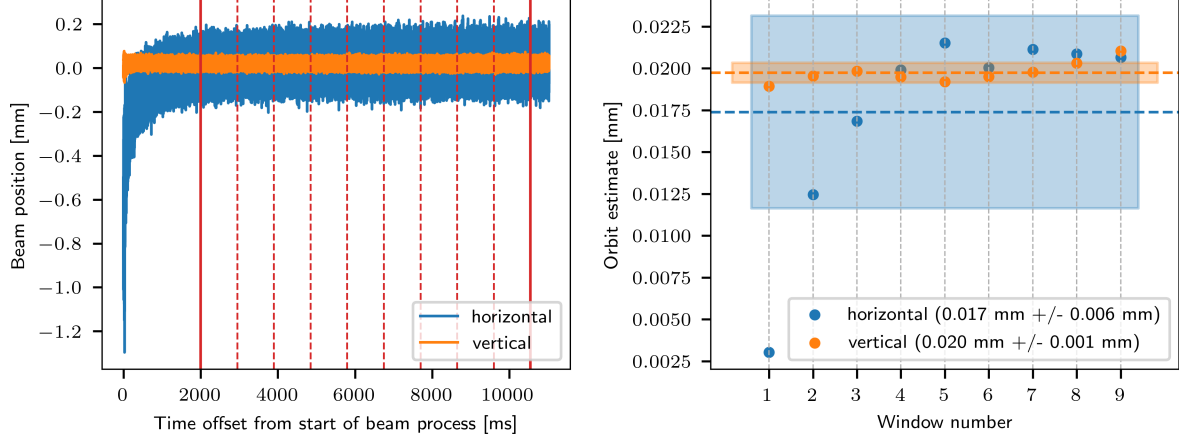
(a) BPM in section 1.



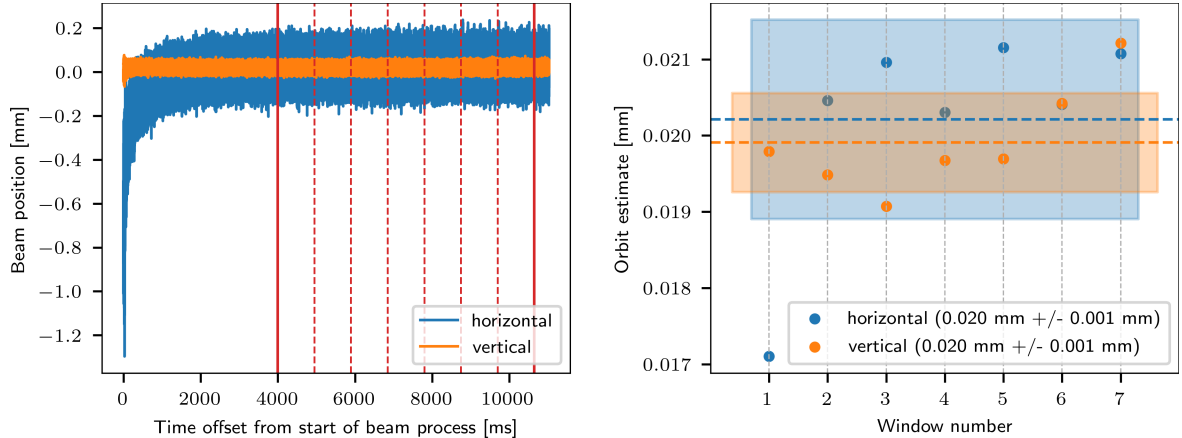
(b) BPM in section 2

**Figure 3.17:** Position data from the horizontal BPMs in sections 1 and 2. The BPM data has been averaged over 1000 consecutive data points, i.e., each data point in the plot corresponds to about 8 ms.

of BPM data. The stability of the orbit measurement is assessed by computing orbit estimates from the remaining time window divided into sub-windows such that each sub-window has the foreseen length of 950 ms. This is achieved by selecting a window from 2.000 ms to 10.550 ms and dividing it into 9 intervals or by selecting a window from 4.000 ms to 10.650 ms and dividing it into 7 intervals as shown in Figure 3.18.



(a) 2 s margin at beginning of flattop.



(b) 4 s margin at beginning of flattop.

**Figure 3.18:** Left: Position data from the horizontal and vertical BPM in section 6 during flattop. The red dashed lines show the 9 intervals of length 950 ms for which the orbit has been computed. Right: The corresponding orbit estimates from the 9 intervals. The shaded area indicates the standard deviation, i.e., the  $\pm 1\sigma$  range.

### 3.4.4 ORM measurement

Due to the significant orbit drift at the beginning of flattop beyond the initial 2 s margin (see Figures 3.17 and 3.18), the first steerer kick value must be dropped for the measurement data for nominal extraction optics. This will add an additional  $0.256\text{ s} + 0.5\text{ s} + 1\text{ s} = 1.756\text{ s}$  margin and, thus, reduce the influence of the orbit drift. For the modified optics the margin had been increased to 4 s, so all 5 steerer kick values can be used.

For each machine cycle, the orbit response  $r_c$  is computed from a least squares fit of the 4 or 5 corresponding steerer kick values. The final response  $r$  is computed as the average over the 5 consecutive cycles which were allocated for each steerer. The orbit response from each cycle is inversely weighted with its squared standard error  $\sigma_c$  from the least squares fit of the

### 3. Estimating quadrupole errors in the presence of degeneracy for the SIS18 synchrotron

---

respective response  $r_c$ :

$$r = \frac{1}{\sum_c \frac{1}{\sigma_c^2}} \sum_c \frac{r_c}{\sigma_c^2} \quad (3.9)$$

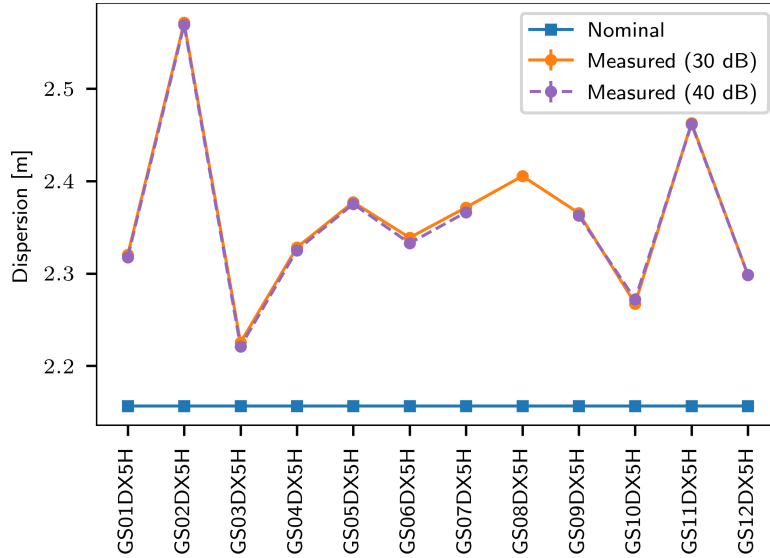
A measurement uncertainty of  $\lesssim 4 \mu\text{m}/\text{mrad}$  has been achieved for the orbit response, with minor variations among the different BPMs. The measurement uncertainty is dominated by the cycle-to-cycle variation as a BPM resolution of  $\lesssim 1 \mu\text{m}$  has been achieved. Figure 3.19 shows the measured ORM for nominal extraction optics. Compared to the simulated ORM from Figure 3.2, it can be observed that the general structure of the ORM is represented by the measured data. The section-to-section symmetry of the horizontal (except for sections 4 and 6) and vertical dimension is reflected and the indicated coupling is weak.



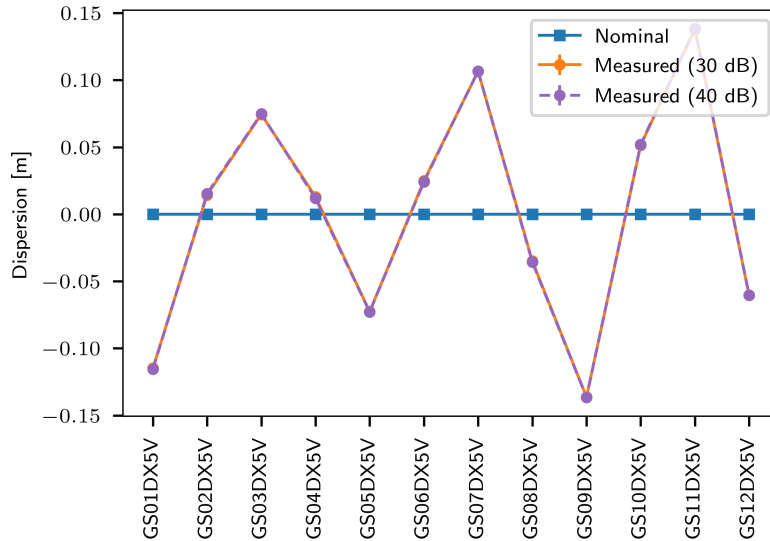


### 3.4.5 Dispersion measurement

Figure 3.20 shows the measured dispersion as well as the model dispersion before and after fitting the ORM. The dispersion has not been included in the fitting.



(a) Horizontal dispersion. For the gain setting 40 dB the horizontal BPM in section 8 malfunctioned and is thus not shown in the plot.



(b) Vertical dispersion. The nominal dispersion is zero because the model is free of coupling.

**Figure 3.20:** Comparison of measured dispersion and model dispersion. The data has been recorded at 30 dB and 40 dB gain setting in TOPOS. The measurement error is on the order of  $1 \times 10^{-3}$  m and, thus, not visible in the plot.

### 3.4.6 Tune measurement

The measured tunes are shown in Figure 3.21. The following values have been measured:

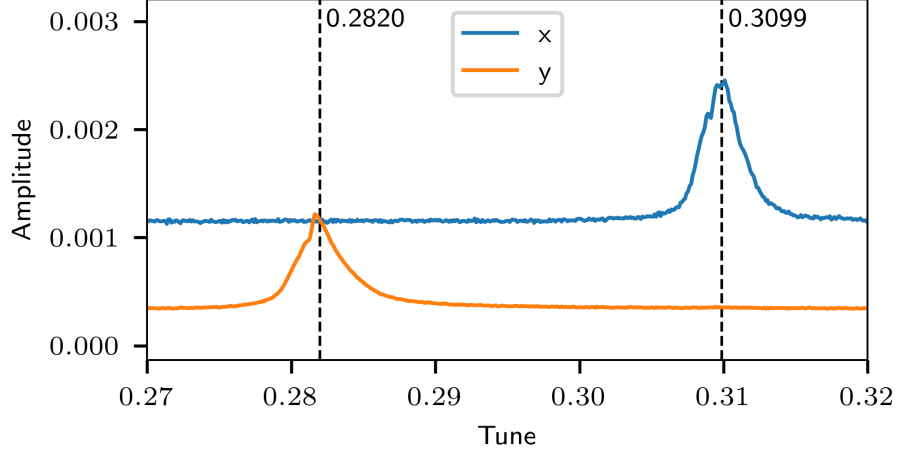
1. Nominal extraction optics:

- $q_h = 0.3099 \pm 0.0014$

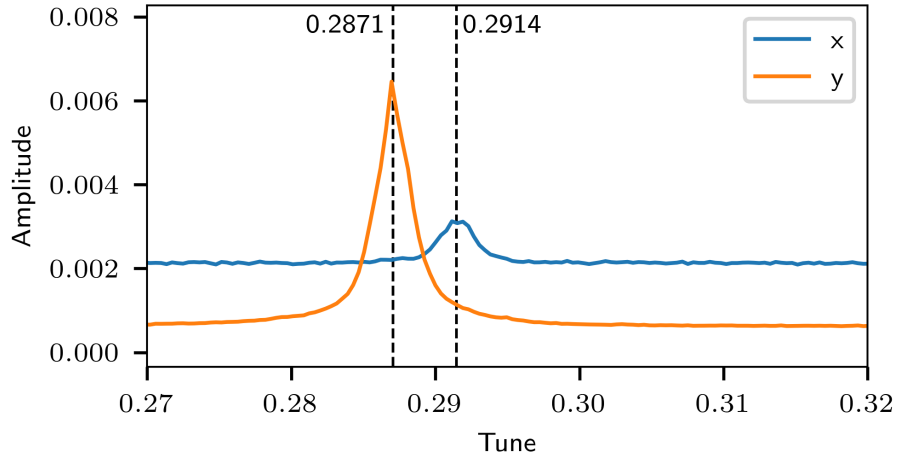
- $q_v = 0.2820 \pm 0.0011$

2. Modified extraction optics:

- $q_h = 0.2914 \pm 0.0008$
- $q_v = 0.2871 \pm 0.0007$



(a) Nominal extraction optics. The model tunes are  $Q_h = 4.290$  and  $Q_v = 3.290$ .



(b) Modified extraction optics. The model tunes are  $Q_h = 4.273$  and  $Q_v = 3.295$ . The measurement for modified optics was performed on a reduced time scale of 6 s to limit the amount of position data generated.

**Figure 3.21:** Measurement of tunes for the two different optics. [75]

### 3.4.7 Fitting of quadrupole errors

Since linear coupling at SIS18 is generally corrected well, the analytical expression for the Jacobian can be used for fitting. The results are compared to those obtained by using the numerical Jacobian based on finite-difference approximation. The quadrupole errors are estimated with Levenberg-Marquardt optimizer. Different approaches for mitigating the quasi-degeneracy are tested in conjunction with the analytical Jacobian approach.

To obtain meaningful results that can be compared, it is important to mitigate the quasi-degeneracy which is mainly driven by the D-T-quadrupole pairs. The methods SVD cutoff, adding  $\Delta K_1 L$  constraints to the Jacobian, and leaving out T-quadrupoles from the fitting are

### 3. Estimating quadrupole errors in the presence of degeneracy for the SIS18 synchrotron

compared in terms of their results. The removal of T-quadrupoles is justified since they attain small strengths during extraction optics and, thus, much smaller errors are expected for this quadrupole family. For comparison, the results obtained without any method for counteracting quasi-degeneracy are referred to as *baseline method*.

For each of the methods, the difference in estimates between the two optics for the F-quadrupoles is presented; that is, the estimates obtained for modified optics subtracted by the estimates obtained for nominal optics. Both estimates are obtained by starting the fitting procedure from the nominal optics model. Ideally, this difference of estimates should be a zigzag pattern between  $-1.2 \times 10^{-3} \text{ m}^{-1}$  and  $0 \text{ m}^{-1}$  since the GS01QS1F family contains every second F-quadrupole (i.e., the ones from odd section numbers).

Figure 3.22 shows the quadrupole error estimates when fitting all quadrupoles together without mitigating quasi-degeneracy. Figure 3.23 shows the quadrupole error estimates when fitting without T-quadrupoles. This removes the quasi-degeneracy from the system.

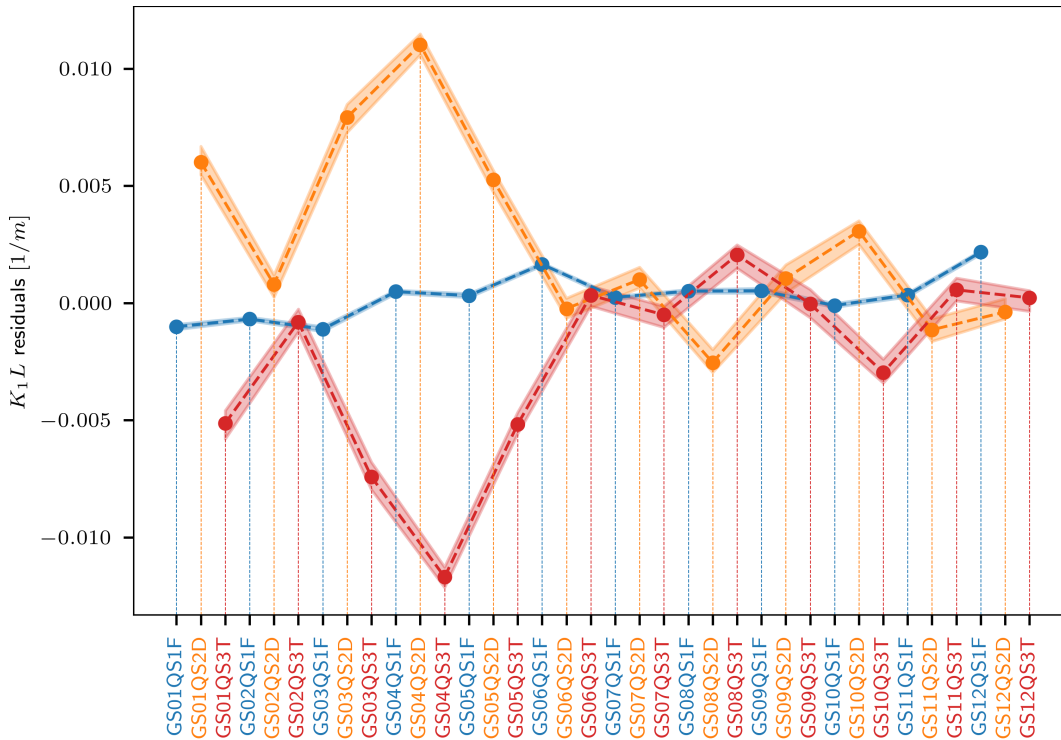


**Figure 3.22:** Estimated quadrupole errors when all quadrupoles are included in the fit. The quasi-degeneracy between D- and T-quadrupoles is clearly visible. The shaded areas indicate the uncertainty of the estimated quadrupole errors.

#### 3.4.7.1 SVD cutoff

This is performed as a two stage process. The first stage uses Levenberg-Marquardt to find a (quasi-degenerate) solution for all the involved parameters: quadrupole errors and gain errors. The second stage freezes the thus found gain errors and restarts fitting of quadrupole errors. During each update step, the system  $J^T J \Delta p = J^T r$  (where  $\Delta p$  is the parameter update and  $r$  the residual vector) is solved by computing  $(J^T J)^{-1}$  via SVD and truncating a predefined number of smallest singular values to zero. If the SVD spectrum shows a clear drop in the magnitude of singular values then cutting the small singular values will be very efficient.

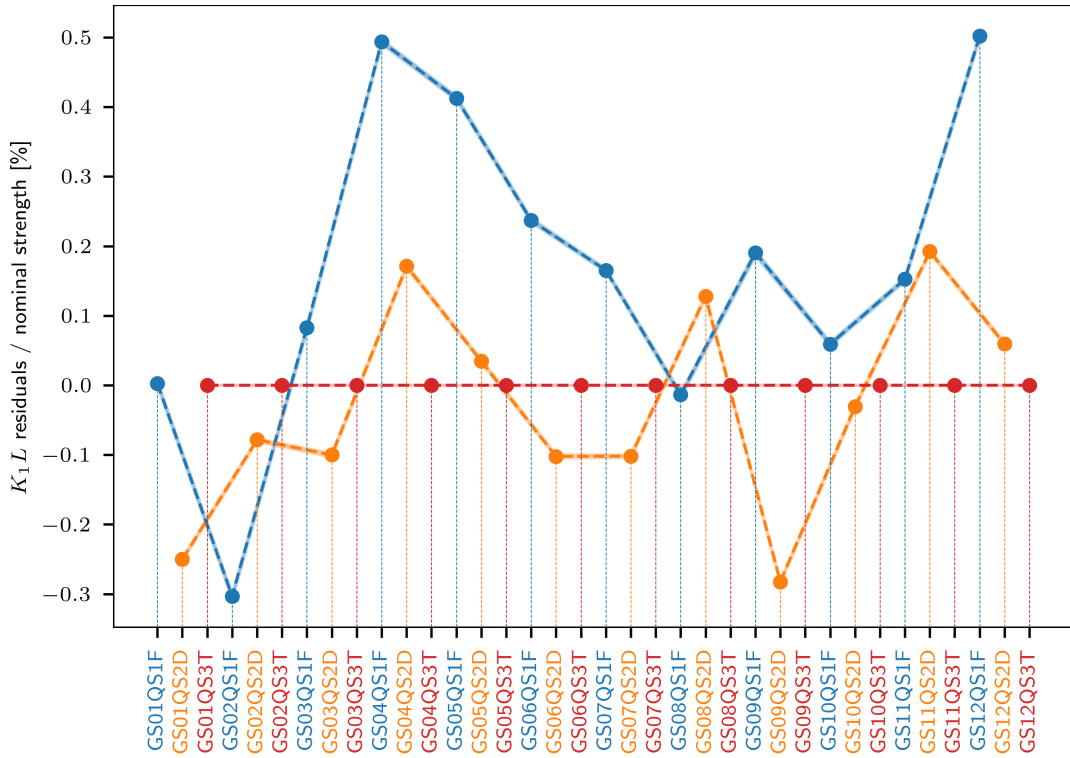


**Figure 3.23:** Estimated quadrupole errors when the T-quadrupoles are not fitted. This eliminates the quasi-degeneracy between D- and T-quadrupoles. The shaded areas indicate the uncertainty of the estimated quadrupole errors. Since the uncertainty of the estimated quadrupole errors is small in this case, it is only slightly visible.

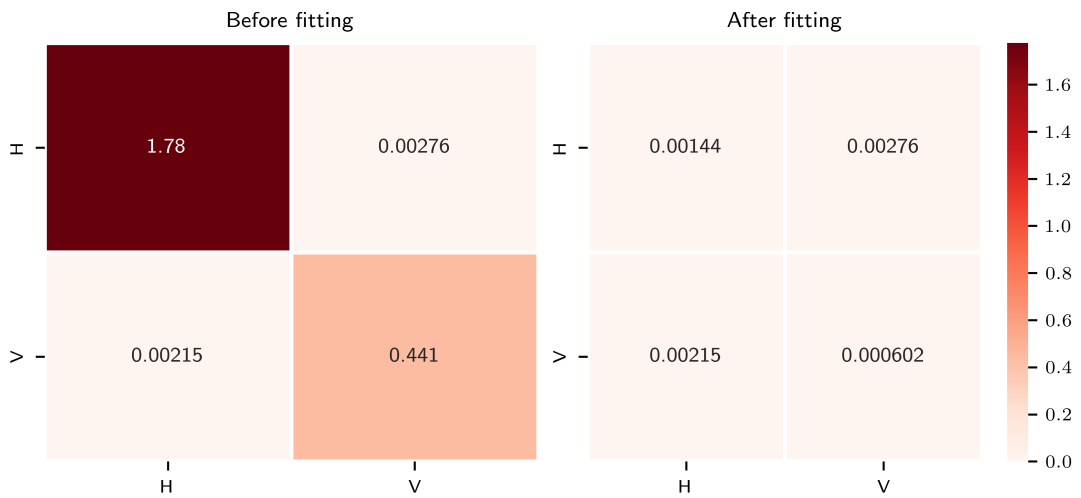


**Figure 3.24:** Mean squared error of the diagonal and coupling blocks of the simulated ORM with respect to the measured ORM before (left) and after (right) fitting. The convergence of the fitting is clearly visible by the reduction of the mean squared error.

### 3. Estimating quadrupole errors in the presence of degeneracy for the SIS18 synchrotron

However, for a more flat spectrum the number of singular values to cut is not obvious and also the resulting estimate might suffer from the truncation. This strongly depends on the use case and the investigated lattice. The optimal cutoff value can be found from simulations, where random orbit uncertainties are cast on the nominal ORM and then inverse modeling with different cutoff values is performed. The one that yields the smallest error in terms of the quadrupole error estimates is then chosen. For the present use case, it has been found that the best results are obtained when the number of cut values is set to 11.

#### 3.4.7.2 $\Delta K_1 L$ weights

This approach adds weights to the Jacobian as described in [74]. The purpose of the weights is to limit the amount of change in the  $\Delta K_1 L$  parameters during each iteration of the fitting process. The pattern of weights  $w$  is determined at every iteration by the following relationship:

$$\mathbf{w} = \sum_{i=1}^N \frac{1}{\lambda_i} \mathbf{v}_i \quad (3.10)$$

where  $\lambda_i$  and  $\mathbf{v}_i$  are, respectively, the  $i$ -th eigenvalue and eigenvector of the  $\hat{J}^T \hat{J}$  matrix originating from the Jacobian  $\hat{J}$  that represents only the  $\Delta K_1 L$  parameters and which is evaluated at zero gain errors. Then  $w_k$  is the weight for the  $k$ -th quadrupole. The magnitude of  $\mathbf{w}$  is chosen a priori by a scan over different possible values and then fixed for every iteration. It should be emphasized that for this approach, the nominal gain Jacobian  $\hat{J}$  has been used not only for the computation of the weights but it also replaced the  $\Delta K_1 L$  part of the actual Jacobian  $J$  which is evaluated at the current gain error estimate during each iteration. This is done because when using  $J$ , the estimated gain errors would obfuscate the degeneracy pattern of the quadrupoles at every iteration. Using  $\hat{J}$ , on the other hand, allows to directly access the quasi-degeneracy patterns and, thus, limit them by adding corresponding weights. Using  $\hat{J}$  in place of  $J$  does not hinder convergence as their agreement is sufficiently close.

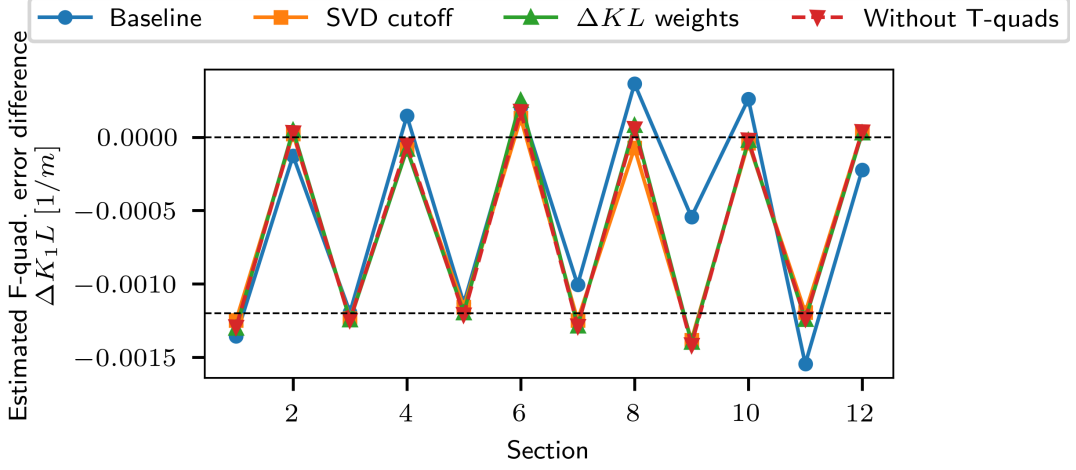
#### 3.4.7.3 Leaving out T-quadrupoles

Since the magnitude of T-quadrupole strengths is one order of magnitude smaller than the one of other quadrupoles, their errors are expected to be similarly smaller. Hence, leaving out T-quadrupoles from the fitting will alter the estimates of other quadrupoles (mainly D-quadrupoles) only by a relatively small amount.

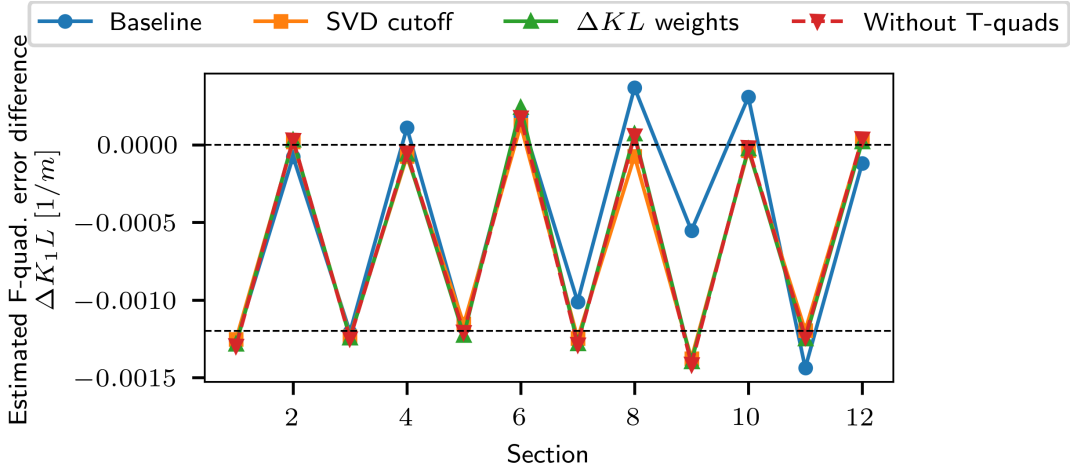
#### 3.4.7.4 Comparison

Figure 3.25 shows a comparison between the three abovementioned strategies for counteracting quasi-degeneracy. Since the quasi-degeneracy is mainly driven by the D-T-quadrupole pairs, and T-quadrupoles have a one order of magnitude smaller nominal strength, leaving out the T-quadrupoles from the fit is expected to effectively eliminate the quasi-degeneracy while yielding accurate results (i.e., close to the actual errors). The method of adding  $\Delta K_1 L$  constraints to the cost function proves similarly efficient as it yields very similar results. The SVD cutoff method shows a slight deviation, mainly because the singular value spectrum is rather flat and removing too many singular values also removes too much information from the Jacobian. The

same figure also shows the results obtained with the numerically computed Jacobian. It can be seen that these results closely match the results obtained with the analytical Jacobian. The SVD cutoff method shows a slight deviation between the two methods because the singular value spectrum of the two Jacobian versions is slightly different.



(a) Results obtained by using the analytical Jacobian.



(b) Results obtained by using the numerical Jacobian.

**Figure 3.25:** Comparison of inverse modeling results for the F-quadrupoles when using different methods for counteracting quasi-degeneracy. The plots show the difference in estimates for the modified optics and the nominal optics. The two optics differ by the manual adjustment of odd section number F-quadrupoles by  $\Delta K_1 L = -1.2 \times 10^{-3} \text{ m}^{-1}$ . All other quadrupoles, including the F-quadrupoles from even section numbers, have not been modified. The dashed lines indicate the expected (ideal) estimates for the quadrupole errors. The label *Baseline* refers to the results obtained from Levenberg-Marquardt fitting without any countermeasure against the quasi-degeneracy. The error bars due to ORM uncertainty are on the order of  $1 \times 10^{-5} \text{ m}^{-1}$  and, thus, are not visible in the plot. [75]

Table 3.2 and Figure 3.26 show an overview of the measured tunes as well as the tunes obtained from the inverse modeling results with the different methods. It can be observed that for all methods except SVD cutoff, the predicted model tunes after fitting match the measured tunes within the measurement uncertainty. The predicted horizontal tune from the SVD cutoff method has a deviation of up to  $\approx 3\sigma$  from the measured horizontal tune. This is due to the rather flat singular value spectrum. The agreement of predicted with measured tunes confirms that the fitted models capture the global optics of the real machine. It also emphasizes the

### 3. Estimating quadrupole errors in the presence of degeneracy for the SIS18 synchrotron

effect of quasi-degeneracy, since also the baseline method reproduces the measured tunes closely albeit the  $\Delta K_1 L$  predictions deviate significantly as can be seen from Figure 3.25.

#### 3.4.8 Fitting of gain errors

For the nominal optics measurement, the gain errors obtained from fitting the orbit response matrix (see Figure 3.19) are shown in Figure 3.27. There are three things to be noted. First, the BPMs consistently show a positive gain error, i.e., the observed response is too strong compared to the model. The sensitivity of the  $50\ \Omega$  terminated system which is used for the BPMs depends on the beam frequency spectrum as explained in [85]. The frequency dependency of the SIS18 BPMs is shown in Figure 3.28 [86]. The relevant frequency is about 20 MHz <sup>7</sup> and, thus, the sensitivity of the BPMs is about  $S_{real} = (140\ \text{mm})^{-1}$ . The set sensitivity values have been derived during the calibration of the old high-impedance-based system and for that reason they deviate from the sensitivity of the  $50\ \Omega$  system which has been installed in February 2021. The set sensitivity values of the BPMs are  $S_{set} = (170\ \text{mm})^{-1}$  [88]. The following relationship describes the dependency of the measured BPM signal  $\Delta V/\Sigma V$  on the position sensitivity  $S_{real}$  of the system and on the transverse beam position  $x_{beam}$  [87]:

$$\frac{\Delta V}{\Sigma V} = S_{real} x_{beam} \quad (3.11)$$

The beam position is thus inferred as the measured signal divided by the assumed sensitivity  $S_{set}$  which is set in the BPM system:

$$x_{inferred} = \frac{1}{S_{set}} \frac{\Delta V}{\Sigma V} = \frac{S_{real}}{S_{set}} x_{beam} \quad (3.12)$$

Thus, the gain error  $e_b$  of the BPMs is determined by:

$$e_b = \frac{S_{real}}{S_{set}} - 1 \quad (3.13)$$

For the above values of the sensitivity, the gain error evaluates to about 0.21. This is larger than the estimated gain error but, nevertheless, the tendency is correctly reflected.

In addition, it can be observed that the horizontal steerers consistently show a noticeable positive gain error, i.e., the applied kicks appear too strong when compared to the model. Also, it can be observed that the vertical steerer in section 11 has a gain which is significantly lower than those of other vertical steerers; this has been observed in [38, Fig. 3.16(b)] as well.

#### 3.4.9 Fitting with dispersion

When the dispersion is included in the fitting process, the resulting predicted dispersion from the fitted model agrees better to the measured dispersion as can be seen from Figure 3.29. Some deviation however remains which suggest that additional, albeit small, model bias is present in the real machine as compared to the model, possibly resulting from field errors of the bending magnets. The resulting quadrupole error estimates change only to a small degree when the dispersion is included in the fitting (compare Figures 3.23 and 3.30).

<sup>7</sup>The relevant frequency range depends on the longitudinal charge distribution, i.e., the bunch length for a Gaussian distribution [87].



**Table 3.2:** Resulting tunes from the various fitting methods compared to measured tunes.

|                     |                        | Nominal optics |        | Modified optics |        |
|---------------------|------------------------|----------------|--------|-----------------|--------|
|                     |                        | $q_h$          | $q_v$  | $q_h$           | $q_v$  |
| Measured            | value                  | 0.3099         | 0.2820 | 0.2914          | 0.2871 |
|                     | uncertainty            | 0.0014         | 0.0011 | 0.0008          | 0.0007 |
| Analytical Jacobian | Baseline               | 0.3098         | 0.2819 | 0.2920          | 0.2876 |
|                     | SVD cutoff             | 0.3129         | 0.2822 | 0.2949          | 0.2879 |
|                     | $\Delta K_1 L$ weights | 0.3095         | 0.2819 | 0.2918          | 0.2876 |
|                     | Without T-quads        | 0.3094         | 0.2819 | 0.2917          | 0.2876 |
| Numerical Jacobian  | Baseline               | 0.3100         | 0.2824 | 0.2917          | 0.2876 |
|                     | SVD cutoff             | 0.3128         | 0.2822 | 0.2948          | 0.2879 |
|                     | $\Delta K_1 L$ weights | 0.3095         | 0.2819 | 0.2918          | 0.2876 |
|                     | Without T-quads        | 0.3094         | 0.2819 | 0.2917          | 0.2876 |

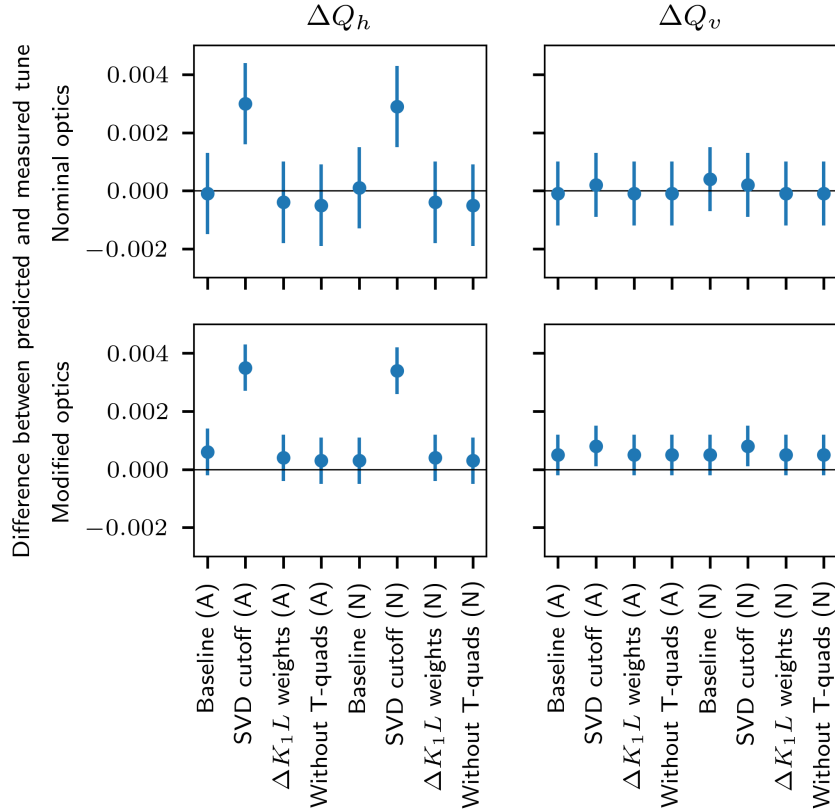


**Figure 3.26:** Difference between predicted and measured tunes for the various optics and inverse modeling methods. Top:  $\Delta Q_h, \Delta Q_v$  for nominal extraction optics. Bottom:  $\Delta Q_h, \Delta Q_v$  for the modified optics. The different methods are indicated on the horizontal axis and are the same for each subplot. (A) and (N) denote, respectively, the usage of analytical and numerical Jacobian. The vertical bars indicate the measurement uncertainty. [75]

### 3. Estimating quadrupole errors in the presence of degeneracy for the SIS18 synchrotron

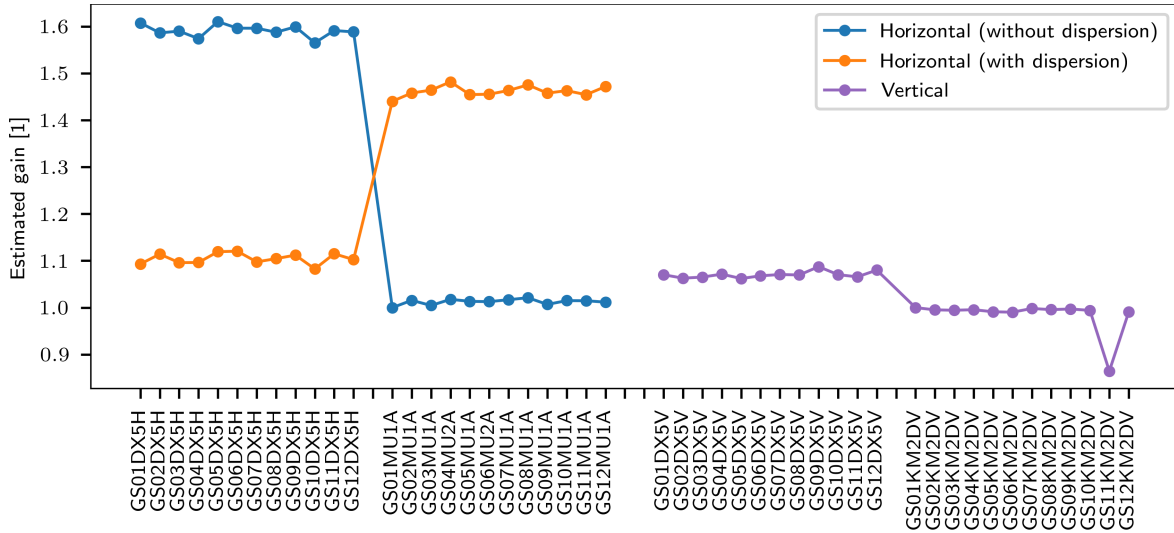
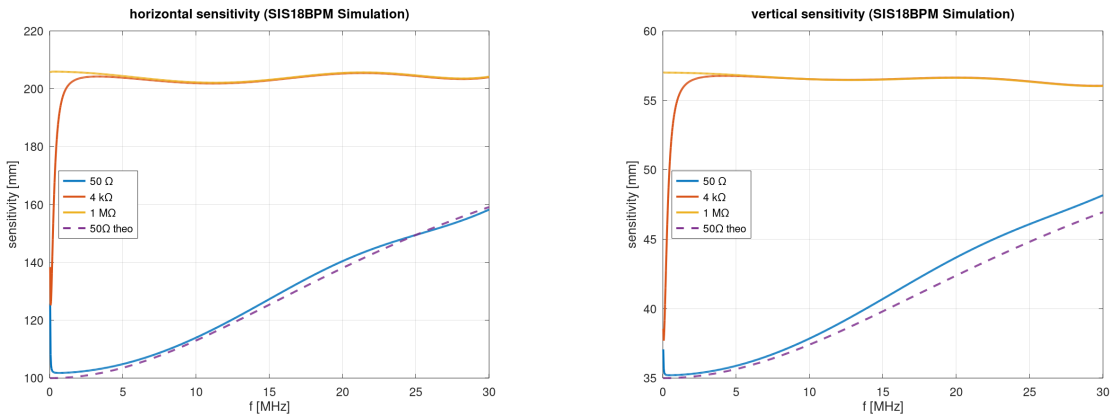


**Figure 3.27:** Estimated BPM and steerer gain errors from fitting the ORM for nominal extraction optics. The horizontal gain errors have been obtained from fitting the ORM with and without including the dispersion. The vertical gain errors have been normalized such that the steerer in section 1 has nominal gain. A similar normalization has been applied for the non-dispersion estimated horizontal gain errors.



(a) Inverse sensitivity  $1/S_x$  for the horizontal SIS18 BPMs.

(b) Inverse sensitivity  $1/S_y$  for the vertical SIS18 BPMs.

**Figure 3.28:** The inverse sensitivity  $1/S$  for the horizontal and vertical SIS18 BPMs [86, Courtesy of T. Reichert]. The values have been obtained from simulations while the dashed curve shows the theory values according to [85].

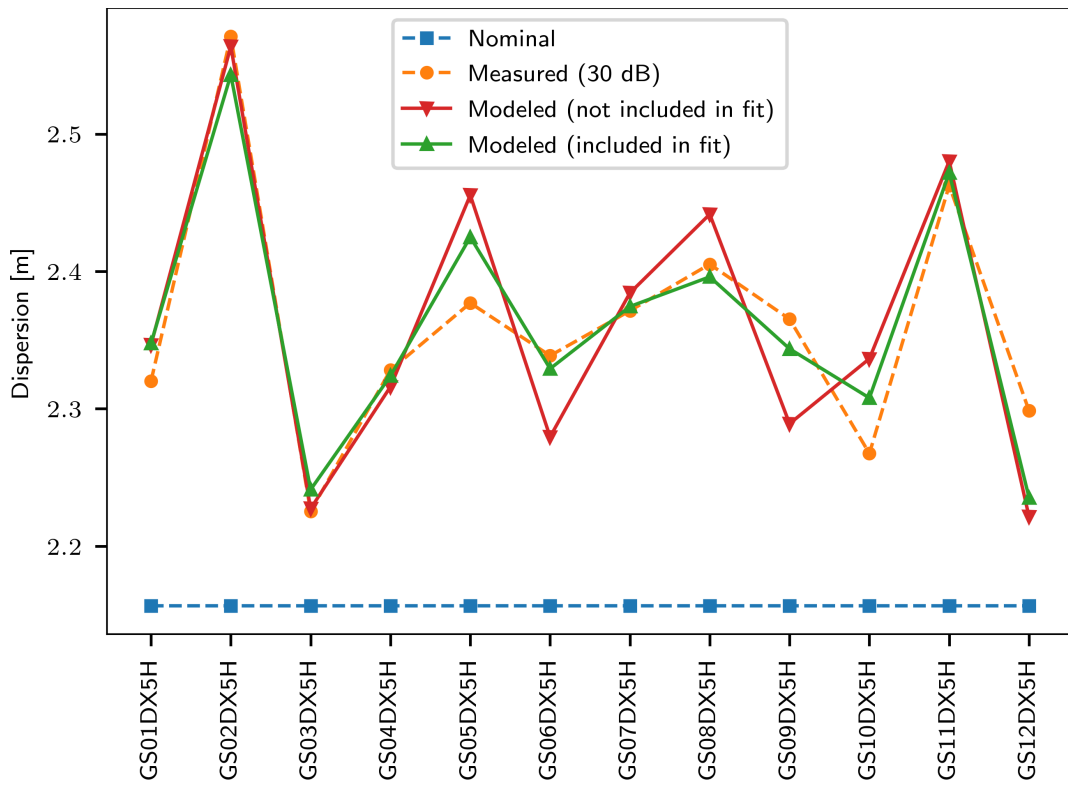


**Figure 3.29:** Measured and estimated dispersion after fitting the ORM with and without the dispersion.

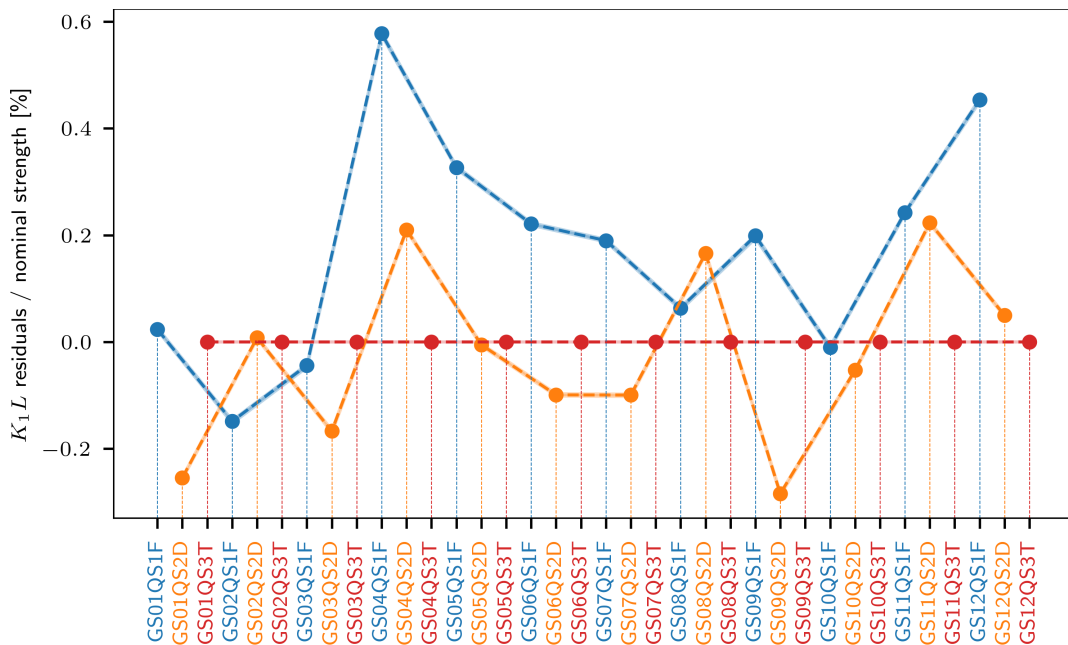


**Figure 3.30:** Estimated quadrupole errors when the T-quadrupoles are not fitted. This eliminates the quasi-degeneracy between D- and T-quadrupoles. The dispersion is included in the fit.



# 4

## Mitigating the effect of quadrupole errors on beam transfer lines with robust optimization

Multipurpose beamlines are used to provide beams to multiple target stations within the beam transport system downstream of a synchrotron. For example, at GSI the beam transport system comprises a complex network of bifurcating beamlines which share multiple common segments and, thus, share a common set of quadrupoles for delivering the beam in an alternating fashion. Figure 4.1 shows a schematic of the GSI High Energy Beam Transport (HEST) system including the various experimental targets and the beamlines that connect them. Such beamlines are usually underconstrained in terms of the feasible quadrupole settings. This means that a beamline has more degrees of freedom — the quadrupoles' strengths — than necessary to achieve the desired beam parameters at its end as well as to minimize beam losses. Because of this underconstrained property, there are many solutions for the quadrupoles' strengths which can be used to satisfy the constraints imposed by the desired beamline performance and the desired beam parameters. Even though the set of constraints may strongly limit the available space of quadrupole configurations, usually, there are still many configurations which can satisfy the constraints. This means that there is no single optimal way in terms of the quadrupoles' strengths to operate such a beamline. Rather, the beamline may be operated with a variety of configurations for the quadrupoles' strengths. However, these specific configurations are non-obvious and, typically, are found by a rather manual procedure and by relying on the experience of accelerator physicists and operators.

Besides the need for a functional quadrupole configuration to successfully operate the beamline, there are additional aspects which may influence the performance of a beamline. These are described in the following. During operation, multipurpose beamlines must regularly change their quadrupole configuration in order to allow beam transfer to different target stations. Therefore, the magnetic hysteresis, if not canceled, will affect the actual strengths of quadrupoles. Also, other effects like thermal drifts of power converters may influence the

#### 4. Mitigating the effect of quadrupole errors on beam transfer lines with robust optimization

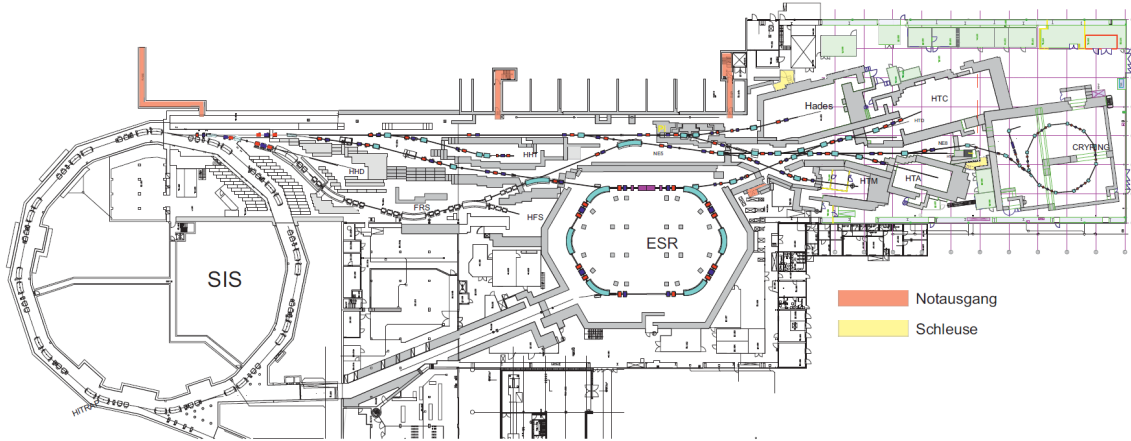


**Figure 4.1:** Schematic of the HEST network of beamlines together with SIS18, ESR and CRYRING [89, Bildrechte: GSI Helmholtzzentrum für Schwerionenforschung GmbH]. The pion production target is part of the HADES beamline which runs along the top of the schematic and it is marked in yellow with "Pi". The TH2DFA screen is located right before the two quadrupoles at the upstream bifurcation point.

effective strength of quadrupoles. These effects result in beamline optics of the real machine which are different from the design values and, typically, it will lead to a degradation of the desired beam properties, especially at the experimental target. This means that even if the used quadrupole configuration has yielded good results during simulations of the beamline, the results obtained on the real beamline may be very different. This is because of the errors or deviations that are present in the quadrupoles as compared to their design parameters. Removing those unwanted effects requires the operators to fine-tune the beamline setting of the real machine which requires additional effort and consumes time that is, as a consequence, not available for other purposes, e.g., running the experiments. Even when a beamline setting is identical to a setting that has been successfully used in the past, it might require fine-tuning by the operators to achieve the same beamline performance as before. This additional effort required from machine operators is a common problem.

Therefore, it would be advantageous if the performance of a chosen beamline configuration is only weakly influenced by the presence of possible quadrupole errors. This increases the probability that the given configuration still satisfies the requirements on the beam parameters and beam losses even under the influence of small quadrupole errors. Such a beamline configuration which is robust against possible quadrupole errors will reduce the time that operators must spend on fine-tuning the optics and, hence, increase the beam-on-target time for experiments.

Beamline quadrupole configurations are usually computed with the help of computer programs, specifically beam optics tools such as MADX. These tools offer so-called matching capabilities which allow one to find solutions in terms of the quadrupoles' strengths that satisfy the desired beamline performance. In this context, the beamline performance is characterized by a set of constraints on the beam parameters that are allowed during passage of the beamline as well as at the experimental target. However, such solutions for the quadrupoles' strengths are found by satisfying the given constraints only and do not take into account the limited

---

precision of the actual strengths of quadrupoles in the real beamline. It is therefore desirable to develop and investigate methods for incorporating the aspect of robustness against possible quadrupole errors into the process of computing beamline configurations.

Similar to how beamline configurations are found via tools like MADX, which solve an optimization problem in the background, also the robust beamline configurations are to be found with the help of optimization algorithms. Hence, this process is referred to as *robust optimization*. The idea of robust optimization has been applied to various other scientific disciplines, too [90, 91].

The goal of this chapter is to present a concrete concept for the robustness of beamline quadrupole configurations which allows one to compare different configurations to each other but also to allow for optimization algorithms to reliably identify those configurations with the help of computer programs. In this context, the computation aspects of evaluating the robustness of configurations are presented as well. Also, the robustness property is approximated with the help of an analytical expression. This allows not only for an interpretation of the robustness in terms of common accelerator physics concepts, but also allows for more efficient computation of such robust configurations. In general, finding robust beamline configurations with computer simulations is very compute intensive. For that reason, it is investigated how the computational efficiency of finding such robust configurations can be improved. In this context, three different approaches are presented and compared with each other. Each approach is compared in terms of its efficiency with the basic computation procedure in order to show the respective improvements. Eventually, the combination of these approaches allows to significantly improve the computation of robust configurations. An efficient computation procedure is desirable since it allows the identification of robust beamline configurations for a variety of beamlines without much overhead.

To verify the presented methods, this chapter presents the experimental results for two distinct beamlines. Sections 4.1 to 4.4 presents a detailed investigation on the beamline robustness using the example of the HEST beamline leading to the TH2DFA fluorescence screen upstream of the pion production target which is shown in Figure 4.2. The pion production target can be moved into the beamline with the help of a dedicated stepper motor. Its purpose is to produce pions during the interaction with the primary ion beam and these pions are then further used by the downstream High Acceptance Di-Electron Spectrometer (HADES) experiment. Besides working with the secondary pion beam, HADES can also work with a low intensity primary ion beam (i.e., when the pion production target is moved out of the beam passage). For pion production it is required to have high numbers of primary beam particles and also to maintain a good focus at the pion production target in order to produce sufficient numbers of pions. A loss of focus at the target decreases the pion yield and causes HADES to collect less data during experimental runs. For primary ion operation, a good beam focus at the HADES experimental target is required. It is necessary that the beam spot size does not increase beyond the size of the target since otherwise the primary beam particles might damage the surrounding equipment. Thus, the stability of the beamline performance is very important. In addition, a stable beamline operation is required to keep the beam losses constantly at a low value. Any increase in beam loss may lead to an increase

#### 4. Mitigating the effect of quadrupole errors on beam transfer lines with robust optimization

---

in the radiation levels by activating surrounding material and, therefore, leads to subsequent issues with radiation protection.

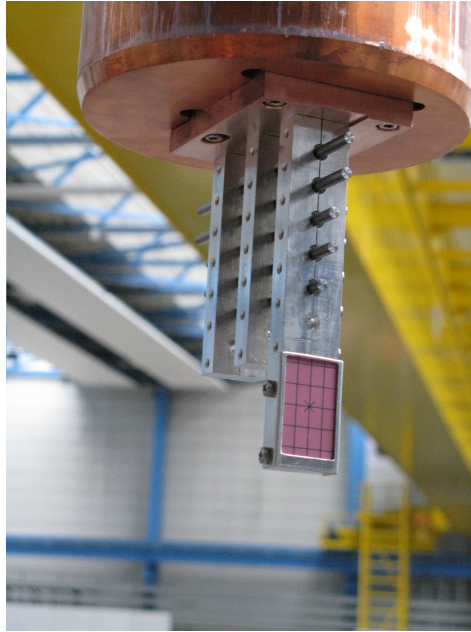


**Figure 4.2:** Photo of the pion production target in the lab [92, Courtesy of C. Dorn]. The different target bars are made of Beryllium and have different lengths. At the bottom, there is a scintillating screen which can be used for basic beam alignment on the target.

The findings which are gathered from the analysis of the HEST beamline are then applied to another beamline from Forschungszentrum Jülich (FZJ) in section 4.5. This beamline serves the so-called BIGKARL experimental area and is located behind the Cooler Synchrotron (COSY). While the polarity of quadrupoles on the HEST beamline network is fixed, the polarity of quadrupoles on the BIGKARL beamline can be changed. Also, some of the BIGKARL quadrupoles share a common power supply while the HEST quadrupoles are individually powered. Thus, the two beamlines vary in the properties of their quadrupole magnets and, therefore, allow to test the presented methods under these different conditions.

A previous analysis of the configuration space for the HADES beamline at GSI is presented in [93].

### 4.1 Configurations of quadrupole strengths for beam transfer lines

Setting up a beamline optics needs to respect various requirements. Typically, the beam should be transported with maximum transmission and it should be focused on the experimental target. The goal of finding a configuration for the quadrupoles of the beamline is to satisfy these requirements. Often, the requirements can be satisfied by multiple distinct configurations of the quadrupoles. That means, there is no single best way to satisfy the requirements, but there is a variety of options.

The part of the HEST beamline leading to the TH2DFA fluorescence screen has an overall length of about 90 m and consists of 9 quadrupoles with fixed polarity. These quadrupoles



are grouped into three doublets and one triplet structure as can be seen from Figure 4.3. Nevertheless, each quadrupole has an individual power supply.

Typically, a satisfying quadrupole configuration for operating the beamline under the given requirements is found via domain knowledge, operator experience and/or with the help of computer programs such as the LMDIF matching functionality from MADX [94]. This functionality allows the user to enter a set of constraints for the beamline properties in terms of the Twiss parameters <sup>1</sup> and the program then varies the quadrupole strengths in a dedicated way such that the final quadrupole strengths lead to beamline properties which meet the previously given constraints. The LMDIF function represents an efficient way to obtain a set of quadrupole strengths which satisfy the constraints because it uses a dedicated optimization algorithm as described in section 2.5.3.3. Therefore, it is advantageous to further reuse the LMDIF function also in the context of finding robust quadrupole configurations, in order to use its computational efficiency. The constraints of the beamlines are chosen such that no losses along the beamlines are expected to occur and that the beam spot size at the target locations is focused. In the case of the HEST beamline, the target location is the TH2DFA fluorescence screen and in the case of the BIGKARL beamline at FZJ, the target location is the MWPC45 profile grid directly upstream of the experimental area. The beam focus at the target locations is realized by constraining the beta functions to appropriate values in the MADX model. Similarly, the beta functions along the beamlines are constrained in order to limit the beam size along the beamline and, thus, to prevent beam losses. Therefore, the optimization constraints for the beamlines are expressed entirely in terms of the beamline optics. This is a useful property, since LMDIF can handle such optics constraints during the optimization procedure. Hence, by expressing the constraints in terms of the beamline optics, full compatibility with LMDIF is achieved.

In the following, a configuration is said to be *satisfying* if it satisfies all optimization constraints which correspond to the beamline requirements. The optimization domain, that is, the space of all possible quadrupole configurations, is denoted with  $\mathcal{D}$ . The sub-space of all satisfying quadrupole configurations is denoted with  $\mathcal{S} \subset \mathcal{D}$ . The shape of this sub-space is not obvious due to the nonlinear nature of the optimization problem (the dependency of Twiss parameters along the beamline is nonlinear with respect to the quadrupoles' strengths). Figure 4.3 shows an example for a satisfying configuration of the TH2DFA beamline. An important requirement is the beam focus at the target location, i.e., at the TH2DFA fluorescence screen. Figure 4.4 shows the beta function at the target in the neighborhood of the example beamline configuration from Figure 4.3; here, neighborhood refers to small quadrupole variations around the original quadrupole strengths. As long as the beta functions remain below the indicated threshold values, the neighboring configurations are also satisfying. However, those configurations for which the beta function exceeds the threshold are not satisfying. It can be observed that the influence of the various quadrupoles on the beta function at the target is different for each quadrupole and that the  $K_1L$ -region containing satisfying configurations is of varying size for each quadrupole.

---

<sup>1</sup>While Twiss parameters originate from the description of synchrotron optics, they can also be used to describe the optics at non-closed beamlines. This requires the knowledge of the Twiss parameters at the beginning of the beamline which can then be propagated downstream with the help of equation 3.8.

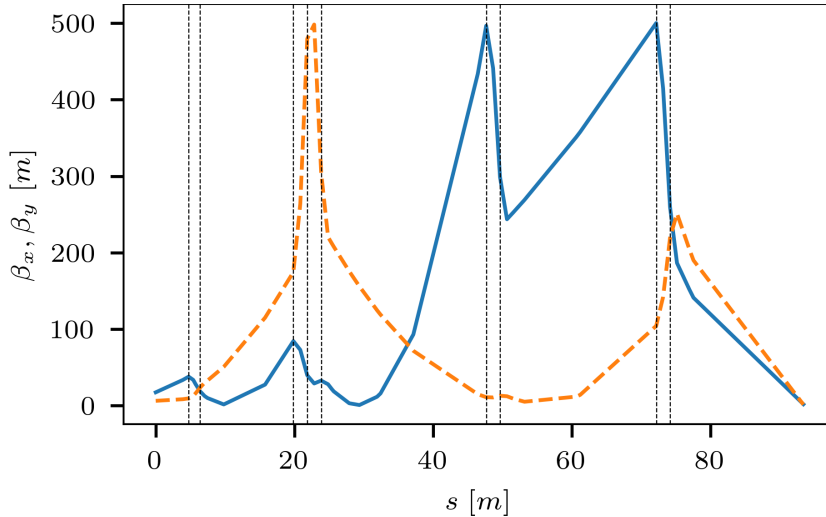


**Figure 4.3:** Beta function along the TH2DFA beamline for an example quadrupole configuration. The TH2DFA fluorescence screen is located at the end of the curves. The blue solid curve shows  $\beta_x$  and the orange dashed curve shows  $\beta_y$ . The vertical lines indicate the positions of the nine quadrupoles along the beamline.

## 4.2 Robustness with respect to quadrupole errors

The robustness of a beamline configuration refers to whether that configuration still satisfies the beamline requirements under the influence of variations of the strengths of the quadrupoles along the beamline. Thus, in the following a configuration is said to be *robust* if, for any variation of quadrupole strengths within predefined boundaries, the losses along the beamline and the beam spot size at the target do not increase beyond their limits imposed by the beamline requirements<sup>2</sup>. It is said to be *non-robust* otherwise, that is, if there exists a subset of all feasible quadrupole variations for which these observables do exceed their limits. However, such a binary classification of beamline configurations does not capture all the nuances that make up a robust configuration. Hence, it is more convenient to work with a continuous robustness score which indicates the degree to which variations of a beamline configuration still obey the beamline requirements.

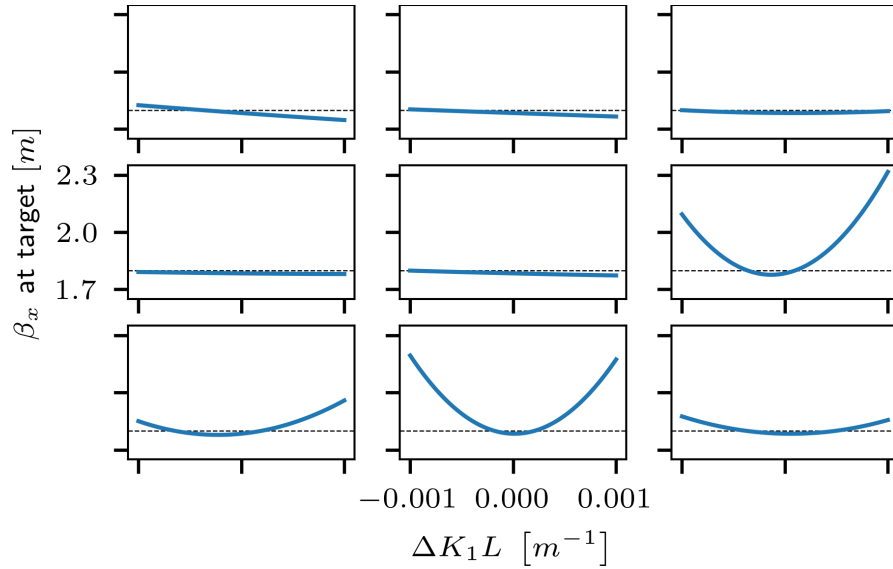
### 4.2.1 Definition of robustness

For the  $i$ th beamline configuration, the space of possible variations is denoted as  $\mathcal{V}_i \subset \mathcal{D}$  where  $\mathcal{V}_i$  could be, for example, a box or ball<sup>3</sup> of a fixed size or radius around the original configuration in terms of the quadrupole strengths. In the following, the robustness score of the  $i$ th beamline configuration is defined as the fraction of the volume of  $\mathcal{V}_i$  that contains only satisfying configurations, divided by the total volume of  $\mathcal{V}_i$ :

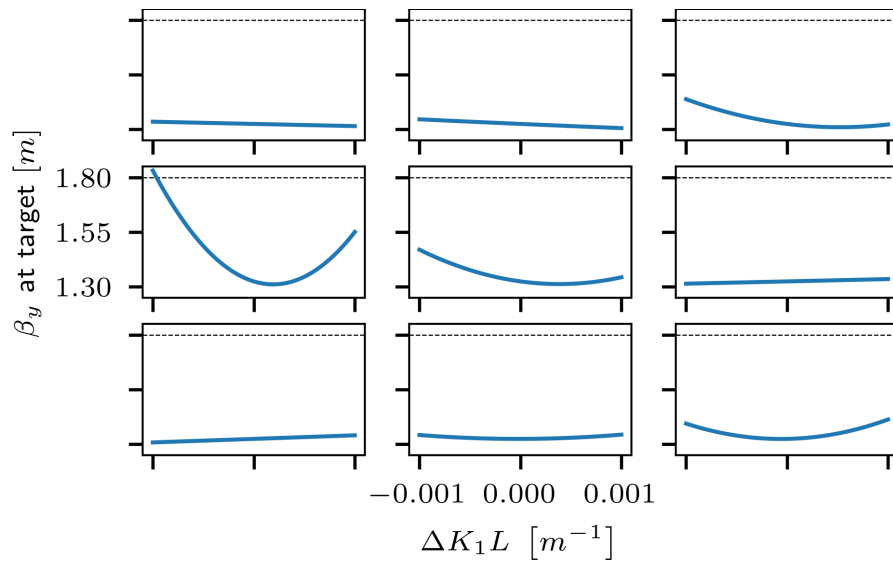
$$\text{robustness} = \frac{|\mathcal{V}_i \cap \mathcal{S}|}{|\mathcal{V}_i|} \quad (4.1)$$

<sup>2</sup>One might also choose the invariance of the beam spot size under the influence of quadrupole errors as an indicator for the robustness. This is analogous by adding an additional constraint that bounds the beta function at the target from below.

<sup>3</sup>Here, the terms *box* and *ball* are used in a mathematical sense and denote the  $n$ -dimensional counterparts of, respectively, a rectangular cuboid and a sphere in three dimensions.



(a) Horizontal beta function.



(b) Vertical beta function.

**Figure 4.4:** Beta functions at the target screen for different quadrupole variations. The nine subplots, from top to bottom and left to right, correspond to the nine quadrupoles of the TH2DFA beamline. The horizontal and vertical axes are the same for each subplot. The horizontal axis indicates a  $\Delta K_1 L$  variation for each of the quadrupoles and the vertical axis indicates the corresponding change of the beta function at the target screen.  $\Delta K_1 L = 0$  corresponds to the example configuration from Figure 4.3 in each of the subplots. The dashed lines at  $\beta_{x,y} = 1.8$  m indicate the beamline constraint at the target that must not be exceeded. It can be observed that the various quadrupoles have a different influence on the resulting beta function. All variations that lie under the dashed line are still satisfying but those that lie above are not.

#### 4. Mitigating the effect of quadrupole errors on beam transfer lines with robust optimization

---

where  $|\cdot|$  denotes the volume of the argument. Thus, the robustness score is bounded by the interval  $[0, 1]$  where a value of 1 implies robustness against all feasible quadrupole errors defined by  $\mathcal{V}_i$ . In the following, the robustness score is simply referred to as *robustness*.

For numerical purposes, the robustness can be evaluated via Monte Carlo simulations which generate random variations within the sub-space  $\mathcal{V}_i$  and check whether these are still satisfying the requirements. More details on the Monte Carlo evaluation of robustness are presented in section 4.2.3.

However, before one can start with evaluating the robustness of a configuration, it is important to make sure that the given configuration can be expected to not yield a low robustness score in the first place because that would lead to wasted compute power. When using LMDIF to produce candidate configuration for robustness evaluation, there is one more aspect that needs to be considered which affects the robustness that can be expected from the produced configurations. This is presented in detail in the next section.

##### 4.2.2 Improving robustness of quadrupole configurations obtained via matching of beta functions

When beamline configurations are obtained via optimization routines such as LMDIF from MADX, they may not be robust by default. This is because LMDIF stops as soon as it manages to get the cost function of the optimization below the user-defined tolerance. If the beta at target is specified to be  $\beta_{x,y} \leq \beta_T$ <sup>4</sup>, then the optimization will stop as soon as this condition is met (for the purpose of illustration, other constraints and stopping criteria are neglected at this point). As a result, one ends up with  $\beta_{x,y} \lesssim \beta_T$ , which is expected to have low robustness since it resides very close to the threshold  $\beta_T$ . In that case, even small variations of the quadrupoles' strengths can cause the beta functions to cross the threshold  $\beta_T$ . Hence, the configurations that are thus found by LMDIF should be fine-tuned in order to improve their robustness. An effective and straightforward option is to perform a second LMDIF matching run which attempts to bring the beta functions at the target towards zero. It takes the previous solution as a starting point and replaces the constraints  $\beta_{x,y} \leq \beta_T$  with  $\beta_{x,y} = 0$ <sup>5</sup>. Since the new constraints can, most likely, not be satisfied, a compromise between the new constraints at the target and the constraints for the beta functions along the beamline will be reached. Typically, this leads to an increase of the beta functions along the beamline and, hence, it is important to keep an extra margin for the beta functions along the beamline during the first LMDIF run, in order to not invalidate configurations during the second LMDIF run. Also, since LMDIF minimizes both beta functions at the target, horizontal and vertical, it is possible that the optimizer trades one dimension for the other, for example, decreasing  $\beta_x$  while increasing  $\beta_y$ , but still reducing the overall cost function. The same can happen when the optimizer trades a smaller beta at target for larger values of the beta functions along the beamline. This can lead to final configurations which do not satisfy the original constraints because their  $\beta$ -functions have increased above the original threshold. The robustness of such

---

<sup>4</sup>If invariability of the beam size is desired, additional constraints  $\beta_{x,y} \geq \beta_L$  may be added.

<sup>5</sup>While it would be possible to use  $\beta_{x,y} = 0$  directly from the beginning, a two-stage approach allows to add dedicated matching constraints during the first LMDIF run which help to improve the robustness of produced configurations as will be described in section 4.3.1. These additional constraints are then removed during the second LMDIF run.

configurations can, however, be nonzero (typically in the lower percent regime), because the  $\beta$ -variations produced by the quadrupole errors reach back into the valid region, i.e., below  $\beta_T$ , even though the  $\beta$ -value of the original configuration lies outside of it. However, because such configurations already infringe the original constraints without applying any quadrupole errors, they can be easily rejected and excluded from the further analysis.

The overall procedure for computing robust configurations is visualized in Figure 4.5. The final step refers to the evaluation of the robustness via Monte Carlo simulations. This step is detailed in the next section.

### 4.2.3 Evaluating robustness of quadrupole configurations

Evaluating the robustness of a configuration requires probing the relevant volume  $\mathcal{V}_i$  which contains the possible quadrupole errors. Since this volume increases exponentially with the number of involved quadrupoles, the systematic probing of the configuration space is not feasible to obtain accurate results. Instead, one can use random Monte Carlo sampling.

In most cases, large numbers of samples are required for the Monte Carlo simulation to yield accurate results and, hence, evaluating the robustness is expensive in terms of compute time. Compute clusters such as the Green IT Cube at GSI allow for a high degree of parallelism, yet the overall elapsed time can be large if scanning through thousands of possible beamline configurations in terms of their robustness.

For the evaluation of robustness, a magnitude of combined quadrupole errors of  $\Delta(K_1L) = 1 \times 10^{-3} \text{ m}^{-1}$  is chosen. This choice is motivated by the fact that the presented methods shall be tested during a dedicated and controlled beamline experiment. Such an experiment will apply artificial quadrupole errors to the beamline and observe the effect of the errors on the beam behavior. Besides the artificially applied quadrupole errors, the beamline quadrupoles will contain already some natural quadrupole errors which are present before any artificial errors are applied. In order to allow for controlled experimental conditions, i.e., a situation where it can be expected that the artificial quadrupole errors are not obfuscated by the presence of the natural errors, the magnitude of artificial errors must be significantly larger than the one of natural errors. The HEST power supplies have an accuracy of approximately 100 ppm and a precision of approximately 200 ppm. Therefore, the total relative uncertainty of the magnets' current setting is about  $\delta = \Delta I/I = 3 \times 10^{-4}$  which also applies to the relative uncertainty of the magnets'  $K_1$  values. The limit for the strength of HEST quadrupoles is approximately  $(K_1L)_{\max} = 0.6 \text{ m}^{-1}$  and, thus, the maximum combined error of the 9 quadrupoles is of the order  $\sqrt{9}\delta(K_1L)_{\max} = 0.54 \times 10^{-3} \text{ m}^{-1}$ . Therefore, an artificial error of combined magnitude  $\Delta(K_1L) = 1 \times 10^{-3} \text{ m}^{-1}$  is sufficiently large to be distinguished from natural errors. The magnitude of the artificial combined error is the magnitude or length of the corresponding vector of individual quadrupole errors. It is noted that for small strengths of individual quadrupoles, this likely overestimates the actual quadrupole error, however, if a configuration is robust with respect to the overestimated errors, it will also be robust with respect to the real errors.

For the following simulation study, a dataset of 10 000 quadrupole configurations for the TH2DFA beamline has been created. These were obtained by randomly sampling an initial setting for the quadrupoles in  $\mathcal{D}$  which was then given as a starting point to the LMDIF

#### 4. Mitigating the effect of quadrupole errors on beam transfer lines with robust optimization

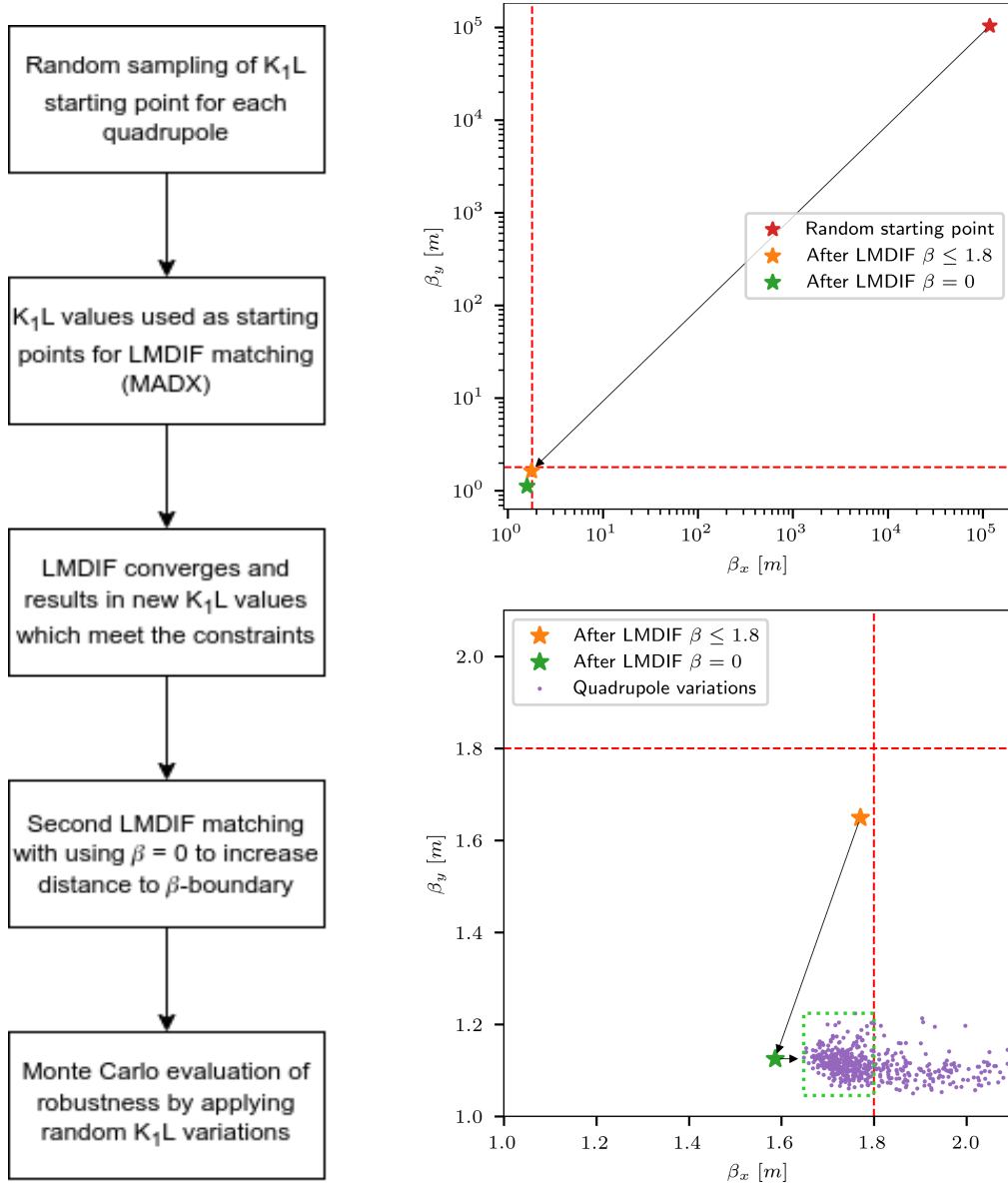


**Figure 4.5:** Left: Flow chart showing the procedure for computing robust beamline configurations. The sequence of steps refers to the computation of a single beamline configuration. The starting point for the procedure are the randomly sampled  $K_1L$  values of quadrupoles. This random sampling ensures the variance when computing multiple configurations by executing the sequence of steps multiple times. The random  $K_1L$  values form the starting point for the LMDIF matching routine from MADX. This matching produces a set of new  $K_1L$  values which satisfy the desired beam parameters. In order to increase the distance of beta functions to their thresholds, another LMDIF matching is performed with  $\beta = 0$  as the constraint for the target location (this causes the configuration to move away from the original threshold  $\beta \lesssim \beta_T$ ). Finally, the robustness of the configuration is evaluated via Monte Carlo simulations. This involves the random generation of  $K_1L$  variations with relevant magnitude and applying them to the previously found configuration. For each random variation, it is checked whether the new configuration, which contains the variation, still yields the desired beam parameters, i.e., whether it is still satisfying. The number of varied configurations which are still satisfying divided by the total number of variations which have been applied is then the computed value for the robustness, similar to equation 4.1.

Right: The same computation procedure is shown in terms of the beta functions at the target location. In the top plot, the beta functions at the very beginning of the procedure, i.e., emerging from the random starting point of  $K_1L$  values, are shown together with the beta functions obtained after the first and second LMDIF steps. In the bottom plot, the beta functions emerging from random quadrupole variations during Monte Carlo are shown as well. Only those variations are satisfying which remain below the red dashed threshold line at  $\beta_T = 1.8$  m; in the plot, these are surrounded by a green dotted rectangle.

matching. As described in section 4.2.2, the LMDIF matching was performed as a two stage process. The first stage, LMDIF-1.8, attempts to bring the beta functions at the target below the desired threshold of 1.8 m while using a set of more-than-necessary strict constraints for the beta functions along the beamline to prevent beam loss. The second stage, LMDIF-0, continues from the first stage's solution and tries to minimize the beta functions at the target towards  $\beta = 0$  m while using a set of constraints for the beta functions along the beamline that is relaxed by 5% with respect to the first stage. Only a small fraction of the random starting points resulted in a successful LMDIF-1.8 matching result ( $\approx 2.53\%$ ). Thus, the generation of this dataset required to scan through about 400 000 possible beamline configurations, performing LMDIF matching for each, which has been realized with the help of the Green Cube computing cluster. For the final 10 000 configurations, the robustness according to definition 4.1 has been computed using 200 000 random quadrupole variations per configuration. The variations of the nine quadrupoles were uniformly distributed inside a 9-ball of radius  $1 \times 10^{-3} \text{ m}^{-1}$  in  $K_1L$ -space around each configuration, corresponding to the nine quadrupoles along the beamline. Figure 4.6 shows a histogram of the robustness scores of all configurations in the dataset. It can be observed that most configurations have low robustness while a few configurations have high robustness. Nevertheless, it is noted that while a robustness of, e.g., 0.8 resides on the high end of the interval  $[0, 1]$  of possible robustness scores, it still implies a 20% chance that the given configuration will fail the beamline requirements which might not be acceptable from the view of the operators or for an experiment which is served by that beamline. The large number of configurations with zero robustness emerge as a result of the LMDIF-0 stage which pushed the beta function at some location, either the target or along the beamline, beyond the allowable threshold in order to further minimize the beta functions at the target (see section 4.2.2). These configurations are not satisfying and, thus, will be excluded from the further analysis. It is easy to reject these configurations as non-robust since they infringe the original constraints of the optimization problem. This dataset is referred to as *baseline* in the following. This is because several improvements of the computation procedure will be presented and are compared to this *baseline* dataset.

Since a Monte Carlo estimate is always subject to statistical errors emerging from the finite number of randomly sampled configurations, also the thus estimated robustness of beamline configurations has an associated Monte Carlo error. Therefore, to assess the quality of a given robustness estimate, it must be described not only by the estimated value but also by its Monte Carlo error. In order to obtain reliable estimates, it is important to investigate the details of the Monte Carlo simulation process and how the results should be interpreted to ensure their reliability. An important parameter in this context is the number of random Monte Carlo samples that are used to derive the estimate. Larger number of samples imply a smaller Monte Carlo error but also impose a larger computation effort. Thus, it is important to investigate how the right balance in terms of the number of Monte Carlo samples can be identified. These details are presented in the next sections.

#### 4.2.3.1 Monte Carlo simulations

The definition of robustness from equation 4.1 refers to an entire sub-space  $\mathcal{V}_i$  of the problem domain  $\mathcal{D}$ . Since the systematic evaluation of that entire sub-space is infeasible, it can be

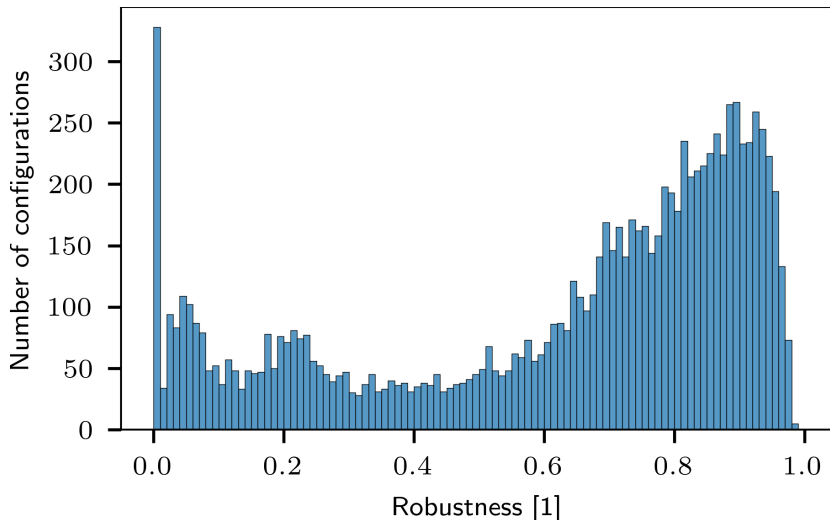


**Figure 4.6:** Histogram plot of the robustness scores for the 10 000 configurations of the baseline dataset. The robustness has been evaluated according to equation 4.1 via Monte Carlo simulations. To do so, for each configuration 200 000 random quadrupole variations have been generated inside the 9-ball of radius  $1 \times 10^{-3} \text{ m}^{-1}$  in  $K_1L$ -space, centered around that configuration. The thus obtained robustness scores of the 10 000 individual configurations are summarized in the histogram.

approximated by randomly sampling variations of the original configuration inside  $\mathcal{V}_i$  and then evaluating the properties of these variations. In the following, the original beamline configuration whose robustness is to be evaluated, is referred to as *root* configuration. The randomly generated variations of this root configuration in  $\mathcal{V}_i$  are referred to as *leaf* configurations. The Monte Carlo simulation takes a root configuration as input and generates a number of leaf configurations from it for which it computes the beta functions to compare them against the original constraints of the root configuration. The robustness is then estimated as the number of leaf configurations which still satisfy the original constraints divided by the total number of generated leaf configurations, according to equation 4.1.

#### 4.2.3.2 Statistical error analysis

Estimating robustness via Monte Carlo simulations is a statistical process which leads to corresponding errors of the estimates. This statistical error, which is introduced by the usage of Monte Carlo simulations, must be accounted for when interpreting the obtained results.

Estimating the fraction of satisfying configurations inside the volume  $\mathcal{V}_i$  is similar to integrating a function  $f$  over the domain  $\mathcal{V}_i$  where  $f(x) \equiv 1$  if  $x$  represents a satisfying configuration and  $f(x) \equiv 0$  otherwise, for  $x \in \mathcal{V}_i$ . For  $N$  Monte Carlo samples, the estimate is given as:

$$\langle f \rangle = \frac{1}{N} \sum_{i=1}^N f(x_i) \quad (4.2)$$



The standard deviation  $\sigma_N$  of the Monte Carlo samples is given by (writing  $f_i \equiv f(x_i)$ ) and using  $f_i^2 = f_i$ ):

$$\begin{aligned}
\sigma_N^2 &= \frac{1}{N-1} \sum_{i=1}^N [f_i - \langle f \rangle]^2 \\
&= \frac{1}{N-1} \left[ \sum_i f_i^2 - 2N\langle f \rangle^2 + N\langle f \rangle^2 \right] \\
&= \frac{1}{N-1} \left[ \sum_i f_i^2 - N\langle f \rangle^2 \right] \\
&= \frac{N}{N-1} [\langle f \rangle - \langle f \rangle^2]
\end{aligned} \tag{4.3}$$

Thus, the standard error of the estimate  $\langle f \rangle$  is given by:

$$\text{standard error of } \langle f \rangle \equiv \frac{\sigma_N}{\sqrt{N}} = \sqrt{\frac{\langle f \rangle - \langle f \rangle^2}{N-1}} \tag{4.4}$$

The standard error has a maximum at  $\langle f \rangle = \frac{1}{2}$  and in order to decrease it to less than or equal to 0.01 the Monte Carlo simulation requires at least 2501 samples.

Alternatively, it can be tested if the robustness  $\rho$  of a given configuration is no less than a desired predefined threshold  $\tau$ , that is,  $\rho \geq \tau$ . This comprises a statistical test with a one-sided alternative. This statistical test has associated Type-I and Type-II errors which are defined in terms of a null hypothesis. In the present context, the null hypothesis is that the robustness of the given configuration is less than  $\tau$ , that is,  $\rho < \tau$ ; this is the complementary statement to the one being tested.

- A type-I error, also known as "false positive", occurs when the null hypothesis is mistakenly rejected despite it's actually true. That is, the configuration is assumed to have a robustness greater than or equal to  $\tau$  when it actually does not.
- A type-II error, also known as "false negative", occurs when the null hypothesis is not rejected despite it's actually false. That is, the configuration is assumed to have a robustness less than  $\tau$  when it actually does not.

Thus, when testing for the robustness via Monte Carlo simulations in this way, one must specify acceptable bounds for the Type-I and Type-II errors. This determines the minimum number of samples needed to satisfy these bounds. In general, a small Type-I error is desirable since this type of error implies trusting an invalid result. The consequence would be to accept a beamline configuration under the assumption that it has a robustness no less than the required threshold  $\tau$  but in reality its robustness is less than the threshold. The Type-II error bound does not have to be that stringent since that type of error only implies that an opportunity to accept a robust configuration is missed and, thus, it will only prolong the computation time to find those configurations. Thus, a suitable choice for the Type-I error is  $\alpha = 1 \times 10^{-3}$  and for the Type-II error is  $\beta = 1 \times 10^{-1}$ .

#### 4. Mitigating the effect of quadrupole errors on beam transfer lines with robust optimization

---

The following relationship can be used to determine the required minimum number of samples to satisfy the error bounds [95]:

$$N = \frac{\tau(1 - \tau) \left( z_{1-\alpha} + z_{1-\beta} \sqrt{\frac{\rho(1-\rho)}{\tau(1-\tau)}} \right)^2}{(\rho - \tau)^2} \quad (4.5)$$

where  $\alpha$  and  $\beta$  are, respectively, the Type-I and Type-II error rates and  $\rho$  is the expected robustness of a configuration. The minimum difference to be distinguished between the actual and estimated robustness is 0.01 and, thus, the denominator evaluates to  $1 \times 10^{-4}$ . In [95] it is shown that the normalized test statistic  $z$

$$z = \frac{\rho - \tau}{\sqrt{\frac{\tau(1-\tau)}{N}}} \quad (4.6)$$

follows the Student's t-distribution under the normal approximation of the binomial distribution. This allows to approximate the percentiles of this distribution by the corresponding percentiles of the normal distribution  $N(0, 1)$ . These percentiles are denoted by  $z_{1-\alpha}$  and  $z_{1-\beta}$ . This approximation is valid if  $N \gtrsim 200$  holds [95].

Table 4.1 shows the minimum number of required samples for various thresholds  $\tau$  according to equation 4.5.

**Table 4.1:** Minimum number of Monte Carlo samples to test whether the robustness  $\rho$  of a given configuration is no less than the threshold  $\tau$  for different values of  $\tau$  according to equation 4.5. The bounds for the Type-I and Type-II error rates are, respectively,  $1 \times 10^{-3}$  and  $1 \times 10^{-1}$ . The minimum difference in terms of the robustness that should be distinguished is 0.01.

| Threshold | Number of samples |
|-----------|-------------------|
| 0.99      | 946               |
| 0.98      | 3138              |
| 0.97      | 4993              |
| 0.96      | 6793              |
| 0.95      | 8550              |

#### 4.2.4 Approximating robustness from Twiss data

While Monte Carlo simulations allow for obtaining accurate estimates of a configuration's robustness, they are also expensive to compute since it requires to compute the Twiss parameters of the beamline optics for each of the leaf configurations. Especially if the configuration turns out to have low robustness, it would have been advantageous to if this property could be assessed before starting the Monte Carlo evaluation. Hence, it is desirable to have a way to assess the robustness of a configuration without directly using Monte Carlo simulations but using a quick approximation method instead. This allows to reject non-promising configurations without much computation effort and, thus, saves great amounts of compute time. In the following, an approach is presented which allows to approximate the robustness of a configuration from only its own Twiss parameters. Three different methods for computing the robustness approximation are compared in terms of their accuracy and their required computation effort.

The transformation of Twiss parameters through a beamline element is described by equation 2.88:

$$\begin{pmatrix} \beta \\ \alpha \\ \gamma \end{pmatrix} = \begin{pmatrix} C^2 & -2SC & S^2 \\ -CC' & SC' + S'C & -SS' \\ C'^2 & -2S'C' & S'^2 \end{pmatrix} \begin{pmatrix} \beta_0 \\ \alpha_0 \\ \gamma_0 \end{pmatrix} \quad (4.7)$$

where  $\begin{pmatrix} C & S \\ C' & S' \end{pmatrix}$  is the  $2 \times 2$  transfer matrix of the beamline element for either the horizontal or the vertical dimension and  $(\beta_0, \alpha_0, \gamma_0)$  are the Twiss parameters for that dimension directly upstream of the beamline element. This transformation applies to uncoupled optics, but can be extended to coupled optics, too. Thus, the Twiss parameters at a downstream location are given by a sequence of matrix multiplications.

The thin lens approximation represents a quadrupole with integrated strength  $K_1L$  by the following transfer matrix:

$$\begin{pmatrix} 1 & 0 \\ \pm K_1L & 1 \end{pmatrix} \quad (4.8)$$

where a negative sign represents a focusing quadrupole. The transfer matrix of a drift space of length  $L$  is given by:

$$\begin{pmatrix} 1 & L \\ 0 & 1 \end{pmatrix} \quad (4.9)$$

For the following derivation, the last quadrupole of the beamline is described by the thin lens approximation. This allows to derive an expression of the Twiss parameters at the target in terms of that quadrupole's strength. The subscript  $\{\beta, \alpha, \gamma\}_0$  is used to denote the Twiss parameters directly upstream of the last quadrupole and  $\{\beta, \alpha, \gamma\}_q$  to denote the Twiss parameters at the exit of the quadrupole.  $\{\beta, \alpha, \gamma\}_t$  denotes the Twiss parameters at the target location which is downstream of the quadrupole. Using equation 4.7, the beta at target is given by the following equation:

$$\beta_t = \beta_q - 2L\alpha_q + L^2\gamma_q \quad (4.10)$$

where  $L$  is the length of the drift space between the last quadrupole and the target.

In the following,  $K$  denotes the last quadrupole's integrated strength  $K_1L$  in order to prevent confusion with the length  $L$  from the drift space. Also, the sign from the focusing transfer matrix is absorbed into  $K$ , i.e.,  $K \equiv -K_1L$ . Thus,  $K < 0$  represents a thin focusing quadrupole with the following transfer matrix for either the horizontal or vertical dimension:

$$\begin{pmatrix} 1 & 0 \\ K & 1 \end{pmatrix} \quad (4.11)$$

#### 4. Mitigating the effect of quadrupole errors on beam transfer lines with robust optimization

---

Finally,  $\Delta \ll K$  denotes an error of the quadrupole's strength, i.e.,  $K \rightarrow K + \Delta$ . This error modifies the Twiss parameters at the exit of the quadrupole in the following way:

$$\begin{aligned}\tilde{\beta}_q &= \beta_q \\ \tilde{\alpha}_q &= \alpha_q - \beta_0 \Delta \\ \tilde{\gamma}_q &= \gamma_q + 2\beta_0 K \Delta - 2\alpha_0 \Delta + \beta_0 \Delta^2 \\ &= \gamma_q - 2\alpha_q \Delta + \beta_0 \Delta^2\end{aligned}\tag{4.12}$$

where  $\tilde{\beta}_q, \tilde{\alpha}_q, \tilde{\gamma}_q$  denote the modified Twiss parameters. This, in turn, leads to a change of the beta function at target,  $\tilde{\beta}_t$ :

$$\tilde{\beta}_t = \beta_t + 2L(\beta_0 - L\alpha_q)\Delta + L^2\beta_0\Delta^2\tag{4.13}$$

This implies that the first order contribution of the error  $\Delta$  is eliminated if  $\alpha_q = \frac{\beta_0}{L}$  holds. Since  $\alpha_q = \alpha_0 - K\beta_0$  this further implies:

$$K = \frac{\alpha_0}{\beta_0} - \frac{1}{L}\tag{4.14}$$

which represents a condition for the strength of the last quadrupole to exhibit robust behavior with respect to the beta at target.

However, if the beta function at the quadrupole,  $\beta_0$ , is large then the second order contribution in equation 4.13 becomes effective and, thus, will influence the robustness, too. This can be seen from Figure 4.4 and Figure 4.3. Those quadrupoles where the beta function is large show a nonlinear dependency for the beta function at the target. Thus, the quantity that combines the linear and quadratic terms may serve as an indicator for the variation of the beta function at the target location:

$$\text{beta variation} \propto \arg \max_{\Delta} |2L(\beta_0 - L\alpha_q)\Delta + L^2\beta_0\Delta^2|\tag{4.15}$$

where  $\Delta$  can assume any value within the relevant bounds.

While the above derivation only addressed the last quadrupole of the beamline, it can be extended to any other quadrupole of the beamline as well. The only aspect which changes is the length of the drift space downstream of the quadrupole. Instead, the drift space between two consecutive quadrupoles can be used for this purpose. If the change of Twiss parameters at the next downstream quadrupole is small, the overall effect on the beta functions at the target can be expected to be small, too, and vice versa.

Besides the variation of the beta function at the target or, in short, *beta variation*, another important aspect for a configuration's robustness is the margin of the beta functions to their corresponding threshold values. If this margin is large then also larger beta variations will not cross the threshold and, thus, the configuration is more robust. In the following, this margin is referred to as *beta margin*.

To obtain an estimate for the robustness, equation 4.15 is computed for each quadrupole and for both  $K_1L \rightarrow K_1L \pm \Delta$  in each of the dimensions, horizontal and vertical. For each dimension, the maximum absolute value of the beta variation is chosen. Then, the resulting

quantities are divided by their corresponding beta margin and the two dimensions are combined in quadrature. Finally, the resulting values for each quadrupole are combined in quadrature and the inverse of this quantity serves as an indicator for the robustness of the configuration. This procedure is illustrated by the pseudocode shown in Program 1.

---

**Program 1** Pseudocode to compute a robustness estimate for a given beamline configuration. `compute_beta_variation` is the selected method for computing the beta variation at the target and must be chosen by the user, e.g., equation 4.15.

---

```

beta_margin(X) ← beta_threshold(X) - beta_at_target(X)
beta_margin(Y) ← beta_threshold(Y) - beta_at_target(Y)
for each quadrupole in Quadrupoles do
  for each dimension in {X,Y} do
    beta_variation(quadrupole, dimension) ← compute_beta_variation(...)
  effect(quadrupole) ← sqrt(
    (beta_variation(quadrupole, X) / beta_margin(X))^2
    + (beta_variation(quadrupole, Y) / beta_margin(Y))^2
  )
estimate = 1/sqrt(sum(effect^2))

```

---

Another option for computing the beta variation is to focus only on the linear term in equation 4.13 and use its magnitude as an indicator. The main difference to the previous approach with equation 4.15 is that when only the linear term is considered, the specific value for  $\Delta$  merely serves as a scaling factor and is the same for each set of Twiss parameters corresponding to a configuration. Thus,  $\Delta$  may be neglected altogether when computing the estimate for robustness. Also, if  $\Delta$  is small a locally linear approximation is suitable. Again, the length of the drift space between two consecutive quadrupoles, or, between the last quadrupole and the target location, is used for the value of  $L$ :

$$\text{beta variation} \propto |\beta_0 - L\alpha_q| \quad (4.16)$$

The above considerations were done with the help of the thin lens approximation for quadrupoles in order to obtain an analytical expression for the variation of the beta function in terms of the quadrupole errors. This introduces an error due to the approximation with thin transfer matrices compared to the thick transfer matrices of the quadrupoles. Nevertheless, also the thick transfer matrices of quadrupoles can be used to obtain estimates for the beta variation at the target. This, however, requires to compute the entire Twiss transformation matrix along the beamline for each of the considered quadrupole errors and, thus, introduces a much greater computational effort than simply using equation 4.16 or even equation 4.15. The beta variation is then computed by considering  $K_1L \rightarrow K_1L \pm \Delta$  for each of the quadrupoles, computing the Twiss parameters at the end of the beamline and choosing the maximum beta variation given by either  $+\Delta$  or  $-\Delta$ . Thus, this method acts as a third option for `compute_beta_variation` in Program 1, besides equation 4.16 and equation 4.15.

A comparison of the three approaches is shown in Figure 4.7. It can be observed that the method of using only the linear contribution via equation 4.16 yields a dependency which is close to the method of using thick quadrupole transfer matrices. While the latter method is more accurate in terms of the Twiss computation via transfer matrices, it is also significantly

#### 4. Mitigating the effect of quadrupole errors on beam transfer lines with robust optimization

---

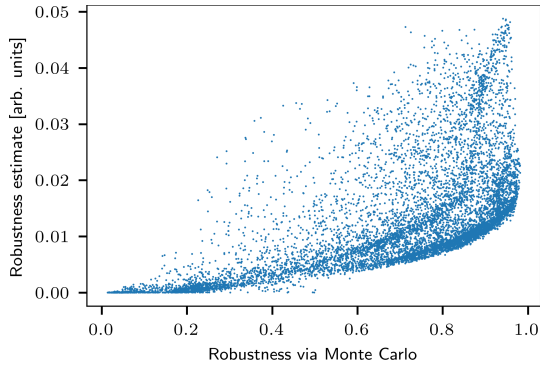
more expensive to compute. Since the method of using equation 4.16 yields very similar results, it can serve as the method for computing robustness approximations to either accept or reject certain configurations in a computationally cheap way before computing the accurate robustness estimate via Monte Carlo simulations. This is done by first collecting the Monte Carlo robustness estimates together with their robustness approximations for a number of configurations during the robust optimization procedure. Then, for any new configuration, it is checked whether the robustness approximation of that configuration lies in the top 10% of robustness approximations of already collected configurations. If it does, its actual robustness is computed via Monte Carlo simulation. Otherwise, the configuration is discarded without the need for computing the Monte Carlo estimate.

### 4.3 Robust optimization

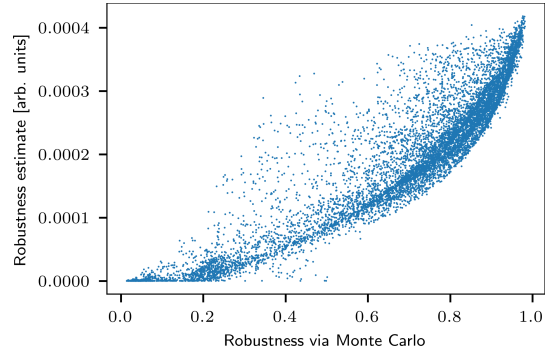
The entire procedure for finding robust beamline configurations is referred to as *robust optimization*. It follows the steps which have been discussed in the previous sections, including two-stage LMDIF matching via MADX ( $\beta \leq \beta_t$  followed by  $\beta = 0$ ), Monte Carlo simulations for robustness computation, and it may use robustness approximation from Twiss parameters in order to speed up the computation. Besides these steps, the baseline procedure, further improvements of the robust optimization procedure are possible in order to increase the efficiency with which high robustness configurations are found. In the following, three further improvements are presented and compared to the baseline procedure. The various improvements can be used together in order to surpass the efficiency of the baseline procedure by a great margin.

First, the baseline procedure for finding robust configurations is reviewed using the example of the TH2DFA beamline. This procedure is also visualized in Figure 4.5. The first step randomly samples configurations within the entire problem domain  $\mathcal{D}$  which comprises the possible  $K_1L$  values of all quadrupoles of the beamline. These random configurations are then given as a starting point to the LMDIF-1.8 matching which uses the constraints  $\beta_{x,y} \leq 1.8$  m at the target screen. The next step is to take the resulting  $K_1L$  values from LMDIF-1.8 matching and use them as a starting point for the subsequent LMDIF-0 matching which uses the constraints  $\beta_{x,y} = 0$  at the target screen. As discussed in section 4.2.2, the additional LMDIF-0 step improves the robustness that can be expected from the configuration. Finally, the robustness of the configuration is computed via Monte Carlo simulations.

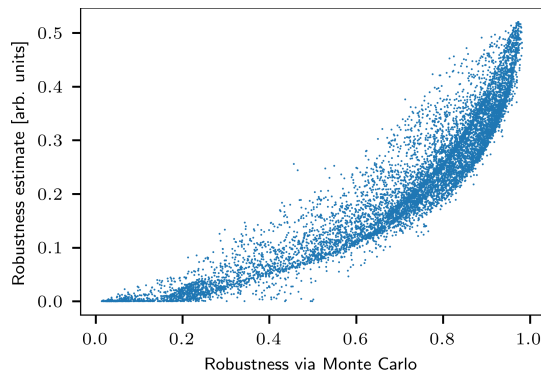
The goal of the robust optimization procedure is to find a configuration which satisfies the beamline requirements and, in addition, has high robustness against possible quadrupole errors. The desired robustness is denoted by  $\tau$  and, thus, the robustness  $\rho$  of a configuration must satisfy  $\rho \geq \tau$  in order to meet the desired robustness. While it is possible to use the above baseline procedure (Random  $\rightarrow$  LMDIF-1.8  $\rightarrow$  LMDIF-0) until a configuration is found which satisfies  $\rho \geq \tau$ , this might require large amounts of compute time or, for high values of  $\tau$ , might not even return a result in an acceptable amount of time. For example, in the dataset for the TH2DFA beamline which contains 10 000 configurations that were generated according to this baseline procedure, there is not a single configuration which satisfies  $\rho \geq 0.99$  and there are only 5 configurations which satisfy  $\rho \geq 0.98$ . Since the success rate of the



(a) Approximating the robustness of configurations when beta variations are computed via equation 4.15.



(b) Approximating the robustness of configurations when beta variations are computed via equation 4.16.



(c) Approximating the robustness of configurations when beta variations are computed by using the thick quadrupole transfer matrices along the entire beamline and the maximum variation is obtained by two-point-probing for the relevant errors  $\pm\Delta$  of each quadrupole. That is,  $(K_1L)_i \rightarrow (K_1L)_i \pm \Delta$  is applied  $\forall i$  where  $i$  refers to the  $i$ th quadrupole. For each  $(K_1L)_i \pm \Delta$  the variation of the beta function at the target with respect to the case where no error is applied is computed.

**Figure 4.7:** Comparison of different methods for approximating the robustness of beamline configurations with methods based on Twiss parameters. These methods are computationally cheap compared to the computation that is required by Monte Carlo simulations. In each of the plots, the horizontal axis indicates the robustness computed via Monte Carlo simulations which serves as a reference value. The vertical axis indicates the robustness approximation corresponding to the respective subplot. These robustness approximations are obtained from Program 1 and each subplot uses a different method for computing the beta variation via `compute_beta_variation` as indicated in Program 1. The caption of each subplot contains information about what method has been used for `compute_beta_variation` for the respective subplot.

#### 4. Mitigating the effect of quadrupole errors on beam transfer lines with robust optimization

---

LMDIF-1.8 matching step was only about 2.5 %, i.e., only 2.5 % of the random starting points could be successfully matched against the beamline constraints, finding a configuration with  $\rho \geq 0.98$  takes about 80 000 LMDIF matching runs (counting LMDIF-1.8 followed by LMDIF-0 as a single LMDIF run) and about 1800 Monte Carlo robustness evaluations (taking into account the LMDIF-0 success rate). The combined LMDIF step takes on average  $6.5 \text{ s} \pm 0.2 \text{ s}$  and robustness evaluation with 3138 leaf configurations (according to Table 4.1) takes about  $26.6 \text{ s} \pm 0.4 \text{ s}$ . Thus, the average total compute time to find one configuration which satisfies  $\rho \geq 0.98$  amounts to about  $158 \pm 4$  hours (on a single computer). Therefore, finding a configuration which high robustness is hardly feasible without access to a computing cluster. Also, for the TH2DFA beamline, by using this procedure the highest robustness that was found is  $\rho \approx 0.98$  and not a single configuration with  $\rho \geq 0.99$  was found. Here it should be noted that  $\rho = 0.98$  implies a chance that the beamline will fail to meet its requirements that is twice as large as for  $\rho = 0.99$  <sup>6</sup>.

In the following, a number of improvements of the baseline robust optimization procedure are presented which allow to decrease the required compute time for finding configurations with high robustness and even allow to find configurations which satisfy  $\rho \geq 0.99$ .

##### 4.3.1 Improved matching criteria by limiting the beta functions in the upstream part of the beamline

The initial LMDIF matching step, which transforms the random starting point for  $K_1L$  values into a set of meaningful values which can be used to satisfy the beamline requirements, is of great importance for the overall optimization procedure. As a gradient-descent algorithm, it is effective in finding a local minimum in its neighborhood (for details about the algorithm, see section 2.5.3.3). An effective measure to increase the robustness of candidate configurations that are produced by the LMDIF step is to add other appropriate matching criteria to this step. These criteria should be chosen in such a way that the robustness which can be expected from the produced configurations is increased.

Such a criterion can be derived from the observation that quadrupoles where the beta functions are large may have a great influence on the variation of the beta functions at the target. This can be seen from equation 4.13 which describes the beta variation at the target as a function of the quadrupole error, as well as from Figure 4.3 in conjunction with Figure 4.4 which show the beta functions of an example configuration at the various quadrupoles as well as the effect of errors of those quadrupoles on the beta function at the target. Thus, it is desirable to limit extreme excursions of the beta functions along the beamline. Typically, the beta functions at the last quadrupole doublet before the target need to attain large values in order to reach the desired focus at the target. However, upstream of the last quadrupole doublet the beta functions can be kept at a moderate level. This is achieved with the help of additional constraints for the LMDIF matching for the beta functions at the upstream part of the beamline. Specifically, for the TH2DFA beamline the beta functions until the fifth quadrupole, i.e., about one third of the total beamline length, has been limited to 20 % of the maximum allowable beta function. While this explicitly limits the beta functions at the first five quadrupoles of the beamline, it also tends to reduce the extent of the beta functions at

---

<sup>6</sup>Comparing different robustness values can be done on a logarithmic scale to reveal these implications.



the downstream quadrupoles. This is because when the beta functions assume already large values at the beginning of the beamline, the beta functions tend to assume a pattern of strong focusing already at upstream quadrupoles which also causes the beta functions to attain large values at those quadrupoles. This is visualized in Figure 4.8 which compares the beta functions from a configuration obtained with the baseline procedure and a configuration obtained when additionally limiting excursions of the beta functions at the first five quadrupoles. It can be observed that due to the additional constraint, the beta functions are smoother in the upstream part of the beamline which causes the effect of those quadrupoles that are located in that part on the beta function at the target to be weaker.

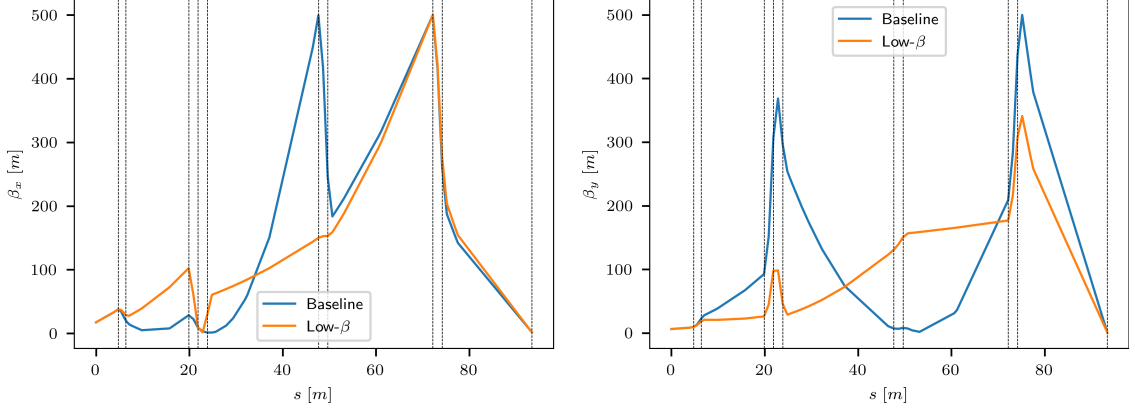


**Figure 4.8:** Comparison of beta functions for a configuration obtained with the baseline procedure and a configuration obtained when additionally limiting excursions of the beta function at the first five quadrupoles of the beamline. The dashed vertical lines indicate the positions of the nine quadrupoles as well as of the target screen (the last vertical line). While the vertical beta function of the baseline configuration has a large excursion in the quadrupole triplet at 20 m, this is prevented with the additional constraint on the beta function for the low- $\beta$  configuration. Nevertheless, this configuration eventually achieves the same beam focus at the target at the end of the beamline.

Figure 4.9 shows a histogram plot which summarizes the robustness scores of many configurations that are obtained with the help of the additional beta function constraint at the beginning of the beamline. Comparing with Figure 4.6, it can be observed that the robustness of produced configurations tends to be higher when the additional constraints on the beta functions are in place.

### 4.3.2 Application of an additional global optimizer

A further improvement of the robust optimization procedure is to exchange the random search, which produces the  $K_1L$  starting points for the initial LMDIF step, with a dedicated optimization algorithm. Since the overall problem domain  $\mathcal{D}$  is vast due to the number of quadrupoles and their  $K_1L$  limits, and since the regions of satisfying configurations in that domain follow a highly nonlinear dependency without any obvious global structure, it is best to use a derivative-free optimizer in order to avoid getting stuck in local minima. The local optimization is already covered by the LMDIF step which is based on a gradient-descent method. Figure 4.10 shows the distance in  $K_1L$ -space that is traveled by the LMDIF steps as a fraction of the maximum possible distance in  $\mathcal{D}$ . The maximum possible distance in  $\mathcal{D}$  is given by the distance between the minimal and maximal  $K_1L$  values of all quadrupoles,

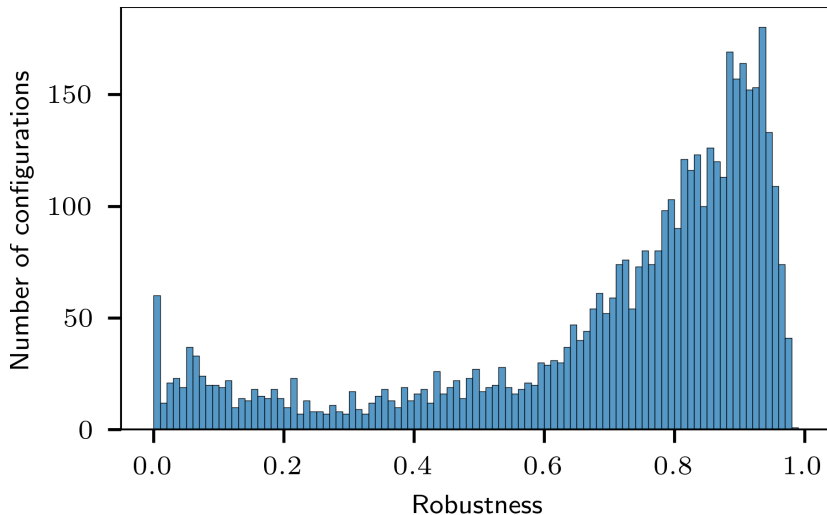


**Figure 4.9:** Histogram plot of the robustness scores of 4500 configurations that are obtained by using additional constraints for the beta functions in the upstream part of the beamline. These additional constraints prevent large excursions of the beta functions at the beginning of the beamline. Such large excursions make the beta function at the target more susceptible to quadrupole errors. By preventing such excursions, the robustness of produced configurations is improved in comparison to the baseline procedure (see Figure 4.6).

i.e.,  $|((K_1L)_{1,\min}, \dots, (K_1L)_{9,\min}) - ((K_1L)_{1,\max}, \dots, (K_1L)_{9,\max})| \approx 1.72 \text{ m}^{-1}$ . The distance that is traveled by LMDIF is given by the difference between the initial starting point for the  $K_1L$  values and the final  $K_1L$  values that it produced. It can be observed that the distance traveled by LMDIF is very small compared to the dimension of the full space  $\mathcal{D}$  and, thus, using a global optimizer helps in efficiently covering the problem domain on a global scale. The purpose of the optimizer is to generate the starting points for the initial LMDIF-1.8 step. The reward returned to the optimizer is the robustness score that is evaluated at the end of the sequence of steps, i.e., after LMDIF-0. The optimizer then attempts to maximize this reward, i.e., the robustness of produced configurations.

Differential evolution [96] is used as a global optimization algorithm. The implementation is from SciPy [97] using a population size of 50 and the `best1bin` strategy. Due to the vast number of possibilities and high computational demand, no exhaustive hyperparameter search has been conducted. However, the results obtained for the various *strategy* options have been compared and they have been found to exhibit only small differences between their results.

Figure 4.11 shows the robustness scores for configurations obtained with the help of the differential evolution optimizer. Compared to the baseline procedure, which is shown in Figure 4.6, the usage of the global optimizer greatly improves the robustness of the produced configurations. Also, the success rate of the LMDIF matching step is increased by the usage of the global optimizer to 3.00%. When the LMDIF fails, e.g., because it gets stuck in a local minimum or it reaches the limits of the  $K_1L$  values, the optimizer is given a reward of zero, i.e., as if it had produced a configuration with robustness equal to 0.

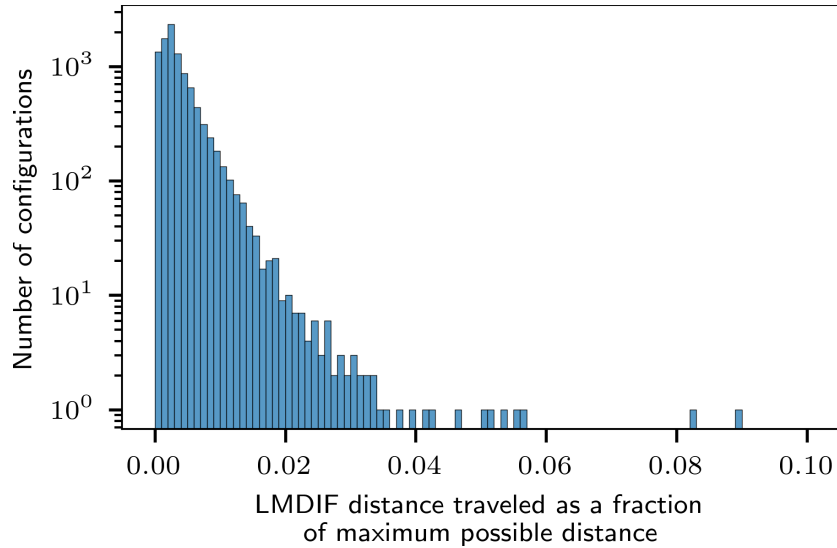


**Figure 4.10:** Distance traveled within the problem domain  $\mathcal{D}$  during the LMDIF matching steps. The distance is measured as the Euclidean distance between the starting point for the LMDIF matching and the final configuration that it produced. It is reported as a fraction of the maximum possible distance in  $\mathcal{D}$ , that is, the diagonal emerging from the boundaries of  $K_1L$  values:  $|((K_1L)_{1,\min}, \dots, (K_1L)_{9,\min}) - ((K_1L)_{1,\max}, \dots, (K_1L)_{9,\max})| \approx 1.72 \text{ m}^{-1}$ . It can be observed that the majority of LMDIF runs change the  $K_1L$  values of the initial configuration by less than 2% of the maximum distance. Taking into account that the volume of the corresponding region scales with power equal to the number of quadrupoles, the volume covered by a single LMDIF run is extremely small compared to the entire volume of  $\mathcal{D}$ .

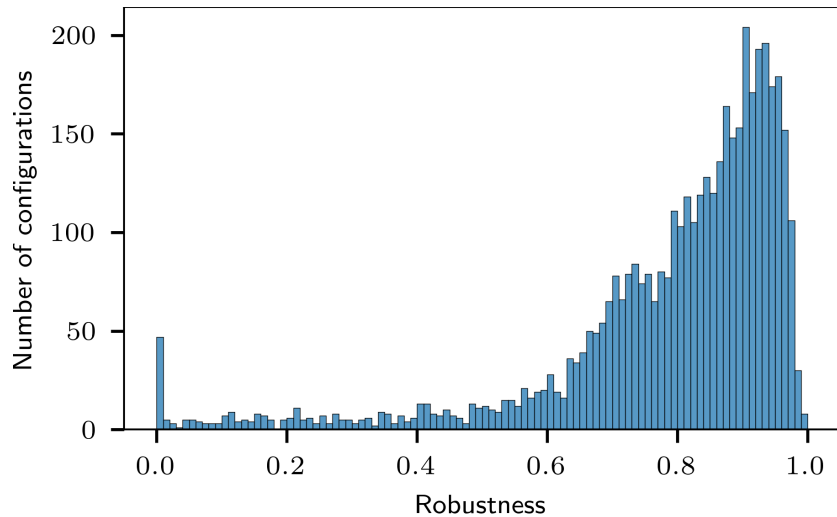


**Figure 4.11:** Histogram plot of the robustness scores of 4375 configurations that are obtained by using a differential evolution optimizer instead of random search to produce the initial  $K_1L$  starting points for the LMDIF step. By using such a global optimizer, the robustness of produced configurations is improved in comparison to the baseline procedure (see Figure 4.6). This dataset contains slightly fewer configurations than the one shown in Figure 4.9. This is because the generation of each dataset ran for a fixed amount of time. Using the differential evolution optimizer rather than random search requires additional compute time and, thus, the number of configurations that could be produced in the available amount of time is slightly smaller for the case which uses the optimizer.

### 4.3.3 Surrogate model for evaluating robustness and for deriving important Twiss parameters

Evaluating the robustness of a configuration via Monte Carlo simulations is costly since it requires to compute the Twiss parameters for thousands of leaf configurations. Section 4.2.4 presented a method for using the Twiss parameters of a configuration to approximate its robustness. These approximations are based on analytical considerations on how the beta functions evolve under the influence of the quadrupoles, represented by thin quadrupole transfer matrices. In a more general sense, the problem of predicting the robustness of a configuration based on its Twiss parameters can be solved by fitting a nonlinear relationship between the Twiss parameters and the robustness for many configurations. This fitting step can be solved with the help of machine learning models.

The machine learning model could then serve as a surrogate model for predicting the robustness of configurations that are produced by the LMDIF step similar to how robustness is approximated based on Program 1 in section 4.2.4. However, another useful property of the surrogate model is that it can be inspected for the importance of the various features that have been used to fit it. These features are the  $K_1L$  values and the Twiss parameters of the various configurations that are produced during the robust optimization procedure. This allows to identify those parameters which are especially influential for the robustness of configurations, namely, those features that are revealed to have high importance in the context of the predictions of the surrogate model. The advantage of this method is that all features, the  $K_1L$  values and the Twiss parameters, can be directly included and constrained in the context of the LMDIF matching step. This allows to derive a set of additional dedicated constraints for the LMDIF step which can then be used to improve the further production of high robustness configurations during the robust optimization procedure. In order to derive the constraints, first a set of configurations together with their robustness needs to be collected. The fitting of the surrogate model is then performed with these configurations and the important features are derived. In order to be usable early during the robust optimization procedure, the surrogate model should work with a few hundred configurations. Random Forest models have this property and, typically, require only small training datasets for fitting.

Following the example of the TH2DFA beamline, a Random Forest regression model [98] has been trained on 250 configurations. Figure 4.12 shows the robustness predictions of the Random Forest model on a test dataset comprised of configurations which have not been used for fitting. It can be observed that the Random Forest model successfully reproduces the robustness scores of configurations.

The method of permutation feature importance is used to assess the importance of each individual feature on the robustness predictions. Permutation feature importance considers one feature at a time and randomly permutes the values of that feature among all configurations in a dedicated test dataset. It then measures by how much the predictions of the model deviate when feature values are permuted compared to when they are not permuted; this is measured via the mean squared error among all configurations in the test dataset. When the prediction of the model changes only by a small degree, this implies that the feature had no great influence on the prediction. If, on the other hand, the predictions change by a large

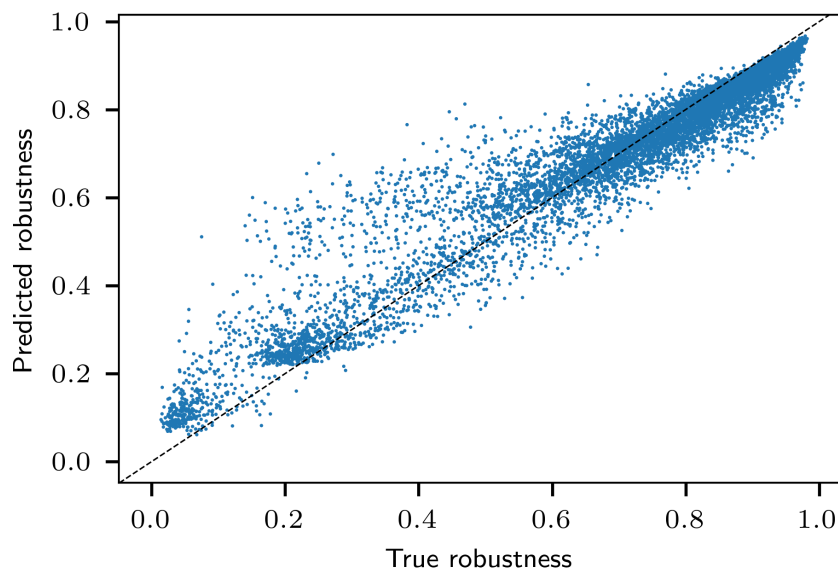


**Figure 4.12:** Robustness predictions from a Random Forest regression model. The model has been trained on the  $K_1L$  values and Twiss parameters of 250 configurations from the baseline dataset and their corresponding robustness scores which range from 0 to 0.975. The remaining configurations, which were not used for fitting, have been used as test data and their robustness predictions are shown in this plot. The implementation of the model is taken from [98] and the model was configured with 200 estimators, a maximum depth of 25 and maximum number of features per split set to 7. The features used for training and predictions are the  $K_1L$  values of the quadrupoles, the beta and alpha functions upstream and downstream of quadrupoles, at the bending magnets as well as at the target. Among these features, some had very high Pearson correlation coefficients. For each group of features that showed correlation coefficients greater than 0.95 only a single feature has been retained and the others have been removed, leaving a total of 53 features. The surrogate model performs poorly when presented with configurations that have zero robustness. This is because only 4 configurations with zero robustness were part of the training set.

#### 4. Mitigating the effect of quadrupole errors on beam transfer lines with robust optimization

---

degree, it means the feature was critical for making accurate predictions and is thus assigned a high feature importance.

For the TH2DFA dataset, it is found that the features  $\beta_{x,gth2qd12}$ , i.e., the horizontal beta function at the GTH2QD12 quadrupole (the ninth quadrupole), and  $\alpha_{y,gth1qd12}$ , the vertical alpha function at the GTH1QD12 quadrupole (the seventh quadrupole), are particularly important. Figure 4.13 shows an overview of the top five most important features as emerging from the feature importance method.

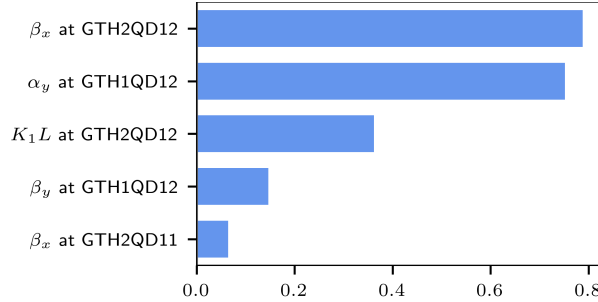


**Figure 4.13:** Feature importance for the fitted random forest surrogate model obtained via the permutation feature importance method. This method considers one feature at a time and randomly permutes the values of that feature among all configurations in a dedicated test dataset. It then measures by how much the predictions of the model deviate when feature values are permuted compared to when they are not permuted; this is measured via the mean squared error among all configurations in the test dataset. When the prediction of the model changes only by a small degree, this implies that the feature had no great influence on the prediction. If, on the other hand, the predictions change by a large degree, it means the feature was critical for making accurate predictions and is thus assigned a high feature importance. The top five most important features are shown in the plot.

Figure 4.14 shows the two most important Twiss parameters,  $\beta_{x,gth2qd12}$  and  $\alpha_{y,gth1qd12}$ , which turned out to be particularly influential for the robustness predictions of the surrogate model. From the plots it can be observed that these Twiss parameters show a clear relationship to the robustness scores of their corresponding configurations. Thus, these Twiss parameters can be used to derive additional constraints for the LMDIF matching step. The appropriate threshold values are deduced from the data as shown in Figure 4.14. The following constraints are then added to the LMDIF matching step:

$$\begin{aligned} \alpha_{y,gth1qd12} &< 2 \\ \beta_{x,gth2qd12} &> 200 \text{ m} \end{aligned} \tag{4.17}$$

Figure 4.15 shows the robustness scores that obtained for the TH2DFA beamline when the additional fitting constraints from equation 4.17 are added to the LMDIF matching step. It can be observed that the additional fitting constraints clearly improve the robustness of the obtained configurations. Since the LMDIF matching step is already used as part of the baseline procedure, adding these constraints does not impose any overhead on the optimization procedure and is straightforward to integrate. The additional constraints also improve the success rate of the LMDIF matching step. The fraction of random starting points which can successfully be matched to the beamline requirements by LMDIF is increased to 3.89%.

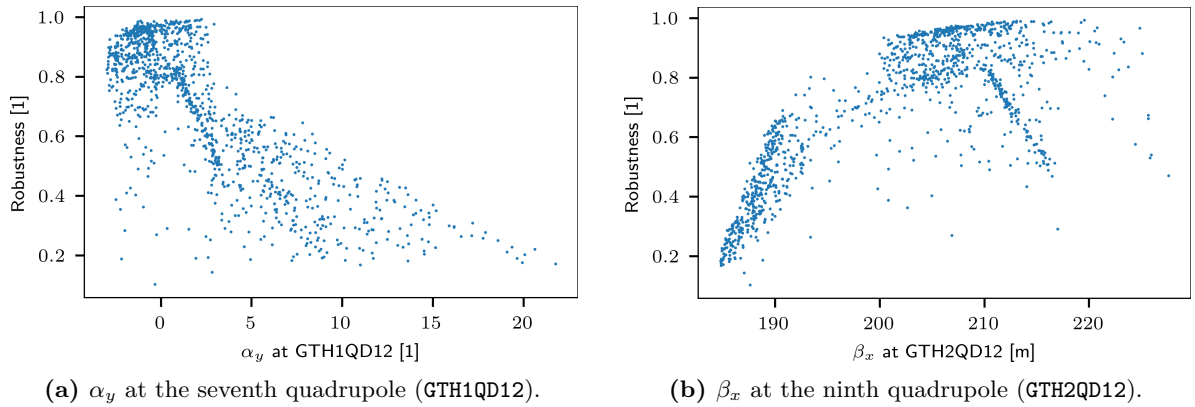


**Figure 4.14:** Robustness of the configurations of the TH2DFA beamline in dependency on the two most important Twiss parameters as identified from Figure 4.13. These Twiss parameters have turned out to be particularly influential for the predictions of the surrogate model. The Twiss parameters for a large number of 1200 configurations are shown in the plots in order to make the dependency clearly visible. However, the features show to be influential already when a smaller number of 250 configurations is used.

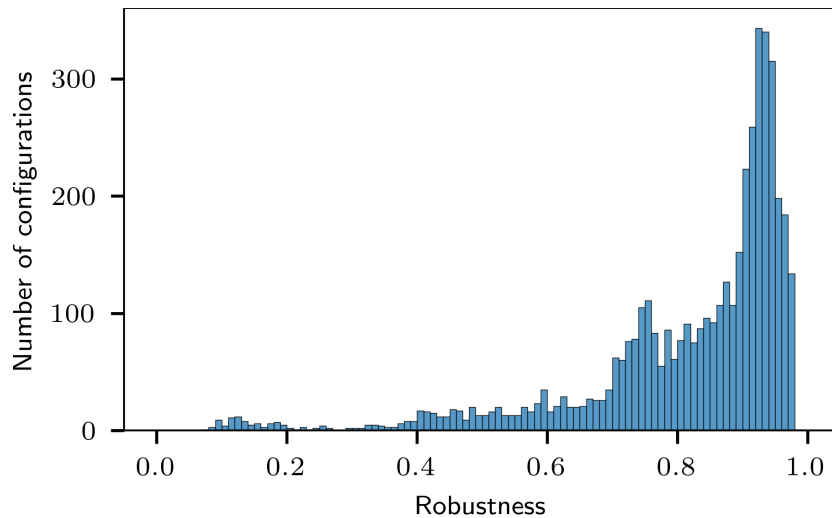


**Figure 4.15:** Histogram plot of the robustness scores of 4500 configurations that are obtained by using additional constraints for the LMDIF matching step. The constraints have been derived from the surrogate model feature importance and are shown in equation 4.17. By using these additional constraints, the robustness of produced configurations is improved in comparison to the baseline procedure (see Figure 4.6).

##### 4.3.4 Comparison of methods

Using a global optimizer as described in section 4.3.2 together with the additional constraints for the LMDIF matching step which have been derived in sections 4.3.1 and 4.3.3, achieves a LMDIF success rate of 4.43% which is higher than the success rates for any of the individual improvement methods. Also, the results in terms of the robustness of the produced configurations are greatly improved when all three methods are combined. The resulting robustness scores are shown in Figure 4.16. From that plot, it can also be observed that, in addition, the maximal achieved robustness has increased, too. Specifically, this dataset contains 4.15% configurations with robustness greater than 0.99. The only other improvement method which achieved a robustness greater than 0.99 is the method of adding LMDIF constraints to limit the beta function excursions in the upstream part of the beamline. However, this approach only yielded a fraction of 0.18% of configurations with robustness greater than 0.99. Also, the fraction of configurations which have a robustness greater than or equal to 0.98 is increased from 0.87% to 16.3%. So, to find a single configuration with robustness no less than 0.98, by using the improvements from the previous sections it would require to compute only  $(0.0443 \cdot 0.163)^{-1} \approx 138$  LMDIF matching runs and  $0.163^{-1} \approx 6$  robustness evaluations which are very accessible numbers. To find a configuration with robustness greater than or equal to 0.99, it is 549 LMDIF evaluations and 24 robustness evaluations which is feasible on a single processor machine. However, in order to identify the additional constraints via surrogate model feature importance, a previous dataset is needed that only uses the global optimizer and limits beta functions at the beginning of beamline, in order to collect a number of configurations which can be used to fit the surrogate model and to derive the important features. By using the global optimizer and the low-beta constraints, a set of 100 configurations<sup>7</sup> together with their Monte Carlo robustness evaluations has been found to be sufficient to achieve a good fit of the surrogate model and, thus, to derive the important features. The computation effort to collect this initial dataset of configurations which satisfy the requirements and, thus, have a nonzero robustness depends on the success rate of the LMDIF matching step for this case. This success rate is 2.89% and, thus, collecting the initial dataset requires an additional  $0.0289^{-1} \cdot 100 \approx 3460$  LMDIF matching steps and 100 robustness evaluations. Therefore, it is rather the collection of the initial dataset which is used for feature importance that drives the computation cost of the optimization procedure. Thus, the average total compute time which is required to find a configuration with robustness  $\rho \geq 0.98$  is about  $7.3 \pm 0.2$  hours. Finding a configuration with robustness  $\rho \geq 0.99$  increases the compute time only slightly to  $8.2 \pm 0.2$  hours due to the constant overhead from collecting the initial feature importance dataset. Compared with the datasets that are obtained without feature importance, the fraction of produced configurations with robustness  $\rho \geq 0.98$  and  $\rho \geq 0.99$  is increased by a factor of at least 19 and 23, respectively. Hence, it would take about 4033 LMDIF evaluations and 117 robustness evaluations, totaling to  $8.1 \pm 0.2$  hours, to find a configuration with robustness  $\rho \geq 0.98$  without using feature importance, but, at the same time, it would require 19 177 LMDIF evaluations and 554 robustness evaluations,

---

<sup>7</sup>It is noted that for Figure 4.12 250 configurations have been used to fit the model, but these configurations were taken from the baseline dataset, i.e., obtained without usage of a global optimizer or the additional low-beta constraints for LMDIF. When these two improvements are used, the robustness of produced configurations is increased such that already 100 configurations are sufficient to achieve a good fit.



totaling to  $39 \pm 1$  hours, to find a configuration with robustness  $\rho \geq 0.99$ . Also, it is noted that a configuration with  $\rho = 0.99$  is twice as robust as a configuration with  $\tau = 0.98$  since the volume of invalidating quadrupole errors is reduced by factor of two. Or, in other words, a configuration with  $\tau = 0.98$  has a chance of failing the beamline requirements that is twice as large as for a configuration with  $\tau = 0.99$ . Furthermore, in most cases it will be desirable to find not only one but many configurations which meet the desired robustness in order to compare them for other properties such as minimal power consumption, for example. The presented improvements allow for generating high robustness configurations in a fast manner, once the initial warm-up phase of collecting the feature importance dataset is surpassed. After the additional LMDIF constraints from derived from the feature importance method are in place, it takes about  $17.6 \pm 0.5$  minutes to generate a configuration with  $\rho \geq 0.98$  and  $70.1 \pm 1.8$  minutes to generate a configuration with  $\rho \geq 0.99$ . Compared to the scenario without using feature importance this reduces the required compute time by a factor of, respectively,  $27.76 \pm 0.04$  and  $33.13 \pm 0.05$ . Due to the small LMDIF success rate in all cases, the majority of the compute time is contributed by the LMDIF matching step<sup>8</sup> while robustness evaluation contributes to a smaller degree.

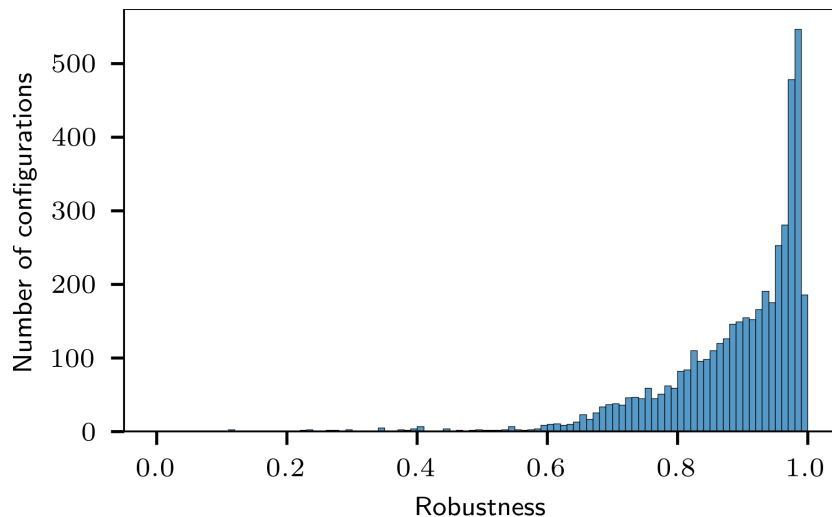


**Figure 4.16:** Histogram plot of the robustness scores of 4480 configurations that are obtained by combining all three improvement methods, i.e., using a global optimizer as well as the low-beta and feature importance constraints for LMDIF. By using these three improvement methods together, the robustness of produced configurations is greatly improved compared to the baseline procedure (see Figure 4.6). This dataset contains slightly fewer configurations than the one shown in Figure 4.9. This is because the generation of each dataset ran for a fixed amount of time. Using the differential evolution optimizer rather than random search requires additional compute time and, thus, the number of configurations that could be produced in the available amount of time is slightly smaller for the case which uses the optimizer.

Table 4.2 compares the LMDIF success rates for the various cases, using the different improvement methods, as well as indicates the fraction of high robustness configurations that is produced for each case.

<sup>8</sup>The total LMDIF compute time is influenced by the LMDIF "call limit" setting. A smaller call limit may cause LMDIF to spend less compute time searching for satisfying configurations in situations where it is infeasible given the random starting point but, on the other hand, it might also discard configurations which, otherwise, would turn out as satisfying when more compute time was allowed.

#### 4. Mitigating the effect of quadrupole errors on beam transfer lines with robust optimization

**Table 4.2:** LMDIF success rates and fraction of high robustness configurations for the different stages and cases. The LMDIF success rate is the percentage of random  $K_1L$  starting points in a dataset that resulted in a successful optimization via the LMDIF matching routine from MADX, i.e., where the  $K_1L$  produced by LMDIF comprised a beamline configuration that satisfied the beamline requirements. There are different reasons why the matching for a given  $K_1L$  starting point might not be successful, e.g., because the matching routine reached the limits for the  $K_1L$  values or because a local minimum is reached which, however, may not satisfy the beamline requirements.  $\rho \geq \tau$  indicates the percentage of configurations in a dataset that have robustness greater than or equal to  $\tau$ ; "—" means that no such configurations were contained in the respective dataset.  $N$  denotes the size of each dataset. The datasets have slightly different sizes, because generation of each ran for a fixed amount of time, capped at 4500 configurations (except for the baseline). The optimizer requires additional compute time and, thus, the number of configurations is slightly smaller for the cases which use the optimizer. LB refers to the case where only the additional LMDIF constraints are used which limit the excursions of the beta function in the upstream part of the beamline ("low-beta"; see section 4.3.1). OPT-LB refers to the case where additionally a differential evolution algorithm is used as a global optimizer to produce initial  $K_1L$  starting points for LMDIF instead of the random search (see section 4.3.2). LB-FI refers to the case where, in addition to the low-beta constraints, the dedicated LMDIF constraints obtained via feature importance are used (see section 4.3.3). Finally, OPT-LB-FI refers to the case where all three improvement methods are combined, i.e., using a global optimizer as well as the low-beta and feature importance constraints for LMDIF.

|           | $N$   | LMDIF-1.8 | LMDIF-0 | Combined | $\rho \geq 0.98$ | $\rho \geq 0.99$ |
|-----------|-------|-----------|---------|----------|------------------|------------------|
| Baseline  | 10000 | 2.53 %    | 89.7 %  | 2.27 %   | 0.05 %           | —                |
| LB        | 4500  | 2.42 %    | 93.4 %  | 2.26 %   | 0.02 %           | —                |
| OPT-LB    | 4375  | 3.00 %    | 96.2 %  | 2.89 %   | 0.87 %           | 0.18 %           |
| LB-FI     | 4500  | 3.97 %    | 98.1 %  | 3.89 %   | 0.02 %           | —                |
| OPT-LB-FI | 4480  | 4.43 %    | 99.8 %  | 4.43 %   | 16.3 %           | 4.15 %           |

While the above described improvement methods allow to find robust beamline configurations in a compute efficient manner, the procedure assumes an error-free beamline description except for the considered quadrupole errors. In reality, however, different errors such as uncertainty of the location of quadrupoles along the beamline or uncertainty of the Twiss parameters at the beginning of the beamline might play a role. While these types of errors could be included by extending the definition of beamline robustness also to these other errors sources, it is still possible to obtain robust configuration even when these errors are not included. Most notably, these types of errors are expected to be static while quadrupole errors might change over time or assume different values due to, e.g., thermal drifts of the power converters or magnetic hysteresis when serving multiple target stations in an alternating fashion. The effect of these types of errors is discussed in the following sections.

##### 4.3.5 Error analysis

In the following, the influence of model bias on the results obtained for robustness is studied. Model bias includes any error of the model which is not captured by the definition of robustness. While the deviations in quadrupole strength are considered as possible errors for the computation of robustness, deviations of other lattice parameters are possible, too. In the following, the effect of Twiss parameter errors and deviations of the longitudinal positions of the quadrupoles on the robustness of the selected configurations is studied. It is noted that instead of assessing these types of errors as a post-computational step, they could be included

directly in the definition of the robustness. However, as will be shown below, the effect of this model bias is manageable.

#### 4.3.5.1 Deviation of Twiss parameters at beginning of beamline

The Twiss transformation along a beamline is a linear transformation in the Twiss parameters:

$$\begin{pmatrix} \beta \\ \alpha \\ \gamma \end{pmatrix}_{target} = M \cdot \begin{pmatrix} \beta \\ \alpha \\ \gamma \end{pmatrix}_{start} \quad (4.18)$$

where  $M$  is the Twiss transfer matrix of the beamline from start to target according to equation 4.7.  $M$  is a function of the various quadrupole strengths and, thus, the quadrupole errors cause a change of the matrix  $M$ . Therefore, when the initial Twiss parameter  $(\beta, \alpha, \gamma)_{start}$  have an associated error, then this error will propagate linearly to the beta function at the target. Thus, the Twiss error is expected to change the beta margin at the target, but the effect on the beta variations is expected to be small, since the matrix  $M$  remains unchanged.

#### 4.3.5.2 Deviation of quadrupole positions

A change  $\Delta_s$  in the position of a quadrupole leads to a local variation of the following form:

$$\begin{pmatrix} 1 & L_d + \Delta_s \\ 0 & 1 \end{pmatrix} \cdot \mathbf{Q} \cdot \begin{pmatrix} 1 & L_u - \Delta_s \\ 0 & 1 \end{pmatrix} \quad (4.19)$$

where  $L_u$  and  $L_d$  are, respectively, the drift length upstream and downstream of the quadrupole which is represented by its transfer matrix  $\mathbf{Q}$ . This change is translated to the Twiss transfer matrix according to equation 4.7 and, thus, the influence on the beta function at the target is a nonlinear function in  $\Delta_s$  with lengthy coefficients though for  $\Delta_s \ll 1$  a linear approximation is justified.

To estimate the effect of such model bias, the robustness scores of Figure 4.16 are reevaluated via Monte Carlo simulations by adding random Twiss parameter variations in the range  $-5\%$  to  $5\%$  and random longitudinal position errors for the quadrupoles in the range  $-10$  mm to  $10$  mm for each leaf configuration. Adding a different random model bias to each leaf configuration, rather than a bias which is fixed for all leaf configurations, provides a statistical estimate for the upper boundary of the expected robustness decline. Figure 4.17 shows the reevaluated robustness scores under the random model bias variations. It can be observed that these decline significantly and leave no high robust configurations. However, it should be emphasized that in reality, the model bias is fixed for a given configuration, so the actual possible variation in all leaf configurations is smaller. Also, such model bias will also lead to a degradation of the root configuration which would be fine tuned in reality, e.g., increasing the beta margin.

Figure 4.18 shows the variations of beta functions at the target for a configuration with robustness 0.9949. These variations represent the various new root configurations that may emerge from the model bias. The quadrupole variations are not shown in this Figure but they induce a spread of beam sizes on top of the spread induced by model bias which leads

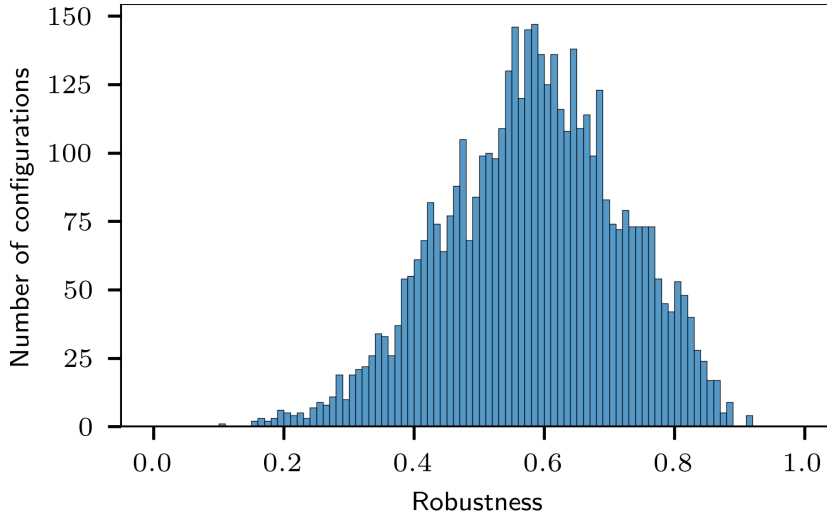


**Figure 4.17:** Reevaluated robustness scores from Figure 4.16 under additional random Twiss parameter variations and longitudinal position errors for the quadrupoles. The ranges for the model bias were, respectively,  $-5\%$  to  $5\%$  (Twiss parameters) and  $-10\text{ mm}$  to  $10\text{ mm}$  (quadrupole positions).

to a further decrease of robustness. As can be observed in the Figure, some model biases also result in beta function which yield a larger beta margin (the left lower quadrant), but all other variations decrease the beta margin in at least one dimension and thus decrease the expected robustness. Since the beta margin in vertical dimension is large, the model bias mostly affects the horizontal dimension and, thus, approximately half of the variations decrease the robustness, so on average it should be 0.5. And indeed, it turns out to be 0.6458.

## 4.4 Experiment at GSI Helmholtzzentrum für Schwerionenforschung

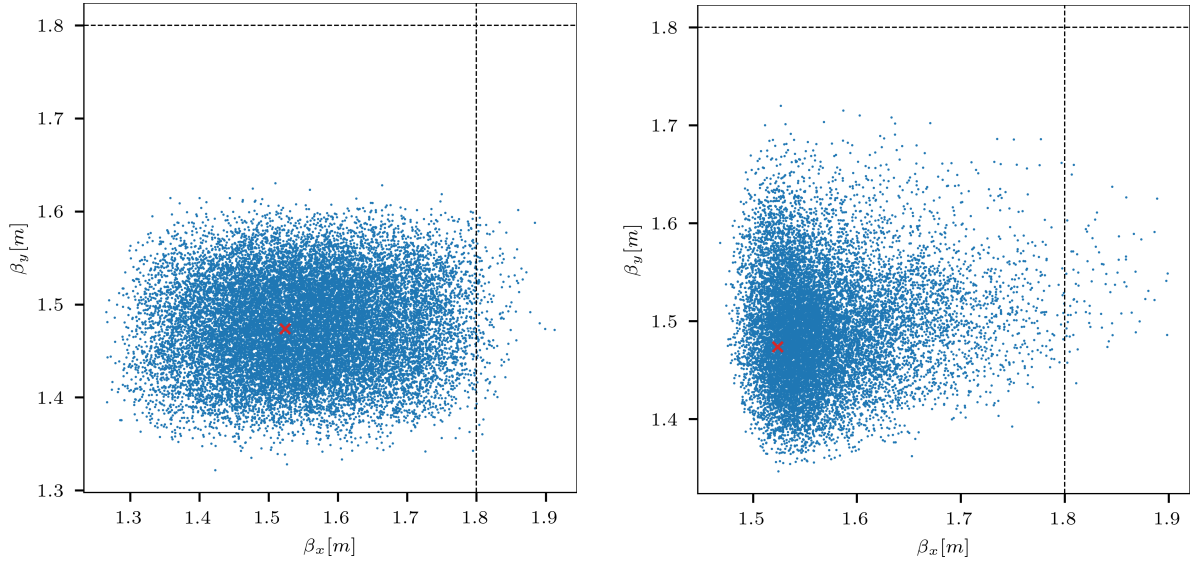
This section compares the measurement of quadrupole configurations with various degrees of beam size variations at the target fluorescence screen TH2DFA against the corresponding findings from simulations. The TH2DFA screen is chosen because the corresponding camera allows to run in triggered mode and can be read out with the help of a Java application and, thus, allows to fully automatize the measurement. Also, the camera is calibrated and directly computes one-dimensional beam profiles from the measured images. Four configurations are tested, one of which shows particularly small beam size variations in the simulated data, i.e., representing a robust configuration. The simulated beta functions of the four configurations are shown in Figure 4.20.

### 4.4.1 Preparation

A fast extraction pattern to the HTP experimental area <sup>9</sup> is used with  $^{40}\text{Ar}^{18+}$  at an energy of 300 MeV per nucleon. Fast extraction ensures that the optics and, thus, the Twiss parameters remain constant during the spill as opposed to quadrupole-driven slow extraction (see section 2.6.1.3). No other pattern is running in parallel in order to minimize the effect of

---

<sup>9</sup>The beam is dumped at the end of the beamline.



(a) Influence of Twiss parameter errors and longitudinal positions errors of quadrupoles.

(b) Influence of random quadrupole strength errors.

**Figure 4.18:** Left: Variations of the beta function at the target screen under the influence of various model errors for a configuration with robustness 0.9949. Errors in the initial Twiss parameters at the beginning of the beamline as well as errors of the longitudinal positions of quadrupoles are considered to be model bias and, thus, cause a shift of the original configuration in terms of the beta functions at the target. The ranges for the model bias are, respectively,  $-5\%$  to  $5\%$  (Twiss parameters) and  $-10\text{ mm}$  to  $10\text{ mm}$  (quadrupole positions).

Right: Variations of the beta function at the target screen for the same original beamline configuration but now under the influence of quadrupole errors. For a real beamline, there will be a combination of both, i.e., a set of model bias errors as in the left plot and a set of quadrupole errors as in the right plot.

In both plots, the red cross indicates the beta functions of the original root configuration without model bias and without quadrupole errors.

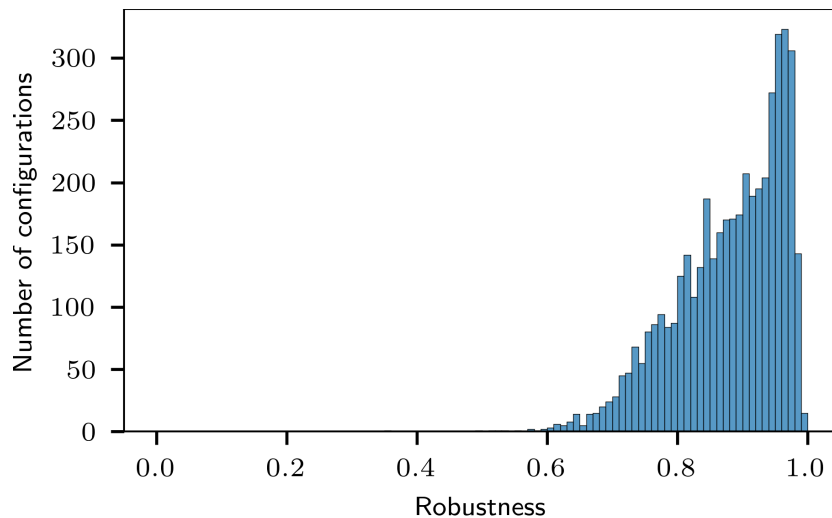


**Figure 4.19:** Reevaluated robustness scores from Figure 4.16 under additional random Twiss parameter variations and longitudinal position errors for the quadrupoles. The ranges for the model bias were, respectively,  $-5\%$  to  $5\%$  (Twiss parameters) and  $-10\text{ mm}$  to  $10\text{ mm}$  (quadrupole positions). Before adding the random quadrupole errors which are used to estimate of the configuration via Monte Carlo sampling, the beamline configuration containing the Twiss errors and quadrupole position errors has been fine tuned with an additional LMDIF-0 step. This step is to emulate the fine-tuning that would be done for a real beamline by e.g., the operating crew.

## 4. Mitigating the effect of quadrupole errors on beam transfer lines with robust optimization

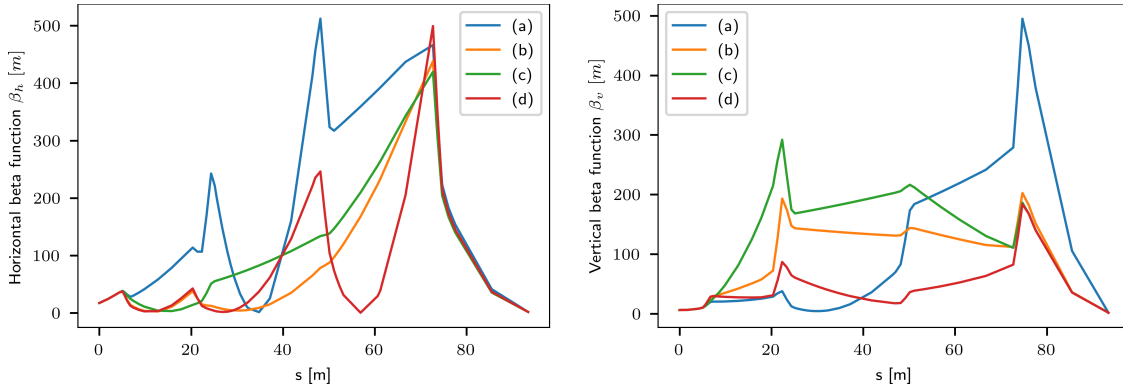


**Figure 4.20:** Beta functions for the four TH2DFA beamline configurations which have been tested during the measurement. The labels (a)-(d) coincide with the four subplots in Figure 4.26. Configuration (d) is the robust configuration.

magnetic hysteresis in the quadrupoles. The experiment uses the beamline until the TH2DFA fluorescence screen, as described in section 4.1. The corresponding UEye-camera can be controlled via the Cupid application and allows for setting a trigger for data taking. The trigger `SIS18:CMD_BEAM_EXTRACTION` is used, i.e., data is taken once per spill. The TH2DFA camera is calibrated and the camera software readily computes one-dimensional beam profiles from the obtained images.

### 4.4.1.1 Emittance measurement

The bending magnets along the beamline have a narrow vertical aperture and, hence, scraping might occur if the beam size is too large. Therefore, the vertical emittance for each tested beamline configuration is measured via a quadrupole scan (see section 2.6.2), using the GTH2QD12 quadrupole and the TH2DFA fluorescence screen. This allows for estimating the effect of scraping by comparing to a reference measurement for the emittance in the synchrotron which is performed with the SIS18 Ionization Profile Monitor (IPM). Because the beamline is not dispersion-free, measuring the horizontal emittance would need additional information about the momentum spread and dispersion. However, the horizontal aperture of magnets along the beamline is much larger than the vertical aperture, so the vertical dimension is critical with regard to scraping.

### 4.4.1.2 Java application for automatizing the measurement

A Java App has been created to automatically control the quadrupoles during the measurement via the LSA API. The TH2DFA camera is controlled via FESA and it can be connected to via the Java API for Parameter Control (JAPC). The same Java App is used for both, applying artificial random quadrupole errors and performing the quadrupole scan. From the perspective of the Java App, the only difference between the artificial quadrupole errors and the quadrupole scan is the specific sequence of updates of quadrupoles' strengths that it has to process during the measurement:

- In case of artificial quadrupole errors, the updates are random updates of the strengths of all quadrupoles along the beamline.

- In case of the quadrupole scan, the updates are sequential updates of the strength of a single quadrupole.

Thus, only that part of the software that is responsible for generating these updates needs to be exchanged between the two measurements; the remainder of the software stays the same. The Java App uses the `de.gsi.lo.bi.cam.device.CameraConnections` class to add a callback to the `imageDataProperty`. This callback is invoked every time the camera is triggered by the control system (trigger `SIS18:CMD_BEAM_EXTRACTION`). The callback function then saves the camera data (image and profiles) and subsequently generates a new update for the quadrupoles' strengths which is submitted via the LSA API. The quadrupole updates and camera data are saved with timestamps, so they can be assigned later during data analysis. Figure 4.21 shows a diagram of the various steps that are performed by the Java App. The Java App is available on the GSI Gitlab server [3]; the main classes are `BeamlineRobustness` (quadrupole errors) and `BeamlineRobustnessLinear` (quadrupole scan).

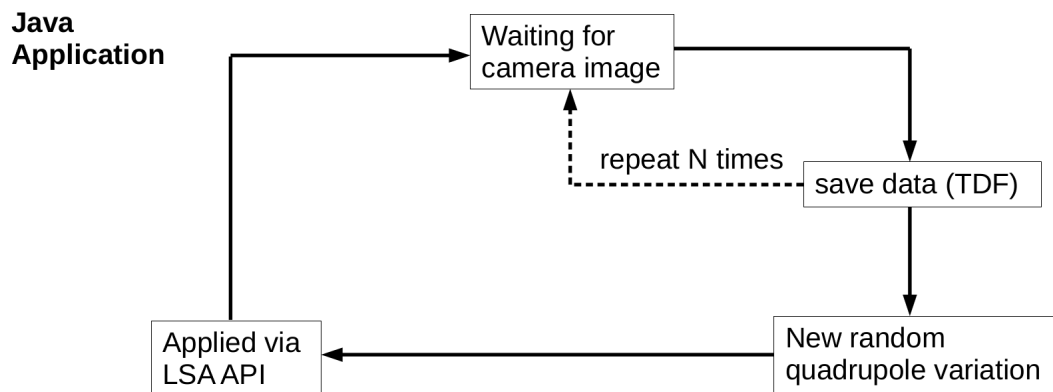


**Figure 4.21:** Diagram for the various steps in the Java App for automated quadrupole control to measure beamline robustness. For the quadrupole scan, the step `New random quadrupole variation` is replaced by a dedicated update of the strength of the quadrupole used for the scan. For a given quadrupole setting, the measurement is performed  $N$  times (e.g.,  $N = 5$ ) in order to obtain an estimate for the measurement uncertainty of the recorded beam sizes.

#### 4.4.2 Results

In the past, significant losses at the bending magnet `GTH3MU1` have been observed and these losses, registered by a nearby Beam Loss Monitor (BLM), might result in an interlock which prevents further accelerator operation. Thus, the setup of each new beamline configuration is started at reduced beam intensity to make sure that the steering is correct and only then the intensity is increased to its nominal value. Saturation at the target screen must be avoided though. Beam steering was performed by the operator crew and good beam focus at the target screen has been achieved. However, during data analysis it has been observed that beam scraping has occurred nevertheless, as shown exemplary in Figure 4.22 for a vertical beam profile. This scraping influences the beam size estimates from the measured beam profiles which are obtained by applying a Gaussian fit to the inner part of the profiles. Because scraping has occurred upstream of the target screen, most likely at one of the bending magnets, the recorded beam profiles may result in distorted beam sizes also for the inner part of the profiles.

#### 4. Mitigating the effect of quadrupole errors on beam transfer lines with robust optimization

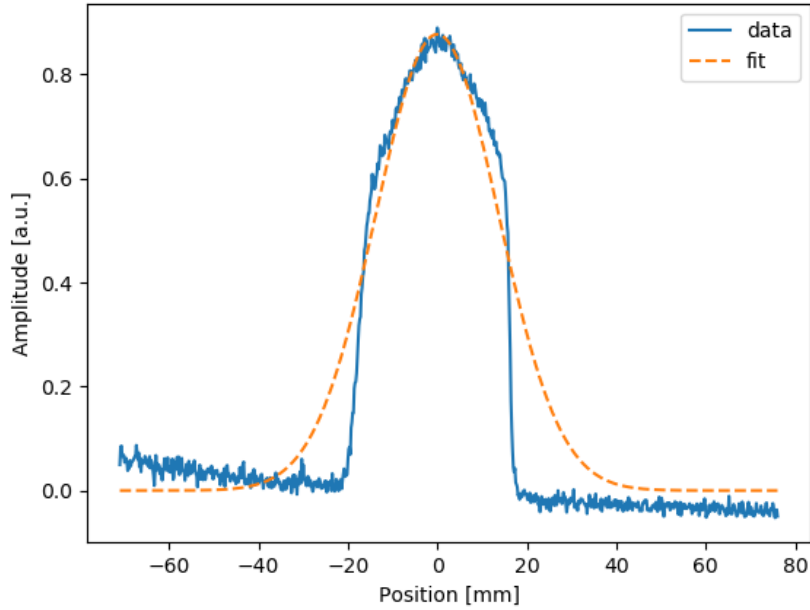
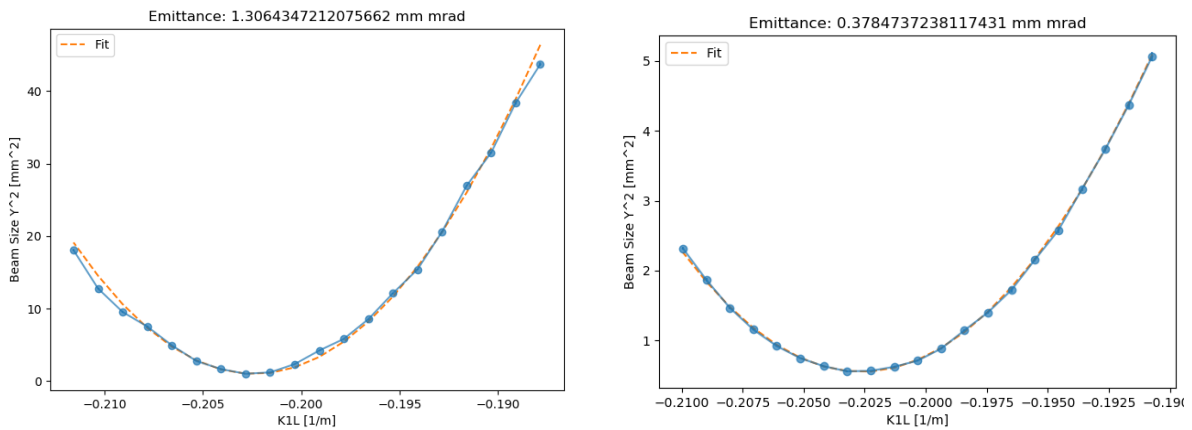


**Figure 4.22:** Example for beam scraping in vertical dimension which might result in a poor fit of the beam profile. Also, since the scraping has occurred upstream, the resulting profiles at the screen are altered, too.

##### 4.4.2.1 Quadrupole scan

The quadrupole scan has been performed as described in section 4.4.1.1 using the GTH2QD12 quadrupole which is located upstream of the TH2DFA screen. Figure 4.23a shows the quadrupole scan for the robust configuration while Figure 4.23b shows the quadrupole scan for one of the non-robust configurations. It can be observed that the estimated emittance for the non-robust configuration is smaller than for the robust configuration which suggests the presence of beam scraping during the measurement.



(a) Quadrupole scan for the robust configuration.

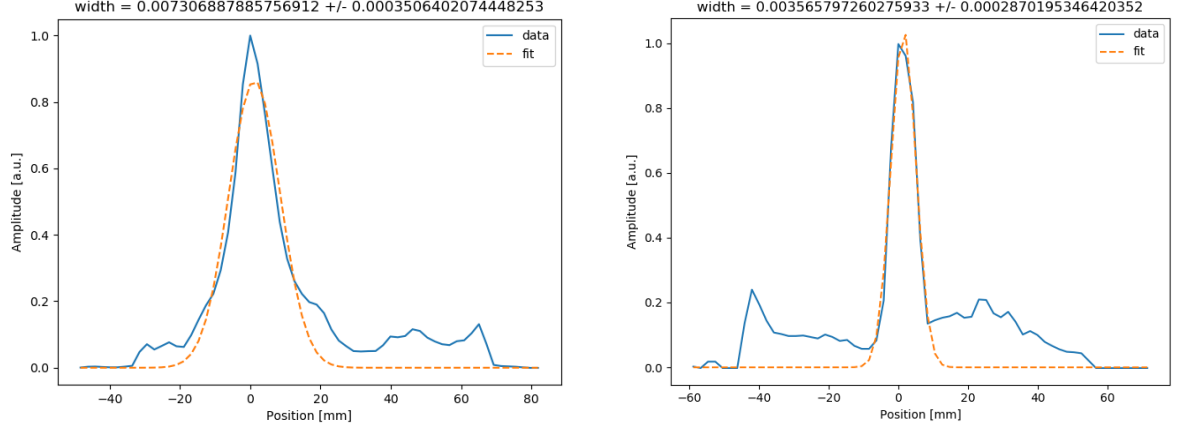
(b) Quadrupole scan for a non-robust configuration.

**Figure 4.23:** Quadrupole scan measurement for different beamline configurations. The GTH2QD12 quadrupole has been used for the measurement which is the quadrupole directly upstream of the target fluorescence screen TH2DFA.



#### 4.4.2.2 IPM measurement

The SIS18 IPMs are used to measure beam profiles in the synchrotron. The values for the emittance are estimated by using the nominal beta functions and dispersion from the MADX model at the location of the IPMs. A momentum spread of  $\frac{\Delta p}{p} = 1 \times 10^{-3}$  is assumed. Figures 4.24a and 4.24b show the IPM measurement for horizontal and vertical dimension. The resulting values for the emittance are  $\epsilon_x = 3.40 \pm 0.40$  mm mrad and  $\epsilon_y = 1.84 \pm 0.30$  mm mrad.



(a) Horizontal beam profile in SIS18. The resulting emittance is  $\epsilon_x = 3.40 \pm 0.40$  mm mrad.

(b) Vertical beam profile in SIS18. The resulting emittance is  $\epsilon_y = 1.84 \pm 0.30$  mm mrad.

**Figure 4.24:** Measured beam profiles obtained with the IPMs at SIS18 during flattop.

#### 4.4.2.3 Measurement of beam size variations

The variations of beam size at the target screen TH2DFA have been measured by applying artificial random quadrupole errors of similar magnitude as the ones that have been applied in the simulations (see section 4.2.3). The simulations produce values for the beta functions and dispersion at the target screen and these are converted to corresponding beam size estimates by taking into account the measured vertical emittance from the quadrupole scan for each tested configuration and the measured horizontal emittance from the IPM measurement; since the horizontal aperture along the beamline, and especially at the bending magnets, is much larger than the vertical aperture, it is expected that the horizontal emittance is preserved throughout the beamline and, thus, the value obtained from the IPM measurement remains valid. The dispersion is obtained from simulations and a momentum spread of  $\frac{\Delta p}{p} = 1 \times 10^{-3}$  is assumed. The beam size is then computed as

$$\sigma_{x,y} = \sqrt{\epsilon_{x,y}\beta_{x,y} + \left(\frac{\Delta p}{p}D_{x,y}\right)^2} \quad (4.20)$$

where  $\epsilon_{x,y}$  is the measured emittance,  $\beta_{x,y}$  and  $D_{x,y}$  are, respectively, the beta function and dispersion obtained from simulations and  $\frac{\Delta p}{p}$  is the momentum spread. The robustness of configurations is computed by assuming the  $\pm 250$   $\mu\text{m}$  interval around the nominal beam sizes to be satisfying. In order to differentiate the effect of the artificial quadrupole errors on the beam size from the effect of natural fluctuations which are present in the accelerator, a so-called baseline measurement has been performed. During this baseline measurement,

#### 4. Mitigating the effect of quadrupole errors on beam transfer lines with robust optimization

---

no artificial quadrupole errors have been applied and the beam size has been recorded over multiple spills. Therefore, the beam size variations from this baseline measurement represent the natural fluctuations of the beam size which are present in the accelerator. Figure 4.26 shows the measured beam size variations together with the variations obtained from the simulated data. The configuration in Figure 4.26d shows particularly small beam size variations which is reflected by the measured data as well. While the variations of beam size agree well for the configurations in Figure 4.26b and Figure 4.26d, the configurations in Figure 4.26a and Figure 4.26c show reduced beam size variations in the measured data as compared to the simulated data. A possible reason is that the larger beam size variations induced by the quadrupole errors also modified the beam size along the beamline in a way that caused scraping of the beam by hitting the aperture. For large variations, this might occur in the horizontal dimension as well. Along the beamline only a few beam loss monitors are installed and so beam loss could not be measured directly, however, it is visible from the beam profiles such as in Figure 4.22. Also, because the beam is not centered in the quadrupoles, the artificial quadrupole errors cause additional steering of the beam which might provoke scraping. This additional steering is visible from the variations of beam position on the target screen during the measurement, as shown in Figure 4.25.

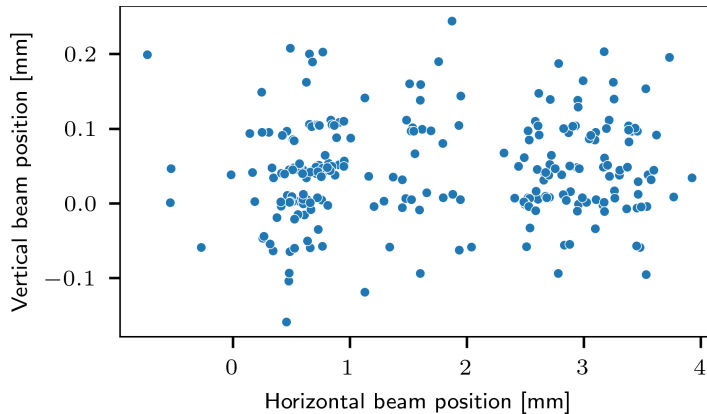


**Figure 4.25:** Variations of beam position at the target screen TH2DFA under the influence of artificial quadrupole errors. It can be observed that the changes in quadrupole strengths provoke significant beam movement, especially in the horizontal dimension. This is a result of the fact that the beam is not fully centered inside the quadrupoles and, hence, the quadrupoles cause additional steering of the beam.

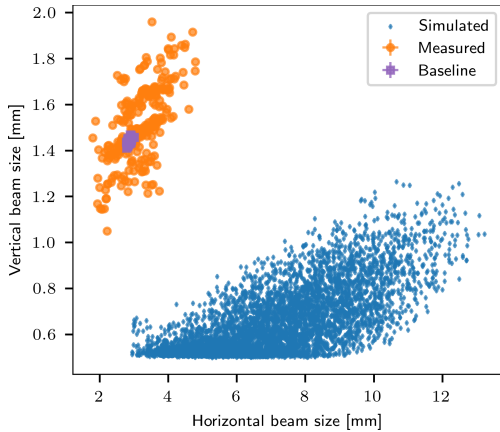
The offset of simulated versus measured beam size variations is likely a result of the imprecise knowledge of the initial Twiss parameters at the beginning of the HEST beamlines that were available for simulations<sup>10</sup>. This is similar to the effect shown in Figure 4.18.

### 4.5 Application to BIGKARL beamline at Forschungszentrum Jülich

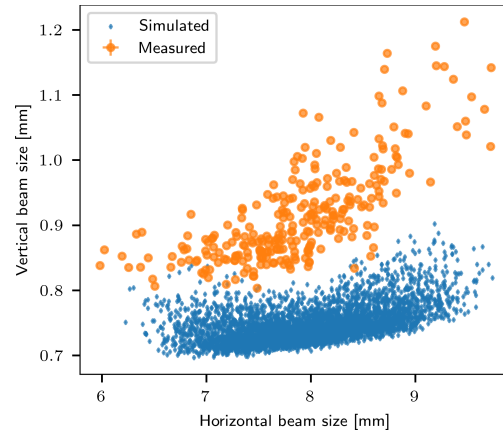
The other beamline, BIGKARL, is located at Cooler Synchrotron (COSY) at Forschungszentrum Jülich. This beamline transports the beam from COSY to the BIGKARL experimental

---

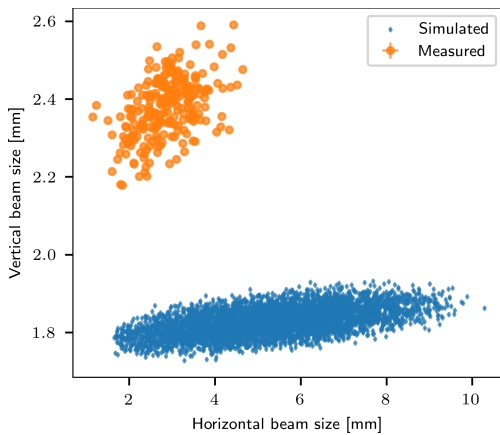
<sup>10</sup>The precise measurement of the initial Twiss parameters is planned by the HEST team for the engineering run 2023/2024.



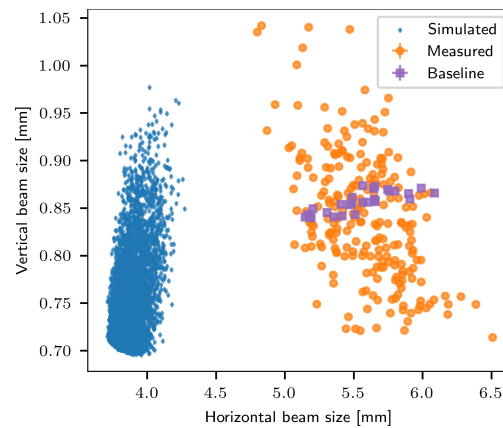
(a) Measured beam size variations for a non-robust configuration. The beam size variations resulting from the artificial quadrupole errors have a large magnitude which becomes also clear when comparing them to the beam size variations from the baseline measurement. The robustness of this configuration is 0.11.



(b) Measured beam size variations for a non-robust configuration. The beam size variations resulting from the artificial quadrupole errors have a large magnitude. The robustness of this configuration is 0.29.



(c) Measured beam size variations for a non-robust configuration. The beam size variations resulting from the artificial quadrupole errors have a large magnitude. The robustness of this configuration is 0.13.



(d) Measured beam size variations for a robust configuration. The beam size variations resulting from the artificial quadrupole errors have a small magnitude, also when compared to the beam size variations from the baseline measurement. While the variations along the y-axis might appear large, in fact, the extent of the y-axis is very small and so the beam size variations are small as well. The robustness of this configuration is 0.98.

**Figure 4.26:** Measured beam size variations for the configurations of the TH2DFA beamline. The subplots show four distinct beamline configurations where (a)-(c) are non-robust and (d) is a robust configuration. For configurations (a) and (d) also a baseline measurement has been conducted (shown as purple squares). This means that the beam size has been continuously recorded without applying any modifications to the accelerator or the beamline. Thus, all beam size variations in the baseline measurement are the result of the natural uncertainties present in the accelerator chain. On top of the baseline measurement, the dedicated beam size variations are shown as orange points. These beam size variations are the result of the artificial quadrupole errors that have been applied over the course of the experiment. Each orange point corresponds to different set of random errors that have been applied to the quadrupoles' strengths. In addition to the measured data, also the beam size variations from the simulated MADX model are shown. The difference between the simulated and measured data is likely a result of the limited precision with which the Twiss parameters at the beginning of the beamline are known and which have been used during simulations. Also, beam scraping during the experiment likely affects the measured beam profiles.

#### 4. Mitigating the effect of quadrupole errors on beam transfer lines with robust optimization

area. The beamline consists of a common part which is located upstream of the BIGKARL-specific part. From the common part various other beamlines branch off as can be seen in Figure 4.27. The optics of the common upstream part must remain fixed during the experiment and, therefore, only the downstream part of the beamline which exclusively leads to the BIGKARL experiment is considered. In the following, this downstream part is simply referred to as "BIGKARL beamline". The BIGKARL beamline, i.e., the BIGKARL specific part, has an overall length of about 40 m and it consists of twelve quadrupoles with arbitrary polarity. The first four quadrupoles have individual power supplies and among the remaining eight quadrupoles there are four pairs distributed in two bracketing patterns (Q45, Q46 and Q48, Q49) as can be seen from the labels of Figure 4.28 which shows the beta functions of an example beamline configuration. Thus, there are eight degrees of freedom in terms of the quadrupoles' power supplies.

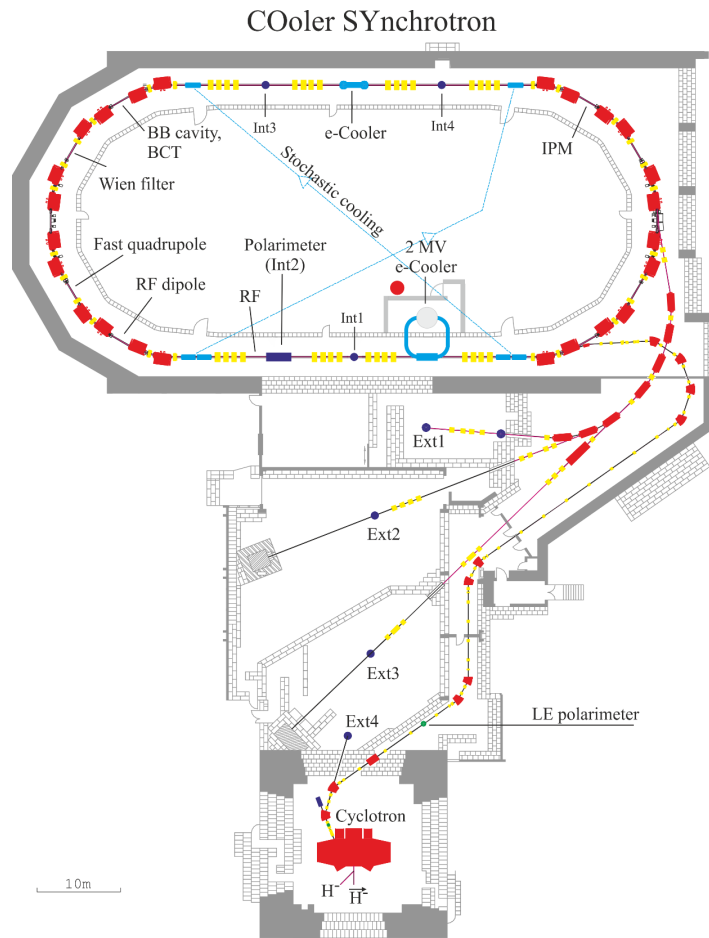


**Figure 4.27:** Schematic of COSY and the beamlines leading to the experimental areas including BIGKARL [99, Courtesy of Forschungszentrum Jülich]. The BIGKARL experimental area is marked with "Ext3" in the schematic. Bending magnets are depicted with red and quadrupoles are depicted with yellow color.

When comparing the description of the BIGKARL beamline to the description of the TH2DFA beamline in section 4.1, it can be seen that the two beamlines are quite different with respect to the installed quadrupoles. Nevertheless, the same methods for identifying robust configurations can be used for both beamlines. This emphasizes the general nature of the methods as well as emphasizes that they can be applied to a variety of beamlines.

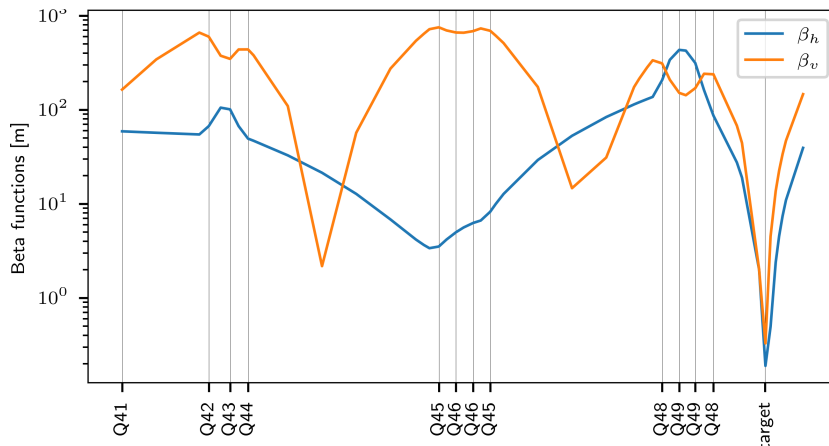


**Figure 4.28:** Beta functions for an example configuration of the BIGKARL beamline. Each vertical line indicates a quadrupole. The labels on the horizontal axis indicate the power supplies of the various quadrupoles. It can be seen that among the eight downstream quadrupoles there are four pairs of quadrupoles where each pair shares a power supply.

### 4.5.1 Simulations

The simulations of the BIGKARL beamline are realized with the help of MADX which is accessed through the cpyrad program [100] for increased efficiency. The MADX file contains the beamline definition as `line` definitions and the shared power supplies of quadrupoles are realized by placing the same quadrupole instance twice in a line (or, once, for the individual quadrupoles). The LMDIF matching step constrains the beta functions at the target profile grid to be less than 2 m in both dimensions. The beta functions cannot be chosen much smaller than these values since during the measurement, the resolution of the profile grid must be respected by the resulting beam size. However, since the corresponding optimization problem with 2 m as the threshold for beta functions is easily solvable<sup>11</sup>, an additional constraint on the dispersion is added, specifically  $-0.1 \text{ m} < D_x < 0.1 \text{ m}$ . The purpose of this additional constraint is to increase the difficulty of the underlying optimization problem, also in terms of the robustness. The beta functions are limited to  $\beta_{x,y} < 750 \text{ m}$  along the entire beamline and an additional constraint is added to limit the beta function to  $\beta_x < 300 \text{ m}$  and  $\beta_y < 600 \text{ m}$  on the first 52 m ( $\approx 77\%$ ) of the beamline in order to limit extreme excursions of the beta functions as discussed in section 4.3.1. The flexibility in terms of quadrupole polarity is respected by adjusting the lower and upper boundaries of the  $K_1$  values for LMDIF matching accordingly.

First, a set of 250 satisfying configurations is collected by using the low beta limit at the beginning of the beamline. These configurations are then inspected for their robustness and a random forest surrogate model is built to predict the robustness scores from  $K_1L$  values and corresponding Twiss data, as discussed in section 4.3.3. This allowed to derive additional constraints on the following variables. The strength of the final quadrupole's power supply Q49 is limited to be negative and the alpha function at the upstream Q48 quadrupoles is limited, too. These additional constraints are then used in a subsequent optimization run which also uses a global differential evolution optimizer as discussed in section 4.3.2. Using the additional

<sup>11</sup>Easy, in this context, means that the LMDIF success rate is very high and, therefore, the constraints are too weak to pose a challenging optimization problem also in terms of the robustness with respect to quadrupole errors.

## 4. Mitigating the effect of quadrupole errors on beam transfer lines with robust optimization

---

constraints obtained from feature importance as well as the global optimizer significantly improves the identified configurations in terms of their robustness.

### 4.5.2 Experimental setup and results

The experiment compares configurations with different robustness scores which are identified from previously simulated data. The stability of the resulting beam sizes at the target screen is used as robustness. This quantity is reliable also in the presence of, e.g., possible Twiss errors at the beginning of the beamline, and is expected to be influenced only very little by model bias errors, as discussed in section 4.3.5. Two configurations with high robustness in terms of their beam size stability are selected and one configuration with low robustness is selected. The goal of the experiment is to verify that the property of beam size stability is reflected by the measured beam size variations when artificial quadrupole errors are introduced to the real beamline.

#### 4.5.2.1 Preparation

The MWPC profile grid with label "4.5" is used as the target where the beam size variations are measured. This profile grid is located directly upstream of the experimental target. The wire spacing of this profile grid is 1 mm. The typical emittance from COSY is  $\epsilon_x \approx 0.5$  mm mrad and  $\epsilon_y \approx 3.0$  mm mrad. This must be taken into account for the selection of the beamline configurations in order to ensure that the resulting beam size is not substantially smaller than the resolution of the profile grid.

The control system allows to set the quadrupoles' strengths via a dedicated Tcl/Tk Graphical User Interface (GUI). This GUI communicates with the quadrupole device controllers over sockets. The same communication channel can be used from other software as well. Thus, a Python application has been created for automatically generating random quadrupole updates and for applying them via the socket connection. Figure 4.29 shows a flow diagram of the application logic. The code is available at [4].

All data is saved via the EPICS Archiver. Quadrupole strengths are logged via PVs `EXBL:BIGKARL:<device>:K1L` and `EXBL:BIGKARL:<device>:PERCENT`. The profile grid also saves its data via EPICS. The beam size at the profile grid is computed via a Gaussian fit by recording the fitted standard deviation (the EPICS PVs are `EXBL:MWPC:45:Profile:[XY]:Fit:Sigma`). A real-time subscription to the profile grid PVs has been established via PyEPICS [101] by adding custom callback functions. This allowed for monitoring the collected data in real-time in order to watch for potential problems with the data acquisition, e.g., if too few data points are collected by the profile grid. The Python application is synced with the COSY cycle via the PV `CTRL:CYCLE:T:10HZ` by waiting for the value that corresponds to the time during the cycle where extraction starts (15 s in cycle). The extraction is set to last 40 s in total. 10 s are allowed for the quadrupoles to assume their new strengths after they have been updated via the socket connection<sup>13</sup>. The time window for data acquisition for each new quadrupole setting was 7 s. The profile grid

---

<sup>12</sup> See footnote <sup>13</sup>.

<sup>13</sup>A large waiting time was chosen to be on the safe side; sometimes the quadrupoles showed a lag of a few seconds.

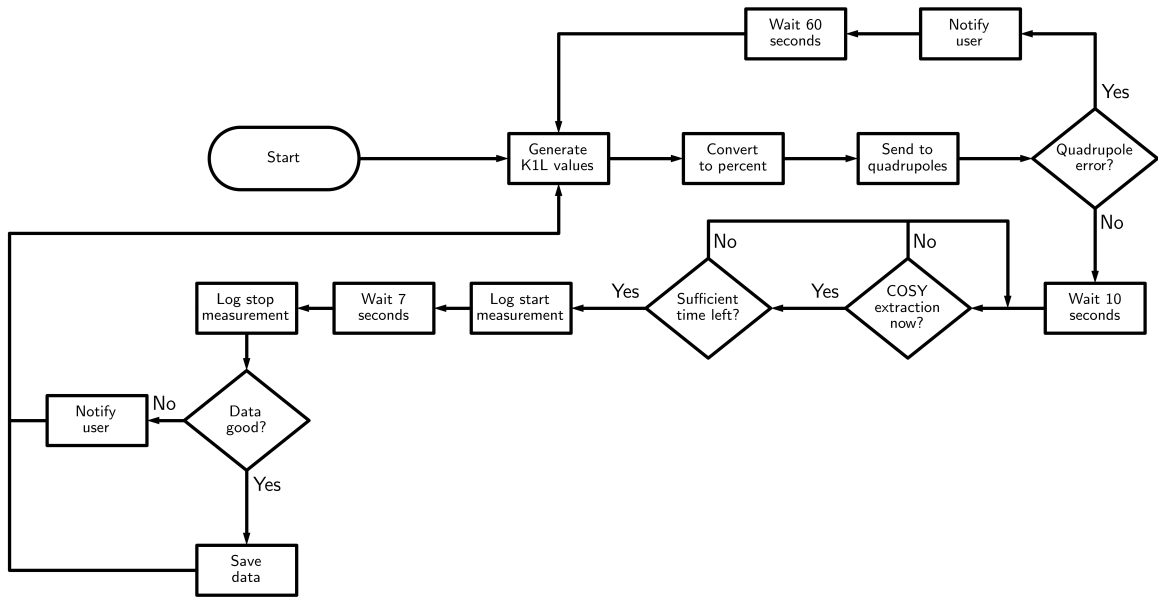


**Figure 4.29:** Flow diagram for the Python application for automatizing the BIGKARL measurement. After  $K_1L$  updates have been sent to the quadrupoles 10s are allowed for the quadrupoles to assume their new strengths<sup>12</sup>. The time window for data acquisition for a given quadrupole setting is 7s.

generates 3 profiles per second. In total, this allows to measure two quadrupole settings per extraction, i.e., per COSY cycle. Stochastic slow extraction is used which works by increasing the momentum distribution of the beam by imposing noise via the RF-system (see section 2.6.1.1). Particles then move into the resonance due to the nonzero chromaticity of the lattice. The optics of the synchrotron do not change during the spill and the momentum spread of extracted particles is small ( $\approx 5 \times 10^{-4}$ ).

#### 4.5.2.2 Results

Three different beamline configurations have been measured under the influence of artificially applied quadrupole errors. Two of the configurations are selected as robust configurations from the simulated data and, hence, are expected to yield only small beam size variations under the influence of the artificial quadrupole errors. For comparison, one non-robust configuration is selected as well which is expected to yield large beam size variations under the influence of the artificial quadrupole errors. The beta functions of the three configurations are shown in Figure 4.30.

For each of the three configurations, a dedicated baseline measurement has been performed in addition. During these baseline measurements, no artificial quadrupole errors have been applied and the beam sizes at the target grid have been recorded over some period of time. Therefore, this baseline measurement can be used to assess the natural fluctuations of the beam size at the target grid which originate from e.g., the upstream accelerator infrastructure such as the synchrotron. Following each baseline measurement, the artificial random variations have been applied to the quadrupoles' strengths and the beam size at the target profile grid has been continuously recorded. The measured beam size variations are shown in Figure 4.31 together with the natural beam size variations which have been recorded during the baseline

#### 4. Mitigating the effect of quadrupole errors on beam transfer lines with robust optimization

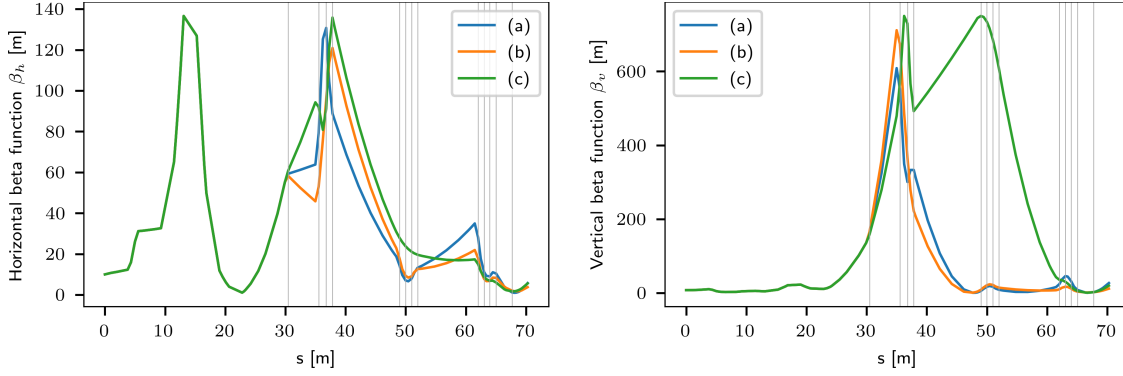
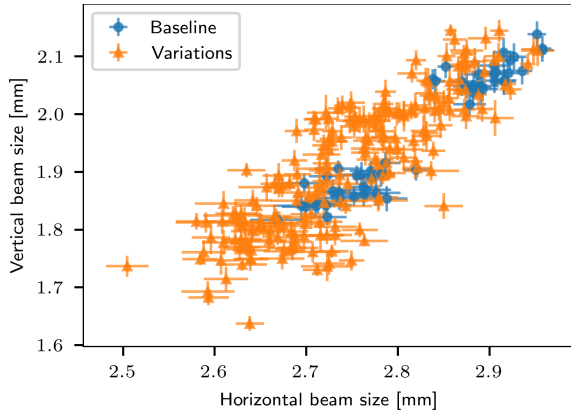


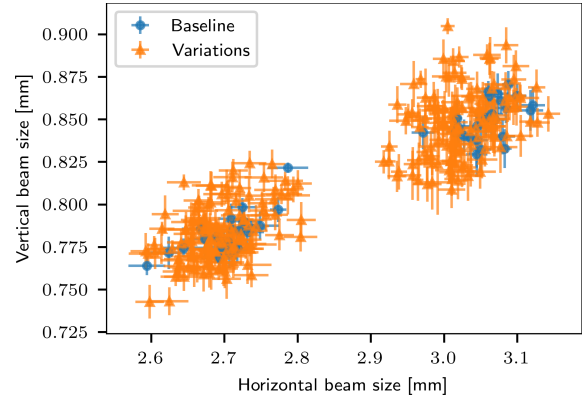
**Figure 4.30:** Beta functions of the configurations used for the measurement at the BIGKARL beamline. The labels (a)-(c) corresponds to the three sub-figures in Figure 4.31. The part of the beamline up to 30 m is the common part downstream of COSY from which the BIGKARL specific part of the beamline branches off. The common part of the beamline used the standard optics and, thus, is the same for each of the configurations. The vertical bars show the positions of the quadrupoles of the BIGKARL specific part of the beamline which have been varied during the experiment. The rightmost vertical bar shows the position of the target profile grid.

measurement. The robustness of configurations is computed by assuming the  $\pm 100 \mu\text{m}$  interval around the nominal beam sizes to be satisfying. The measurement was done with a long slow extraction process of 40 s which allowed to test two random quadrupole variations per spill. One measurement was toward the beginning of the spill and the other towards the end of the spill. The beam size did change slightly during the spill and, for that reason, there are two islands in the measured beam size data visible. They correspond to the two different points in time during the spill. As can be seen from Figures 4.31a and 4.31b, for the two robust configurations the applied quadrupole errors result in beam size variations which are comparable to the natural fluctuations recorded during the baseline measurement. That is, the applied quadrupole errors changed the beam size at the target only to a small degree. Complementary to that, the measurement of the non-robust configuration in Figure 4.31c shows substantially larger beam size variations for the same range of quadrupole errors as compared to the variations of the baseline measurement. Therefore, the quadrupole variations have a much larger impact on the resulting target beam size for the non-robust configuration as compared to the two robust configurations.

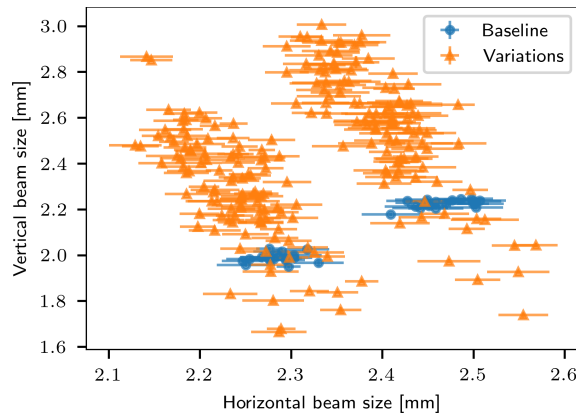




(a) Beam size measurement for a beamline configuration with high robustness. The recorded beam size variations under artificial quadrupole errors are comparable to the natural baseline fluctuations, i.e., the artificial errors affect the beam size only to a small degree. The robustness of this configuration is 0.85.



(b) Beam size measurement for a beamline configuration with high robustness. The recorded beam size variations under artificial quadrupole errors are comparable to the natural baseline fluctuations, i.e., the artificial errors affect the beam size only to a small degree. The robustness of this configuration is 0.97.



(c) Beam size measurement for a beamline configuration with low robustness. The recorded beam size variations under artificial quadrupole errors are significantly larger than the natural baseline fluctuations, i.e., the artificial errors greatly affect the beam size, especially in the vertical dimension. The robustness of this configuration is 0.32.

**Figure 4.31:** Measured beam size variations for the three different beamline configurations tested on the BIGKARL beamline. The blue points, labeled "baseline", represented a measurement of the beam size when nothing has been changed on the beamline or on the accelerator in general. That is, the blue baseline measurement represents the natural beam size fluctuations at the target profile grid that are present from the accelerator infrastructure. On top of that are the orange points, labeled "variations", which represent the measurement of beam size during when artificial quadrupole errors have been applied to the beamline. Each orange beam size variation corresponds to a different artificial random set of quadrupole errors that have been applied. For each spill from COSY, which lasted 40s, two sets of artificial random quadrupole errors could be applied and recorded in terms of the beam size measurement. One measurement was toward the beginning of the spill and the other towards its end. The beam size coming from COSY did change slightly during the spill and, for that reason, there are two islands of blue and orange points in the measured beam size data visible. They correspond to the two different points in time during the spill.



# 5

## Conclusions & Outlook

This thesis studied the dependency of quasi-degeneracy on the placement of BPMs and steerers for extracting linear optics and model errors from closed orbit measurements. It has been found that different BPM and steerer placements can noticeably affect the degree of quasi-degeneracy and, thus, influence the quality of the lattice information that is extracted from the measured orbit response matrix. These findings emphasize the importance of studying the effect of BPM and steerer placements during the design phase of new accelerators.

In order to investigate the influence of BPM and steerer placements, an analytical expression for the Jacobian matrix has been derived, relating quadrupole errors along with BPM and steerer gain errors to the orbit response matrix. This analytical Jacobian has been used to show which BPM and steerer placements cause the Jacobian to be rank deficient and, thus, cause the inverse problem to be ill-defined which outlines the theoretical limitations of the method. In a lattice, the consecutive placement of quadrupoles with neither BPM nor steerer in between can cause a rank deficiency in the Jacobian. When fitting either the horizontal or vertical ORM alone, segments of three or more consecutive quadrupoles cause a rank deficiency. When fitting the horizontal and vertical ORM together, segments of six or more quadrupoles cause a rank deficiency (or, for  $Q_x - Q_y = \text{integer}$ , segments of five or more quadrupoles). A rank deficiency in the Jacobian implies that the corresponding quadrupole strengths cannot be determined uniquely from the measured ORM data, even in the absence of BPM errors.

It has further been demonstrated that the analytical expression for the Jacobian can be used during the fitting procedure in place of the conventional numerical Jacobian which is computed via finite-difference approximation. A single Twiss computation is sufficient to construct the analytical Jacobian, which allows for substantially reduced computation time compared to the numerical Jacobian approach. The scaling of the computation in terms of the number of relevant lattice elements is improved by a factor  $N_{steerers} \times N_{quadrupoles}$  by using the analytical Jacobian approach. The inverse modeling process by using the analytical Jacobian approach has been tested with large scale simulations and also with dedicated measurements conducted at the heavy-ion synchrotron SIS18 at GSI. The fitting procedure has been tested in conjunction with various methods for mitigating quasi-degeneracy. The results obtained with the analytical Jacobian agree well with those obtained with the numerical Jacobian.

The developed fitting method, including the computation of the analytical Jacobian, has been implemented as a Python package and has been made available on the Python Package Index [1].

The measurement campaign at SIS18 has been prepared with a dedicated focus on reaching high precision for the measurement results. The measurements achieved an orbit uncertainty of  $\lesssim 1 \mu\text{m}$  and an orbit response uncertainty of  $\lesssim 5 \mu\text{m}/\text{mrad}$ . A dedicated Java application has been developed in order to fully automatize the measurement of the Orbit Response Matrix including the measurement of the dispersion. This Java application is available on the GSI Gitlab server [2]. The experimental setup as well as the Java application are extensible and, thus, form the basis for high precision ORM measurements also at other accelerators of the GSI and future FAIR campus.

In summary, chapter 3 of this thesis explored the dependency of quasi-degeneracy on the placement of BPMs and steerers and, thus, provides insight into how adequate numbers and locations for these devices can be chosen for newly designed lattices in order to allow for a tractable and well conditioned inverse problem. For large scale machines, such as LHC, with a large number of BPMs and steerers, the size of the corresponding Jacobian matrix may be too big to be fully utilizable. A practical solution is to select a subset of all ORM elements for the fitting procedure. A profound understanding of the impact of resulting BPM and steerer placements on the (quasi-)degeneracy can help in guiding the selection. In addition, using the analytical Jacobian during fitting can provide a more computationally efficient solution for inverse modeling by circumventing the method of computing the Jacobian via finite-difference approximation.

The second part of this thesis, chapter 4, studied the influence of quadrupole gradient errors on the performance of beam transfer lines with respect to the experimental requirements. In general, it is possible to estimate such quadrupole errors in a transfer line with methods similar to the ones presented in chapter 3, however, this requires dedicated beam time which is then not available for running the experiments. Therefore, chapter 4 studied a complementary, preventative approach with the goal to reduce the influence of possible quadrupole gradient errors on the performance of the beam transfer line. This has been achieved by identifying dedicated configurations for the strengths of quadrupoles in a transfer line which distinguish themselves by an increased robustness against possible quadrupole errors in terms of the resulting performance of the transfer line. Such robust quadrupole configurations allow for an increased stability of the beamline performance and, thus, guarantee stable experimental conditions while also reducing the time that operators must spend for re-tuning the transfer lines.

First, the concept of beamline robustness has been introduced in terms of the feasible quadrupole configurations. This allowed to assess and compare different quadrupole configurations in terms of their robustness with respect to quadrupole errors. Further, the beamline robustness has been assessed with the help of an analytical expression which has been derived from the propagation of Twiss parameters along the beamline. The analytically obtained results have then been verified by large-scale simulations which systematically explored the relevant quadrupole configuration space of the TH2DFA beamline. The simulations were based on MADX with the LMDIF optimization routine and, thus, allow for a high degree

---

of compatibility with existing lattice descriptions. With the help of this simulation data, further characteristic properties of robust quadrupole configurations have been identified. It has been found that the magnitude of the beta functions in the upstream part of the transfer line significantly affects the resulting robustness at the experimental target. Also, it has been found that by using a differential evolution optimization routine on top of the MADX internal LMDIF routine, the robustness of produced quadrupole configurations could be significantly enhanced. As a third improvement, the usage of a surrogate model for predicting robustness scores which has been fitted on Twiss data and  $K_1L$  strengths of the individual quadrupole configurations has been explored. It has been found that by applying a feature importance method to the fitted surrogate model, additional deciding parameters for the transfer line could be extracted. By inserting the extracted parameters and their boundaries as constraints into the original LMDIF routine, the robustness scores of produced quadrupole configurations could be significantly enhanced. Finally, the three improvement methods have been used in conjunction to significantly increase the computation efficiency for finding robust quadrupole configurations via dedicated simulations and optimization routines. This computation process is referred to as *robust optimization*.

Two beamlines have been used to present and experimentally verify the studied methods, one located at GSI Helmholtzzentrum für Schwerionenforschung and the other at Forschungszentrum Jülich (FZJ). While the polarity of quadrupoles of the GSI beamline is fixed, the polarity of those of the FZJ beamline is variable. In addition, some of the quadrupoles of the FZJ beamline share a common power supply. For that reason, the two beamlines represent quite different conditions, however, it has been shown that the presented methods can be used equally well for both beamlines. The theoretical findings and simulation results have been verified by dedicated experiments for both beamlines, at GSI and Forschungszentrum Jülich. The measurement data confirm the properties of quadrupole configurations in terms of the robustness of the beam size variation at the target profile monitors, as previously identified from simulation data. Dedicated software has been developed for both measurements in order to fully automatize the data taking and the artificial quadrupole variations. The software is available as Java and Python applications on the Gitlab servers of GSI and FZJ [3, 4]. These results form the basis for dedicated robust optimization for a wide variety of beamlines of the GSI HEST infrastructure as well as provide the tools for experimentally verifying the robustness property of employed quadrupole configurations. Also for the future transfer lines of the FAIR accelerator complex these results will be helpful and the developed methods can be reused.



# References

- [1] Dominik Vilsmeier. *accinv (version 0.1.0.post1)*. <https://pypi.org/project/accinv/>. 2022.
- [2] D. Vilsmeier and J. Fitzek. *Java App for automating the ORM measurement*. <https://git.gsi.de/d.vilsmeier/orm-measurement-april-2021-lsa-trim/-/tree/experiment-july-2021>. Commit a04a8da6. 2021.
- [3] D. Vilsmeier and J. Fitzek. *Java Application for Automated Control of Quadrupoles during Beamline Measurement*. <https://git.gsi.de/d.vilsmeier/orm-measurement-april-2021-lsa-trim/-/tree/beamline-robustness-measurement-2021-06-11>. Commit 9e549943. 2021.
- [4] Dominik Vilsmeier. *BIGKARL Messung*. <https://gitlab.cce.kfa-juelich.de/d.vilsmeier/bigkarl-messung>. Commit 04e325ef. 2021.
- [5] Rolf Wideröe. “Über ein neues Prinzip zur Herstellung hoher Spannungen”. In: *Archiv für Elektrotechnik* 21.4 (1928), pp. 387–406. DOI: 10.1007/BF01656341.
- [6] Max Steenbeck. “Device for producing electron rays of high energy”. US Patent 2,103,303. 1935. URL: <https://patents.google.com/patent/US2103303A/en>.
- [7] D. W. Kerst and R. Serber. “Electronic Orbits in the Induction Accelerator”. In: *Phys. Rev.* 60 (1 July 1941), pp. 53–58. DOI: 10.1103/PhysRev.60.53.
- [8] M. S. Livingston et al. “Design Study for a Three-Bev Proton Accelerator”. In: *Review of Scientific Instruments* 21.1 (1950), pp. 7–22. DOI: 10.1063/1.1745428.
- [9] J. P. Blewett et al. “Magnet. Part I—Design”. In: *Review of Scientific Instruments* 24.9 (1953), pp. 737–742. DOI: 10.1063/1.1770823.
- [10] John P. Blewett. “Accelerator design and construction in the 1950s”. In: *Pions to Quarks: Particle Physics in the 1950s*. Ed. by Laurie Mark Brown, Max Dresden, and LillianEditors Hoddeson. Cambridge University Press, 1989, pp. 162–179. DOI: 10.1017/CB09780511563942.016.
- [11] CERN. *Fifty years of the CERN Proton Synchrotron*. CERN-2011-004. edited by S. Gilardoni and D. Manglunki. 2011.
- [12] Ernest D. Courant, M. Stanley Livingston, and Hartland S. Snyder. “The Strong-Focusing Synchrotron—A New High Energy Accelerator”. In: *Phys. Rev.* 88 (5 Dec. 1952), pp. 1190–1196. DOI: 10.1103/PhysRev.88.1190.
- [13] Nicholas Christofilos. “Focussing system for ions and electrons”. US Patent 2,736,799. 1950. URL: <https://patents.google.com/patent/US2736799A/en>.

## REFERENCES

---

- [14] E.D Courant and H.S Snyder. “Theory of the alternating-gradient synchrotron”. In: *Annals of Physics* 3.1 (1958), pp. 1–48. ISSN: 0003-4916. DOI: 10.1016/0003-4916(58)90012-5.
- [15] J. B. Adams, M. G. N. Hine, and J. D. Lawson. “Effect of Magnet Inhomogeneities in the Strong-Focusing Synchrotron”. In: *Nature* 171.4360 (1953), pp. 926–927. DOI: 10.1038/171926a0.
- [16] J.B. Adams and M.G.N. Hine. *The choice of magnet sector arrangement in the strong focusing synchrotron*. Tech. rep. Geneva, Switzerland: CERN, 1953. URL: <http://cds.cern.ch/record/2262345>.
- [17] J. B. Adams. “The alternating gradient proton synchrotron”. In: *Il Nuovo Cimento Series 2*.supplement issue 1 (1955), pp. 355–374. DOI: 10.1007/BF02746095.
- [18] E. D. Courant. *Early history of the Cosmotron and AGS at Brookhaven*. Tech. rep. Upton, New York: Brookhaven National Lab., 1985. URL: <https://digital.library.unt.edu/ark:/67531/metadc1065208/>.
- [19] Akio Morita et al. “Measurement and correction of on- and off-momentum beta functions at KEKB”. In: *Phys. Rev. ST Accel. Beams* 10 (7 July 2007), p. 072801. DOI: 10.1103/PhysRevSTAB.10.072801.
- [20] Y. Ohnishi et al. “Optics Measurements and Corrections at the Early Commissioning of SuperKEKB”. In: *Proc. of International Particle Accelerator Conference (IPAC’16), Busan, Korea, May 8-13, 2016* (Busan, Korea). International Particle Accelerator Conference 7. Geneva, Switzerland: JACoW, June 2016, pp. 3782–3784. ISBN: 978-3-95450-147-2. DOI: doi:10.18429/JACoW-IPAC2016-THPOR007.
- [21] M. Lee and Scott Clearwater. “GOLD: Integration of model-based control systems with artificial intelligence and workstations”. SLAC-PUB-4396, Invited talk presented at the Workshop on Model-Based Accelerator Controls, Brookhaven National Laboratory, Upton, New York, August 17, 1987. Aug. 1987.
- [22] W.J. Corbett, M. J. Lee, and V. Ziemann. “A Fast Model-Calibration for Storage Rings”. In: *Proc. PAC’93*. Particle Accelerator Conference 15. May 1993, pp. 108–110.
- [23] J Safranek. “Experimental determination of storage ring optics using orbit response measurements”. In: *Nuclear Instruments and Methods in Physics Research Section A: Accelerators, Spectrometers, Detectors and Associated Equipment* 388.1 (1997), pp. 27–36. ISSN: 0168-9002. DOI: 10.1016/S0168-9002(97)00309-4.
- [24] Laurent S. Nadolski. “LOCO Fitting Challenges and Results for SOLEIL”. In: *ICFA Beam Dyn.Newslett.* 44 (2007), pp. 69–81.
- [25] L. S. Nadolski. “Use of LOCO at Synchrotron SOLEIL”. In: *Proceedings of EPAC08, Genoa, Italy*. 2008, pp. 3131–3133.
- [26] Martin Spencer. “LOCO at the Australian Synchrotron”. In: *ICFA Beam Dyn.Newslett.* 44 (2007), pp. 81–91.
- [27] R. Dowd et al. “Achievement of ultralow emittance coupling in the Australian Synchrotron storage ring”. In: *Phys. Rev. ST Accel. Beams* 14 (1 Jan. 2011), p. 012804. DOI: 10.1103/PhysRevSTAB.14.012804.



- [28] M. Aiba et al. “Comparison of linear optics measurement and correction methods at the Swiss Light Source”. In: *Phys. Rev. ST Accel. Beams* 16 (1 Jan. 2013), p. 012802. DOI: 10.1103/PhysRevSTAB.16.012802.
- [29] R. Bartolini et al. “High-level Software for Diamond Commissioning and Operation”. In: *Proceedings of EPAC 2006, Edinburgh, Scotland*. 2006, pp. 3065–3067.
- [30] G. Benedetti et al. “LOCO in the ALBA Storage Ring”. In: *Proceedings of IPAC2011, San Sebastián, Spain*. 2011, pp. 2055–2057.
- [31] M.J. McAteer et al. “Preliminary Results of Linear Optics From Orbit Response in the CERN PSB”. In: *Proc. of International Particle Accelerator Conference (IPAC’13), Shanghai, China, May 12-17, 2013* (Shanghai, China). International Particle Accelerator Conference 4. Geneva, Switzerland: JACoW, May 2013, pp. 1973–1975. ISBN: 978-3-95450-122-9.
- [32] J. Wenninger. “Orbit Response Measurements at the SPS”. CERN-AB-2004-009. 2004.
- [33] K. Fuchsberger. “LOCO for LHC”. Presented at the workshop on Optics Measurements, Corrections and Modeling for High-Performance Storage Rings. 2011.
- [34] T. Summers and J. Kewisch. “RHIC orbit response analysis with LOCO Run 12”. C-A/AP/479;BNL-100574-2013-IR. Mar. 2013.
- [35] C.-Y. Tan et al. “Measurement and Correction of the Fermilab Booster Optics with LOCO”. In: *Proc. 6th International Particle Accelerator Conference (IPAC’15), Richmond, VA, USA, May 3-8, 2015* (Richmond, VA, USA). International Particle Accelerator Conference 6. Geneva, Switzerland: JACoW, June 2015, pp. 586–588. ISBN: 978-3-95450-168-7. DOI: <https://doi.org/10.18429/JACoW-IPAC2015-MOPMA020>.
- [36] C.-Y. Tan et al. “Optics Corrections with LOCO in the Fermilab Booster”. In: *Proc. of International Particle Accelerator Conference (IPAC’16), Busan, Korea, May 8-13, 2016* (Busan, Korea). International Particle Accelerator Conference 7. Geneva, Switzerland: JACoW, June 2016, pp. 3385–3387. ISBN: 978-3-95450-147-2. DOI: [doi: 10.18429/JACoW-IPAC2016-THPMR002](https://doi.org/10.18429/JACoW-IPAC2016-THPMR002).
- [37] K. Blasche and B. Franczak. “SIS Status Report”. In: *GSI Scientific Report 1990*. Ed. by U. Grundinger. Darmstadt, Germany: Gesellschaft für Schwerionenforschung mbH, Mar. 1991, pp. 387–388.
- [38] Angelina Parfenova. “Linear and nonlinear Response Matrix and its application to the SIS18 synchrotron”. PhD thesis. Frankfurt, Germany: Johann Wolfgang Goethe-Universität, 2008.
- [39] R. Bär et al. “SIS Operation at High Beam Intensities”. In: *Proceedings of EPAC’98, Stockholm, Sweden*. 1998, pp. 499–501.
- [40] P. Spiller et al. “The FAIR Heavy Ion Synchrotron SIS100”. In: *Journal of Instrumentation* 15.12 (Dec. 2020), T12013. DOI: 10.1088/1748-0221/15/12/T12013.
- [41] G. Franchetti and S. Sorge. “Effect of beam loss on long-term beam survival in SIS100”. In: *GSI Scientific Report 2012*. Ed. by Katrin Große. Planckstr. 1, 64291 Darmstadt, Germany: GSI Helmholtzzentrum für Schwerionenforschung GmbH, May 2013, p. 233.

## REFERENCES

---

- [42] V. Kornilov et al. “SIS100 Beam Dynamics Challenges Related to the Magnet System”. In: *Proc. 9th International Particle Accelerator Conference (IPAC'18), Vancouver, BC, Canada, April 29-May 4, 2018* (Vancouver, BC, Canada). International Particle Accelerator Conference 9. Geneva, Switzerland: JACoW Publishing, June 2018, pp. 3172–3175. ISBN: 978-3-95450-184-7. DOI: 10.18429/JACoW-IPAC2018-THPAF080.
- [43] Adrian Oeftiger. *Impact of Field Errors of Quadrupole Units on Beam Losses at SIS100 Injection*. Tech. rep. GSI-2021-00450. Planckstr. 1, 64291 Darmstadt, Germany: GSI Helmholtzzentrum für Schwerionenforschung GmbH, Nov. 2021. URL: [https://wiki.gsi.de/pub/SIS100BD/BeamDynamicsReports/SIS100\\_BeamLoss\\_QuadrupoleUnit\\_FieldErrors.pdf](https://wiki.gsi.de/pub/SIS100BD/BeamDynamicsReports/SIS100_BeamLoss_QuadrupoleUnit_FieldErrors.pdf).
- [44] X. Huang et al. “Optimization of the Booster to SPEAR Transport Line for Top-Off Injection”. In: *Proceedings of PAC09, Vancouver, BC, Canada*. 2009, pp. 1641–1643.
- [45] W. Bartmann. “Transfer Lines”. In: *Proceedings of the CAS-CERN Accelerator School: Beam Injection, Extraction and Transfer, Erice, Italy, 10-19 March 2017* (Erice, Italy). CERN Yellow Reports: School Proceedings 5/2018. CERN-2018-008-SP. CH-1211 Geneva 23, Switzerland: CERN, 2018, pp. 507–532. ISBN: 978-92-9083-509-7. DOI: <https://doi.org/10.23730/CYRSP-2018-005.507>.
- [46] David J. Griffiths. *Elektrodynamik - Eine Einführung*. München, Germany: Pearson Education Deutschland GmbH, 2011. ISBN: 978-3-86894-057-2.
- [47] Helmut Wiedemann. *Particle Accelerator Physics*. Basel, Switzerland: Springer International Publishing AG, 2019. ISBN: 978-3-319-18316-9. DOI: 10.1007/978-3-319-18317-6.
- [48] D. A. Edwards and M. J. Syphers. *An Introduction to the Physics of High Energy Accelerators*. WILEY-VCH Verlag GmbH & Co. KGaA, 2004. ISBN: 978-0-471-55163-8.
- [49] Andrzej Wolski. *Beam Dynamics in High Energy Particle Accelerators*. London: Imperial College Press, 2014. ISBN: 978-1-78326-279-3. DOI: 10.1142/p899.
- [50] Andy Wolski. “Linear Dynamics”. Lecture notes. 2012.
- [51] Friedhelm Kuypers. *Klassische Mechanik*. Weinheim, Germany: WILEY-VCH Verlag GmbH & Co. KG aA, 2010. ISBN: 978-3-527-40989-1.
- [52] Karl L Brown et al. *TRANSPORT: a computer program for designing charged-particle beam-transport systems*. CERN Yellow Reports: Monographs. Geneva: CERN, 1980. DOI: 10.5170/CERN-1980-004.
- [53] F. Ch. Iselin. “Lie Transformations and Transport Equations for Combined-Function Dipoles”. In: *Particle Accelerators* 17 (1985), pp. 143–155.
- [54] Liam Healy. “Lie Algebraic Methods for Treating Lattice Parameter Errors in Particle Accelerators”. PhD thesis. College Park, MD, USA: University of Maryland, 1986.
- [55] H. Burkhardt et al. “Improved TEAPOT Method and Tracking with Thick Quadrupoles for the LHC and its Upgrade”. In: *Proc. IPAC'13*. Geneva, Switzerland: JACoW Publishing, 2013, MOPWO027, pp. 945–947.
- [56] J. J. Stoker. *Non-linear Vibrations*. Interscience Publishers, New York, 1950.

- [57] S. Y. Lee. *Accelerator Physics (Fourth Edition)*. WSPC, 2018. ISBN: 978-9813274785.
- [58] Frank Olver et al. *The NIST Handbook of Mathematical Functions*. en. Cambridge University Press, New York, NY, 2010.
- [59] David A. Brannan, Matthew F. Espen, and Jeremy J. Gray. *Geometry*. Cambridge University Press, 1999. DOI: 10.1017/CB09780511807503.
- [60] Albert Tarantola. *Inverse Problem Theory and Methods for Model Parameter Estimation*. Society for Industrial and Applied Mathematics, 2005. DOI: 10.1137/1.9780898717921.
- [61] Philip Wolfe. “Convergence Conditions for Ascent Methods”. In: *SIAM Review* 11.2 (1969), pp. 226–235. DOI: 10.1137/1011036.
- [62] Haskell B. Curry. “The method of steepest descent for non-linear minimization problems”. In: *Quart. Appl. Math.* 2 (1944), pp. 258–261. DOI: 10.1090/qam/10667.
- [63] Peter Deuffhard. “Least Squares Problems: Gauss-Newton Methods”. In: *Newton Methods for Nonlinear Problems: Affine Invariance and Adaptive Algorithms*. Berlin, Heidelberg: Springer Berlin Heidelberg, 2011, pp. 173–231. ISBN: 978-3-642-23899-4. DOI: 10.1007/978-3-642-23899-4\_4.
- [64] Kenneth Levenberg. “A method for the solution of certain non-linear problems in least squares”. In: *Quart. Appl. Math.* 2 (1944), pp. 164–168. DOI: 10.1090/qam/10666.
- [65] Donald W. Marquardt. “An Algorithm for Least-Squares Estimation of Nonlinear Parameters”. In: *Journal of the Society for Industrial and Applied Mathematics* 11.2 (1963), pp. 431–441. DOI: 10.1137/0111030.
- [66] I. C. F. IPSEN, C. T. KELLEY, and S. R. POPE. “RANK-DEFICIENT NONLINEAR LEAST SQUARES PROBLEMS AND SUBSET SELECTION”. In: *SIAM Journal on Numerical Analysis* 49.3/4 (2011), pp. 1244–1266. ISSN: 00361429.
- [67] J. Eriksson et al. “Regularization Methods for Uniformly Rank-Deficient Nonlinear Least-Squares Problems”. In: *Journal of Optimization Theory and Applications* 127.1 (Oct. 2005), pp. 1–26. DOI: 10.1007/s10957-005-6389-0.
- [68] M.G. Minty and F. Zimmermann. *Measurement and Control of Charged Particle Beams*. Berlin Heidelberg New York: Springer-Verlag, 2003. ISBN: 978-3-540-44187-8. DOI: 10.1007/978-3-662-08581-3\_13.
- [69] P. J. Bryant. “Resonant Extraction”. In: *Proceedings of the CAS–CERN Accelerator School: Beam Injection, Extraction and Transfer, Erice, Italy, 10-19 March 2017* (Erice, Italy). CERN Yellow Reports: School Proceedings 5/2018. CERN-2018-008-SP. CH-1211 Geneva 23, Switzerland: CERN, 2018, pp. 315–344. ISBN: 978-92-9083-509-7. DOI: <https://doi.org/10.23730/CYRSP-2018-005.507>.
- [70] Y. Kobayashi and H. Takahashi. “Improvement Of The Emittance In The Resonant Beam Ejection”. In: *6th International Conference on High-Energy Accelerators*. 1967, pp. 347–351.
- [71] S. van der Meer. *Stochastic extraction, a low-ripple version of resonant extraction*. Tech. rep. Geneva: CERN, 1978. URL: <http://cds.cern.ch/record/118881>.

## REFERENCES

---

- [72] L Badano et al. *Proton-Ion Medical Machine Study (PIMMS)*, 1. 2000. URL: <https://cds.cern.ch/record/385378>.
- [73] Xiaobiao Huang. “Beam Diagnosis and Lattice Modeling of the Fermilab Booster”. PhD thesis. Bloomington, IN: Indiana University, Aug. 2005.
- [74] Xiaobiao Huang, James Safranek, and Greg Portman. “LOCO with Constraints and Improved Fitting Technique”. In: *ICFA Beam Dyn. Newslett.* 44 (2007), pp. 60–69.
- [75] D. Vilsmeier, R. Singh, and M. Bai. “Inverse modeling of circular lattices via orbit response measurements in the presence of degeneracy”. In: *Phys. Rev. Accel. Beams* 26 (3 Mar. 2023). The following note serves to clearly distinguish the contribution of the main author - the PhD candidate - from the contributions of all other authors such that the contribution of the PhD candidate can be evaluated in the scope of this thesis. The contribution of the main author was to develop the mathematical derivations, to design and perform the simulations, to design and perform the experiment, to analyse the simulation and experimental data, to create the required software and to write the majority of the manuscript including all figures. The contributions of the co-authors were to share ideas, to involve in discussions, to give feedback on derivations and results, to assist during the experiment and to contribute towards the introduction and conclusion sections of the manuscript., p. 032803. DOI: 10.1103/PhysRevAccelBeams.26.032803.
- [76] D. Vilsmeier. *DiPAS - A framework for differentiable simulations of particle accelerators*. <https://pypi.org/project/DiPAS/>. version 2.0. 2022.
- [77] A. Reiter and R. Singh. “Comparison of beam position calculation methods for application in digital acquisition systems”. In: *Nuclear Instruments and Methods in Physics Research Section A: Accelerators, Spectrometers, Detectors and Associated Equipment* 890 (2018), pp. 18–27. DOI: 10.1016/j.nima.2018.02.046.
- [78] Sajjad Hussain Mirza et al. “Closed orbit correction at synchrotrons for symmetric and near-symmetric lattices”. In: *Phys. Rev. Accel. Beams* 22 (7 July 2019), p. 072804. DOI: 10.1103/PhysRevAccelBeams.22.072804.
- [79] Zeus Martí. *Analytical derivatives of the orbit response matrix and dispersion for LOCO fit*. Tech. rep. ACDIV-2017-01. Carrer de la Llum 2-26, 08290 Cerdanyola del Vallès, Barcelona, Spain: ALBA Synchrotron, Jan. 2017.
- [80] Andrea Franchi, Simone Maria Liuzzo, and Zeus Martí. “Analytic formulas for the rapid evaluation of the orbit response matrix and chromatic functions from lattice parameters in circular accelerators”. arXiv:1711.06589 [physics.acc-ph]. 2023. URL: <https://arxiv.org/abs/1711.06589>.
- [81] Ph. Amstutz et al. “Confining continuous manipulations of accelerator beam-line optics”. In: *Phys. Rev. Accel. Beams* 20 (4 Apr. 2017), p. 042802. DOI: 10.1103/PhysRevAccelBeams.20.042802.
- [82] Fredrik Johansson et al. *mpmath: a Python library for arbitrary-precision floating-point arithmetic (version 1.2.1)*. <https://mpmath.org/>. Feb. 2021.
- [83] Garry J. Tee. “Eigenvectors of block circulant and alternating circulant matrices”. In: *Res. Lett. Inf. Math. Sci.* 8 (2005), pp. 123–142.

- [84] Sajjad Hussain Mirza et al. “Performance of the closed orbit feedback systems with spatial model mismatch”. In: *Phys. Rev. Accel. Beams* 23 (7 July 2020), p. 072801. DOI: 10.1103/PhysRevAccelBeams.23.072801.
- [85] Mukesh Kumar et al. “Analytical expression for position sensitivity of linear response beam position monitor having inter-electrode cross talk”. In: *Nuclear Instruments and Methods in Physics Research Section A: Accelerators, Spectrometers, Detectors and Associated Equipment* 844 (2017), pp. 90–95. ISSN: 0168-9002. DOI: 10.1016/j.nima.2016.11.048.
- [86] Courtesy of Thomas Reichert. 2023.
- [87] P Forck, P Kowina, and D Liakin. “Beam position monitors”. In: *CAS - CERN Accelerator School: Beam Diagnostics*. 2009, pp. 187–228. DOI: 10.5170/CERN-2009-005.187.
- [88] Oleksandr Chorniy. Private Communication. 2023.
- [89] Bildrechte: GSI Helmholtzzentrum für Schwerionenforschung GmbH, <https://www.gsi.de/work/beschleunigerbetrieb/beschleuniger/hest>. 2023.
- [90] Aharon Ben-Tal, Laurent El Ghaoui, and Arkadi Nemirovski. *Robust Optimization*. Princeton University Press, 2009. ISBN: 9780691143682.
- [91] Sven Leyffer et al. “A survey of nonlinear robust optimization”. In: *INFOR: Information Systems and Operational Research* 58.2 (2020), pp. 342–373. DOI: 10.1080/03155986.2020.1730676.
- [92] Courtesy of Christoph Dorn. 2023.
- [93] Mariusz Sapinski and Dominik Vilsmeier. *Analysis of GSI HADES beamline configuration space*. arXiv:2002.04226 [physics.acc-ph]. DOI: 10.48550/arXiv.2002.04226.
- [94] H. Grote and F. Schmidt. “MAD-X: An upgrade from MAD8”. In: *Conf. Proc. C* 030512 (2003). <https://mad.web.cern.ch/mad/>, version 5.06.01, p. 3497.
- [95] Bernard Rosner. *Fundamentals of Biostatistics (Seventh Edition)*. Brooks/Cole, Cengage Learning, 2011. ISBN: 978-0-538-73349-6.
- [96] Ji Qiang and Chad Mitchell. “A Unified Differential Evolution Algorithm for Global Optimization”. In: *IEEE Transactions on Evolutionary Computation*. (June 2014). URL: <https://www.osti.gov/biblio/1163659>.
- [97] Pauli Virtanen et al. “SciPy 1.0: Fundamental Algorithms for Scientific Computing in Python”. In: *Nature Methods* 17 (2020), pp. 261–272. DOI: 10.1038/s41592-019-0686-2.
- [98] F. Pedregosa et al. “Scikit-learn: Machine Learning in Python”. In: *Journal of Machine Learning Research* 12 (2011), pp. 2825–2830.
- [99] Bildrechte: Forschungszentrum Jülich. 2023.
- [100] Thomas Gläßle. *cpymad - Cython binding to MAD-X*. <https://pypi.org/project/cpymad/>, version 1.10.0.
- [101] Matthew Newville. *PyEpics: Epics Channel Access for Python*. <https://pypi.org/project/pyepics/>, version 3.4.3. 2020.

## REFERENCES

---

- [102] Oliver Sim Brüning. “Linear imperfections”. In: *CAS - CERN Accelerator School: Intermediate Accelerator Physics* (2006). DOI: 10.5170/CERN-2006-002.129.
- [103] V. Sajaev. “Simulation of Linear Lattice Correction of an Energy-Recovery Linac Designed for an APS Upgrade”. In: *Proc. LINAC’08*. Linear Accelerator Conference 24. JACoW Publishing, Geneva, Switzerland, 2008, TUP027.
- [104] Rogelio Tomas Garcia et al. “Average beta-beating from random errors”. In: *CERN-ACC-NOTE* (Mar. 2018). URL: <https://cds.cern.ch/record/2307589>.
- [105] Joel G. Broida and S. Gill Williamson. *A Comprehensive Introduction to Linear Algebra*. Addison-Wesley, 1986, Theorem 4.15.
- [106] *PARI/GP version 2.13.4*. available from <https://pari.math.u-bordeaux.fr/>. The PARI Group. Univ. Bordeaux, 2022.



# Appendix

## A.1 Transfer matrix between two lattice positions

The transfer matrix between two lattice positions  $s_1$  and  $s_2$  is given in terms of the corresponding Twiss parameters  $(\beta_1, \alpha_1)$  and  $(\beta_2, \alpha_2)$  and the phase advance difference  $\Delta\mu \equiv \mu(s_2) - \mu(s_1) > 0$  by the following expression [48]:

$$M(s_2|s_1) = \begin{pmatrix} \sqrt{\frac{\beta_2}{\beta_1}} (\cos \Delta\mu + \alpha_1 \sin \Delta\mu) & \sqrt{\beta_1 \beta_2} \sin \Delta\mu \\ -\frac{1+\alpha_1\alpha_2}{\sqrt{\beta_1\beta_2}} \sin \Delta\mu + \frac{\alpha_1-\alpha_2}{\sqrt{\beta_1\beta_2}} \cos \Delta\mu & \sqrt{\frac{\beta_1}{\beta_2}} (\cos \Delta\mu - \alpha_2 \sin \Delta\mu) \end{pmatrix} \quad (\text{A.1})$$

## A.2 One-turn transfer matrix in exponential form

The following relationship is shown:

$$\exp(J\mu) = I \cos(\mu) + J \sin(\mu) \quad (\text{A.2})$$

where  $J^2 = -I$ .

The Taylor series of the exponential function is given by:

$$\exp(J\mu) = \sum_{k=0}^{\infty} \frac{(J\mu)^k}{k!} \quad (\text{A.3})$$

Separating the even and odd terms and using  $J^2 = -I$  leads to the following expression:

$$\begin{aligned} \exp(J\mu) &= \sum_{k=0}^{\infty} \frac{(J\mu)^{2k}}{(2k)!} + \sum_{k=0}^{\infty} \frac{(J\mu)^{2k+1}}{(2k+1)!} \\ &= \sum_{k=0}^{\infty} (J^2)^k \frac{\mu^{2k}}{(2k)!} + \sum_{k=0}^{\infty} J (J^2)^k \frac{\mu^{2k+1}}{(2k+1)!} \\ &= I \sum_{k=0}^{\infty} (-1)^k \frac{\mu^{2k}}{(2k)!} + J \sum_{k=0}^{\infty} (-1)^k \frac{\mu^{2k+1}}{(2k+1)!} \end{aligned} \quad (\text{A.4})$$

The first term in the above equation is the Taylor series for  $\cos(\mu)$  and the second term is the Taylor series for  $\sin(\mu)$ . Thus, the expression evaluates to  $I \cos(\mu) + J \sin(\mu)$ .

### A.3 Slicing of thick BPMs and steerers for linear closed orbits

In a real machine, BPMs and steerers are devices with a finite length along the beamline. In simulations, however, the steerers must be sliced in order to apply their kicks to the beam coordinates <sup>1</sup>. Likewise, the orbit must be recorded at a number of specified locations. In the following it is shown that for a steerer, it does not matter how many slices are used and where they are placed, so as long as the slices and their associated kicks are distributed symmetrically around the center of the steerer. For a BPM, the orbit evolves linearly and, thus, can be linearly sampled. In both cases, a single slice at the center of the device suffices.

#### A.3.1 Slicing of steerer

Let  $L$  be the length of the steerer and  $\delta$  the total kick that the beam receives after having passed the kicker. The basic case is placing a single slice in the center of the steerer:

$$\dots \mid \dots \tag{A.5}$$

where  $\dots$  indicates a drift space and  $\mid$  indicates a thin steerer slice. Each of the drifts has length  $\frac{L}{2}$  and the entire kick  $\delta$  is applied in the center of the steerer. The resulting transfer map is:

$$\begin{aligned} \vec{\eta}_1 &= R_{\frac{1}{2}} \left( R_{\frac{1}{2}} \vec{\eta} + \vec{\delta} \right) \\ &= R \vec{\eta} + R_{\frac{1}{2}} \vec{\delta} \\ &= R \vec{\eta} + \vec{\delta} + \begin{pmatrix} \frac{L\delta}{2} \\ 0 \end{pmatrix} \end{aligned} \tag{A.6}$$

where  $\vec{\eta} = \begin{pmatrix} \eta \\ \eta' \end{pmatrix}$  and  $\vec{\delta} = \begin{pmatrix} 0 \\ \delta \end{pmatrix}$  and  $R_{\frac{1}{2}}$  indicates the transfer matrix for a drift space with half the length of the steerer and  $R$  corresponds to a drift with the entire length.

The general solution is to use  $N + 1$  slices with  $N$  drift spaces between them. Each drift has individual length  $L_i$  ( $i = 1 \dots N$ ), resulting in transfer matrix  $R_i$ , and each slice applies an individual kick  $\delta_i$  ( $i = 0 \dots N$ ) to the beam <sup>2</sup>.

$$\begin{array}{cccccccc} \mid & \dots & \mid & \dots & \mid & \dots & \mid & \dots & \mid \\ \delta_0 & L_1 & \delta_1 & L_2 & \delta_2 & L_3 & \delta_3 & & L_N & \delta_N \end{array} \tag{A.7}$$

This implies that  $\sum_{i=0}^N \delta_i = \delta$  and  $\sum_{i=1}^N L_i = L$ . In the following, it is assumed that the slices and drifts are placed symmetrically around the steerer center, i.e.  $\delta_i = \delta_{N-i}$  and  $L_i = L_{N+1-i}$ .

---

<sup>1</sup>MADX uses "edge" slicing for Twiss computation, i.e. each thick KICKER is represented by two thin slices, one at the entrance and the other at the exit of the kicker, separated by a drift space equal to the length of the kicker.

<sup>2</sup>This slicing pattern does not exclude the possibility to start and end with a drift space since one may choose  $\delta_0 = \delta_N = 0$



The transfer map is given by:

$$\begin{aligned}
 & R_N \left( \dots R_3 \left( R_2 \left( R_1 \left( \vec{\eta} + \vec{\delta}_0 \right) + \vec{\delta}_1 \right) + \vec{\delta}_2 \right) + \vec{\delta}_3 \dots \right) + \vec{\delta}_N \\
 &= R\vec{\eta} + \vec{\delta}_N + \sum_{i=0}^{N-1} \left[ \prod_{k=i+1}^N R_k \right] \vec{\delta}_i
 \end{aligned} \tag{A.8}$$

The above expression can be simplified by using the fact that the product of individual drift transfer matrices  $R_k$  is a transfer matrix that corresponds to the combined length of individual drifts. The product  $\prod_{k=i+1}^N R_k$  involves all drift spaces downstream of the slice  $\delta_i$  all the way to the exit of the steerer. Hence, the product spans the corresponding fractional length of the steerer. By defining  $\lambda_i = \sum_{k=1}^i L_k$ , the product can be expressed as:

$$\prod_{k=i+1}^N R_k = \begin{pmatrix} 1 & L - \lambda_i \\ 0 & 1 \end{pmatrix} \tag{A.9}$$

In equation A.8 one can ignore the terms  $Rx$  and  $\delta_N$  since they do not affect the change in position which is induced by the steerer ( $\delta_N$  only contributes to the change in divergence). The only relevant term is

$$\sum_{i=0}^{N-1} \left[ \prod_{k=i+1}^N R_k \right] \delta_i = \sum_{i=0}^{N-1} \begin{pmatrix} 1 & L - \lambda_i \\ 0 & 1 \end{pmatrix} \begin{pmatrix} 0 \\ \delta_i \end{pmatrix} \tag{A.10}$$

The contribution to the divergence of this term sums up to  $\delta - \delta_N$  and together with the term  $\vec{\delta}_N$  from equation A.8 this yields the total kick  $\vec{\delta}$  similar to equation A.6. The contribution to the position is

$$\begin{aligned}
 \sum_{i=0}^{N-1} (L\delta_i - \lambda_i\delta_i) &= L(\delta - \delta_N) - \sum_{i=0}^{N-1} \lambda_i\delta_i \\
 &= L(\delta - \delta_N) - \sum_{i=1}^{N-1} \lambda_i\delta_i
 \end{aligned} \tag{A.11}$$

The last equality holds because  $\lambda_0 = 0$  by definition. By using  $\delta_i = \delta_{N-i}$  (i.e. slices are placed symmetrically around the center of the steerer), the sum can be rewritten as (assuming  $N$  is odd; for  $N$  is even, see below):

$$\sum_{i=1}^{N-1} \lambda_i\delta_i = \sum_{i=1}^{(N-1)/2} (\lambda_i + \lambda_{N-i})\delta_i \tag{A.12}$$

Similarly,  $L_i = L_{N+1-i}$  and, therefore,  $\lambda_i + \lambda_{N-i} = L$ . Because  $N$  is odd, summing  $\delta_i$  from  $i = 0$  to  $(N-1)/2$  yields  $\frac{\delta}{2}$  and, thus:

$$\sum_{i=1}^{(N-1)/2} (\lambda_i + \lambda_{N-i})\delta_i = L\frac{\delta}{2} - L\delta_0 \tag{A.13}$$

Therefore, equation A.11 evaluates to

$$L(\delta - \delta_N) - L\frac{\delta}{2} + L\delta_0 = \frac{L\delta}{2} \tag{A.14}$$

If  $N$  is even, equation A.12 is slightly modified:

$$\begin{aligned}
 \sum_{i=1}^{N-1} \lambda_i \delta_i &= \sum_{i=1}^{(N-2)/2} (\lambda_i + \lambda_{N-i}) \delta_i + \lambda_{\frac{N}{2}} \delta_{\frac{N}{2}} \\
 &= L \frac{\delta - \delta_{\frac{N}{2}}}{2} - L\delta_0 + \lambda_{\frac{N}{2}} \delta_{\frac{N}{2}} \\
 &= L \frac{\delta - \delta_{\frac{N}{2}}}{2} - L\delta_0 + \frac{L}{2} \delta_{\frac{N}{2}} \\
 &= L \frac{\delta}{2} - L\delta_0
 \end{aligned} \tag{A.15}$$

The result is, however, the same as for equation A.13.

Therefore, it does not matter how steerers are sliced in simulations, so as long as the slices are placed symmetrically around the center of the steerer. Using a single slice at the center of the steerer fulfills this purpose <sup>3</sup>.

### A.3.2 Slicing of BPM

The closed orbit at the location of a BPM is given by equation 2.109. Under linear optics, the Twiss parameters evolve inside a drift space, i.e. inside the BPM, in the following way:

$$\begin{aligned}
 \beta(s) &= \beta_0 - 2\alpha_0 s + \gamma_0 s^2 \\
 \alpha(s) &= \alpha_0 - \gamma_0 s \\
 \gamma(s) &= \gamma_0
 \end{aligned} \tag{A.16}$$

where  $\beta_0, \alpha_0, \gamma_0$  are the Twiss parameters at the beginning of the element and  $s$  is the path length along the lattice. With the help of equation 2.67, the phase advance  $\mu(s)$  is given by:

$$\mu(s) = \int_0^s \frac{1}{\beta(\tilde{s})} d\tilde{s} = \arctan(\gamma_0 s - \alpha_0) + \arctan(\alpha_0) \tag{A.17}$$

Hence, the cos term in equation 2.109 can be rewritten as:

$$\cos(\pi Q - |\mu(s) - \mu(s_i)|) = \frac{1}{\sqrt{\gamma_0 \beta(s)}} [\cos \phi \mp (\alpha_0 - \gamma_0 s) \sin \phi] \tag{A.18}$$

where  $\phi = \pi Q \pm \mu(s_i) \mp \arctan(\alpha_0)$ ; the upper and lower signs refer to, respectively, the case where the absolute value argument is positive or negative. The factor  $\frac{1}{\sqrt{\beta(s)}}$  cancels the  $\sqrt{\beta(s)}$  dependence from equation 2.109. Therefore, inside a drift space, the expression for the closed orbit is a linear function in  $s$  inside a drift space.

## A.4 Derivative of orbit response with respect to quadrupole strength

*This section has previously been published in Phys. Rev. Accel. Beams. Details are given in [75].*

---

<sup>3</sup>For other beamline elements, e.g., quadrupoles, the slicing pattern and number of slices are, however, very important. Among all possible slicing patterns, the TEAPOT slicing pattern gives an optimal approximation of the  $R_{21}$  matrix element of the thick quadrupole transfer matrix [55] (see section 2.2.3.9).

Starting with the orbit response  $r_{bs}$  induced by steerer  $s$  and measured by BPM  $b$ :

$$r_{bs} = \underbrace{\sqrt{\beta_b \beta_s}}_A \underbrace{\frac{1}{2 \sin(\pi Q)}}_B \underbrace{\cos(\pi Q - |\mu_b - \mu_s|)}_C \quad (\text{A.19})$$

The derivative  $\frac{d}{d(K_1 L)_k} r_{bs} \equiv r'_{kbs}$  is:

$$r'_{kbs} = A'BC + AB'C + ABC' \quad (\text{A.20})$$

In the following the individual derivatives  $A', B', C'$  are derived.

$$A' = \frac{1}{2\sqrt{\beta_b \beta_s}} [\beta'_b \beta_s + \beta_b \beta'_s] \approx -\frac{\beta_k}{2} \sqrt{\beta_b \beta_s} [\Psi_{ks} + \Psi_{kb}] = -A \frac{\beta_k}{2} [\Psi_{ks} + \Psi_{kb}] \quad (\text{A.21})$$

where we have used the formula for the beta beating from equation 2.123:

$$\beta'_s \approx -\beta_s \beta_k \underbrace{\frac{\cos(2\pi Q - 2|\mu_k - \mu_s|)}{2 \sin(2\pi Q)}}_{\Psi_{ks}} \quad (\text{A.22})$$

and similarly for  $\beta'_b, \Psi_{kb}$ .

$$B' = -\frac{1}{2} \frac{\cos(\pi Q)}{\sin(\pi Q)^2} \pi Q' \approx -B \frac{\beta_k}{2} \frac{1}{2 \tan(\pi Q)} \quad (\text{A.23})$$

where we have used the formula for the tune change induced by a quadrupolar error from equation 2.116:

$$Q' \approx \frac{\beta_k}{4\pi} \quad (\text{A.24})$$

$$C' = -C \tan(\pi Q - |\mu_b - \mu_s|) \left[ \frac{\beta_k}{4} - \frac{\mu_{\max} - \mu_{\min}}{|\mu_{\max} - \mu_{\min}|} (\mu'_{\max} - \mu'_{\min}) \right] \quad (\text{A.25})$$

where we have assumed  $\cos(\pi Q - |\mu_b - \mu_s|) \neq 0$  (i.e.  $r_{bs} \neq 0$ ) and reordered the terms  $\mu_b, \mu_s$  inside  $\cos(\pi Q - |\mu_b - \mu_s|)$  such that the argument of the absolute value is positive, i.e.  $|\mu_b - \mu_s| = |\max(\mu_b, \mu_s) - \min(\mu_b, \mu_s)|$  and  $\mu_{\max} \equiv \max(\mu_b, \mu_s), \mu_{\min} \equiv \min(\mu_b, \mu_s)$ . In that case  $\frac{\mu_{\max} - \mu_{\min}}{|\mu_{\max} - \mu_{\min}|} = 1$  and we are only left with the derivative  $\mu'_{\max} - \mu'_{\min} = (\mu_{\max} - \mu_{\min})'$ . To compute this derivative we consider the change in local phase advance  $\Delta\mu_i$  induced by a small quadrupolar error  $\Delta(K_1 L)_k$  [102]:

$$\begin{aligned} \mu_i &= \mu_{0,i} + \Delta\mu_i \\ \mu_i &= \int_{s_0}^{s_i} \frac{1}{\beta(\tau)} d\tau + \mu_{s=s_0} \\ &= \int_{s_0}^{s_i} \frac{1}{\beta_0(\tau) + \Delta\beta(\tau)} d\tau + \mu_{s=s_0} \\ &= \int_{s_0}^{s_i} \frac{1}{\beta_0(\tau)} \cdot \frac{1}{1 + \frac{\Delta\beta(\tau)}{\beta_0(\tau)}} d\tau + \mu_{s=s_0} \\ &\approx \int_{s_0}^{s_i} \frac{1}{\beta_0(\tau)} d\tau - \int_{s_0}^{s_i} \frac{\Delta\beta(\tau)}{\beta_0(\tau)^2} d\tau + \mu_{s=s_0} \end{aligned} \quad (\text{A.26})$$

## A. Appendix

---

where the subscript 0 indicates the unperturbed optics functions, i.e. without quadrupole error, and we have used the fact that Taylor series are multiplicative. Considering the difference  $\mu_{\max} - \mu_{\min}$  we thus obtain:

$$\mu_{\max} - \mu_{\min} = \int_{s_{\min}}^{s_{\max}} \frac{1}{\beta_0(\tau)} d\tau - \int_{s_{\min}}^{s_{\max}} \frac{\Delta\beta(\tau)}{\beta_0(\tau)^2} d\tau \quad (\text{A.27})$$

where  $s_{\min}, s_{\max}$  denote the corresponding longitudinal lattice positions. Since  $\mu_{\max} - \mu_{\min} = \mu_{0,\max} + \Delta\mu_{\max} - \mu_{0,\min} - \Delta\mu_{\min} = (\mu_{0,\max} - \mu_{0,\min}) + \Delta(\mu_{\max} - \mu_{\min})$  we obtain:

$$\Delta(\mu_{\max} - \mu_{\min}) = - \int_{s_{\min}}^{s_{\max}} \frac{\Delta\beta(\tau)}{\beta_0(\tau)^2} d\tau \quad (\text{A.28})$$

By using the expression for the beta beating this can be rewritten as:

$$\Delta(\mu_{\max} - \mu_{\min}) = \Delta(K_1 L)_k \frac{\beta_{0,k}}{2 \sin(2\pi Q_0)} \int_{s_{\min}}^{s_{\max}} \frac{\cos(2\pi Q_0 - 2|\mu_{0,k} - \mu_0(\tau)|)}{\beta_0(\tau)} d\tau \quad (\text{A.29})$$

Approximating the derivative with  $(\mu_{\max} - \mu_{\min})' \approx \frac{\Delta(\mu_{\max} - \mu_{\min})}{\Delta(K_1 L)_k}$  and using  $\frac{d}{d\tau} \mu_0(\tau) = \frac{1}{\beta_0(\tau)}$  with integration by substitution we obtain:

$$\mu'_{\max} - \mu'_{\min} = \frac{\beta_{0,k}}{2 \sin(2\pi Q_0)} \int_{\mu_{0,\min}}^{\mu_{0,\max}} \cos(2\pi Q_0 - 2|\mu_{0,k} - u|) du \quad (\text{A.30})$$

In the following we drop the subscript 0 for nominal values, as there is no further ambiguity.

Hence, all derivatives  $\{A, B, C\}'$  can be written as  $-\{A, B, C\} \frac{\beta_k}{2} f_{\{A,B,C\}}$ , i.e the derivative  $r'_{kbs}$  can be written as a product of  $r_{bs}$ , the beta function at the respective quadrupole and a sum of the factors  $f_{\{A,B,C\}}$ :

$$\begin{aligned} \frac{dr_{bs}}{d(KL)_k} = -r_{bs} \frac{\beta_k}{2} \left\{ \frac{1}{2 \tan(\pi Q)} + \frac{\tan(\pi Q - |\mu_b - \mu_s|)}{2} \right. \\ \left. + \Psi_{ks} + \Psi_{kb} \right. \\ \left. - \frac{\tan(\pi Q - |\mu_b - \mu_s|)}{\sin(2\pi Q)} \int_{\min(\mu_b, \mu_s)}^{\max(\mu_b, \mu_s)} \cos(2\pi Q - 2|\mu_k - u|) du \right\} \end{aligned} \quad (\text{A.31})$$

The integral in equation A.31 can be solved by taking into account the absolute value function that is part of the integrand. Therefore, we need to divide the integration domain in order to resolve it. For any quadrupole  $k$ , there are three distinct cases: (A)  $\mu_{\min} < \mu_{\max} < \mu_k$ , (B)  $\mu_{\min} < \mu_k < \mu_{\max}$ , (C)  $\mu_k < \mu_{\min} < \mu_{\max}$ . For cases (A) and (C) the argument of the absolute value assumes the same sign on the entire integration domain and, hence, there is no need to split the integration domain. For case (B) it needs to be split in  $[\mu_{\min}, \mu_k]$  and

$[\mu_k, \mu_{\max}]$ . The solutions are:

$$\begin{aligned} & \int_{\mu_{\min}}^{\mu_{\max}} \cos(2\pi Q - 2|\mu_k - u|) du = \\ & = \begin{cases} (A) & \sin(\mu_{\max} - \mu_{\min}) \cos(2\pi Q - |\mu_k - \mu_{\max}| - |\mu_k - \mu_{\min}|) \\ (B) & \sin(|\mu_k - \mu_{\min}|) \cos(2\pi Q - |\mu_k - \mu_{\min}|) + \sin(|\mu_k - \mu_{\max}|) \cos(2\pi Q - |\mu_k - \mu_{\max}|) \\ (C) & \sin(\mu_{\max} - \mu_{\min}) \cos(2\pi Q - |\mu_k - \mu_{\max}| - |\mu_k - \mu_{\min}|) \end{cases} \end{aligned} \quad (A.32)$$

Hence, the result for cases (A) and (C) is similar and a distinction has to be made between the two different cases (A,C) for which both  $\mu_{\min}, \mu_{\max}$  are either upstream or downstream of the quadrupole and (B) for which  $\mu_{\min}$  is upstream and  $\mu_{\max}$  is downstream of the quadrupole.

## A.5 Derivative of orbit response with respect to quadrupole strength for beamlines

*This section has previously been published in Phys. Rev. Accel. Beams. Details are given in [75].*

For beamlines, or more generally, non-closed lattices, we have the following formula for the orbit response at BPM  $b$  induced by steerer  $s$  [103]:

$$r_{bs} = \begin{cases} \sqrt{\beta_b \beta_s} \sin(\mu_b - \mu_s) & , \mu_b > \mu_s \\ 0 & , \text{otherwise} \end{cases} \quad (A.33)$$

The relation for  $\frac{\Delta\beta}{\beta}$  for non-closed lattices to first order is given by [104]:

$$\frac{\Delta\beta_x}{\Delta(K_1 L)_k} = -\beta_k \beta_x \sin(2\mu_x - 2\mu_k) \quad (A.34)$$

where the subscript  $x$  refers to the point of measurement and  $k$  refers to the quadrupole;  $\mu_x > \mu_k$  is assumed since only downstream regions are affected.

Taking the derivative of  $r_{bs}$  with respect to  $\Delta(K_1 L)_k$  one obtains the following:

$$r_{kbs} \equiv \frac{dr_{bs}}{d\Delta(K_1 L)_k} = \begin{cases} 0 & , \mu_k < \mu_s \\ -r_{bs} \beta_k \frac{\sin(\mu_b - \mu_k) \sin(\mu_k - \mu_s)}{\sin(\mu_b - \mu_s)} & , \mu_k > \mu_s \end{cases} \quad (A.35)$$

This can be expanded into  $\cos(\mu_k)^2$ ,  $\sin(\mu_k)^2$  and  $\cos(\mu_k) \sin(\mu_k)$  terms with their respective coefficient vectors.

Compared with the Jacobian for a circular lattice, the beamline Jacobian additionally has some of its elements zeroed. Thus, the rank of the beamline Jacobian for a given BPM/steerer placement must be less than or equal to the rank of the corresponding circular lattice Jacobian. Simulations show that it is rank deficient for the cases **Sh, Sv, Q5+, Bh, Bv** but has full rank for **Sh, Sv, Q4, Bh, Bv**.

## A.6 Proof: S,Q3,B Jacobian is rank deficient

This section has previously been published in *Phys. Rev. Accel. Beams*. Details are given in [75].

The trigonometric expressions in the Jacobian equation 3.3 can be expanded in terms of  $\mu_k$  by using the identities  $\cos(x \pm y) = \cos(x)\cos(y) \mp \sin(x)\sin(y)$ ,  $\sin(x \pm y) = \sin(x)\cos(y) \pm \cos(x)\sin(y)$ ,  $\sin(2x) = 2\sin(x)\cos(x)$ ,  $\cos(2x) = \cos(x)^2 - \sin(x)^2$ ,  $1 = \cos(x)^2 + \sin(x)^2$ . The resulting expression can be grouped by terms containing  $\cos(\mu_k)^2$ ,  $-\sin(\mu_k)^2$  and  $2\cos(\mu_k)\sin(\mu_k)$ . This allows to represent each column of the Jacobian by a set of three coefficient vectors, one for each of the trigonometric terms. These coefficient vectors contain the phase advances of BPMs/steerers and their structure only depends on whether the BPM/steerer placement is of type A ( $\mu_{\min} < \mu_{\max} < \mu_k$ ), type B ( $\mu_{\min} < \mu_k < \mu_{\max}$ ) or type C ( $\mu_k < \mu_{\min} < \mu_{\max}$ ), where  $\mu_{\min} \equiv \min(\mu_b, \mu_s)$  and  $\mu_{\max} \equiv \max(\mu_b, \mu_s)$ . Since the quadrupole triplets of **S,Q3,B** are not interleaved by BPMs/steerers, the structure of coefficient vectors is the same for each quadrupole in a triplet. In fact, these three coefficient vectors can be used for more than three consecutive quadrupoles as well since the coefficient vectors only need to be multiplied by the three trigonometric factors containing  $\mu_k$  for a given quadrupole in order to generate the corresponding column of the Jacobian. Hence, this proof applies to **S,Q3+,B** BPM/steerer placements as well. Thus, one set of three coefficient vectors is sufficient to generate the Jacobian columns for a full quadrupole  $n$ -tuple with  $n \geq 3$ . This means that there are a total of  $3N$  coefficient vectors, one 3-tuple per quadrupole  $n$ -tuple in each of the  $N$  sections. These column vectors form the column span of any **S,Qn+,B** Jacobian for  $n \geq 3$ . The structure of these coefficient vectors, in terms of the phase advance types A, B, C, is shown exemplarily for  $N = 4, n = 3$  in program 2.

We use the following set of abbreviations to simplify the notation:

$$\begin{aligned}
u &\equiv \mu_{\max} + \mu_{\min} \\
v &\equiv \mu_{\max} - \mu_{\min} \\
T &\equiv \tan(\pi Q - |\mu_{\max} - \mu_{\min}|) = \tan(\pi Q - v) \\
\tilde{T} &\equiv \frac{1}{2 \tan(\pi Q)} + \frac{T}{2}
\end{aligned} \tag{A.36}$$

Further, (1) is used to represent  $\cos(\mu_k)^2$ , (2) for  $-\sin(\mu_k)^2$  and (3) for  $2\cos(\mu_k)\sin(\mu_k)$ . The specific expressions for the coefficient vectors, in dependence on the trigonometric factor (1,2,3) and type (A,B,C), are shown in table A.1.

The expressions in table A.1 can be further simplified by noting the following relationships:

$$\begin{aligned}
\cos(v) - T \sin(v) &= \frac{\cos(\pi Q)}{\cos(\pi Q - v)} \\
\cos(2\pi Q - v) + T \sin(2\pi Q - v) &= \frac{\cos(\pi Q)}{\cos(\pi Q - v)} \\
\tilde{T} &= \frac{\cos(\pi Q)}{\cos(\pi Q - v)} \frac{\cos(v)}{2 \sin(\pi Q) \cos(\pi Q)}
\end{aligned} \tag{A.37}$$

**Program 2** This schematic shows the Jacobian elements' types A,B,C for  $N = 4$  sections and  $n = 3$  quadrupoles forming a triplet in each of the sections. The quadrupoles in a triplet are labeled F,D,T. [i] stands for the  $i$ th BPM and  $\langle i \rangle$  stands for the the  $i$ th steerer. As can be seen, the quadrupoles within a triplet all share the same type for each BPM/steerer pair.

| section: | 1   | 2   | 3   | 4   |
|----------|-----|-----|-----|-----|
| quad:    | FDT | FDT | FDT | FDT |
| -----    |     |     |     |     |
| [1]<1>   | BBB | AAA | AAA | AAA |
| [1]<2>   | CCC | AAA | AAA | AAA |
| [1]<3>   | CCC | BBB | AAA | AAA |
| [1]<4>   | CCC | BBB | BBB | AAA |
| [2]<1>   | BBB | BBB | AAA | AAA |
| [2]<2>   | CCC | BBB | AAA | AAA |
| [2]<3>   | CCC | CCC | AAA | AAA |
| [2]<4>   | CCC | CCC | BBB | AAA |
| [3]<1>   | BBB | BBB | BBB | AAA |
| [3]<2>   | CCC | BBB | BBB | AAA |
| [3]<3>   | CCC | CCC | BBB | AAA |
| [3]<4>   | CCC | CCC | CCC | AAA |
| [4]<1>   | BBB | BBB | BBB | BBB |
| [4]<2>   | CCC | BBB | BBB | BBB |
| [4]<3>   | CCC | CCC | BBB | BBB |
| [4]<4>   | CCC | CCC | CCC | BBB |

Thus,  $2 \frac{\cos(\pi Q)}{\cos(\pi Q - v)}$  is a common factor for all expression in table A.1 and removing this factor does not alter the rank of the matrix. We therefore obtain the simplified expressions shown in table A.2.

Let  $\tilde{J}$  be the column-wise stack of the  $3N$  coefficient vectors emerging from the simplified expressions in table A.2. Since all the used simplifications preserved the column span of the Jacobian (up to constant factors), the nullspace and thus the rank of  $\tilde{J}$  is similar to that of the original Jacobian  $J$ . Thus, it is sufficient to show that  $\tilde{J}$  is rank deficient, i.e. that there exists a vector  $\vec{v}$  such that  $\tilde{J} \cdot \vec{v} = \vec{0}$ . This matrix multiplication involves the row-wise summation of the various coefficient vectors that make up the matrix  $\tilde{J}$ . Each row contains at most the three distinct types A,B,C (see schematic 2). Thus, each row-wise sum is of the form

**Table A.1:** Expressions for the coefficient vectors for the different types A,B,C. The relationship  $\cos(x) + \cos(y) = 2 \cos(\frac{x+y}{2}) \cos(\frac{x-y}{2})$  has been used to combine the cos terms originating from the  $\Psi_{ks}$  and  $\Psi_{kb}$  terms. Note that for each (A,B,C), the only difference in the (1) and (2) expressions is the sign of the trailing terms.

|     |   |                                                                                   |
|-----|---|-----------------------------------------------------------------------------------|
| (1) | A | $2 \cos(2\pi Q + u) [\cos(v) - T \sin(v)] + \tilde{T}$                            |
|     | B | $2 \cos(u) [\cos(2\pi Q - v) + T \sin(2\pi Q - v)] - 2T \sin(2\pi Q) + \tilde{T}$ |
|     | C | $2 \cos(2\pi Q - u) [\cos(v) - T \sin(v)] + \tilde{T}$                            |
| (2) | A | $2 \cos(2\pi Q + u) [\cos(v) - T \sin(v)] - \tilde{T}$                            |
|     | B | $2 \cos(u) [\cos(2\pi Q - v) + T \sin(2\pi Q - v)] + 2T \sin(2\pi Q) - \tilde{T}$ |
|     | C | $2 \cos(2\pi Q - u) [\cos(v) - T \sin(v)] - \tilde{T}$                            |
| (3) | A | $2 \sin(2\pi Q + u) [\cos(v) - T \sin(v)]$                                        |
|     | B | $2 \sin(u) [\cos(2\pi Q - v) + T \sin(2\pi Q - v)]$                               |
|     | C | $-2 \sin(2\pi Q - u) [\cos(v) - T \sin(v)]$                                       |

## A. Appendix

**Table A.2:** Simplified expressions for the coefficient vectors for the different types A,B,C. The common factor  $2\frac{\cos(\pi Q)}{\cos(\pi Q - v)}$  has been removed from the expressions in table A.1.

|     |   |                                                                                                                         |
|-----|---|-------------------------------------------------------------------------------------------------------------------------|
| (1) | A | $\cos(2\pi Q + u) + \frac{\cos(v)}{4 \sin(\pi Q) \cos(\pi Q)}$                                                          |
|     | B | $\cos(u) + \left[ \frac{\cos(v)}{4 \sin(\pi Q) \cos(\pi Q)} - \frac{\sin(2\pi Q) \sin(\pi Q - v)}{\cos(\pi Q)} \right]$ |
|     | C | $\cos(2\pi Q - u) + \frac{\cos(v)}{4 \sin(\pi Q) \cos(\pi Q)}$                                                          |
| (2) | A | $\cos(2\pi Q + u) - \frac{\cos(v)}{4 \sin(\pi Q) \cos(\pi Q)}$                                                          |
|     | B | $\cos(u) - \left[ \frac{\cos(v)}{4 \sin(\pi Q) \cos(\pi Q)} - \frac{\sin(2\pi Q) \sin(\pi Q - v)}{\cos(\pi Q)} \right]$ |
|     | C | $\cos(2\pi Q - u) - \frac{\cos(v)}{4 \sin(\pi Q) \cos(\pi Q)}$                                                          |
| (3) | A | $\sin(2\pi Q + u)$                                                                                                      |
|     | B | $\sin(u)$                                                                                                               |
|     | C | $-\sin(2\pi Q - u)$                                                                                                     |

$\sum_{X \in \{A,B,C\}} \rho_X \cdot \{(1), X\} + \sum_{X \in \{A,B,C\}} \sigma_X \cdot \{(2), X\} + \sum_{X \in \{A,B,C\}} \tau_X \cdot \{(3), X\}$  where  $\rho_X$  stands for the sum of entries in  $\vec{v}$  corresponding to type  $\{(1), X\}$  in the coefficient matrix and similarly  $\sigma$  refers to type (2) and  $\tau$  to type (3). If we require  $\sum_{X \in \{A,B,C\}} (\rho_X - \sigma_X) = 0$  then the terms involving  $\frac{\cos(v)}{4 \sin(\pi Q) \cos(\pi Q)}$  in table A.2 vanish. Thus, we can create a further simplified matrix that consists of the expressions in table A.2 with these terms removed and augmented by an additional row which enforces the condition  $\sum_{X \in \{A,B,C\}} (\rho_X - \sigma_X) = 0$  which allowed the removal of those terms. The new version is shown in table A.3. It should be noted that this is not an equivalence transformation, but the nullspace of the new matrix is contained in the nullspace of the original matrix. Hence, it is sufficient to show that the new matrix represented by table A.3 is rank deficient.

**Table A.3:** Further simplified expressions for the coefficient vectors for the different types A,B,C. The additional requirement  $\sum_{X \in \{A,B,C\}} (\rho_X - \sigma_X) = 0$  has to be satisfied.

|     |   |                                                              |
|-----|---|--------------------------------------------------------------|
| (1) | A | $\cos(2\pi Q + u)$                                           |
|     | B | $\cos(u) - \frac{\sin(2\pi Q)}{\cos(\pi Q)} \sin(\pi Q - v)$ |
|     | C | $\cos(2\pi Q - u)$                                           |
| (2) | A | $\cos(2\pi Q + u)$                                           |
|     | B | $\cos(u) + \frac{\sin(2\pi Q)}{\cos(\pi Q)} \sin(\pi Q - v)$ |
|     | C | $\cos(2\pi Q - u)$                                           |
| (3) | A | $\sin(2\pi Q + u)$                                           |
|     | B | $\sin(u)$                                                    |
|     | C | $-\sin(2\pi Q - u)$                                          |

We can reorder the various terms of  $\tilde{J}$  to construct a new matrix  $\tilde{M}$  such that the columns of  $\tilde{M}$  correspond to  $\rho_i + \sigma_i$ ,  $\tau_i$  and  $\rho_i - \sigma_i$  (in that order) where  $i$  refers to the  $i$ -th column of the three matrices containing all type-(1,2,3) terms. This reordering preserves the dot product  $\tilde{J} \cdot \vec{v} = \tilde{M} \cdot \vec{v}$ . Only the  $\rho_i - \sigma_i$  terms depend on  $v$  while the other terms depend on  $u$ . The overall matrix thus consists of a column-wise stack of three sub-matrices corresponding to



$\rho_i + \sigma_i$ ,  $\tau_i$  and  $\rho_i - \sigma_i$  and has the following form:

$$\tilde{M} = \begin{bmatrix} & M^{\rho+\sigma} & & M^\tau & & M^{\rho-\sigma} & & & & \\ & & & & & & & & & \\ 0 & \dots & 0 & 0 & \dots & 0 & 1 & \dots & & 1 \end{bmatrix} \quad (\text{A.38})$$

The additional last row enforces the condition  $\sum_{X \in \{A,B,C\}} (\rho_X - \sigma_X) = 0$ . While the original Jacobian  $J$  has shape  $N^2 \times 3N$  (for  $N$  sections), the new matrix  $\tilde{M}$  has shape  $(N^2 + 1) \times 3N$ . By the above derivation, there exists a vector from the nullspace of  $\tilde{M}$  (given that the nullspace is not empty) that is contained in the nullspace of  $J$ . That is, if  $\tilde{M}$  is rank deficient it follows that  $J$  is rank deficient. Thus, it is sufficient to show that  $\tilde{M}$  is rank deficient. Because the rank of a matrix does not change under row- or column-wise multiplication with a nonzero constant, the common factor  $\frac{\sin(2\pi Q)}{\cos(\pi Q)}$  can be removed from the  $M^{\rho-\sigma}$  matrix leaving it with only  $\sin(\pi Q - v)$  terms.

Since the Gram matrix  $A^T A$  of any  $m \times n$  matrix  $A$  ( $m \geq n$ ) has the same rank as the original matrix  $A$ , it is sufficient to show that the Gram matrix of  $\tilde{M}$  is rank deficient. Since the Gram matrix is a square matrix, its determinant can be computed from the original matrix via the Cauchy-Binet formula [105]:

$$\det(\tilde{M}^T \tilde{M}) = \sum_{\alpha \in \text{INC}(m,n)} \det(\tilde{M}[\alpha|\underline{n}])^2 = 0 \quad (\text{A.39})$$

where  $\underline{n}$  denotes the set of numbers  $\{1, 2, \dots, n\}$  and  $\text{INC}(m, n)$  denotes the set of all strictly increasing functions from  $\underline{m}$  to  $\underline{n}$ ;  $\tilde{M}[\alpha|\underline{n}]$  denotes the sub-matrix of  $\tilde{M}$  that emerges from selecting the rows with indices given by  $\alpha$  and column indices given by  $\underline{n}$ .

Equation A.39 implies that the determinants of all individual sub-matrices  $\tilde{M}[\alpha|\underline{n}]$  need to be zero.

To further simplify the involved expressions, we make use of the identities  $\cos(x) = \frac{1}{2}(e^{ix} + e^{-ix})$  and  $\sin(x) = \frac{1}{2i}(e^{ix} - e^{-ix})$  which allow to replace the various cos, sin terms with the following expressions:

$$\begin{aligned} \cos(\mu_{\max} + \mu_{\min}) &= \frac{p^2 q^2 + 1}{2pq} \\ \cos(2\pi Q + \mu_{\max} + \mu_{\min}) &= \frac{p^2 q^2 g^4 + 1}{2pqq^2} \\ \cos(2\pi Q - \mu_{\max} - \mu_{\min}) &= \frac{p^2 q^2 + g^4}{2pqq^2} \\ \sin(\mu_{\max} + \mu_{\min}) &= \frac{p^2 q^2 - 1}{2ipq} \\ \sin(2\pi Q + \mu_{\max} + \mu_{\min}) &= \frac{p^2 q^2 g^4 - 1}{2ipqq^2} \\ \sin(2\pi Q - \mu_{\max} - \mu_{\min}) &= \frac{p^2 q^2 - c^4}{2ipqq^2} \\ \sin(\pi Q - \mu_{\max} + \mu_{\min}) &= \frac{q^2 g^2 - p^2}{2ipqg} \end{aligned} \quad (\text{A.40})$$

## A. Appendix

---

where  $p \equiv e^{i\mu_{\max}}$ ,  $q \equiv e^{i\mu_{\min}}$ ,  $g \equiv e^{i\pi Q}$  for the given values of  $\mu_{\max}, \mu_{\min}$  in each row.

It is sufficient to show the rank deficiency for the  $N = 3, n = 3$  (i.e. 3 sections containing quadrupole triplets) case; the general case  $N > 3$  follows from the symmetric placement of lattice elements from one section to another and  $n > 3$  follows from the fact that the same set of three coefficient vectors is sufficient to generate the Jacobian columns of any quadrupole  $n$ -tuple, i.e.  $\tilde{M}$  is a  $(N^2 + 1) \times 3N$  matrix independent of  $n$ .

The expressions in equation A.40 can be further simplified by multiplying columns 1,2,3 of  $\tilde{M}$  (containing only cos terms) by  $2g^2$ , columns 4,5,6 (containing only sin terms) by  $2ig^2$  and columns 7,8,9 (containing only sin terms) by  $2ig$ . Then the first row can be multiplied by  $(2ig)^{-1}$  and each other row can be multiplied by their respective  $pq$  whose inverse occurs in every element across a row. Note that these elementary row/column operations preserve the rank of the matrix. This yields the further simplified expressions given by:

$$\begin{aligned}
\cos(\mu_{\max} + \mu_{\min}) &\rightarrow p^2 q^2 g^2 + g^2 \\
\cos(2\pi Q + \mu_{\max} + \mu_{\min}) &\rightarrow p^2 q^2 g^4 + 1 \\
\cos(2\pi Q - \mu_{\max} - \mu_{\min}) &\rightarrow p^2 q^2 + g^4 \\
\sin(\mu_{\max} + \mu_{\min}) &\rightarrow p^2 q^2 g^2 - g^2 \\
\sin(2\pi Q + \mu_{\max} + \mu_{\min}) &\rightarrow p^2 q^2 g^4 - 1 \\
\sin(2\pi Q - \mu_{\max} - \mu_{\min}) &\rightarrow p^2 q^2 - g^4 \\
\sin(\pi Q - \mu_{\max} + \mu_{\min}) &\rightarrow q^2 g^2 - p^2
\end{aligned} \tag{A.41}$$

Thus, the resulting matrix, with cos, sin terms being replaced by equation A.41, contains only various polynomial terms as elements. With the help of a computer algebra system such as PARI/GP [106] it can be shown that the determinants of all  $9 \times 9$  sub-matrices of the simplified  $10 \times 9$  matrix  $\tilde{M}$  are identical to zero. From this follows that  $\tilde{M}$  is rank deficient, according to equation A.39. An example program is given by program 3.

It is worth noting that the proof does not make any assumptions on the values of  $\mu_{b,j}, \mu_{s,j}, Q$ . Thus, the rank deficiency holds for arbitrary values of  $\mu_{b,j}, \mu_{s,j}, Q$  and does not restrict the optics nor the specific placement of BPMs or steerers in terms of their phase advance.

---

**Program 3** PARI/GP program for verifying that the determinant of every  $9 \times 9$  sub-matrix of the  $10 \times 9$   $\tilde{M}$  matrix for the  $N = 3$  case is identical to zero. The simplifications from A.41 have been applied. The following abbreviations are used:  $\{a, b, c\} \equiv e^{i\mu_b, \{1,2,3\}}$ ,  $\{d, e, f\} \equiv e^{i\mu_s, \{1,2,3\}}$ ,  $g \equiv e^{i\pi Q}$ . PARI/GP version 2.13.4 has been used. The program can be run by copying it into a file `main.gp` and then running `path/to/gp2c-run main.gp` followed by typing `compute()`.

---

```
compute() =
{
M = [0,0,0,0,0,0,1,1,1;
a^2*d^2*g^2+g^2,a^2*d^2*g^4+1,a^2*d^2*g^4+1,a^2*d^2*g^2-g^2,a^2*d^2*g^4-1,a^2*d^2*g^4-1,a^2*g^2-d^2,0,0;
a^2*e^2*g^2+g^2,a^2*e^2*g^2+g^2,a^2*e^2*g^4+1,a^2*e^2*g^2-g^2,a^2*e^2*g^2-g^2,a^2*e^2*g^4-1,a^2*g^2-e^2,a^2*g^2-e^2,0;
a^2*f^2*g^2+g^2,a^2*f^2*g^2+g^2,a^2*f^2*g^2+g^2,a^2*f^2*g^2-g^2,a^2*f^2*g^2-g^2,a^2*f^2*g^2-g^2,a^2*f^2*g^2-f^2,a^2*g^2-f^2,a^2*g^2-f^2;
d^2*b^2+g^4,d^2*b^2*g^4+1,d^2*b^2*g^4+1,d^2*b^2-g^4,d^2*b^2*g^4-1,d^2*b^2*g^4-1,0,0,0;
d^2*c^2+g^4,d^2*c^2*g^2+g^2,d^2*c^2*g^4+1,d^2*c^2-g^4,d^2*c^2*g^2-g^2,d^2*c^2*g^4-1,0,d^2*g^2-c^2,0;
b^2*e^2+g^4,b^2*e^2*g^2+g^2,b^2*e^2*g^4+1,b^2*e^2-g^4,b^2*e^2*g^2-g^2,b^2*e^2*g^4-1,0,b^2*g^2-e^2,0;
b^2*f^2+g^4,b^2*f^2*g^2+g^2,b^2*f^2*g^2+g^2,b^2*f^2-g^4,b^2*f^2*g^2-g^2,b^2*f^2*g^2-g^2,0,b^2*g^2-f^2,b^2*g^2-f^2;
e^2*c^2+g^4,e^2*c^2+g^4,e^2*c^2*g^4+1,e^2*c^2-g^4,e^2*c^2-g^4,e^2*c^2-g^4,e^2*c^2*g^4-1,0,0,0;
c^2*f^2+g^4,c^2*f^2+g^4,c^2*f^2*g^2+g^2,c^2*f^2-g^4,c^2*f^2-g^4,c^2*f^2*g^2-g^2,0,0,c^2*g^2-f^2];
for (row = 1, 10, print(matdet(M[~row,])));
}
```

---

## A.7 Proof: $\mathbf{Sh}, \mathbf{Sv}, \mathbf{Q6}, \mathbf{Bh}, \mathbf{Bv}$ Jacobian is rank deficient

*This section has previously been published in Phys. Rev. Accel. Beams. Details are given in [75].*

The proof for the  $\mathbf{Sh}, \mathbf{Sv}, \mathbf{Q6}, \mathbf{Bh}, \mathbf{Bv}$  placement is analogous to the one obtained for  $\mathbf{S}, \mathbf{Q3}, \mathbf{B}$  (appendix A.6). Instead of three coefficient vectors there are six coefficient vectors, three for each dimension. These coefficient vectors are orthogonal since the horizontal coefficient vectors only have nonzero entries in the horizontal part of the Jacobian while the vertical coefficient vectors only have nonzero entries in the vertical part of the Jacobian and the two parts of the Jacobian are entirely separate. Hence, we can construct a matrix similar to  $\tilde{M}$  in equation A.38 but now the matrix is a block diagonal of shape  $(2N^2 + 2) \times 6N$  where the upper-left block is the  $\tilde{M}$  for the horizontal dimension and the lower-right block is the  $\tilde{M}$  for the vertical dimension. Both blocks independently induce a rank deficiency as shown in A.6. Thus, the rank deficiency for the  $\mathbf{Sh}, \mathbf{Sv}, \mathbf{Q6}, \mathbf{Bh}, \mathbf{Bv}$  Jacobian is twice the one for  $\mathbf{S}, \mathbf{Q3}, \mathbf{B}$ .



Publiziert unter der Creative Commons-Lizenz Namensnennung (CC BY) 4.0 International.  
Published under a Creative Commons Attribution (CC BY) 4.0 International License.  
<https://creativecommons.org/licenses/by/4.0/>